Author:
Yang, Limin

Title:
Cobalt and beryllium in diamond

experimental and first-principles calculations of magnetic and electronic properties

Cobalt and Beryllium in Diamond: Experimental and First-Principles Calculations of Magnetic and Electronic Properties

Limin Yang

School of Chemistry
University of Bristol

A dissertation submitted to the University of Bristol in accordance with the requirements of the degree of Doctor of Philosophy in the Faculty of Science.

August 2021

Word count: ~ 37700

ABSTRACT

Diamond is a special material with extraordinary mechanical and electrical properties. To extend its applications to more areas, in this thesis, we implemented the preparation and characterisation of magnetic diamond film composites and the theoretical study of n-type doping of diamond. Diamond with modified magnetic and electronic properties may find applications in electromagnetic devices and be used in extreme environments.

In the experimental section, we studied the preparation and properties of magnetic diamond composites, in which patterned magnetic material (Co nanoparticles or thin films) were used as part of the substrate to grow diamond film by chemical vapour deposition (CVD), aiming at imbuing ferromagnetic properties to the diamond film. Co was patterned by laser cutting or lift-off fabrication. After CVD diamond growth, the patterned Co was coated with a diamond film. The magnetic signal from the underlying Co was detected by magnetic force microscopy (MFM) through the 1 – 2 μm thick diamond film. Due to the robustness of diamond, the diamond film is expected to work as a protective layer, which will provide a comprehensive protection to magnetic devices.

The basic components required for making semiconductor devices are n- and p-type semiconductor materials. While p-type diamond can be made easily by boron doping, the preparation of n-type diamond remains problematic. The maturity of density-functional theory and the development of high-performance computing make it possible to simulate the electronic or magnetic properties of a given system. In the theoretical sections, we used the CRYSTAL 17 package to study the probability of using Be or Be-N clusters as dopants for making n-type diamond. Various substitutional and interstitial defect positions were investigated in terms of the thermodynamic, magnetic and electrical properties. Our calculation results suggest that it is hard to bring useable n-type semiconductivity to diamond at room temperature by single-element doping of Be. The ground-state of Be in diamond is a single substitutional defect, which imparts p-type semiconductivity to the diamond, but this has a high activation energy of ~ 1.2 eV. Although Be

situated at an alternative tetrahedral interstitial site makes diamond n-type semiconductive and works as a shallow donor with the defect level 0.47 eV below the conduction band, this defect has a formation energy ~ 8.7 eV higher than that of the single substitutional defect, and so is unlikely to form.

For the theoretical study of Be-N clusters in diamond, Be and N were found to enhance the incorporation of each other, and therefore they are situated at adjacent single substitutional sites to reach the minimum energy state. The Be_sN_3 and Be_sN_4 clusters (a single substitutional Be in the centre, surrounded by 3 or 4 substitutional N atoms) behave as shallow donors in diamond, with donor levels of 0.51 and 0.46 eV below the conduction band minimum. The formation of such clusters requires a coincidence of Be and its surrounding N atoms. A two-step preparation scheme was proposed for making such complex clusters, *i.e.*, VN_3 and VN_4 complexes can be made first, followed by the ion implantation of Be into the vacancies. The theoretical study in this thesis may provide some new ideas to the preparation of n-type diamond.

PUBLICATIONS

1. L. Yang, N. L. Allan, M. D. Williams and P. W. May, First-principles theoretical study of Be-doped diamond: electronic and magnetic properties, (in preparation, will be submitted to *Carbon*, this paper contributed to Chapter 4)
2. L. Yang, N. L. Allan, M. D. Williams and P. W. May, Theoretical study of Be-N clusters in diamond (in preparation, this paper contributed to Chapter 5)
3. L. Yang, J. Kačmarčík, Z. Li, X. Liang, R. Zulkharnay, S. Zhou, B. D. Howchen, P. Szabó, Y. Li, H. Rubahn, P. Samuely, V. V. Moshchalkov, P. W. May, and G. Zhang, Room-temperature ferromagnetism and enhanced Hall mobility in annealed hybrids of boron-doped diamond and magnetic nanoparticles (in preparation, will be submitted to *Applied Physics Letters* or *Journal of Applied Physics*, collaborative project, results are not included in this thesis)

ACKNOWLEDGEMENTS

It is such a blessing to come to the UK and study here with amazing supervisors and colleagues. It is also a special experience to finish the study during the global coronavirus pandemic. All these things remind me how precious this study opportunity is and there are so many lovely people I should give thanks to.

My sincere gratitude goes to my supervisor Prof. Paul May, who guided me in the research and helped me build up the academic skills in the four years of study. This thesis would not have been finished and submitted on time without his support. My thanks also go to Prof. Neil Allan for supervising my computational work, to Prof. Neil Fox for his insightful comments and encouragement, and to Dr. Gufei Zhang at University of Southern Denmark for supervising the side project and supporting my research.

I also want to thank Drs Max Williams, Fabian Fogarty and Tahani Almutairi for the helpful advice and discussions of the theoretical work. Thanks go to Dr. James Smith for training me on the many facilities in the lab, to Ed Smith for training me on the many reactors and laser-cutting machine, to Ramiz Zulkharnay, Michael James and Robbie Mackenzie for training me to use various other equipment in the diamond lab. Also, thanks to Dr. Jean-Charles Eloi for doing SEM and Dr. Robert Harniman for the AFM measurements, and to Dr. Serkan Kaya for the training and help of the lift-off experiment in the University Cleanroom.

To my friends Dominic Palubiski, Adam Kirwan and Matt Brumwell, thank you for the good times spent together in the lab and out of the lab. To all the brothers and sisters in Trinity Church Bristol and Bristol Chinese Baptist Church, to my friends Su Liu and Xian Zhang, thank you all for enriching my life and helping me explore the most important things in life. Thanks to Chinese Scholarship Council and University of Bristol for the financial support.

COVID-19 STATEMENT

A lot of the work in this thesis were performed during the Covid-19 pandemic, which caused a lot of delays and problems. Due to the long-term lockdown and restrictions, I was not able to go to the lab regularly to do many experiments. A lot of research activities such as the preparations of patterned Co and diamond film growth (in Chapter 3) were curtailed as a result. More samples with better performance would have been made if they were not curtailed. Also, most calculation jobs (Chapters 4 and 5) were submitted and data downloaded at home using the VPN service. The low downloading and uploading speeds made it take a long time and many times the connections with the BlueCrystal were lost while transferring files and they had to be restarted. The thesis and manuscripts for publications were also written at home during the time of Covid restrictions. Because of the Covid restrictions, I was not able to meet my supervisors in person and therefore not able to discuss the progress easily. Therefore, the publications were also delayed.

AUTHOR'S DECLARATION

I declare that the work in this dissertation was carried out in accordance with the requirements of the University's Regulations and Code of Practice for Research Degree Programmes and that it has not been submitted for any other academic award. Except where indicated by specific reference in the text, the work is the candidate's own work. Work done in collaboration with, or with the assistance of, others, is indicated as such. Any views expressed in the dissertation are those of the author.

SIGNED: ..... DATE: .....

TABLE OF CONTENTS

LIST OF ABBREVIATIONS

AFM	atomic force microscope
BDD	boron doped diamond
BSE	back-scattered electron
CBM	conduction band minimum
CVD	chemical vapour deposition
DFT	density functional theory
DLC	diamond like carbon
DOS	density of states
E_{b}	binding energy
E_{c}	conduction band edge
EDX	energy-dispersive X-ray spectroscopy
E_{f}	formation energy
EMM	empirical marker method
ESI	electrospray ionization
E_{v}	valence band edge
E_{XC}	exchange-correlation energy
FM	ferromagnetic
FOV	field of view
GGA	generalized gradient approximation
GTO	Gaussian-type orbital
HCP	hexagonal closed-packed
HF	Hartree-Fock
HFCVD	hot-filament chemical vapour deposition
HPHT	high-pressure high-temperature

HSE	Heyd-Scuseria-Ernzerhof
LDA	local-density approximation
LSDA	local-spin-density approximation
MFM	magnetic force microscope
PBE	Perdew-Burke-Ernzerhof
PEEM	photoemission electron microscopy
QCM	quartz crystal microbalance
SCD	single crystal diamond
SCF	self-consistent field
SE	secondary electrons
SEM	scanning electron microscopy
STO	Slater-type orbital
TEM	transmission electron microscopy
TZVP	triple zeta valence polarisation
VBM	valence band maximum

LIST OF TABLES

LIST OF FIGURES

CHAPTER 1

INTRODUCTION

This chapter presents a general introduction to diamond science and technology. It is comprised of five parts. The first part details some basic information and properties of diamond. The second part describes the technology used for synthesis of diamond. The third part introduces magnetic properties of diamond. The fourth part is about the electronic properties of diamond, the fifth section is a review of n-type doping of diamond, and the last section is an outline of the results sections of this thesis.

1.1 Overview of diamond

When it comes to diamond, the first impression is likely to be that of shiny jewellery. The name diamond originates from the ancient Greek word "*adamas*", which means unbreakable [1]. Because of its high reflectance and sparkly appearance, diamond is widely used as a gemstone in neckless and rings, especially for in engagements and weddings. As Marylin Monroe famously sang, "Diamonds are a girl's best friend". Due to its high price, diamond is not only a symbol for love, but also a symbol for wealth and social status.

In nature, diamonds were formed millions or even billions of years ago deep (150–200 km) underground, where both pressure (4–6 GPa) and temperature (900–1200 °C) were extremely high [2]. They are brought to the surface in volcanic eruptions, where they are now accessible via mining. Before the emergence of lab-grown diamond, the only source of diamond was from diamond mines, which were (and still are) under the strict control of only a few companies in the world [3]. This remains one of the most important reasons that diamonds are so expensive. Even after the emergence of synthetic diamond technology, diamond for jewellery

usage still mainly comes from diamond mines in countries such as South Africa, Australia, Canada and Russia. In recent years, some jewellery companies have been synthesizing gem-quality diamonds using the fabrication methods detailed later. These 'lab-grown' gem diamonds are now becoming available in jewellery stores at lower cost than natural stones, and this may significantly change the diamond gem market in the next few years.

Although diamond looks so beautiful and elegant, it has a simple elemental composition. Pure diamond is an allotrope of carbon. Each carbon atom in diamond is sp^3 hybridised; the 2s orbital is mixed with the three 2p orbitals to form 4 identical sp^3 orbitals which repel each other to form a tetrahedral shape. Each sp^3 orbital contains one electron from the central carbon, allowing occupancy by a second electron from a neighbouring carbon, forming a covalent sigma bond between the 2 C atoms. The 4 bonds have the same length of 1.54 Å, forming a tetrahedral, face-centred cubic structure, as illustrated in Figure 1.1. In diamond, all the valence electrons participate in the covalent bonding. There are no free electrons available to move through the lattice, so pure diamond is an electrical insulator. These covalent bonds are so strong that a high level of energy is required to break them. This is why diamond has a very high melting point [4].

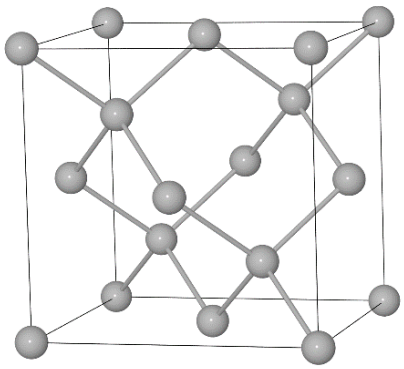

Figure 1.1. Lattice structure of diamond.

The special configuration of carbon atom gives diamond a number of superlative physical properties. Diamond is the hardest material in natural world, with a hardness of 10 on Mohs scale [5]. Diamond has a high wear resistance [6], low friction coefficient (~ 0.1 for lubricated friction against Al [7]), high Young's modulus (~ 1050 GPa [8]), high thermal conductivity (~ 22 W cm^{-1} K^{-1} [9]) and low

thermal expansion coefficient (1×10^{-6} K^{-1} at 20 °C [10]). Due to these advantages, diamond has been widely applied in mechanical engineering, especially in cutting tools for high-precision machining.

Diamond is also chemically stable, not reactive with any acid or alkali. For this reason, some acids are often used for the purification of diamond [11]. Due to the inertness of diamond, diamond has found new application for electroanalysis [12] such as water treatment [13]. The electrodes made of diamond can last for a long time without chemical corrosion. Nano sized diamond has very low toxicity with few harmful biological effects when ingested. Therefore, it has found a broad application in biomedical areas such drug delivery and biomonitoring [14].

Diamond is transparent from 225 nm (ultraviolet) to the far infrared, only having a small absorption band from 2.5 to 6.5 μm [15]. Moreover, due to the large band gap of diamond (~ 5.47 eV [16]), its transparency is not degraded even at high temperature and radiant intensity. Therefore, diamond is a promising material for optical engineering, and has been used for high-power laser optics and windows [17].

In addition, diamond is a promising candidate for next-generation semiconductors because of its wide band gap, high thermal conductivity and high breakdown field [16]. This will be discussed later.

1.2 Synthesis of diamond

The extraordinary properties of diamond have been attracting research for nearly two centuries. Once it was proven that diamond is an allotrope of carbon [18], researchers started searching for methods to synthesise it. There are two main methods to synthesize diamond, high-pressure high-temperature (HPHT) methods and chemical vapour deposition (CVD). There are many differences between these two methods which will be explained in the next sections.

1.2.1 High-pressure high-temperature preparation

Before introducing this method, it is necessary to look into phase transition between diamond and graphite, the two allotropes of carbon. The difference

between them lies in the different bonding types giving rise to two distinct structures. Under some specific circumstance, diamond and graphite can transform between each other.

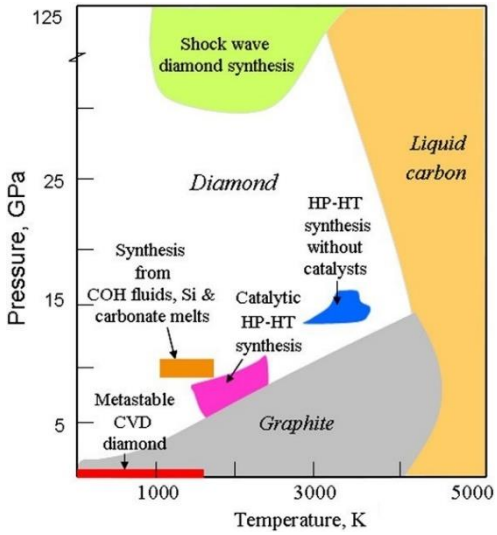

Figure 1.2. Phase diagram of carbon [19].

Figure 1.2 shows the phase diagram of carbon. As can be seen, diamond, compared with graphite, is the more stable phase at high pressure and high temperature. However, diamond is thermodynamically a metastable phase at room pressure and temperature. Although the enthalpy difference between diamond and graphite is only 2.9 kJ mol^{-1} [20], this does not mean that diamond will convert into graphite spontaneously. In fact, there is a huge energy barrier between diamond and graphite such that the conversion between diamond and graphite is almost impossible at room pressure and temperature. It is also due to this high energy barrier between diamond and graphite that means they can both exist under the same conditions.

According to the phase diagram of carbon, when the pressure and temperature increase beyond certain values, graphite should convert into diamond, although the activation barrier still makes this a very slow process. This is the way diamond forms naturally. Carbon that is buried deep underground (50 km) is subjected to huge pressures and temperatures. The presence of metallic impurities (such as Ni) in the rocks act as catalysts. The carbon dissolves into these impurities, and when the metal becomes saturated, the carbon precipitates out; due to the ambient high-

pressure high-temperature conditions, the carbon crystallises as 'natural' diamond.

HPHT synthesis mimics this natural diamond formation process. In 1955, synthetic diamonds were reported for the first time by the lab of the General Electric Company [21]. A belt-type apparatus was employed to generate a static high pressure, and salt-like carbides were used as the starting material [22]. The salt-like carbides contained not only carbon, but also some transition metals such as iron, which worked as catalyst. Since then, to get higher and more stable pressures, researchers have designed many different types of multi-anvil, high pressure apparatus, such as tetrahedral-anvil apparatus [23], cubic-anvil apparatus [24] and split-sphere apparatus [25].

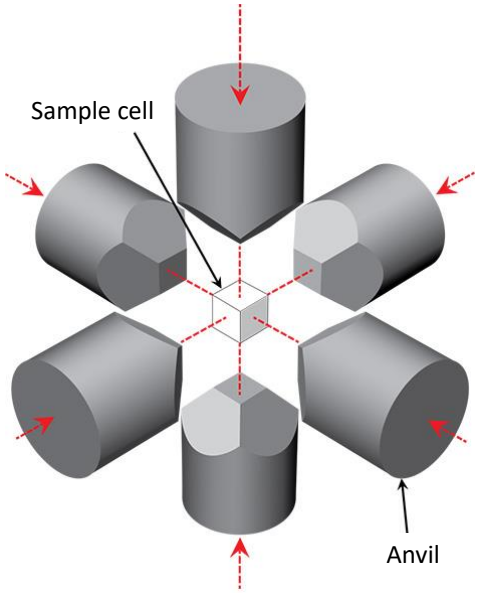

Figure 1.3. Schematic diagram of a HPHT cubic-anvil apparatus [26].

For the HPHT method, the difficulty lies in the generation of high and durable pressure. The operating principles of HPHT multi-anvil apparatus are similar [27]. For example, Figure 1.3 shows a schematic diagram of a HPHT cubic-anvil apparatus. The whole apparatus is usually driven by pairs (2, 4 or 6) of hydraulic rams, distributed uniformly around the body. High pressure goes through multi stages and increases further when reaching the small polyhedron assembly in the centre. High temperature is realized by electrical heating. The raw material in the centre is usually a mixture of graphite and catalysts such as Fe, Ni and Co [28]. A

catalyst is often used to accelerate the reaction and lower the pressure required to transform graphite to diamond. Even though it is possible to convert graphite to diamond directly without any catalyst, a much higher pressure (> 10 GPa) and temperature must be satisfied [29].

The HPHT method has been used since the 1950s to synthesize small diamond particles of size up to ~1 mm. Because some nitrogen becomes incorporated into the diamond during the HPHT process, the diamonds are often a yellowish/brown, which makes them unsuitable for jewellery. However, they are still used for cutting tools, milling and saws, and so-called 'industrial diamonds' remain a multi-million-dollar industry today.

Recently, the HPHT process has been improved to grow large, colourless, gem-quality diamond, and this is beginning to have an impact on the gemstone market.

Apart from the static high-pressure synthesis, there is also another way named detonation synthesis [30]. In this way, high pressure and high temperature are generated through explosion of TNT in a sealed oxygen-free environment. The shockwave fuses together the carbon atoms from the high explosive within microseconds [31]. The diamonds obtained in this way are usually nano sized, and these are often used for seeding (see later), cooling, polishing and even drug delivery [32].

1.2.2 Chemical vapour deposition

As shown in Figure 1.2, diamond is metastable at low pressure. This means it is not possible to grow diamond under thermodynamic control under these conditions; however, it is possible using kinetic control. CVD is a process that decomposes a carbonaceous gas and deposits sp^3-hybridized carbon onto a substrate. Compared with the HPHT method, CVD does not need as much energy and can grow diamond without using an expensive metallic catalyst. Given the nature of the CVD process, it can grow large single-crystal diamond gemstones or diamond film onto different substrates of various shapes, making it more widely applicable.

The attempts to grow diamond under low pressure started in around 1950, when several groups from the world, including the lab of General Electric, tried many

methods to grow diamond using different gases such as CO, CH_4, CCl_4 and CBr_4 [33]. In 1962, low-pressure synthesis of diamond was reported by Eversole, who used hydrocarbons and carbon monoxide as precursor gases [34], but the growth rate was very slow due to high content of graphite in the product. In 1968, John Angus' group improved this process by introducing hydrogen into the system [35]. Because hydrogen could etch the unwanted graphite, the growth rate was increased and the purity greatly improved. A big advance occurred in 1982, when Matsumoto *et al.* from National Institute for Research in Inorganic Materials (NIRIM) in Japan built a reactor that could grow diamond at the rate of microns per hour, and this reactor became the prototype of hot filament reactors [36, 37]. In 1983, the same group at NIRIM built the first microwave CVD reactor with a maximum growth rate of ~ 3 μm/h [38].

After about 40 years' development, CVD reactors have evolved into different types. Depending upon the different methods of activating the precursor gas (usually methane and hydrogen), CVD reactors can be divided into a few types, such as hot filament CVD (HFCVD), microwave CVD (MWCVD), radio-frequency (RF) CVD [39] and laser-assisted CVD, and for each of them there are various configurations [1]. Here, the HFCVD reactors and one type of MWCVD reactor are introduced because they are both popular.

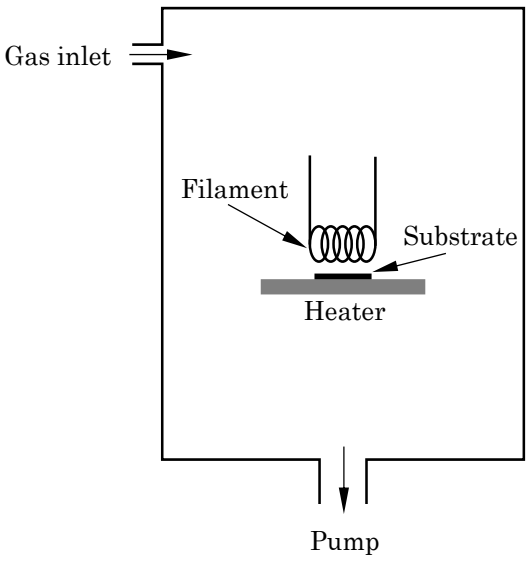

Figure 1.4. Schematic diagram of a HFCVD reactor.

Figure 1.4 shows a schematic diagram of a HFCVD reactor. The chamber is connected to a pump to pump out all the air (base pressure typically 10 mTorr), and to maintain it at the correct process pressure (~ 20–30 Torr) during operation. The filament, which is usually a thin tantalum or tungsten wire, is electrically heated to a temperature of 2000 °C. This activates the precursor gases, as well as providing radiant heat to increase the temperature of the nearby substrate to ~ 800 – 900 °C. Diamond is deposited on a substrate such as Si, which sits on a heater directly below (3-5 mm) the filament. The heater is pre-heated to provide a uniform temperature distribution and to avoid internal stresses in the sample. The gas mixture (typically 1% CH_4 in H_2) is flowed into the chamber and is decomposed on the filament surface into a 'soup' of chemically reactive species, such as C and H atoms, CH, CH_2 and CH_3 species, C_2, C_2H, C_2H_2, etc. These species diffuse around the chamber, any that land onto the substrate may deposit as a carbon coating. sp^2 carbon (graphitic) phases are rapidly etched back into the gas phase, whilst sp^3 (diamond) phases remain and propagate the diamond film.

Overall, a HFCVD reactor is cheap, durable, easy to construct and easy to operate; however, it also has some disadvantages. Because the metallic filaments are sensitive to some gases, such as oxygen, the kinds of precursor gas are very limited. Metal particles evaporated from the hot filaments can also contaminate the growing diamond film. Although these impurity concentrations are very low, they can be a serious problem for some electronic applications, *e.g.*, semiconductor devices. Furthermore, the reactor power is limited by the melting point of the filaments to typically ~ 500 W, which limits the growth rate of diamond to typically 0.5 – 1 μm h^{-1}.

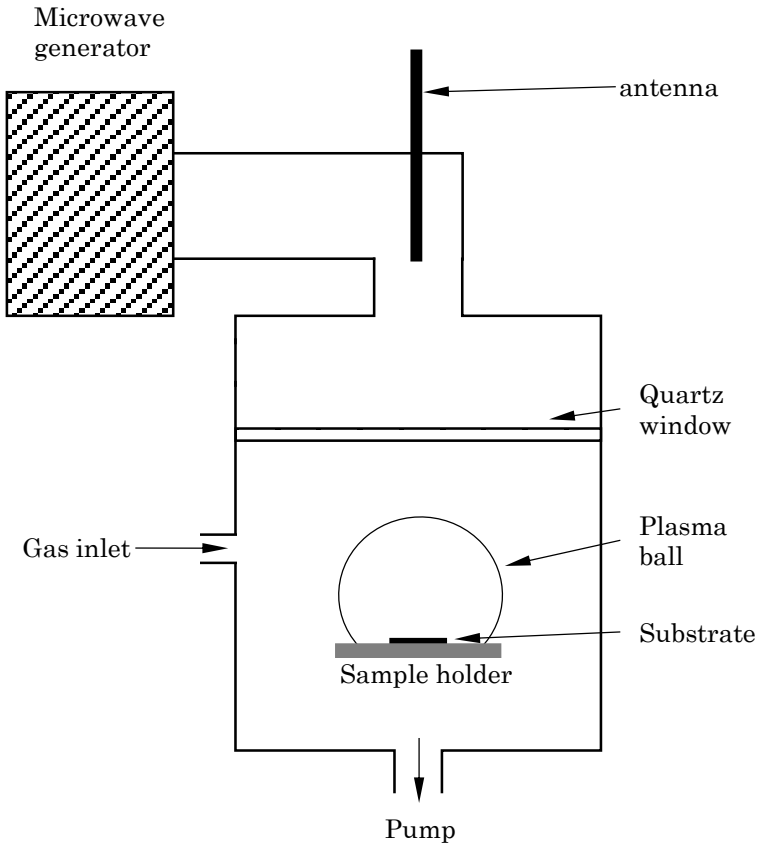

Figure 1.5. Schematic diagram of an ASTeX-type MWCVD reactor.

A microwave (MW) CVD reactor uses microwaves to activate the precursor gas. A schematic diagram of a typical MWCVD reactor is shown in Figure 1.5. The MWCVD reactor shown in Figure 1.5 was first commercialized by the ASTeX company, so it is also known as an "ASTeX-type" reactor. In this reactor, the chamber is divided into two parts by quartz window. The volume above the window is at atmospheric pressure and usually has air or dry nitrogen blown over it to keep the window cool. The volume beneath the quartz window is connected to a rotary pump which can evacuate it to a base pressure of ~10 mTorr. During CVD, the process gases are flowed into this lower chamber via appropriate mass flow controllers, while the process pressure is controlled between 10-200 Torr using a butterfly valve that throttles the pump. A plasma is generated by the application of microwave power, which is launched into the chamber via an antenna. The chamber is a tuned cavity, such that the distance from the top to the bottom is a whole number of half-wavelengths of the MW (2.54 GHz). The quartz window is transparent to microwaves, so even though there will be two nodes (maxima in the

MW transmission power) close to the top and bottom of the chamber, the one at the top will not strike a plasma because the pressure there is too high. Conversely, at the node in the low-pressure region close to the bottom of the chamber where the substrate sits, the power density is high and the pressure is low, and thus a ball-shape plasma is formed. The high-energy plasma activates the flowing gas, setting up a chemical soup in the same way as described above, leading to deposition onto substrate. Both the plasma power and pressure of the chamber can be adjusted to get the desired growth rate and diamond quality, and the shape of plasma changes with the changing of pressure and power.

Compared with an HFCVD reactor, a MWCVD reactor is more complicated to set up, more difficult to operate and substantially more expensive. However, its advantages are that, without a filament, the diamond is less contaminated and the process is more environmentally friendly. The lack of a filament also means that there are far fewer restrictions on the gas types that can be used. A MW reactor can operate with O_2 or Cl_2 gas mixtures, which allows much greater flexibility in process gas mixtures. Further, there are no restrictions upon the power-levels used, and a MWCVD reactor can generally work at much higher powers (1-50 kW, with 5 kW being typical) compared with an HFCVD reactor, which leads to diamond growth rates that could also be 10 times faster. Therefore, MWCVD is an efficient way to grow large-size and high-quality diamond film and single crystals, and is the method of choice for most researchers to deposit diamond films for electronic applications.

1.3 Magnetism in diamond

Magnetic materials have found many applications in mechanical engineering, electronics, biological engineering and the military. For instance, Co-Cr-Pt, a magnetic alloy, has been widely used in hard-disk drives for data storage [40]. Some biocompatible materials, such as magnetic colloidal nanoparticles, have been applied for molecular imaging [41] and drug delivery [42, 43]. For some materials showing both magnetic and semiconductor properties, their charge state (n or p type) and spin state (up or down) can be controlled at the same time. The coexisting properties of charge and spin allow a total control of spin polarization

[44], which can be used to make diluted magnetic semiconductors [45] and to make spin transistors working as both switches and data-storage media [46] at the same time.

The magnetic behaviours of materials can be divided into five types, which will be explained in the following.

1. Diamagnetism

Diamagnetism is the most common magnetic property of materials. In diamagnetic materials, there are no unpaired electrons, therefore, no magnetic moment. When diamagnetic material is placed in magnetic field, a negative magnetization is produced, making it repelled by the magnetic field.

2. Paramagnetism

For a paramagnetic material, due to the presence of unpaired electrons, the electrons spin directions will align with the external magnetic field and be attracted by a magnet. However, because thermal motion disturbs the spin directions, the magnetization drops to zero when external magnetic field is removed.

3. Ferromagnetism

Compared with paramagnetic material, the atomic moment in ferromagnetic material is stronger. Typical ferromagnetic materials are iron, cobalt and nickel. They show a large net magnetization in a magnetic field and part of the magnetization will be remained even after the external magnetic field is removed.

4. Ferrimagnetism

In Ferrimagnets, there are two phases, generating two magnetic moments in different directions. These two magnetic moments are not equal, giving a net magnetic moment to the system. Therefore, ferrimagnetism is similar to ferromagnetism.

5. Antiferromagnetism

In a ferrimagnetic material, when the two magnetic moments are equal but still in opposite orientations, they will cancel each other and the net magnetic moment will be zero. This magnetic property is called antiferromagnetism.

Therefore, the existence of unpaired electrons is essential to give an element or a compound magnetic moment. For example, one of the most commonly used magnetic elements, Fe, with an electron configuration of $[Ar]3d^6 4s^2$, has four unpaired electrons in its 3d subshell if it is in a high spin configuration, making it show strong ferromagnetism. Co ($[Ar]3d^7 4s^2$), with three unpaired electrons in the 3d subshell in a high spin configuration, also shows ferromagnetic properties.

As we know, in diamond, for each carbon atom, the four valence electrons ($2s2p^3$) participate in the formation of 4 identical covalent bond. This closed-shell configuration means that there are no free, unpaired electrons in diamond. Therefore, pure diamond does not show any ferromagnetic characteristics. Actually, pure diamond shows a diamagnetism ($\chi_m = -5.9 \times 10^{-6} cm^{-3} mol^{-1}$) [47, 48]. However, due to the presence of defects, which can occur in either natural or lab-grown diamond, there are possibilities to produce magnetic diamond with free, unpaired electrons. Magnetic diamond is undoubtedly a new promising material which could extend the applications of diamond to more areas.

1.3.1 Magnetic elements in diamond

A very direct way to imbue diamond with magnetic properties is by doping it with a magnetic element. This kind of doping has been achieved deliberately and accidentally. For example, during HPHT synthesis of diamond, transition metals such as Fe, Co and Ni are often selected as catalysts [22]. These ferromagnetic elements can become incorporated into the diamond crystals making the synthetic diamond magnetic. These elements could potentially be situated within the lattice as point defects, or on the surface of diamond. Research shows that these three elements do not have the same incorporation probability. Experimental results indicate that compared with Co and Ni, Fe is less likely to be incorporated into the diamond lattice, even though Fe is usually used as a main catalyst in HPHT diamond synthesis [28]. This experimental result agrees with *ab initio* calculations

showing that among those three metals, Ni is the most stable impurity, followed by Co, while Fe does not appear to be very stable in diamond, the reason being the large radius of Fe [49].

Considering the rigid crystalline structure of diamond, it is not easy to dope diamond with large atom, such as Fe. Nevertheless, there are still some ways to do this, for example, by ion-implantation [50]. Chen *et al.* prepared Fe-doped nanodiamond particles by using high-dose ion-implantation of Fe (3×10^{15} cm^{-3}); the internal stress from lattice damage was partially relieved by a post thermal anneal at 600 °C [51]. Because Fe is implanted inside of diamond lattice, this kind of magnetic diamond is free from toxicity and could be applied for magnetic resonance imaging of living cells [52].

Compared with doping Fe or other magnetic elements into the diamond lattice, it is much easier to coat the surface of diamond with them instead. For example, Fe-coated magnetic nanodiamond was prepared from diamond-ferrocene mixtures by microwave irradiation, and the prepared ferromagnetic nanodiamond could be used for cellular imaging [53]. In addition to the preparation of magnetic nanodiamond, Fe-coated [54] and Ni-coated [55] micron-sized diamond composites were fabricated by electroless plating. Fe and Ni work as binding materials and this kind of micron-scale magnetic diamond can be used as abrasive powders to make cutting tool for polishing and grinding.

For CVD diamond, it is a different situation because the CVD process does not use a metallic catalyst. Instead, doping experiments have been attempted by using magnetic substrates, *e.g.*, steel, even though this is not an ideal substrate for diamond growth. Experiment shows that when stainless steel was used as a substrate in diamond CVD, ferromagnetic Fe diffused from the substrate into the diamond film, making the deposited film show ferromagnetic properties [56]. However, this work did not report whether the Fe diffused into diamond lattice itself or into the sp^2 grain boundary regions. Researchers have also tried to dope Fe into CVD diamond using ion-implantation and tested the magnetic properties. However, even at high implantation doses (30–600 ppm of Fe), they could only find localised paramagnetic centres resulting from disorder (such as damage and

vacancies) while the whole sample was still dominated by the diamagnetism of diamond [57].

1.3.2 Magnetic diamond without metallic impurities

Metal-free magnetic diamond is a special kind of diamond that does not contain any metal but exhibits magnetism. The magnetic moment is believed to come from the electron configuration of carbon rather than metallic impurities. Compared with magnetic diamond containing metallic impurities, metal-free magnetic diamond is much safer and more biocompatible, which makes it specifically suitable for biological engineering such as fluorescence imaging and drug delivery. The formation of ferromagnetism in metal-free diamond is very complicated, and not yet fully understood. So far, there are two theories to explain the origin of ferromagnetism in metal-free magnetic diamond.

The first theory attributes the origin of ferromagnetism to a mixture of sp^2 and sp^3 structures. Theoretical calculations indicate that in carbon materials, if sp^3-hybridized carbon atoms are linked with sp^2-hybridized carbon forming a stable three-dimensional structure, the resulting magnetic moment could be very high [58]. This prediction suggested a possible method to make carbon material ferromagnetic without adding metallic elements. Proton irradiation can make graphite show ferromagnetic properties, and the mixed sp^2 and sp^3 structure induced by proton bombardment and implantation was suggested to be the origin of the magnetism [59, 60]. Nitrogen and carbon ion implantation can also make diamond ferromagnetic, and similar structural modifications were suggested to be the origin of ferromagnetism [61]. However, *ab initio* calculations indicated that the mixed sp^2-sp^3 structure was unstable [62].

Another explanation is that hydrogen plays a key role in the ferromagnetism of carbon materials and a high ratio of H/C leads to high magnetization [63, 64]. *Ab initio* simulations indicated that when hydrogen is adsorbed into vacancies of graphite, the vacancy-hydrogen complex will be magnetic and the sample will give a macroscopic magnetic signal [65]. Experiments showed that the carbon-hydrogen bond on the surface of graphite exhibits a ferromagnetic state [66].

Ferromagnetism was also detected in hydrogenated boron-doped nanodiamond films [67]. In this case, hydrogenation on the surface, rather than the sp^2 – sp^3 bonding defect, was suggested to be the origin of ferromagnetism.

Metal-free ferromagnetic nanodiamond has even been produced commercially [68], which was obtained through modification of laser assisted synthesized nanodiamond [69]. In this magnetic diamond, the content of metallic impurities was substantially lower than that found in nanodiamond produced by the normal detonation method, which did not show any obvious magnetic behaviour. However, the origin and mechanism of this metal-free magnetic diamond were not disclosed.

1.3.3 Diamond film grown on magnetic material

Magnetic particles and thin films may have applications for nanoscale magnetic data storage [70], magnetic detection [71] and logic devices [72]. Figure 1.6 shows a schematic diagram of longitudinal magnetic recording [70]. Magnetization directions of different magnetic regions or separate magnetic particles, which represent the binary number 1 or 0, can be read and written by a moving magnetic head. The active magnetic layer must be protected from wear and tear, or from damage by any potential read-write head by a non-magnetic, non-conducting, robust material [73]. Considering the super stability of diamond, diamond film could be used as a protective layer to protect these magnetic regions for the application in extreme environment.

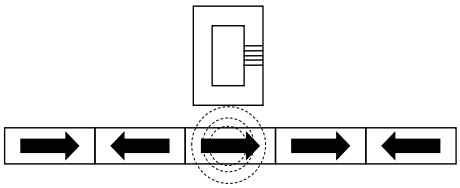

Figure 1.6. Schematic of longitudinal magnetic recording.

Another potential application of diamond film is to be used as a protective layer for magnetic logic devices. Magnetic logic devices are composed of patterned magnetic wire or film, which are designed based on their magnetic effect. Magnetization states, *i.e.*, spin up or down, can be controlled by an electric input signal, while the state can be maintained without a continuous electrical input.

Therefore, magnetic logic devices consume less energy and dissipate less heat compared with the conventional CMOS electronics [74]. It also has the advantages of small size and high switching speed [72, 75]. Logic commands such as AND, OR and NOT can be realized through a well-designed magnetic structure. For example, Figure 1.7 shows a schematic diagram of a Y-shaped AND gate [72, 75]. Only when (1,1) is the input, can the two magnetic domains converge into a combined output, which represent "1".

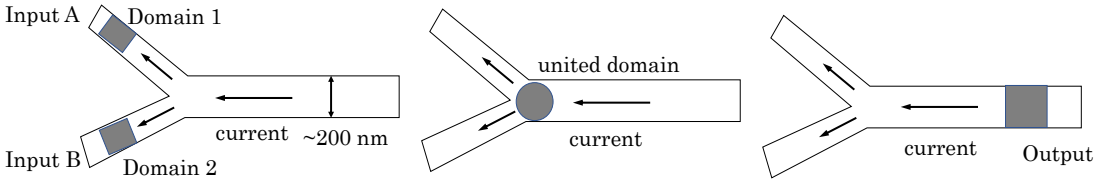

Figure 1.7. Schematic diagram of an AND logic gate in the domain-wall form [75]. The shaded areas represent magnetic domains.

Diamond is a robust material. The strong covalent bonding of diamond ensures that it can survive in strong acid or alkali environment. Diamond also has a high radiation hardness, almost one order of magnitude higher than that of Si at higher radiation energies [76]. These advantages make diamond film a good candidate as protective layer in extreme pH environments such as sewage or high radiation areas such as outer space.

A possible way to use diamond as a protective layer is to directly grow the diamond as a thin coating on to existing magnetic thin films. However, not all materials can be used as substrates for diamond growth. The most common substrate material, Si, has melting point over 1000 °C, a similar thermal expansion coefficient compared with diamond, and low carbon solubility. These characteristics make Si an excellent substrate for diamond growth. Unlike Si, however, most magnetic materials such as Fe, Ni and Co, are not suitable as substrate materials for diamond growth. The first problem is that these materials tend to promote the growth of sp^2 graphitic carbon, rather than sp^3 diamond. Indeed, they can even convert deposited sp^3 carbon into sp^2 carbon, making deposition of diamond film very difficult. Another issue is that these magnetic elements have high solubilities

for carbon at high temperatures. For example, the solubility of C in Co is ~1 at.% at 900 °C [77]. During diamond CVD, although Co is able to form a carbide layer on its surface, the carbide layer is not stable enough for diamond to form [78, 79], because the C in the surface carbide continually dissolves into the bulk Co. Therefore, for Co substrates, diamond nucleation will only occur after the substrate is saturated with C. At this point, the substrate is effectively composed of only cobalt carbide, which has very different magnetic properties to those of Co metal. The same problem occurs for Fe. Diamond growth on Fe is notoriously difficult, and can only occur at low deposition temperatures, which produces low quality diamond. Even when these problems are overcome using carefully controlled CVD conditions, it was found that the diamond layer deposited onto Fe was easily delaminated [56]. Therefore, to get high-quality diamond grown on to a magnetic substrate, a protective interlayer material is essential.

1.4 Electrical properties of diamond

Diamond is a promising material for next generation semiconductors due to a number of reasons, including its wide bandgap and high thermal conductivity [80]. A detailed comparison between diamond and some other semiconductor materials are listed in Table 1.1. Among these parameters, band gap is one of the most important parameters of semiconductor materials because it determines the maximum working temperature of a semiconductor. For example, Si, as the most popular material in the semiconductor industry, has a band gap of ~ 1.1 eV at 300 K [81]. After being doped as n- or p-type, the excitation energy will be much smaller than 1.1 eV. This means Si can be used as a semiconductor at low temperatures; however, at higher temperatures the thermal energy will be sufficient to promote electrons from the valence band into the empty conduction balance, making the material conductive. As such, the maximum working temperature for Si semiconductor devices is ~ 150 °C [82]. Other semiconductor materials with larger band gaps, such as SiC, can work up to ~ 700 °C. Diamond has a band gap of ~ 5.47 eV [16], which is higher than most other semiconductor materials. This wide band gap allows it to work at temperatures up to 1000 °C [83], depending of the energy levels of the dopant within the band gap.

Another important technical issue for semiconductor devices is thermal management [84, 85]. Nowadays, semiconductor devices are becoming smaller and consuming more power, therefore generating a lot of heat. The excess heat must be dissipated, otherwise it will influence the function of semiconductor and the performance of the whole device. For this reason, a high thermal dissipation capability is essential for semiconductor material. A straightforward way is to use a heat sink (such as a fan or radiator), connected to the hot device using a material with high thermal conductivity. Diamond has excellent thermal conductivity (~22 W cm^{-1} K^{-1} [9]), which is much better than that of Si (~ 1.5 W cm^{-1} K^{-1}). This high thermal conductivity allows diamond to be used as a heat spreading layer, transporting the localised heat from the (Si or GaN) device to an external heat sink. This allows the device to work at a high power while remaining cool, and also enables the device to be made smaller in size. These benefits also apply if diamond is itself used as the semiconductor, which is possible if it is doped appropriately. In addition, diamond has high breakdown field and carrier mobility, and high radiation hardness, which make diamond advantageous as a semiconductor material.

Table 1.1. Comparison between diamond and other semiconductor materials [16]

Materials	Si	4H-SiC	GaN	Natural Diamond	CVD Diamond
Bandgap (eV)	1.1	3.2	3.44	5.47	5.47
Breakdown field (MV cm^{-1})	0.3	3	5	10	10
Electron mobility (cm^2 V^{-1} s^{-1})	1450	900	440	200-2800	4500
Hole mobility (cm^2 V^{-1} s^{-1})	480	120	200	1800-2100	3800
Thermal conductivity (W cm^{-1} K^{-1})	1.5	5	1.3	22	24

However, converting pure diamond from an insulator to a semiconductor is not easy. An essential step is to dope different elements into the diamond lattice; for diamond (Group IV) this usually involves adding Group III elements (*e.g.*, boron) for p-type behaviour [86], or Group V elements (*e.g.*, phosphorus, nitrogen) for n-type behaviour [87, 88]. Generally, the higher the concentration of dopants that can be incorporated, the higher the carrier concentration and hence the electrical

conductivity that can be achieved, which is essential for many devices. However, many potential dopants have a low solubility in diamond (*e.g.*, P), which reduces their usefulness as dopants. Other potential dopant atoms are too large to fit into the small, stiff diamond structure without causing severe distortion of the lattice, with associated degradation of the required properties associated with diamond. Even if a dopant atom is small enough to fit into the diamond lattice at high concentrations without causing excessive distortion (*e.g.*, N), the acceptor or donor energy levels may be too deep into the band gap such that the excitation energy is much greater than room temperature [89]. In this case (*e.g.*, diamond doped with N), the 'doped diamond' remains effectively an insulator that is not much use for electronic devices – except at high temperatures. A further consideration is that some potential dopants (*e.g.*, Li) can reside on substitutional lattice sites or in interstitial positions [87, 90]. Substitutional Li acts as a p-type dopant, whereas interstitial Li acts as an n-type dopant. However, it is experimentally very difficult (if not impossible) to ensure that all the Li is incorporated entirely in one specific site, and so the two defects compensate for each other and Li-doped diamond is often insulating [91].

Despite these difficulties, there have been some successes with doping diamond. Preparing p-type diamond is fairly easy. The most common and efficient way to make p-type diamond is by doping boron (B) into the diamond lattice. Due to the small size and the negative formation energy in diamond [90], B can be substitutionally doped into diamond without distorting the diamond lattice too much. Substitutional B introduces an acceptor level which lies just above the valence band with activation energy of ~ 0.35 eV [92]. By changing the concentrations of B in diamond, the conducting properties of diamond can be controlled from semiconducting to metallic and even to a superconducting state at a temperature of 3 K [67].

Various methods have been used to introduce B into diamond. One well-established way is adding B-containing molecules into the source gas mixtures in hot filament or microwave reactors during CVD diamond growth [93]. For example, B-doped diamond showing p-type conductivity has been obtained by mixing B_2H_6 in the reactant gas during CVD process [86]. Apart from adding B-containing

molecules into precursor gas, boron ion implantation was also employed to prepare highly conducting p-type diamond [94].

1.5 Review of n-type doping of diamond

It is required to have n- and p-type semiconductor materials together in order to form a p-n junction, which is the basic component for making semiconductor electronic devices such as diodes, transistors and even more complicated integrated circuits. However, in terms of the preparation of n-type diamond, due to the rigid lattice of diamond, it is relatively difficult to introduce conventional n-type dopant atoms used for Si into diamond because nearly all of them have a large size relative to that of carbon [1]. Different elements have been studied as dopants to make n-type diamond, but none of them has given a very satisfactory result so far. Table 1.2 lists some potential n-type dopants for diamond. Each of them will be introduced in the following part.

Table 1.2. Energy levels of the common n-type dopants for diamond.

Dopants	Ionization energy (eV)	References
Nitrogen	~ 1.7	[89, 95]
Phosphorus	~ 0.6	[88, 96-99]
Sulfur	~ 0.15 – 1.63	[100-104]
Lithium	~ 0.1 – 0.2	[87, 105, 106]
Sodium	~ 0.3	[87, 107]

1.5.1 Nitrogen

Nitrogen (N) is the most common impurity in natural and synthetic diamond, and incorporates into the diamond lattice in different forms [108, 109]. Nitrogen impurities mainly occupy substitutional sites, sometimes adjacent to a vacancy. Depending on the N concentration, gemstone diamond can be classified into type I (with N impurities) and type II (almost no N) [110]. Moreover, on the basis of the positions of N in diamond, type I diamond can be further divided into different subtypes. Figure 1.8 shows a simple classification of type I diamond. For example, N atoms can exist as clusters in substitutional sites of diamond. This type of

diamond is known as type Ia [111], which is the majority (> 95 %) N-containing defect found in natural diamond [112]. N can also occupy a single substitutional site of diamond. This type of diamond is classified into type Ib and almost all the HPHT-synthetic diamond is of this type [112-114].

One reason that N is such a dominant impurity is because N is small enough to substitute for carbon with little perturbation of the diamond lattice. Compared with other potential n-type dopants such as P, As, Na and Li, nitrogen is the only dopant having an atomic radius smaller than that of carbon atom [115]. Therefore, N is relatively easily incorporated into diamond, with concentrations of 1900 atomic ppm (*i.e.*, 2.1×10^{20} cm^{-3}) being reported [116].

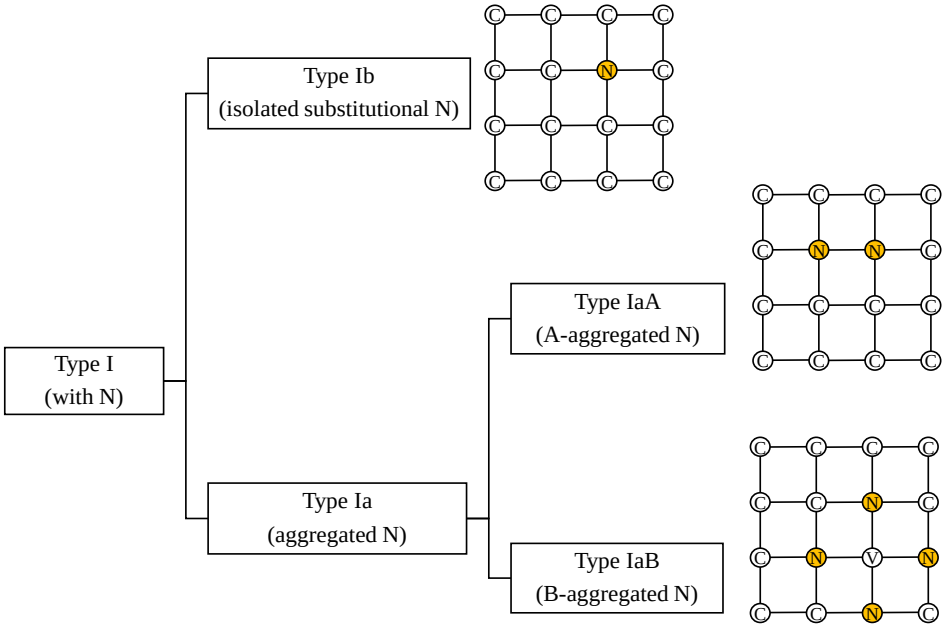

Figure 1.8. Classification of diamond with nitrogen impurities. C, N and V represent carbon, nitrogen and vacancy, respectively [110].

1.5.1.1 The C-centre

In type Ib diamond, N impurities exist at single substitutional site, also known as the C-centre in spectroscopy studies [117]. In theory, as a group V element, each substitutional N introduces one more valence electron into the diamond lattice, which can potentially make diamond conductive. Kajihara et al. [87] indicated in an *ab initio* calculation that substitutional N has a negative formation energy (-3.4 eV) in diamond, which is the lowest among N, P, Li and Na, explaining the

abundance of nitrogen impurities in diamond. However, there were also positive formation energies (up to 10 eV) reported for substitutional N, which was perhaps due to different calculation methods [118, 119].

As the most abundant element in air, nitrogen can easily enter the diamond lattice and form a C-centre when the HPHT method is employed, even though the HPHT diamond is not very suitable for electrical use. The HPHT method can prepare diamond with a very high concentration of nitrogen (~ 10^{20} cm^{-3}) using boron nitride as a container during the synthesis process [116]. An effective way to prepare high-quality N-doped diamond is by mixing an N-containing gas (N_2 or NH_3) with methane and hydrogen during the CVD process. The N concentration in diamond can be adjusted by changing the concentration of the nitrogen source gas in the gas-feed mixture [95, 120, 121], with a concentration of up to ~ 10^{19} cm^{-3} in (100) single crystal diamond being achieved [121]. Ion implantation was also used to introduce nitrogen into diamond, followed by a high-temperature annealing treatment to remove the implantation-induced damage to the diamond lattice [122]. In this method, the nitrogen concentration was reported to be as high as 4×10^{18} cm^{-3} and almost half of the implanted N occupied the single substitutional site, as in the type Ib diamond.

By measuring the photoconduction and optical absorption of a type Ib diamond, it was found that single substitutional N has a deep donor level which lies 1.7 eV below the conduction band [89]. This result is widely accepted and agrees with the measurements of a standard CVD diamond film using a constant-photoconductivity method [95]. Because of this deep donor level, type Ib diamond is usually highly resistive at room temperature and its electrical properties cannot be determined by conventional electrical methods, such as Hall-effect measurements. Instead, other techniques such as optical absorption, photoconductivity or electron spin resonance, have been used to quantify the conductivity [123]. This high activation energy means that N-doped diamond is not very useful for semiconductor devices at room temperature.

1.5.1.2 The A-Centre and B-Centre

As illustrated in Figure 1.8, the A-Centre (in type IaA diamond) consists of a pair of N atoms substituting two nearest C atoms in diamond [117]. Nitrogen in the A-Centre has an ionization energy of 4.0 eV [124], which is even deeper than the C-Centre. The B-Centre (in type IaB diamond) is composed of four N atoms and a vacancy in the centre [117], on the other hand, does not show any donor property at all [110].

1.5.1.3 The NV Centre

One of the N-related centres that cannot be ignored is the NV centre. NV centre consists of a substitutional N and an adjacent vacancy in diamond. NV centre can be found in diamond prepared from CVD using N-containing gas [125] or diamond treated after ion implantation of nitrogen [126]. NV centre can exist in negative (NV^-) or neutral (NV^0) charge states, which are characterized by different photoluminescence spectra [127, 128]. The electron spins of NV centre especially of the NV- can be manipulated by magnetic field, microwave field or light, and the corresponding fluorescence signals can be detected [129]. NV centre is very sensitive to electric and magnetic field and has a nano-scale resolution. Therefore, even though NV centre is not electrically active, it has found wide applications in quantum realm such as quantum detection and computing [129, 130].

1.5.2 Phosphorus

Another group V element, phosphorus (P), is also a candidate for the n-type diamond. Unfortunately, P has an atomic radius larger than C. Therefore, the solubility of P in diamond is rather low. Due to the large size, P also distorts the diamond lattice and in doing so degrades the mechanical and electrical properties of the material [131]. Nevertheless, P has been proved to be a shallow donor, so its electrical parameters such as carrier mobility can be measured using the conventional Hall-effect measurements.

1.5.2.1 Theoretical work on P-doped diamond

Although P is believed to be a shallow donor, there is no agreement on the donor-level energy value. It was first predicted by first-principle calculations that substitutional P should be a shallow donor in diamond, having an energy level of ~ 0.2 eV below the conduction band, but its formation energy was predicted to be as high as ~ 10.7 eV, corresponding to a low equilibrium solubility even at high temperatures [90]. There were also other calculations indicating that the donor level of P is at ~ 0.37 eV, with a formation energy of ~ 6.65 eV [132]. The difference in the calculation results could be due to the different settings during geometry optimization.

1.5.2.2 Experimental work on P-doped diamond

The experimental work of P-doped diamond has been greatly studied by CVD using P-containing gases as the dopant source. Using diphosphorus pentaoxide (P_2O_5) as the P source, P-doped polycrystalline diamond film were prepared in a hot-filament CVD reactor [133]. The carrier concentration and mobility were measured as ~ 10^{15} cm^{-3} and 50 cm^2 V^{-1} s^{-1} and the activation energy was 0.05 eV. Phosphine (PH_3) gas was also selected as a source to make P-doped diamond film in a CVD plasma reactor [134]. As the PH_3 concentration increased from 39.36 to 98.40 ppm, the corresponding activation energies decreased from 1.16 to 0.84 eV. Using PH_3 as dopant source, P can be incorporated into both single-crystal and polycrystalline diamond, but due to the grain boundaries in polycrystalline diamond, the P concentration in polycrystalline films is much higher than that in single-crystal film [135]. The quality of P-doped diamond is influenced by the growth conditions. A higher temperature and lower methane concentration are preferred to make high-quality P-doped diamond [136].

The P dopant also has different effects on different facets of diamond. First, it was found that the P-doped {111} surface exhibited a better surface quality, which was much smoother than the {100} surface when PH_3 was used as the dopant source [137]. Therefore, {111} diamond was believed to be a better candidate for making P-doped diamond. Using CVD, n-type conductivity with activation energy of ~ 0.6

eV and P concentrations $10^{17} – 10^{18}$ cm^{-3} were obtained on the {111} surface of a Ib diamond [88]. However, the low P solubility meant that the carrier mobility was less than 240 $cm^2 V^{-1} s^{-1}$ at room temperature, making this P-doped diamond poorly conducting. In another research, infra-red absorption was employed to study the electrical properties of P-doped {111} diamond with increasing PH_3 addition to the gas mixture. It was found that the P concentration in the film reached 2×10^{19} cm^{-3} and the activation energy was ~ 0.6 eV [98].

Having a high concentration of dopant is a straightforward way to achieve higher carrier mobility, but it can also be realized with optimized growth conditions even at lower dopant concentration. For example, Katagiri et al. [97] obtained P-doped {111} diamond film using an optimized plasma-assisted CVD with a mobility of 660 $cm^2 V^{-1} s^{-1}$ but with a P concentration of only ~ 10^{15} cm^{-3}.

The {111} diamond surface is difficult to use for devices for various reasons [138], whereas the {100} diamond surface is preferred. As such, n-type semiconductivity was also obtained on the {100} surface with good quality [139] using optimized growth conditions that were different from those used for {111} diamond. Despite the doping concentration not being as high as that for the {111} surface, the highest mobility reported on P-doped {100} was 350 $cm^2 V^{-1} s^{-1}$ at room temperature [139]. Later, a higher mobility of 570 $cm^2 V^{-1} s^{-1}$ was achieved on a P-doped {100} diamond at room temperature, although the doping concentration was only 2×10^{19} cm^{-3} [140].

So far, substitutional P seems to be the best candidate to make n-type diamond. In 2001, a p-n junction was successfully fabricated by Koizumi et al. [141] via combining B- and P-doped diamond films on {111} surface, and the good diode characteristics were observed. At present, P-doped diamond with higher carrier mobility and low resistivity is required to make viable devices. However, methods to increase P concentration usually introduce too much damage into diamond, which inhibits device performance. Therefore, for P-doped diamond, more theoretical understanding and better doping techniques are still needed.

1.5.3 Sulfur

Sulfur (S) is another potential n-type dopant. It has a similar atomic radius to P and these two dopants were often studied and compared with each other. However, for both experimental and theoretical work, the conclusions regarding S-doped diamond are not as clear as those for P-doped diamond. The main controversies lie in whether S is a shallow donor or not.

1.5.3.1 Theoretical calculations of S-doped diamond

According to first-principle calculations by Saada et al. [100], neutral S in diamond should be a shallower donor (0.15 eV) than P (0.6 eV). However, the most stable state of S in diamond is the double ionized S^{2+}, which does not act as a donor, while the less stable S^{+} state acts as a donor with a donor level of 0.5 eV. Later work by Miyazaki et al. [101] suggested that single substitutional S is actually a deep donor (1.1 – 1.2 eV), while the S complexes with any N, B and vacancies present form shallow donor states (0.4 – 0.5 eV) with very high formation energies, meaning low doping efficiencies. In another *ab initio* theoretical study, an even deeper donor level of 1.63 eV was reported for the single substitutional S [102]. Later, a shallow donor level of 0.38 eV was reported for substitutional S by examining its band structures in a DFT calculation [142]. After comparing P and S as potential dopants, Wang et al. [132] suggested that S not only is a deeper donor (0.77 eV), but also has a lower solubility than P. Moreover, there is a chance that the small amount of introduced S donors may be compensated by other defects such as vacancy centres [103].

Despite of these disagreement about the energy level of substitutional S, there is less argument about the symmetry structures of S-doped diamond. Most researchers believe that the most stable geometry structure of diamond with single substitutional S is the C_{3v} symmetry [101-103, 132, 142-144]. However, very recent research suggested that the C_{2v} symmetry is more stable than C_{3v}, and the stability order, can be influenced by the supercell size employed during calculation [145].

1.5.3.2 Experimental work on S-doped diamond

In 1999, S doping of diamond was attempted on a Ib (100) diamond by introducing hydrogen sulfide (H_2S) to the reactant gas during microwave plasma CVD. The report claimed the deposited material showed n-type semiconductivity with a carrier mobility of 597 $cm^2 V^{-1} s^{-1}$ at room temperature, carrier concentration of 1.4×10^{13} cm^{-3} and ionization energy of 0.38 eV [146, 147]. However, this work was soon re-examined by Kalish et al. [148], showing that an unintentional amount of B was introduced into the sample at the same time, which made the sample actually p-type semiconductive and the final measurements incorrect. Almost at the same time, ion implantation of S was employed by Hasegawa et al. [149] to achieve n-type semiconductivity on a (100) diamond, with a reported activation energy of 0.19 – 0.33 eV and a S concentration $8 \times 10^{19} – 3 \times 10^{20}$ cm^{-3}. Two years later, optical and electrical measurements were employed together to characterize a S-doped (100) diamond prepared with H_2S during CVD, but the S concentration was detected to be extremely low and the conductivity was as low as in undoped diamond [150].

So far, S does not seem to be a good candidate for n-type diamond. There are too many unanswered questions and unproven reports. More comprehensive theoretical and experimental work is needed to reveal the interaction between S and diamond.

1.5.4 Lithium

At first sight, Li should form a p-type dopant if situated on a substitutional site (because it has 3 electrons less than C), but an n-type dopant if it sits on an interstitial site (as the 2s electron should be easily ionised and enter the conduction band). However, in reality things are more complicated than this, and detailed *ab initio* calculations are needed to work out the electronic structure in different circumstances. Also, Li atoms diffuse rapidly through diamond at high temperatures (especially if grain boundaries are present), and tends to meet up with other Li atoms or other impurities to form stable defect clusters. The clusters

are often electrically inactive, making Li-doped diamond poor conductors or non-conducting.

1.5.4.1 Theoretical work of Li-doped diamond

According to first-principle calculations by Kajihara et al. [90], Li prefers the tetrahedral interstitial site in diamond and is a shallow donor, with a donor level very close to the conduction band minimum. However, Li is very diffusive in diamond even at room temperature, so it is very mobile and very likely to form complexes/clusters with other impurities in diamond, trapping Li in an electrically inactive form [151]. Moreover, the trapped Li complex often compensates the remaining donors, resulting in a high-resistivity state [152]. Yilmaz et al. [153] indicated that Li atoms in adjacent interstitial sites of diamond are very likely to break the nearest C-C bonds and to form a cluster, which will be a very deep and inactive donor. Therefore, to make interstitially doped Li into a shallow donor in diamond, Li must be controlled at a relatively low concentration and mono-dispersed. In other *ab initio* calculations, they confirmed that interstitial Li is a shallow donor, with its donor level approximately 0.1 eV below the conduction band minimum of diamond [87], but the high positive formation energy (9.8 eV reported in [90] and 5.5 eV in [87]) may inhibit Li incorporation.

1.5.4.2 Experimental work on Li-doped diamond

Different processing methods such as in-diffusion, ion implantation and using Li-containing gas during CVD have been employed to prepare Li-doped diamond.

Okumura et al. [154] suggested that even though Li can be incorporated into a diamond film by in-diffusion to generate donor states, the electrical properties of the diamond did not change very much. This was attributed to the compensation of Li donors by high-density acceptor states in the band gap. It was reported by Nijenhuis et al. [155] that the in-diffusion method only introduces Li on the surface of diamond, which is not very useful for a diamond-based semiconductor material. Popovici et al. [156], on the other hand, obtained Li-doped diamond with n-type conductivity using diffusion of Li. The Li concentration was measured as high as $(3 – 4) \times 10^{19}$ cm^{-3} and carrier mobility was 50 cm^2 V^{-1} s^{-1}.

Ion implantation is believed to be a good method to introduce interstitial dopants because it is less likely to replace the host C atoms [90]. Buckley-Golder et al. [157] prepared Li-doped diamond using ion implantation and integrated the Li-doped diamond into a p-n junction, which displayed a good current-voltage characteristic below 350 °C. Prawer et al. [105] measured the activation energy of Li doped diamond (0.2 eV) obtained by ion-implantation, but suggested that the conductivity of Li-doped diamond can be attributed to the hopping of implanted impurities rather than thermal activation. Restle et al. [158] measured the proportions of Li in different sites of a Li-doped diamond made through ion implantation, and found that 40% of the doped Li atoms were in tetrahedral interstitial sites, while the percentages of Li atoms in substitutional and irregular sites were 17% and 43%, respectively. Li implantation can be employed at room temperature or high temperature (> 800 °C), but room-temperature implantation is more likely to induce graphitization on diamond surface [159].

The third method to dope Li into diamond is by introducing a Li-containing gas into the gas mixture during CVD growth. For example, lithium tert-butoxide ($LiOC_4H_9$) was used during microwave plasma or hot-filament CVD to make Li-doped diamond [160-162], but the electrical properties were not studied in these works. Borst et al. [106] placed Li_2O power into microwave CVD reactor and obtained n-type Li-doped diamond with activation energy of 0.16 eV by Hall-measurements.

Regarding the diffusion problem of Li in diamond, Cytermann et al. [91] measured the depth profiles of Li in diamond, but showed that the Li diffusion only happened in polycrystalline diamond where abundant grain boundaries exist, therefore it is still possible to realize n-type doping by Li in a single-crystalline diamond. Similar results were observed by Sung et al. [163] that the diffusion of Li mainly goes through grain boundaries of a polycrystalline diamond. Therefore, to obtain Li-doped diamond with n-type conductivity, high-quality single-crystalline diamond should be the priority. Another way to overcome the mobility of Li is using co-doping, which will be explained later.

1.5.5 Sodium

Sodium (Na) is a potential shallow donor when situated at an interstitial site in diamond. As an alkali metal, Na has been studied and compared with Li in many aspects. Compared with Li, Na is less diffusive, therefore more stable and more electrically active as donor. However, it has a higher formation energy than Li, which can lead to a lower solubility.

1.5.5.1 Theoretical calculation of Na-doped diamond

Theoretical calculations suggest that Na at an interstitial site in diamond may behave as a shallow donor and prefers a tetrahedral interstitial site over the hexagonal interstitial site [87, 90, 107, 152]. However, Lombardi et al. [152, 164, 165] indicated that Na is more stable as a substitutional acceptor than an interstitial donor. The donor level of the Na in a tetrahedral interstitial site was calculated to be ~0.3 eV below the conduction band minimum [87]. Moreover, interstitial Na has an activation energy of 1.4 – 1.6 eV for diffusion, which is higher compared with that for interstitial Li of 0.85 eV [90, 107]. This makes Na more stable than Li as a donor up to a moderately high temperature. On the other hand, the formation energy of interstitial Na in diamond is about 15.3 eV, compared with ~ 5.5 eV for Li [87]. This high positive formation energy makes Na more difficult to incorporate into diamond and leads to an extremely low equilibrium solubility.

1.5.5.2 Experimental work on Na-doped diamond

There are only a few experimental reports about Na-doped diamond. Due to the high formation energy of interstitial Na, it is difficult to introduce Na into diamond lattice. Ion implantation or kinetic trapping during growth were predicted as effective ways to make Na-doped diamond [90]. Hunn et al. [166] used ion implantation to prepare Na-doped single-crystal diamond, followed by high-temperature annealing to remove the implantation-induced damage. The implanted layers (~ 100 nm) exhibited semiconductivity, with a reported Na concentration of 4.5×10^{19} cm^{-3} at 550 °C, an activation energy of 0.42 eV, and an electron mobility of 10 cm^2 V^{-1} s^{-1}. Prawer et al. [105] also introduced Na into

diamond by ion implantation followed by a post annealing, but suggested that conductivity could be induced by carriers hopping rather than thermal activation of donors. Borst et al. [106] grew Na-doped diamond by adding Na_2O powder into a microwave CVD reactor during diamond growth. Unfortunately, the resistivity of the resulting sample was too high and the electrical parameters could not be determined.

1.5.6 Co-doping

Most of the potential dopants mentioned above either have high activation energy or high formation energy, which inhibit the doping efficiency and the performance of the doped diamond. Co-doping is a strategy using at least two dopants, which can solve the problem of compensation. Appropriate co-doping can not only increase the dopant solubility, but also increase the carrier mobility by lowing the activation energy [167]. So far, there have only been a few co-doping strategies proposed for n-type diamond.

1.5.6.1 Hydrogen and phosphorus

Hydrogen is an essential element for CVD diamond growth and is energetically favourable to bond with B, P and S in diamond [168]. *Ab initio* calculations found that the antibonding site of H around a substitutional P (Figure 1.9) is the most stable state for the H-P complex [102, 169]. The negative binding energy between H and P can help to increase the doping concentration of P. However, H also works as an acceptor, which can be expressed as: $P + H \rightarrow P^+ + H^-$. Sque et al. [103, 144] pointed out that the H-P complex can generate very deep donor levels in diamond. In order to generate enough free donors, some annealing treatment may be helpful to remove part H atoms and to form a new P-H-P complex [169].

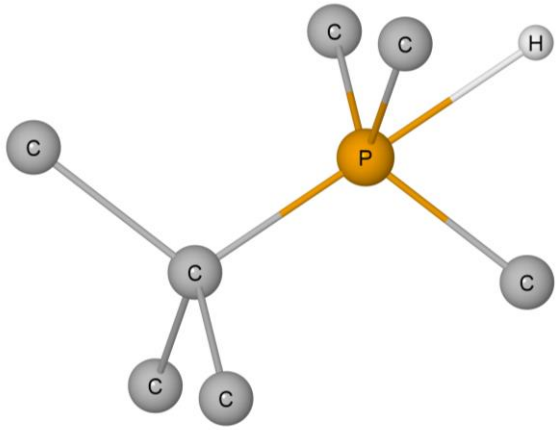

Figure 1.9. The structure of a H-P complex with a H at antibonding site around a substitutional P [169].

1.5.6.2 Hydrogen and sulfur

Theoretical calculations indicated that the most stable state for the H-S complex also includes a H at an antibonding site around a substitutional P, with a negative binding energy of -2.18 eV [102]. The calculated donor level of the H-S complex is about 1.0 eV below the conduction band, which is shallower than a single substitutional S of 1.4 eV [144, 169]. Two H atoms are required to fully passivate S, compared with one H for P. Therefore, compared with H-P, the H-S complex is more likely to generate a shallow donor state [168].

1.5.6.3 Boron and lithium

B is believed to be able to immobilize Li, preventing cluster formation and therefore making Li an active donor in diamond. Based on this assumption, Halliwell et al. [170] prepared B-Li co-doped diamond using Li_3N and B_2H_6 as dopant sources. However, the electrical conductivities of the samples were dominated by the p-type property of B. The reason may be that too many Li atoms were compensated by B, or the diamond lattice was distorted by Li atom. Lee et al. [171] prepared Li/B co-doped polycrystalline diamond films, followed by a hydrogen plasma treatment. Measurements showed n-type semiconductivity, but the origin of this was not clear.

1.5.6.4 Boron and nitrogen

In an *ab initio* calculation by Katayama-Yoshida et al. [169], a donor level of 1.17 eV was obtained for the N-B-N complex, compared with 1.93 eV of a single N. It was suggested that the large negative binding energy (-4.57 eV) for the N-B-N complex could make the activation energy lower than 1.17 eV [169]. Croot et al. [172] compared B-N complexes composed of different numbers of B and N atoms, and found that BN_2 (N-B-N) and BN_3 are the two most promising candidates for n-type property, but their excitation energies are still above 1.0 eV. Fortunately, the negative binding energy for the B-N complex might make it possible work as shallow n-type donor.

1.5.6.5 Boron and sulfur

DFT calculations by Tang et al. [104] showed that the formation energies of the B/S complexes decreased with increasing B concentration, indicating that B increased the doping efficiency. When B:S = 1:1, the most stable structure was obtained with B and S atoms being substitutionally doped and adjacent to each other.

Experimentally, boron and sulfur doped diamond was prepared using H_2S and trimethylboron during microwave CVD growth [173]. It was found that the conducting properties changed from n- to p-type with increasing B/S ratio, but it was not confirmed whether the donor level was from S or not. Li et al. [174] obtained B-S co-doped n-type diamond by microwave CVD using dimethyl disulfide and boron dioxide, measured a lower activation energy (0.39 eV) comparing with S-doped diamond (0.52 eV) and showed that B improved the crystalline quality of diamond film at the same time.

1.5.6.6 Lithium and nitrogen

Moussa et al. [175] devised a substitutional LiN_4 defect structure that contains a substitutional Li in the centre and tetrahedrally coordinated by four N atoms (Figure 1.10). DFT calculations predicted this complex to be a shallow donor with activation energy of 0.27 ± 0.06 eV. However, this defect is tricky to create due to

its very special structure in that a preformed VN_4 (a vacancy with four nearest substitutional N) complex might be needed [175]. In another first-principles calculation, Delun et al. [176] proved that the LiN_4 complex not only is a shallow donor (0.14 eV) , but also has a negative formation energy (-2.137 eV), compared with the positive formation energies (8.635 eV) of interstitial Li. Conejeros et al. [177] also predicted this LiN_4 structure to be n-type semiconductive but also indicated that the donor level is mainly from the carbon atoms around the defect.

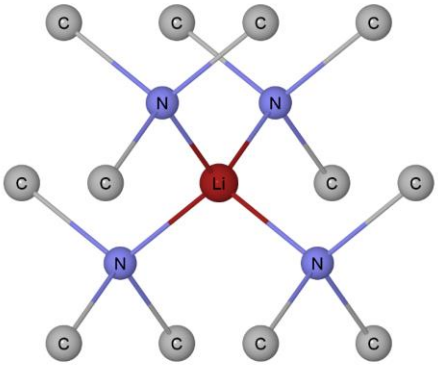

Figure 1.10. The LiN_4 complex structure with a substitutional Li in the centre, surrounded by four substitutional N atoms [175].

However, Othman et al. [178] prepared Li-N co-doped single crystal and polycrystalline diamond films by using Li_3N powder and NH_3 gas as sources. The type of the Li/N complex was unknown and the resistance of the samples was too high, indicating the Li/N complex was inactive.

1.5.6.7 Beryllium and hydrogen

In a first-principles calculation, Yan et al. [179] studied the Be-H complex where Be was placed in the tetrahedral centre and bonded with a H atom in the centre between Be and C, or in the centre between nearest and the second-nearest C atoms. Even though n-type semiconductivity was observed, they suggested Be and H have very weak interaction around the Fermi level and the H can act as an acceptor to compensate Be. Therefore, H should be avoided when doping Be.

1.6 Thesis outline

This thesis presents the results from a series of experimental studies and theoretical calculations related to modifying the magnetic and electrical properties of diamond to produce a material useful for novel electronic devices. The thesis will be presented in 6 chapters. Chapter 2 describes the experimental methods and computational theory involved in the thesis. Chapters 3 to 5 are the main body of the thesis. Chapter 3 is about the growth and characterization of diamond on patterned Co. Chapters 4 and 5 focus on the theoretical study of Be and Be-N clusters in diamond, respectively. Chapter 6 is the conclusion chapter.

1.7 References

[1] P.W. May, Diamond thin films: a 21st-century material, Philos. Trans. R. Soc. A 358 (2000) 473-495.

[2] F.R. Boyd, J.J. Gurney, S.H. Richardson, Evidence for a 150–200-km thick Archaean lithosphere from diamond inclusion thermobarometry, Nature 315 (1985) 387-389.

[3] N. Munier, Diamonds, dependence and De Beers: monopoly capitalism and compliance with the Kimberley Process in Namibia, Rev. Afr. Polit. Econ. 43 (2016) 542-555.

[4] X.F. Wang, S. Scandolo, R. Car, Carbon phase diagram from ab initio molecular dynamics, Phys. Rev. Lett. 95 (2005) 4.

[5] G. Will, P.G. Perkins, A scientific approach to hardness: the hardness of diamond and cubic boron nitride, Mater. Lett. 40 (1999) 1-4.

[6] N. Dubrovinskaia, S. Dub, L. Dubrovinsky, Superior wear resistance of aggregated diamond nanorods, Nano Lett. 6 (2006) 824-826.

[7] P. Hollman, O. Wanstrand, S. Hogmark, Friction properties of smooth nanocrystalline diamond coatings, Diam. Relat. Mater. 7 (1998) 1471-1477.

[8] C.A. Klein, G.F. Cardinale, Young's modulus and Poisson's ratio of CVD diamond, Diam. Relat. Mater. 2 (1993) 918-923.

[9] J.E. Graebner, S. Jin, G.W. Kammlott, et al., Unusually high thermal conductivity in diamond films, Appl. Phys. Lett. 60 (1992) 1576-1578.

[10] C.H. Xu, C.Z. Wang, C.T. Chan, K.M. Ho, Theory of the thermal expansion of Si and diamond, Phys. Rev. B 43 (1991) 5024-5027.

[11] D. Mitev, R. Dimitrova, M. Spassova, et al., Surface peculiarities of detonation nanodiamonds in dependence of fabrication and purification methods, Diam. Relat. Mater. 16 (2007) 776-780.

[12] J. Iniesta, P.A. Michaud, M. Panizza, et al., Electrochemical oxidation of phenol at boron-doped diamond electrode, Electrochim. Acta 46 (2001) 3573-3578.

[13] S. Vasilie, F. Manea, A. Baciu, A. Pop, Dual use of boron-doped diamond electrode in antibiotics-containing water treatment and process control, Process Saf. Environ. Protect. 117 (2018) 446-453.

[14] K. Turcheniuk, V.N. Mochalin, Biomedical applications of nanodiamond, Nanotechnology 28 (2017) 27.

[15] R. Mildren, J. Rabeau, Optical engineering of diamond, John Wiley & Sons 2013.

[16] C.J.H. Wort, R.S. Balmer, Diamond as an electronic material, Mater. Today 11 (2008) 22-28.

[17] E. Woerner, C. Wild, W. Mueller-Sebert, P. Koidl, CVD-diamond optical lenses, Diam. Relat. Mater. 10 (2001) 557-560.

[18] S. Tennant, IV. On the nature of the diamond, Philos. Trans. R. Soc. 87 (1797) 123-127.

[19] L.F. Dobrzhinetskaya, Microdiamonds - Frontier of ultrahigh-pressure metamorphism: A review, Gondwana Res. 21 (2012) 207-223.

[20] M.N.R. Ashfold, P.W. May, C.A. Rego, N.M. Everitt, Thin film diamond by chemical vapour deposition methods, Chem. Soc. Rev. 23 (1994) 21-30.

[21] F.P. Bundy, H.T. Hall, H.M. Strong, R.H. Wentorfjun, Man-Made Diamonds, Nature 176 (1955) 51-55.

[22] H.P. Bovenkerk, F.P. Bundy, H.T. Hall, et al., Preparation of Diamond, Nature 184 (1959) 1094-1098.

[23] H.T. Hall, Some High - Pressure, High - Temperature Apparatus Design Considerations: Equipment for Use at 100 000 Atmospheres and 3000°C, Rev. Sci. Instrum. 29 (1958) 267-275.

[24] J. Osugi, K. Shimizu, K. Inoue, K. Yasunami, A compact cubic anvil high pressure apparatus, Rev. Phys. Chem. Jpn 34 (1964) 1-6.

[25] N. Kawai, S. Endo, The Generation of Ultrahigh Hydrostatic Pressures by a Split Sphere Apparatus, Rev. Sci. Instrum. 41 (1970) 1178-1181.

[26] U.F. D'Haenens-Johansson, A. Katrusha, P. Johnson, W. Wang, Large Colorless HPHT-Grown Synthetic Gem Diamonds from New Diamond Technology, Russia, Gems Gemol. 51 (2015).

[27] R.C. Liebermann, Multi-anvil, high pressure apparatus: a half-century of development and progress, High Press. Res. 31 (2011) 493-532.

[28] X. Jia, S. Hayakawa, W. Li, et al., Cobalt impurities in synthetic diamond, Diam. Relat. Mater. 8 (1999) 1895-1899.

[29] T. Irifune, A. Kurio, S. Sakamoto, et al., Ultrahard polycrystalline diamond from graphite, Nature 421 (2003) 599-600.

[30] N.R. Greiner, D.S. Phillips, J.D. Johnson, F. Volk, Diamonds in detonation soot, Nature 333 (1988) 440-442.

[31] A.E. Aleksenskii, M.V. Baidakova, A.Y. Vul', et al., Effect of hydrogen on the structure of ultradisperse diamond, Phys. Solid State 42 (2000) 1575-1578.

[32] V. Yu. Dolmatov, Detonation synthesis ultradispersed diamonds: properties and applications, Russ. Chem. Rev. 70 (2001) 607-626.

[33] J.C. Angus, Diamond synthesis by chemical vapor deposition: The early years, Diam. Relat. Mater. 49 (2014) 77-86.

[34] W.G. Eversole, Synthesis of diamond, US Patents, 1962.

[35] J.C. Angus, H.A. Will, W.S. Stanko, Growth of Diamond Seed Crystals by Vapor Deposition, J. Appl. Phys. 39 (1968) 2915-2922.

[36] S. Matsumoto, Y. Sato, M. Tsutsumi, N. Setaka, Growth of diamond particles from methane-hydrogen gas, J. Mater. Sci. 17 (1982) 3106-3112.

[37] S. Matsumoto, Y. Sato, M. Kamo, N. Setaka, Vapor Deposition of Diamond Particles from Methane, Jpn. J. Appl. Phys. 21 (1982) L183-L185.

[38] M. Kamo, Y. Sato, S. Matsumoto, N. Setaka, Diamond synthesis from gas phase in microwave plasma, J. Cryst. Growth 62 (1983) 642-644.

[39] S. Matsumoto, Chemical vapour deposition of diamond in RF glow discharge, J. Mater. Sci. Lett. 4 (1985) 600-602.

[40] G.W. Qin, Y.P. Ren, N. Xiao, et al., Development of high density magnetic recording media for hard disk drives: materials science issues and challenges, Int. Mater. Rev. 54 (2009) 157-179.

[41] D. Jańczewski, Y. Zhang, G.K. Das, et al., Bimodal magnetic–fluorescent probes for bioimaging, Microsc. Res. Tech. 74 (2011) 563-576.

[42] M. Colombo, S. Carregal-Romero, M.F. Casula, et al., Biological applications of magnetic nanoparticles, Chem. Soc. Rev. 41 (2012) 4306-4334.

[43] M. Arruebo, R. Fernández-Pacheco, M.R. Ibarra, J. Santamaría, Magnetic nanoparticles for drug delivery, Nano Today 2 (2007) 22-32.

[44] H. Ohno, Making nonmagnetic semiconductors ferromagnetic, Science 281 (1998) 951-956.

[45] W. Liu, H. Zhang, J.-a. Shi, et al., A room-temperature magnetic semiconductor from a ferromagnetic metallic glass, Nat. Commun. 7 (2016) 13497.

[46] S. Sugahara, J. Nitta, Spin-Transistor Electronics: An Overview and Outlook, Proc. IEEE 98 (2010) 2124-2154.

[47] B.D. Cullity, C.D. Graham, Introduction to magnetic materials, John Wiley & Sons 2011.

[48] W.M. Haynes, W.M. Haynes, D.R. Lide, T.J. Bruno, CRC handbook of chemistry and physics: a ready-reference book of chemical and physical data, Ninety-seven edition. ed., CRC Press, Boca Raton, Florida, 2017.

[49] K. Johnston, A. Mainwood, Transition metals in diamond: Do chemical trends arise from ab initio calculations?, Physica B Condens. Matter 308 (2001) 565-568.

[50] M.A. Nastasi, J.W. Mayer, Ion implantation and synthesis of materials, Springer 2006.

[51] C.H. Chen, I.C. Cho, H.S. Jian, H. Niu, Fe doped Magnetic Nanodiamonds made by Ion Implantation, Sci. Rep. 7 (2017) 5.

[52] B.R. Lin, C.H. Chen, S. Kunuku, et al., Fe Doped Magnetic Nanodiamonds Made by Ion Implantation as Contrast Agent for MRI, Sci. Rep. 8 (2018) 6.

[53] I.P. Chang, K.C. Hwang, C.S. Chiang, Preparation of Fluorescent Magnetic Nanodiamonds and Cellular Imaging, J. Am. Chem. Soc. 130 (2008) 15476-15481.

[54] B. Yang, W.Z. Lu, W. Feng, et al., Adsorption and deposition of micro diamond particles in preparing diamond magnetic abrasives by electroless composite plating, Diam. Relat. Mater. 73 (2017) 137-142.

[55] Z. Zuo, B. Hu, H. Chen, et al., Effect of activators on the properties of nickel coated diamond composite powders, J. Mater. Sci. Technol. 33 (2017) 1409-1415.

[56] H.G. Zanin, A.C. Peterlevitz, R.F. Teofilo, et al., Synthesis and Characterization of Magnetic Nanocrystalline Diamond Films, Ferroelectrics 436 (2012) 96-100.

[57] R. Hohne, P. Esquinazi, V. Heera, H. Weishart, Magnetic properties of ion-implanted diamond, Diam. Relat. Mater. 16 (2007) 1589-1596.

[58] A.A. Ovchinnikov, V.N. Spector, ORGANIC FERROMAGNETS - NEW RESULTS, Synth. Met. 27 (1988) B615-B624.

[59] K.H. Han, D. Spemann, P. Esquinazi, et al., Ferromagnetic spots in graphite produced by proton irradiation, Adv. Mater. 15 (2003) 1719-+.

[60] P. Esquinazi, D. Spemann, R. Hohne, et al., Induced magnetic ordering by proton irradiation in graphite, Phys. Rev. Lett. 91 (2003) 4.

[61] S. Talapatra, P.G. Ganesan, T. Kim, et al., Irradiation-induced magnetism in carbon nanostructures, Phys. Rev. Lett. 95 (2005) 4.

[62] L. Pisani, B. Montanari, N.M. Harrison, Stability of the ferromagnetic state in a mixed sp2-sp3 carbon system, Phys. Rev. B 80 (2009) 4.

[63] K. Murata, H. Ushijima, H. Ueda, K. Kawaguchi, A stable carbon-based organic magnet, J. Chem. Soc., Chem. Commun. (1992) 567-569.

[64] K. Murata, H. Ushijima, H. Ueda, K. Kawaguchi, Magnetic properties of amorphous-like carbons prepared from tetraaza compounds by the chemical vapour deposition (CVD) method, J. Chem. Soc., Chem. Commun. (1991) 1265-1266.

[65] P.O. Lehtinen, A.S. Foster, Y.C. Ma, et al., Irradiation-induced magnetism in graphite: A density functional study, Phys. Rev. Lett. 93 (2004) 4.

[66] H. Ohldag, P. Esquinazi, E. Arenholz, et al., The role of hydrogen in room-temperature ferromagnetism at graphite surfaces, New J. Phys. 12 (2010) 10.

[67] G. Zhang, T. Samuely, Z. Xu, et al., Superconducting Ferromagnetic Nanodiamond, ACS Nano 11 (2017) 5358-5366.

[68] E. Perevedentseva, A. Karmenyan, Y.C. Lin, et al., Multifunctional biomedical applications of magnetic nanodiamond, J. Biomed. Opt. 23 (2018).

[69] E. Perevedentseva, D. Peer, V. Uvarov, et al., Nanodiamonds of Laser Synthesis for Biomedical Applications, J. Nanosci. Nanotechnol. 15 (2015) 1045-1052.

[70] D. Weller, M.F. Doerner, Extremely High-Density Longitudinal Magnetic Recording Media, Annu. Rev. Mater. Sci. 30 (2000) 611-644.

[71] D.C. Noll, D.G. Nishimura, A. Macovski, Homodyne detection in magnetic resonance imaging, IEEE Trans. Med. Imag. 10 (1991) 154-163.

[72] D.A. Allwood, G. Xiong, C.C. Faulkner, et al., Magnetic domain-wall logic, Science 309 (2005) 1688-1692.

[73] R. Wood, Future hard disk drive systems, J. Magn. Magn. Mater. 321 (2009) 555-561.

[74] J.A. Currivan, Y. Jang, M.D. Mascaro, et al., Low Energy Magnetic Domain Wall Logic in Short, Narrow, Ferromagnetic Wires, IEEE Magn. Lett. 3 (2012) 3000104-3000104.

[75] H. Awano, Investigation of domain wall motion in RE-TM magnetic wire towards a current driven memory and logic, J. Magn. Magn. Mater. 383 (2015) 50-55.

[76] W. de Boer, J. Bol, A. Furgeri, et al., Radiation hardness of diamond and silicon sensors compared, Phys. Status Solidi A 204 (2007) 3004-3010.

[77] K. Ishida, T. Nishizawa, The C-Co(Carbon-Cobalt) system, J. Ph. Equilibria 12 (1991) 417-424.

[78] M. Kawarada, K. Kurihara, K. Sasaki, Diamond synthesis on a metal substrate, Diam. Relat. Mater. 2 (1993) 1083-1089.

[79] R. Haubner, A. Lindlbauer, B. Lux, Diamond deposition on chromium, cobalt and nickel substrates by microwave plasma chemical vapour deposition, Diam. Relat. Mater. 2 (1993) 1505-1515.

[80] S. Fujita, Wide-bandgap semiconductor materials: For their full bloom, Jpn. J. Appl. Phys. 54 (2015) 12.

[81] W. Bludau, A. Onton, W. Heinke, Temperature dependence of the band gap of silicon, J. Appl. Phys. 45 (1974) 1846-1848.

[82] W. Wondrak, Physical limits and lifetime limitations of semiconductor devices at high temperatures, Microelectron. Reliab. 39 (1999) 1113-1120.

[83] A. Vescan, I. Daumiller, P. Gluche, et al., Very high temperature operation of diamond Schottky diode, IEEE Electron Device Lett. 18 (1997) 556-558.

[84] M. Mahalingam, Thermal management in semiconductor device packaging, Proc. IEEE 73 (1985) 1396-1404.

[85] V.K. Dwivedi, R. Gopal, S. Ahmad, Fabrication of very smooth walls and bottoms of silicon microchannels for heat dissipation of semiconductor devices, Microelectron. J. 31 (2000) 405-410.

[86] N. Fujimori, H. Nakahata, T. Imai, Properties of Boron-Doped Epitaxial Diamond Films, Jpn. J. Appl. Phys. 29 (1990) 824-827.

[87] S.A. Kajihara, A. Antonelli, J. Bernholc, R. Car, Nitrogen and potential n-type dopants in diamond, Phys. Rev. Lett. 66 (1991) 2010-2013.

[88] S. Koizumi, T. Teraji, H. Kanda, Phosphorus-doped chemical vapor deposition of diamond, Diam. Relat. Mater. 9 (2000) 935-940.

[89] R.G. Farrer, On the substitutional nitrogen donor in diamond, Solid State Commun. 7 (1969) 685-688.

[90] S.A. Kajihara, A. Antonelli, J. Bernholc, N-Type Doping and Diffusion of Impurities in Diamond, Mater. Res. Soc. Symp. Proc. 162 (1989) 315.

[91] C. Cytermann, R. Brener, R. Kalish, Search for diffusion of Li implants in natural and polycrystalline CVD diamond, Diam. Relat. Mater. 3 (1994) 677-680.

[92] V.V. Srikanth, P. Sampath Kumar, V.B. Kumar, A brief review on the in situ synthesis of boron-doped diamond thin films, Int. J. Electrochem. 2012 (2012).

[93] R. Kalish, Doping of diamond, Carbon 37 (1999) 781-785.

[94] G. Braunstein, R. Kalish, Effective p - type doping of diamond by boron ion implantation, J. Appl. Phys. 54 (1983) 2106-2108.

[95] E. Rohrer, C.F.O. Graeff, R. Janssen, et al., Nitrogen-related dopant and defect states in CVD diamond, Phys. Rev. B 54 (1996) 7874-7880.

[96] S. Koizumi, M. Suzuki, n-Type doping of diamond, Phys. Status Solidi A 203 (2006) 3358-3366.

[97] M. Katagiri, J. Isoya, S. Koizumi, H. Kanda, Lightly phosphorus-doped homoepitaxial diamond films grown by chemical vapor deposition, Appl. Phys. Lett. 85 (2004) 6365-6367.

[98] E. Gheeraert, S. Koizumi, T. Teraji, et al., Electronic states of phosphorus in diamond, Diam. Relat. Mater. 9 (2000) 948-951.

[99] I. Stenger, M.-A. Pinault-Thaury, T. Kociniewski, et al., Impurity-to-band activation energy in phosphorus doped diamond, J. Appl. Phys. 114 (2013) 073711.

[100] D. Saada, J. Adler, R. Kalish, Sulfur: A potential donor in diamond, Appl. Phys. Lett. 77 (2000) 878-879.

[101] T. Miyazaki, H. Okushi, A theoretical study of a sulfur impurity in diamond, Diam. Relat. Mater. 10 (2001) 449-452.

[102] T. Nishimatsu, H. Katayama-Yoshida, N. Orita, Theoretical study of hydrogen-related complexes in diamond for low-resistive n-type diamond semiconductor, Physica B Condens. Matter 302-303 (2001) 149-154.

[103] S.J. Sque, R. Jones, J.P. Goss, P.R. Briddon, Shallow Donors in Diamond: Chalcogens, Pnictogens, and their Hydrogen Complexes, Phys. Rev. Lett. 92 (2004) 017402.

[104] L. Tang, R. Yue, Y. Wang, N-type B-S co-doping and S doping in diamond from first principles, Carbon 130 (2018) 458-465.

[105] S. Prawer, C. Uzan - Saguy, G. Braunstein, R. Kalish, Can n - type doping of diamond be achieved by Li or Na ion implantation?, Appl. Phys. Lett. 63 (1993) 2502-2504.

[106] T.H. Borst, O. Weis, Electrical characterization of homoepitaxial diamond films doped with B, P, Li and Na during crystal growth, Diam. Relat. Mater. 4 (1995) 948-953.

[107] J. Bernholc, S.A. Kajihara, C. Wang, et al., Theory of native defects, doping and diffusion in diamond and silicon carbide, Mater. Sci. Eng. B 11 (1992) 265-272.

[108] P.R. Briddon, R. Jones, Theory of impurities in diamond, Physica B Condens. Matter 185 (1993) 179-189.

[109] W. Kaiser, W.L. Bond, Nitrogen, A Major Impurity in Common Type I Diamond, Phys. Rev. 115 (1959) 857-863.

[110] A.T. Collins, Intrinsic and extrinsic absorption and luminescence in diamond, Physica B Condens. Matter 185 (1993) 284-296.

[111] R.M. Chrenko, R.E. Tuft, H.M. Strong, Transformation of the state of nitrogen in diamond, Nature 270 (1977) 141-144.

[112] C.M. Breeding, J.E. Shigley, The “type” classification system of diamonds and its importance in gemology, Gems Gemol. 45 (2009) 96-111.

[113] J. Walker, Optical absorption and luminescence in diamond, Rep. Prog. Phys. 42 (1979) 1605-1659.

[114] A. Mainwood, Nitrogen and nitrogen-vacancy complexes and their formation in diamond, Phys. Rev. B 49 (1994) 7934-7940.

[115] M.N.R. Ashfold, J.P. Goss, B.L. Green, et al., Nitrogen in Diamond, Chem. Rev. 120 (2020) 5745-5794.

[116] H. Kanda, M. Akaishi, S. Yamaoka, Synthesis of diamond with the highest nitrogen concentration, Diam. Relat. Mater. 8 (1999) 1441-1443.

[117] B. Dischler, Handbook of Spectral Lines in Diamond: Volume 1: Tables and Interpretations, Springer Science & Business Media 2012.

[118] S. Sholihun, H.P. Kadarisman, P. Nurwantoro, Density-Functional-Theory Calculations of Formation Energy of the Nitrogen-Doped Diamond, Indones. J. Chem. 18 (2018) 749-754.

[119] A.M. Ferrari, S. Salustro, F.S. Gentile, et al., Substitutional nitrogen in diamond: A quantum mechanical investigation of the electronic and spectroscopic properties, Carbon 134 (2018) 354-365.

[120] A.M. Zaitsev, N.M. Kazuchits, V.N. Kazuchits, et al., Nitrogen-doped CVD diamond: Nitrogen concentration, color and internal stress, Diam. Relat. Mater. 105 (2020) 107794.

[121] M.A. Lobaev, A.M. Gorbachev, S.A. Bogdanov, et al., Influence of CVD diamond growth conditions on nitrogen incorporation, Diam. Relat. Mater. 72 (2017) 1-6.

[122] R. Kalish, C. Uzan-Saguy, B. Philosoph, et al., Nitrogen doping of diamond by ion implantation, Diam. Relat. Mater. 6 (1997) 516-520.

[123] R. Kalish, The search for donors in diamond, Diam. Relat. Mater. 10 (2001) 1749-1755.

[124] G. Davies, Properties and growth of diamond, Inst of Engineering & Technology 1994.

[125] I.I. Vlasov, V.G. Ralchenko, A.V. Khomich, et al., Relative Abundance of Single and Vacancy-Bonded Substitutional Nitrogen in CVD Diamond, Phys. Status Solidi A 181 (2000) 83-90.

[126] J. Meijer, B. Burchard, M. Domhan, et al., Generation of single color centers by focused nitrogen implantation, Appl. Phys. Lett. 87 (2005) 261909.

[127] Y. Mita, Change of absorption spectra in type-Ib diamond with heavy neutron irradiation, Phys. Rev. B 53 (1996) 11360-11364.

[128] H.B. Dyer, F.A. Raal, L. Du Preez, J.H.N. Loubser, Optical absorption features associated with paramagnetic nitrogen in diamond, Philos. Mag. A 11 (1965) 763-774.

[129] M.W. Doherty, N.B. Manson, P. Delaney, et al., The nitrogen-vacancy colour centre in diamond, Phys. Rep. 528 (2013) 1-45.

[130] M.W. Doherty, J. Michl, F. Dolde, et al., Measuring the defect structure orientation of a single NV− centre in diamond, New J. Phys. 16 (2014) 063067.

[131] S. Koizumi, M. Kamo, Y. Sato, et al., Growth and characterization of phosphorus doped n-type diamond thin films, Diam. Relat. Mater. 7 (1998) 540-544.

[132] L.G. Wang, A. Zunger, Phosphorus and sulphur doping of diamond, Phys. Rev. B 66 (2002) 4.

[133] K. Okano, H. Kiyota, T. Iwasaki, et al., Synthesis of n-type semiconducting diamond film using diphosphorus pentaoxide as the doping source, Appl. Phys. A 51 (1990) 344-346.

[134] G.S. Gildenblat, S.A. Grot, A. Badzian, The electrical properties and device applications of homoepitaxial and polycrystalline diamond films, Proc. IEEE 79 (1991) 647-668.

[135] S.N. Schauer, J.R. Flemish, R. Wittstruck, et al., Phosphorus incorporation in plasma deposited diamond films, Appl. Phys. Lett. 64 (1994) 1094-1096.

[136] S. Koizumi, M. Kamo, Y. Sato, et al., Growth and characterization of phosphorous doped {111} homoepitaxial diamond thin films, Appl. Phys. Lett. 71 (1997) 1065-1067.

[137] S. Koizumi, Growth and Characterization of Phosphorus Doped n-Type Diamond Thin Films, Phys. Status Solidi A 172 (1999) 71-78.

[138] L.F. Sutcu, C.J. Chu, M.S. Thompson, et al., Atomic force microscopy of (100), (110), and (111) homoepitaxial diamond films, J. Appl. Phys. 71 (1992) 5930-5940.

[139] H. Kato, S. Yamasaki, H. Okushi, n-type doping of (001)-oriented single-crystalline diamond by phosphorus, Appl. Phys. Lett. 86 (2005) 222111.

[140] H. Kato, T. Makino, S. Yamasaki, H. Okushi, n-type diamond growth by phosphorus doping on (0 0 1)-oriented surface, J. Phys. D Appl. Phys. 40 (2007) 6189-6200.

[141] S. Koizumi, K. Watanabe, M. Hasegawa, H. Kanda, Ultraviolet Emission from a Diamond pn Junction, Science 292 (2001) 1899-1901.

[142] H. Zhou, Y. Yokoi, H. Tamura, et al., Quantum Chemical Calculations of Sulfur Doping Reactions in Diamond CVD, Jpn. J. Appl. Phys. 40 (2001) 2830-2832.

[143] T. Miyazaki, Theoretical Studies of Sulfur and Sulfur-Hydrogen Complexes in Diamond, Phys. Status Solidi A 193 (2002) 395-408.

[144] S.J. Sque, R. Jones, J.P. Goss, P.R. Briddon, Shallow donors in diamond: pnictogen and chalcogen hydrogen defects, Physica B Condens. Matter 340-342 (2003) 80-83.

[145] H. Yu, N. Gao, H. Li, et al., Structural model of substitutional sulfur in diamond, Chin. Phys. B 28 (2019) 088102.

[146] I. Sakaguchi, M. N.-Gamo, Y. Kikuchi, et al., Sulfur: A donor dopant for n-type diamond semiconductors, Phys. Rev. B 60 (1999) R2139-R2141.

[147] M. Nishitani-Gamo, E. Yasu, C. Xiao, et al., Sulfur-doped homoepitaxial (001) diamond with n-type semiconductive properties, Diam. Relat. Mater. 9 (2000) 941-947.

[148] R. Kalish, A. Reznik, C. Uzan-Saguy, C. Cytermann, Is sulfur a donor in diamond?, Appl. Phys. Lett. 76 (2000) 757-759.

[149] M. Hasegawa, D. Takeuchi, S. Yamanaka, et al., n-Type Control by Sulfur Ion Implantation in Homoepitaxial Diamond Films Grown by Chemical Vapor Deposition, Jpn. J. Appl. Phys. 38 (1999) L1519-L1522.

[150] E. Gheeraert, N. Casanova, A. Tajani, et al., n-Type doping of diamond by sulfur and phosphorus, Diam. Relat. Mater. 11 (2002) 289-295.

[151] J.P. Goss, P.R. Briddon, Theoretical study of Li and Na as n-type dopants for diamond, Phys. Rev. B 75 (2007) 075202.

[152] E.B. Lombardi, A. Mainwood, A first principles study of lithium, sodium and aluminum in diamond, Diam. Relat. Mater. 17 (2008) 1349-1352.

[153] H. Yilmaz, B.R. Weiner, G. Morell, Formation of lithium clusters and their effects on conductivity in diamond: A density functional theory study, Diam. Relat. Mater. 16 (2007) 840-844.

[154] K. Okumura, J. Mort, M. Machonkin, Lithium doping and photoemission of diamond thin films, Appl. Phys. Lett. 57 (1990) 1907-1909.

[155] J. te Nijenhuis, G.Z. Cao, P.C.H.J. Smits, et al., Incorporation of lithium in single crystal diamond: diffusion profiles and optical and electrical properties, Diam. Relat. Mater. 6 (1997) 1726-1732.

[156] G. Popovici, M.A. Prelas, T. Sung, et al., Properties of diffused diamond films with n-type conductivity, Diam. Relat. Mater. 4 (1995) 877-881.

[157] I.M. Buckley-Golder, R. Bullough, M.R. Hayns, et al., Post-processing of diamond and diamond films: a review of some Harwell work, Diam. Relat. Mater. 1 (1991) 43-50.

[158] M. Restle, K. Bharuth-Ram, H. Quintel, et al., Lattice sites of ion implanted Li in diamond, Appl. Phys. Lett. 66 (1995) 2733-2735.

[159] R. Job, M. Werner, A. Denisenko, et al., Electrical properties of lithium-implanted layers on synthetic diamond, Diam. Relat. Mater. 5 (1996) 757-760.

[160] R. Zeisel, C.E. Nebel, M. Stutzmann, et al., Photoconductivity Study of Li Doped Homoepitaxially Grown CVD Diamond, Phys. Status Solidi A 181 (2000) 45-50.

[161] H. Sachdev, R. Haubner, B. Lux, Lithium addition during CVD diamond deposition using lithium tert.-butanolat as precursor, Diam. Relat. Mater. 6 (1997) 494-500.

[162] H. Sternschulte, M. Schreck, B. Stritzker, et al., Lithium addition during CVD diamond growth: influence on the optical emission of the plasma and properties of the films, Diam. Relat. Mater. 9 (2000) 1046-1050.

[163] G. Popovici, T. Sung, S. Khasawinah, et al., Forced diffusion of impurities in natural diamond and polycrystalline diamond films, J. Appl. Phys. 77 (1995) 5625-5629.

[164] E.B. Lombardi, A. Mainwood, K. Osuch, Ab initio study of lithium and sodium in diamond, Phys. Rev. B 76 (2007) 155203.

[165] E.B. Lombardi, A. Mainwood, Li and Na in diamond: A comparison of DFT models, Physica B Condens. Matter 401-402 (2007) 57-61.

[166] J.D. Hunn, N.R. Parikh, M.L. Swanson, R.A. Zuhr, Conduction in ion-implanted single-crystal diamond, Diam. Relat. Mater. 2 (1993) 847-851.

[167] J. Zhang, K. Tse, M. Wong, et al., A brief review of co-doping, Front. Phys. 11 (2016) 117405.

[168] E.B. Lombardi, A. Mainwood, K. Osuch, Interaction of hydrogen with boron, phosphorus, and sulfur in diamond, Phys. Rev. B 70 (2004) 205201.

[169] H. Katayama-Yoshida, T. Nishimatsu, T. Yamamoto, N. Orita, Codoping method for the fabrication of low-resistivity wide band-gap semiconductors in p-type GaN,

p-type AlN and n-type diamond: prediction versus experiment, J. Phys. Condens. Matter 13 (2001) 8901-8914.

[170] S.C. Halliwell, P.W. May, N.A. Fox, M.Z. Othman, Investigations of the co-doping of boron and lithium into CVD diamond thin films, Diam. Relat. Mater. 76 (2017) 115-122.

[171] W.S. Lee, J. Yu, T.Y. Lee, Study on the Li and B Co-doped diamond thin film, J. Mater. Sci. 40 (2005) 5549-5551.

[172] A. Croot, M.Z. Othman, S. Conejeros, et al., A theoretical study of substitutional boron-nitrogen clusters in diamond, J. Phys. Condens. Matter 30 (2018) 10.

[173] S.C. Eaton, A.B. Anderson, J.C. Angus, et al., Co-doping of Diamond with Boron and Sulfur, Electrochem. Solid-State Lett. 5 (2002) G65.

[174] R. Li, X. Hu, H. Shen, X. He, Co-doping of sulfur and boron in CVD-diamond, Mater. Lett. 58 (2004) 1835-1838.

[175] J.E. Moussa, N. Marom, N. Sai, J.R. Chelikowsky, Theoretical Design of a Shallow Donor in Diamond by Lithium-Nitrogen Codoping, Phys. Rev. Lett. 108 (2012) 226404.

[176] Z. Delun, L. Tang, Y. Geng, et al., First-principles calculation to N-type LiN Co-doping and Li doping in diamond, Diam. Relat. Mater. 110 (2020) 108070.

[177] S. Conejeros, M.Z. Othman, A. Croot, et al., Hunting the elusive shallow n-type donor – An ab initio study of Li and N co-doped diamond, Carbon 171 (2021) 857-868.

[178] M.Z. Othman, P.W. May, N.A. Fox, P.J. Heard, Incorporation of lithium and nitrogen into CVD diamond thin films, Diam. Relat. Mater. 44 (2014) 1-7.

[179] C.X. Yan, Y. Dai, B.B. Huang, et al., Shallow donors in diamond: Be and Mg, Comput. Mater. Sci. 44 (2009) 1286-1290.

CHAPTER 2

EXPERIMENTAL TECHNIQUES AND COMPUTATIONAL THEORY

This chapter introduces the experimental techniques and facilities, including diamond seeding, growth, modification and characterisation facilities used for the work in this thesis. The computational theories and tools such as Hartree-Fock theory, density functional theory and CRYSTAL 17 software package are also introduced in this chapter.

2.1 Diamond growth

2.1.1 Substrates

Polycrystalline diamond film is normally grown on substrate materials such as Si, Mo and W. Among these, Si is a popular substrate material due to many advantages such as cheap price, high melting point, the ability to form a limited carbide layer and low thermal expansion coefficient [1]. In this thesis, n-type Si substrate (Resistivity: 1 – 30 ohm-cm, Si-Mat Ltd) was used for polycrystalline diamond film growth. It was doped by phosphorus, and has been polished on one side and has a very thin (10 nm) native oxide layer on the surface. This n-type Si is electrically conductive, making it a perfect substrate for SEM observation and electrospray ionization seeding (see section 2.1.2).

All the substrates were cut into dimensions required (10 mm × 10 mm or so) using the in-house Oxford laser micromachining tool (section 2.2.1) and cleaned by methanol in an ultrasonic water bath for 10 min before use.

2.1.2 Diamond seeding

Seeding is an important step when a non-diamond substrate is used for hot-filament diamond CVD. The nucleation rate of diamond on a clean, smooth non-diamond substrate is very slow, while diamond seeding or abrasion of the surface can help to speed up the nucleation rate by a factor of 100 or more, as well as ensure the uniform growth of diamond film over the whole substrate area.

The conventional nucleation enhancement method is manual abrasion, which involves simply polishing the Si substrate with diamond powders. As well as creating micron-sized scratches in the Si surface, the abrasion process can embed nano-size diamond fragments into the substrate, which act as seeds for high-density diamond nucleation [1]. Manual abrasion is easy to operate and can be used for most substrate materials; however, it is hard to keep the consistency of each manual operation. The scratching also damages the insulating capping layer SiO_2, which is useful for studying the electrical properties of the sample, and cannot guarantee a uniformly distributed seeding.

Therefore, a novel method was employed for diamond seeding in this thesis. The method was based on the electrospray ionization (ESI) technique [2]. It utilised a suspension of detonation nanodiamond dispersed in deionized water (0-0.05 μm, 97.5 cts/kg, agglomerate free, Microdiamant). 10 drops (~ 100 μL) of this original suspension were dispersed in 30 mL methanol in a vial and sonicated for 30 min before use. The resulting suspension was well dispersed and stable for days. As shown in Figure 2.1, the diamond seeding suspension was added to a syringe attached to an electrically insulated box, and a high voltage (~ 35 kV) was applied to the metal needle. The seeding suspension was attracted to a grounded substrate positioned a few cm away from the needle tip (nozzle), and so was sprayed through the nozzle as ionised aerosols. The nozzle hole size is crucial and must take into account the size of the particle in the seeding solution. A small emitter can be blocked by agglomerated clumps diamond crystals, but a nozzle that is too large will spray these aggregations as clumps onto the substrate and lead to a poor seeding uniformity [3]. We used a syringe needle (26G) as a nozzle, which was optimal for nanodiamond seeding to be uniformly distributed onto the substrate.

The Si substrate was attached to a grounded platen using conductive carbon tape, and rotated at about 1000 rpm to improve uniformity of seed deposition.

ESI seeding has several advantages over manual abrasion. For example, it does not damage the substrate surface and can generate a higher uniformity and density of seeding. It also allows substrates with 3-dimensional nanostructures, such as pillars and needles, to be seeded. To achieve the best electrospray results, it is better to use conductive substrates, otherwise charge build-up occurs, deflecting the ion path and affecting uniformity. Therefore, the n-type Si worked better than the undoped Si for ESI.

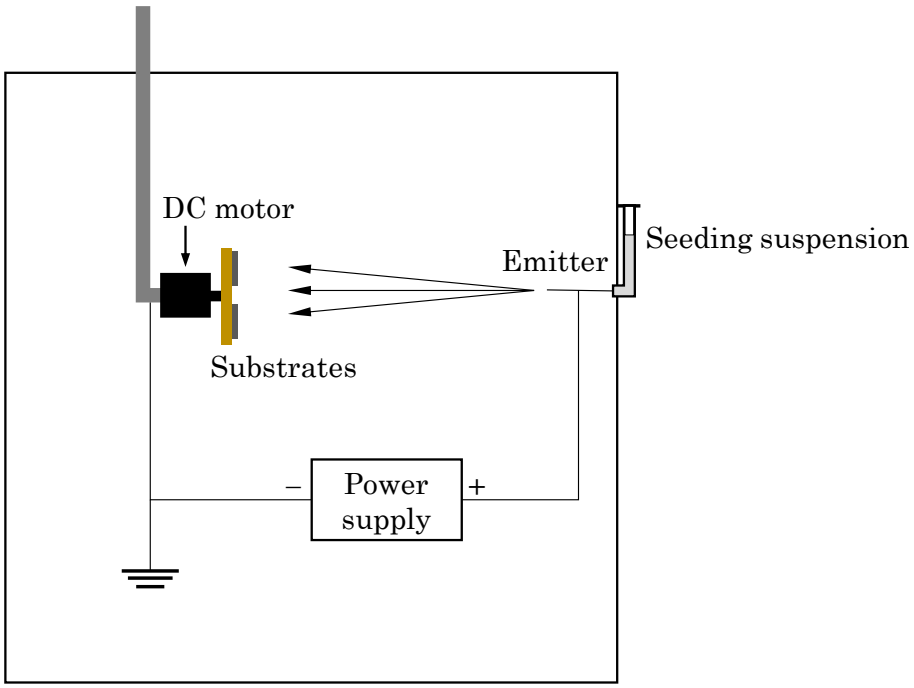

Figure 2.1. Schematic diagram of electrospray ionization.

2.1.3 Hot-filament CVD

A schematic diagram of a hot-filament CVD reactor has been given in chapter 1. Pre-seeded samples to be coated were put into one of two hot filament CVD reactors for growing diamond films. One reactor was dedicated to growing undoped diamond films, while the other was solely for boron-doped diamond. Boron contaminates a reactor and is difficult to remove – and since it takes only a trace amount of B to be incorporated into diamond to change its conductivity, the two processes required separate reactors. Both reactors were connected to rotary

pumps allowing them to be evacuated to a base pressure of ~ 50 mTorr (measured using a Pirani gauge) prior to deposition.

For depositing undoped diamond, only hydrogen (200 sccm, 99.99%, BOC Ltd) and methane (2 sccm, 99.99%, Air Liquide Ltd) were introduced into the chamber. The gas flow was controlled by mass flow controllers (MFCs) and the chamber was maintained at a process pressure of 20 Torr using a manually controlled needle valve which throttled the pumping speed. The process pressure was monitored using a capacitance manometer gauge. Reactant gases were activated into radicals by the high temperature generated by hot filaments made of three tantalum wires, which were resistively heated to temperatures of 2400 K (checked using a 2-colour pyrometer) using a DC power supply (typically 25 A, ~10 V). Diamond was deposited on the substrate which was placed on a resistively heated sample holder situated ~ 5 mm below the filaments. The substrate heater (4 A, 5 V) could raise the substrate temperature to ~ 400 °C by itself, but the radiant heat from the proximity of the heated filaments increased this further to ~ 900 °C. Under these conditions, the typical diamond growth rate was ~ 0.5 μm per hour. Due to the random nature of the seeding process, films grown in this way were always microcrystalline, with faceted polycrystalline morphologies.

A carbide layer forms on the tantalum wires after a few minutes of running. The carbide layer protected the filaments from further reaction and from metal evaporation, but also made them brittle. Therefore, normally the filaments had to be changed for each run.

The formation of diamond in a CVD reactor is a complex process but can be explained in Figure 2.2 [4]. First, reactant gases such as hydrogen and methane are introduced into the reactor chamber. These gases are 'activated' by the heat generated from filaments, which is sufficient to decompose the gases into fragments, atoms and radicals, which react together to form a reactive chemical 'soup'. Reactive products such as methyl radicals (CH_3) and H atoms are transported to the substrate surface by convection or diffusion. An H atom bonded to a C on the substrate surface is then abstracted by the gas-phase atomic H, to form a stable H_2 molecule, leaving behind a surface radical. A gas-phase CH_3

radical then bonds to this surface radical, adding one carbon to the diamond lattice. This process of H abstraction followed by CH_3 addition repeats many times, gradually building up the diamond structure atom-by-atom [1, 5, 6].

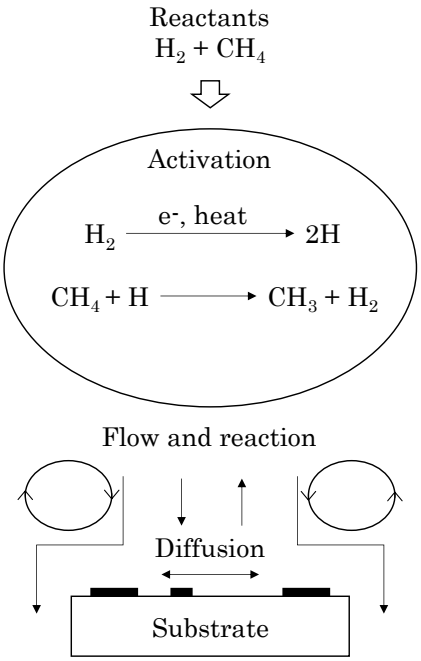

Figure 2.2. Schematic diagram of diamond CVD process [4].

For boron-doped diamond, diborane (B_2H_6, ≤ 1 sccm) was introduced as well as hydrogen and methane. The conductivity of the resulting diamond depended directly upon the amount of diborane added to the gas mixture during growth. Thus, the electrical conductivity of the diamond could be controlled from insulating to semiconducting, and then to metallic by increasing the diborane flow.

2.1.4 Diamond film growth mode

When discussing the growth mode of thin films on the nano scale, in a small local area the substrate can be simplified to be a flat surface. As illustrated in Figure 2.3, the thin-film growth modes can be classified into three types [7, 8]: (a) Volmer-Weber type, (b) Frank-van der Merwe type and (c) Stranski-Krastanov type.

The Volmer-Weber mode is also known as 'island-growth', in which the film atoms or species combine with each other and form clusters rather than attach on the substrate surface. As shown in Figure 2.3a, in this mode, the binding force between

film atoms is stronger than that between film atoms and the substrate surface, which leads to the growth of the film in three dimensions, and the formation of isolated islands. When there are enough islands formed on the surface, the gaps between the islands are filled and the islands merge to form a continuous film.

Alternatively, if the binding force between the film atoms and the substrate surface is stronger than that between the film atoms, the film atoms will stick on the substrate surface and follow a two-dimensional growth. This mode is called Frank-van der Merwe type. The growth of a new layer does not start until the previous layer is complete. Therefore, the growth of the film is strictly layer-by-layer and the mode is also known as 'layer growth'.

The third type, Stranski-Krastanov mode, is a combination of the island growth mode and the layer growth mode, so is known as 'island/layer growth'. After a certain thickness is reached in the layer-by-layer growth mode, the film growth will follow the island growth mode and begin to grow in three dimensions.

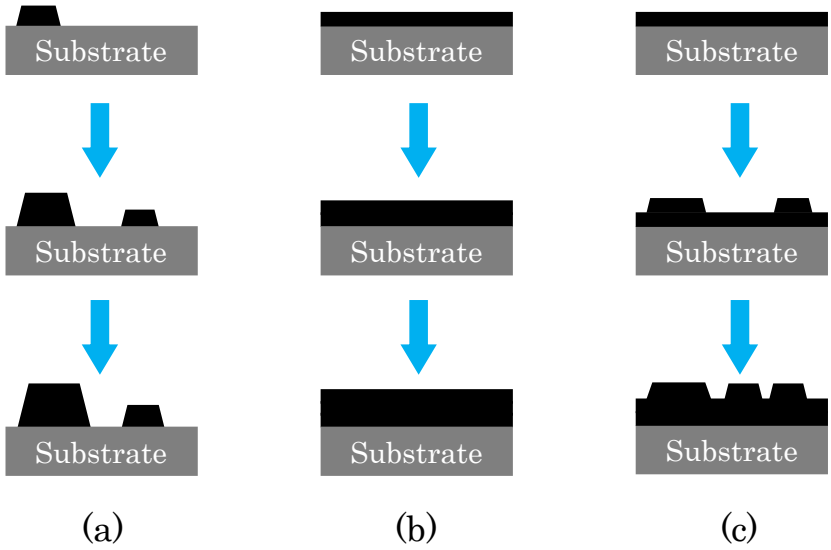

Figure 2.3. Typical modes of thin film growth: (a) Volmer-Weber type, (b) Frank-van der Merwe type and (c) Stranski-Krastanov type.

The epitaxial growth of CVD diamond film on Si, Mo or W follows the island growth mode [9-11], *i.e.*, polycrystalline islands appear first, then the individual islands coalesce into a film. Due to this nature, it is difficult to obtain ultra-smooth diamond film directly from CVD, and therefore homogeneous diamond seeding is necessary to reduce the surface roughness.

2.2 Material modification

2.2.1 Laser machining

Laser cutting is a technique that uses a high-power laser beam to irradiate the surface of a material. The high-power focused laser can melt or evaporate the surface atoms so that the material can be cut through or microstructured on the surface. Laser cutting is capable of machining most types of common materials and especially useful for the cutting or surface processing of superhard materials, such as diamond [12-16].

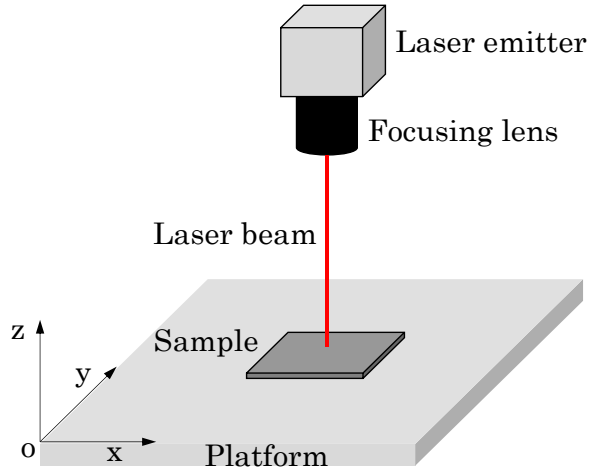

Figure 2.4. Schematic diagram of laser cutting process.

A laser micromachining system (Alpha 532, Oxford) was used to cut Si and diamond. The micromachining system is based on a 532 nm wavelength nanosecond laser. As shown in Figure 2.4, the laser is fixed and focused onto the sample through a lens. The sample is attached to a stage connected with servomotors which control movement of the stage in the *x*, *y* and *z* directions under computer control. To achieve the most efficient cutting, the laser must be focused on the sample in the *z* direction.

Motion of the servomotors were controlled via the computer by the standard motion control computer language, G code, which was entered through the *Cimita* program (Oxford Lasers Ltd). This allowed the user to control the cutting speed, depth of cut, and even shape of the cut (straight lines, circles, rectangles, or any shape predefined in the software).

2.2.2 Thermal evaporation

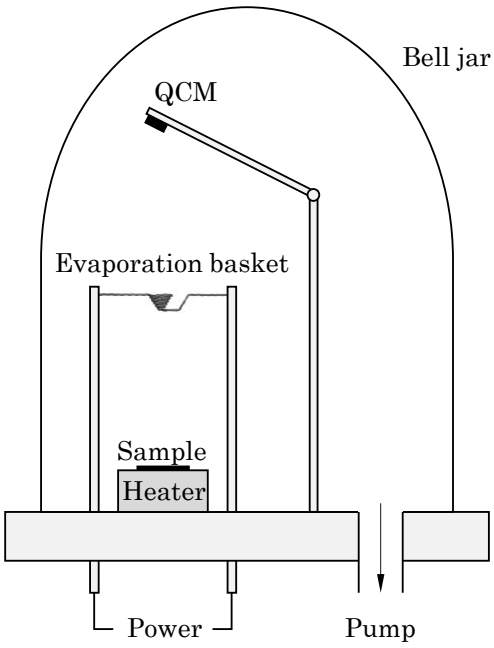

Figure 2.5. Schematic diagram of the thermal evaporator.

A thermal evaporator (Edwards E306A) was used to evaporate metal on Si substrate or diamond samples, for the purposes of making electrical contacts, etc. A schematic diagram of the thermal evaporator is shown in Figure 2.5. It can be divided into the following parts.

1) High vacuum chamber

The evaporation process was carried out in a bell jar connected to a rotary pump and a diffusion pump with a base pressure of 6×10^{-6} mbar. This high vacuum environment facilitated metal evaporation without oxidation and also protected the samples from any possible contamination from the background air.

2) Sample holder

The sample was placed on the sample holder, which was equipped with a heater underneath. The heater was set to around 150 °C to preheat the sample to evaporate any adsorbates from the surface before processing, and to reduce the temperature difference between the sample and filament during thermal evaporation. Without this, the thermal shock when the tungsten container was

heated on might cause the Si substrate to shatter. The temperature of the sample holder was monitored and controlled by a temperature control system.

3) Vaporisation source

The metal to be evaporated (usually in the form of lumps, pellets or ribbon) was placed into a coiled evaporation container made of tungsten (wire diameter 0.5 mm, Alfa Aesar Ltd). Due to the high melting point of tungsten, the container can be heated to temperatures over 2000°C without losing its structural integrity or evaporating W atoms onto the substrate. Current (~50 A) from a power supply was applied to the tungsten container and increased slowly, and the tungsten basket glowed red/white hot, until the source metal in the tungsten container started to evaporate, and was reduced to zero slowly when the required thickness was reached.

4) Thickness monitor

A quartz crystal microbalance (QCM) was installed inside the chamber to monitor the thickness of the evaporated metal in real time as evaporation proceeded. The QCM measured the mass of metal deposited onto a vibrating quartz disc. As the mass of the metal layer increases, the vibrational resonance frequency of the quartz changes. Thus, the QCM, can measure the mass of the evaporated metal with very high precision, and using the known density of the metal this mass was converted to thickness to an accuracy of ± 0.1 nm thickness.

Cobalt wire (0.5 mm diameter, 99.995 %, Alfa Aesar Ltd) was employed in the thermal evaporation for the purpose of lift-off microfabrication and growing diamond on Co film (~36 nm). To protect the photoresist material from degradation by overheating, the sample with photoresist was processed without turning on the heater. Co was also evaporated (~18 nm) on Si to study the growth process of diamond on Co. Aluminium wire (1.0 mm diameter, 99.999%, Alfa Aesar Ltd) and titanium wire (0.125 mm, 99.6%, Goodfellow Ltd) were deposited as interlayer (~ 15 nm) between Co and diamond.

2.2.3 Lift-off microfabrication

Lift-off is a technique using sacrificial material (*e.g.*, photoresist) to fabricate micro- or nano-patterned thin films on the surface of substrate such as Si. It is especially useful for patterning the hard-to-etch materials such as gold or platinum, which are difficult to pattern by dry or wet etching [17]. The microstructured surface can be made with a great geometrical complexity, which has wide applications in analytical chips or "lab-on-a-chip" devices [18].

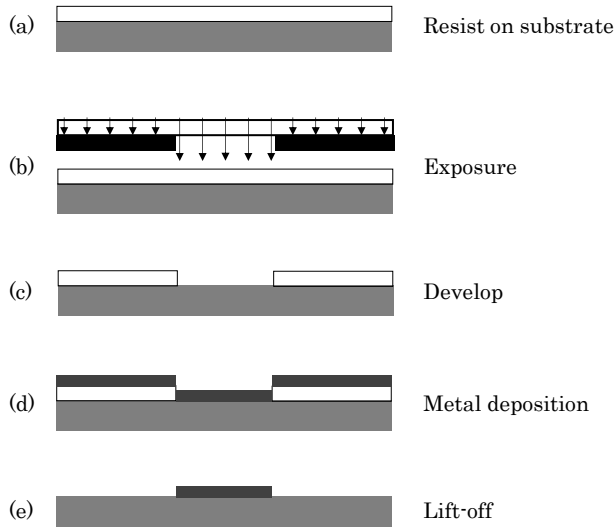

Figure 2.6. Lift-off process.

The main process of lift-off can be explained in Figure 2.6 [19]. First, in step (a), a thin sacrificial photoresist layer is deposited on a clean substrate (*e.g.*, Si) by spin coating. Then in step (b), the resist is exposed to UV light through a mask bearing the required pattern. The substrate is then dipped into a developer solvent to form patterned resist features on the substrate, as shown in step (c). During the developing process, depending on the different types of the resist material used, the exposed area will be removed or saved. If a positive resist is used, the exposed area becomes soluble to the developer therefore will be removed, and the unexposed portion will remain. Conversely, if it is a negative resist, the exposed area will become insoluble and stay on the substrate, but the unexposed area will be dissolved. In step (d), the required metal is then deposited onto the substrate with patterned resist by sputtering or thermal evaporation, forming a layer over all the features. Finally in step (e), the residual photoresist is removed using a

particular solvent such as acid or acetone, or O_2 plasma 'ash' step, and only the metal film having direct contact with the substrate will stay on the surface.

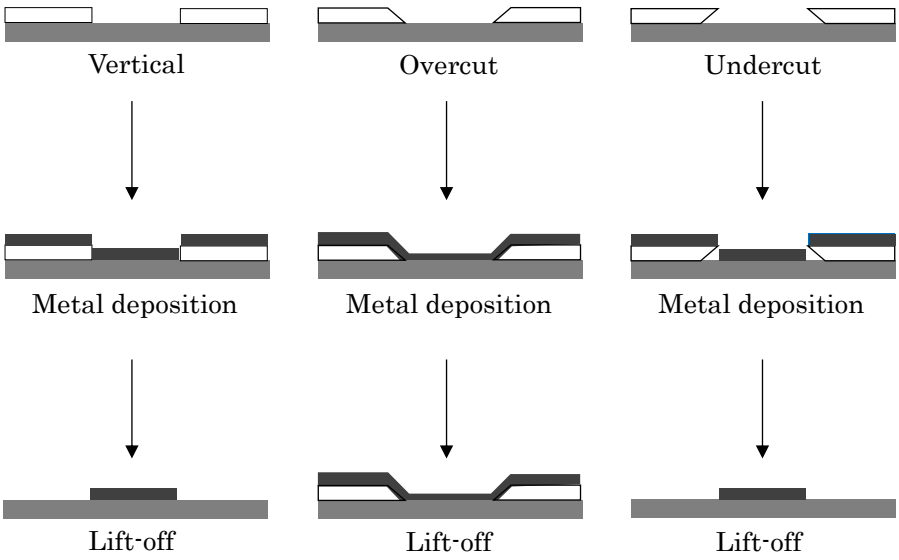

Figure 2.7. Lift-off process of different resist profiles.

A critical factor that influences the lift-off result is the profile of the developed photoresist. The resist profile in Figure 2.6 has an ideal vertical shape, which allows a near perfect transfer of the mask pattern. However, due to the UV exposure gradient, the developed resist profile is often different. After development, three different profiles of resist may be obtained. As summarized in Figure 2.7, according to the different resist sidewall angles, the resist profiles can be divided into vertical (90°), overcut (< 90°) and undercut (> 90°) [19]. When the resist profile is overcut, the deposited metal will become one continuous film that cannot be separated easily, so lift-off becomes difficult or even impossible. Only when the resist profile is vertical or undercut, can the "unwanted" metal film be lifted off. The resist profile is influenced by the exposure dose and development time [17].

In order to facilitate the lift-off process, a bi-layer resist lift-off scheme [20-22] can be employed. The schematic diagram is shown in Figure 2.8. Instead of spin-coating one resist layer on the substrate, two different photoresist layers are coated on the substrate sequentially. The lower resist layer dissolves faster in the developer than the upper layer, so that an undercut resist profile can be obtained.

Compared with the single-layer lift-off process, the bi-layer scheme favours the formation of undercut profile, and therefore the fabrication of patterned metal film with more reliability.

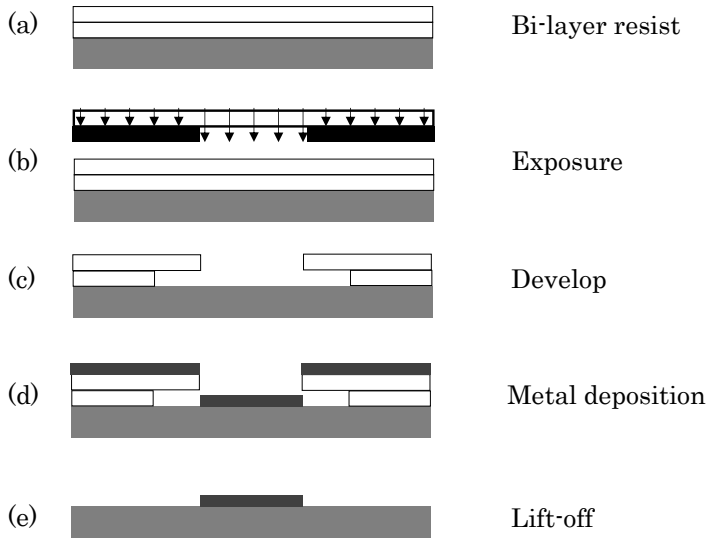

Figure 2.8. Lift-off process using bi-layer resist.

In this thesis, we have studied the possibility of growing diamond on patterned magnetic films (see Chapter 3), which were fabricated using a standard lift-off process. The bi-layer resist scheme (LOR+S1805 resist stack, MicroChem Corp.) was used. A Karl Suss MJB3 Mask Aligner was used to transfer the pattern from mask to resist. The lift-off process was done in the cleanroom (School of Physics, UoB) except the metal deposition, which was finished in the diamond lab.

2.3 Material characterization

2.3.1 SEM and TEM

Scanning electron microscopy (SEM) scans the sample with a focused, high-energy beam of electrons, and collects, amplifies and re-images the information to characterize the sample morphology. Because wavelength of electrons is much smaller than that of photons, SEM has much higher resolution than that of optical microscopy.

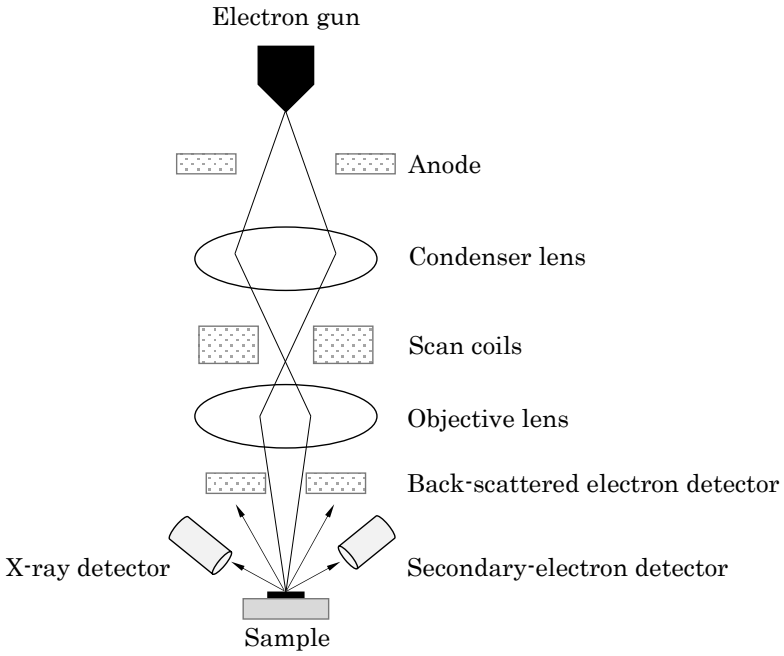

Figure 2.9. A schematic diagram of a scanning electron microscope.

The schematic diagram of a SEM is displayed in Figure 2.9. An electron beam emitted by the electron gun is focused onto the sample surface in a high vacuum chamber. The incident (primary) electrons can excite electrons in the sample surface, which are then emitted into vacuum. These "secondary electrons" (SE) are collected by the secondary-electron detector and processed into an image. Since secondary electrons come from the surface or the near-surface region, SE images are very useful for the inspection of topography of the sample surface.

Alternatively, some primary electrons can be elastically scattered and collected by the back-scattered-electron detector. The back-scattered electron (BSE) signal depends on the atomic number of the specimen; the higher the atomic number, the brighter the signal. Therefore, BSE images can help to distinguish different elements or phases.

An SEM is often equipped with an energy-dispersive X-ray spectroscopy (EDX or EDS) system. When the high-energy beam (electrons or X-ray) hits the inner shell of an element, the electron can be excited, leaving a vacancy. Then, the electron in the outer shell of high energy moves to the vacancy in the inner shell. Due to the energy difference between the outer shell and the inner shell, X-rays will be released as the form of energy. The energies of the X-rays are unique to the specific

element they originate from, so these energies can be used to analyse the element distribution of the sample surface. Since EDX relies on the excitation of the inner-shell electron and the movement of the outer-shell electron, it cannot detect the light elements such as H and He, which only have one shell of electrons.

Transmission electron microscopy (TEM) is a technique in which electrons are transmitted through a sample to form an image. The samples need to be very thin to make sure the electron beam can pass through. Compared with SEM, TEM has higher magnification, but is also more difficult to operate and the samples are more difficult to prepare.

SEM images were obtained in a JSM-IT300 produced by JEOL. This instrument has a magnification of up to 300,000× and resolution of nano-level. It is also equipped with EDX (Oxford Instruments) for element analysis. A JEOL 2100F TEM having sub-nanometre resolution was employed for taking images for magnetic nano particles.

2.3.2 Atomic force microscopy

Atomic force microscopy (AFM) is an analytical technique to characterize the surface structure of solid materials including insulators. It obtains information of the surface by detecting the interaction between the sample surface and a cantilever probe. The microcantilever is extremely sensitive to weak forces, enabling AFM to have a high spatial resolution, even down to the atomic level.

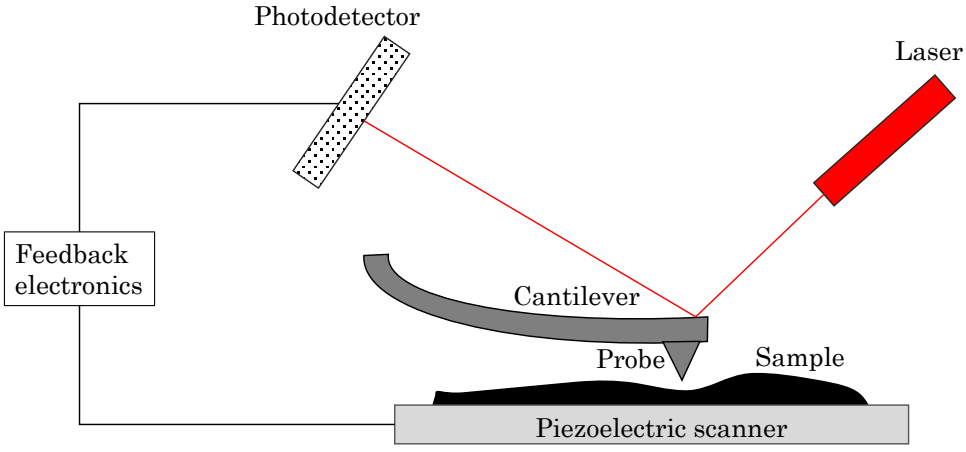

Figure 2.10. Schematic diagram of an AFM.

A schematic diagram of an AFM is shown in Figure 2.10. The cantilever is fixed at one end, while the other end is attached to a very sharp probe (radius < 10 nm [23]). The tip of the probe is in contact with the sample (contact mode), or very close to the sample (non-contact mode), or tapping the sample (tapping mode) [24]. The sample sits on a piezoelectric scanner, which allows it to move in *x*, *y* and *z* directions with extremely high precision. During scanning, the probe is dragged across the sample surface and changes height in the *z* direction over the surface topography. A laser is reflected by the cantilever onto a photodetector so that the deflection of the cantilever, and hence the morphology of the sample is recorded. There are very small attractive or repulsive forces between probe and sample surface. This force is maintained by moving the piezoelectric scanner in *x*, *y* and *z* directions, feeding back information of the morphology. The combination of photodetector and piezoelectric scanner enable an AFM to make atomic-resolution measurements.

A magnetic force microscope (MFM) is a special type of AFM. MFM obtains the magnetic information of a sample by scanning it with a magnetic tip and measuring the magnetic interaction. A typical MFM characterization requires two scans, a standard AFM scan in tapping mode which detects the van der Waals interactions between the probe and the sample, and a magnetic scan in non-contact mode detecting the long-range magnetic interactions [25]. In the first scan, the topography of the sample is determined, while in the second scan, the magnetic field gradient can be detected.

In the non-contact mode, the cantilever can be treated as a damped harmonic oscillator [26]. The cantilever oscillates, and its spring constant is modified by the magnetic field during measurement. As a result, the frequency, amplitude and phase of the oscillating cantilever are also influenced by magnetic field gradient [25]. As the probe is lifted away from the surface, the van der Waals interaction is negligible, and the shift of frequency, amplitude and phase can reflect the long-range magnetic interaction. MFM images are sensitive to surface morphology, therefore it requires the sample surface to be flat in order to detect the magnetic field gradient accurately. One approach to compensate the topography-induced error is by running the second MFM scan at a 'constant-distance mode', *i.e.*,

keeping the distance from the probe to the sample surface at a constant, as shown in Figure 2.11. When scanning a rough surface at constant-distance mode, the cantilever has to adjust its position in *z* direction according to the path obtained from the first topography scan. However, it requires much more time to finish than the 'constant-height mode', *i.e.*, running the scan at a fixed height.

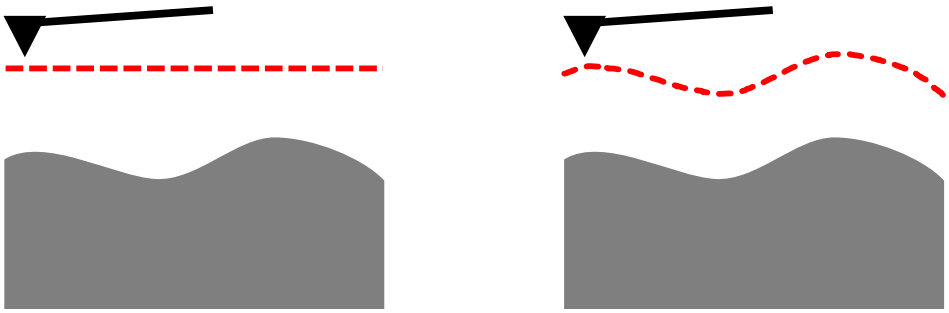

Constant-height mode Constant-distance mode

Figure 2.11. Two operating modes: constant-height mode and constant-distance mode of MFM.

A Bruker AFM system, Bruker Multimode instrument fitted with a Nanoscope V controller, a Picoforce extender and a magnetic tip was used for the characterization of morphology and magnetic properties of diamond film grown on Co. It has an extremely high resolution to nano-level. This part will be presented in Chapter 3.

2.3.3 Raman spectroscopy

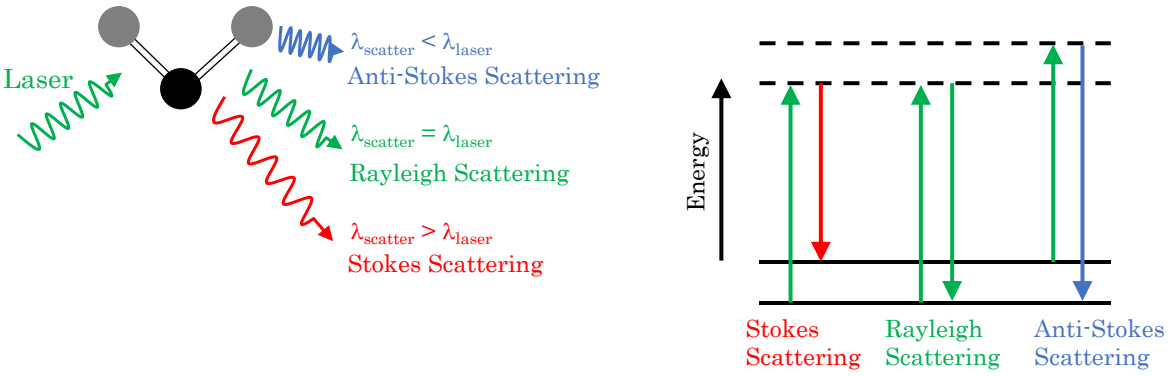

Figure 2.12. Schematic diagram of Raman spectroscopy.

Raman spectroscopy is based on the scattering of light by molecules. A schematic diagram showing the principles behind Raman spectroscopy is shown in Figure 2.12. When a laser beam hits a molecule, most photons are elastically scattered (Rayleigh scattering), such that the scattered light has the same energy and wavelength, and the molecule does not change in energy. However, a very small percentage of the photons will be scattered inelastically which gives rise to Raman scattering. In this case, the molecules absorb the photon energy and become excited into a higher vibrational state. When the vibrationally excited molecule relaxes by emitting a photon, there are three possible outcomes. It can lose a photon of the same energy as that which it absorbed – in which case the molecule relaxes back down to its original state and this is Rayleigh scattering. Alternatively, it can relax to vibrational levels higher or lower than the original level, and in these cases the emitted photon will have less (Stokes' scattering) or more energy (anti-Stokes scattering), respectively than the original photon. For Stokes scattering, which forms the majority of the Raman scattering, the scattered light will have longer wavelength than the original laser beam. For anti-Stokes's scattering, the scattered light has a shorter wavelength than the laser.

By measuring the energy (wavelength) difference between the incident and the scattered light, Raman spectra can be determined. Raman spectra are unique for each molecule because they act as a fingerprint of the molecule's vibrational energy levels. For example, graphite (sp^2 carbon) and diamond (sp^3 carbon) have different vibrational modes, which give rise to different Raman spectra [27]. Therefore, Raman can be used to characterize diamond. The most representative Raman spectra of diamond and graphite materials are diamond at 1332 cm^{-1}, disordered graphite (D band) at 1355 cm^{-1}, amorphous carbon at 1550 cm^{-1}, and crystalline graphite (G band) at 1580 cm^{-1}, respectively [28].

A Renishaw 2000 laser Raman spectrometer was used to evaluate diamond quality. Raman spectra were obtained using a green laser of wavelength 514 nm. This Raman spectrometer is equipped with an optical microscope (Leica 020-520.007 DM/LP, magnification 500×), which enables it to take images and choose the area for Raman characterisation.

2.4 Computational theory

2.4.1 Many-body Schrödinger equation

In the beginning of 20th century, quantum mechanics was developed to study the quantum world. At the atomic scale, materials are collections of electrons and nuclei, which interact and reach a dynamically balanced state. The interactions include the Coulomb repulsion between electrons, the repulsion between nuclei, and the attraction between electron and nuclei [29].

The motions of the quantum particles, such as an electron, can be described by the Schrödinger equation. A simple form of the time-independent Schrödinger equation is,

$$\widehat{H}\Psi = E\Psi \tag{2.1}$$

where Ψ is the wave function of the system, $\widehat{H}$ is the Hamiltonian operator and E is the energy of the system. For a system containing M nuclei and N electrons, the equation can be expressed as [29],

$$\left[-\sum_i \frac{\hbar^2}{2m_e}\nabla_i^2 - \sum_I \frac{\hbar^2}{2M_I}\nabla_I^2 + \frac{1}{2}\sum_{i\neq j}\frac{e^2}{4\pi\epsilon_0}\frac{1}{|\mathbf{r}_i-\mathbf{r}_j|} + \frac{1}{2}\sum_{I\neq J}\frac{e^2}{4\pi\epsilon_0}\frac{Z_I Z_J}{|\mathbf{R}_I-\mathbf{R}_J|} - \sum_{i,I}\frac{e^2}{4\pi\epsilon_0}\frac{Z_I}{|\mathbf{r}_i-\mathbf{R}_I|}\right]\Psi = E_{\text{tot}}\Psi \tag{2.2}$$

Where i and j run from 1 to N, I and J run from 1 to M, respectively. In this equation, e is the electron charge, ϵ_0 the permittivity of vacuum, Z_I the atomic numbers, m_e the electron mass, $\mathbf{r}$ the vector specifying coordinates of electrons, $\mathbf{R}$ the vector specifying the coordinates of nuclei and E_{tot} the total energy of the system. This equation is called many-body Schrödinger equation, which contains almost all the information of a system in equilibrium. If this equation can be solved, then all the properties of the system, such as electronic or optical properties, can be determined.

However, the complexity of the solution increases exponentially with the increase of size of the system, which is known as the “exponential wall”. Apart from very

small molecules, such as H_2, it is impossible to solve the many-body Schrödinger equation directly. Therefore, researchers have been seeking other possible methods to solve this equation.

2.4.2 Born-Oppenheimer approximation

Since the mass of the nucleus is much greater than that of electrons, the electrons move much faster than the nucleus. Therefore, the motion of nucleus and electrons can be treated separately. When dealing with the motion of electrons, the nucleus can be considered to be fixed. When dealing with the motion of nucleus, it can be assumed that fast-moving electrons establish a uniformly distributed negative charge field, and the nucleus is moving in such a negative charge field.

Within this Born-Oppenheimer approximation [30], the wave function of the system can be written as the product of the nucleus wave function $\chi(\mathbf{R})$ and the electron wave function $\phi(\mathbf{r}, \mathbf{R})$:

$$\Psi(\mathbf{r}, \mathbf{R}) = \chi(\mathbf{R})\phi(\mathbf{r}, \mathbf{R}) \tag{2.3}$$

Through the Born-Oppenheimer approximation, the nucleus and electrons can be treated separately, and the multi-particle system is simplified to a multi-electron system. The Born-Oppenheimer approximation is accurate in many cases. It reduces the difficulty of quantum mechanics processing, and is therefore widely used in molecular-structure research, condensed-matter physics, quantum chemistry, chemical reaction dynamics and other fields [31].

2.4.3 Hartree-Fock (HF) approximation

The motion of electrons and nucleus is separated by the Born-Oppenheimer approximation, but the Schrödinger equation of the system is still a many-body problem. Due to the Coulomb repulsion between the electrons, it is still impossible to solve the many-electron system.

Hartree [32] pointed out that the wave function of a many-electron system can be expressed as the product of single-electron functions:

$$\phi(\mathbf{r}) = \phi_1(\mathbf{r_1})\phi_2(\mathbf{r_2}) \dots \phi_n(\mathbf{r_n}) \tag{2.4}$$

However, this equation was obtained without considering the antisymmetric properties of wave function. Fock improved the equation by replacing the product of wave function with a Slater determinant [33]:

$$\phi = \frac{1}{\sqrt{N!}} \begin{vmatrix} \phi_1(x_1) & \phi_2(x_1) & \cdots & \phi_n(x_1) \\ \phi_1(x_2) & \phi_2(x_2) & \cdots & \phi_n(x_2) \\ \vdots & \vdots & \vdots & \vdots \\ \phi_1(x_n) & \phi_2(x_n) & \cdots & \phi_n(x_n) \end{vmatrix} \tag{2.5}$$

where $x_i = (r_i, \sigma_i)$, in which r_i and σ_i represent coordinates and the spin of the electron, respectively. This Slater determinant is an ideal expression which meets the criteria of antisymmetry of wave function and Pauli exclusion principle.

The Hartree-Fock (HF) equation of a single electron can be expressed as:

$$\left[-\nabla^2 + V(\mathbf{r}) - \int \mathrm{d}r' \frac{\rho(\mathbf{r}') - \bar{\rho}^{HF}(\mathbf{r}, \mathbf{r}')}{|\mathbf{r} - \mathbf{r}'|}\right] \phi_i(\mathbf{r}) = E_i \phi_i(\mathbf{r}) \tag{2.6}$$

where $\rho(\mathbf{r}')$ is the electron charge distribution, $\bar{\rho}^{HF}(\mathbf{r}, \mathbf{r}')$ the exchange distribution, and $\phi_i(\mathbf{r})$ the wave function of a single electron.

Overall, based on the Born-Oppenheimer approximation, the HF equation assumes that in a multi-electron system, all electrons move in a uniform field around the nuclei. By using the HF approximation, the many-body Schrödinger equation is simplified to single-electron equations of N electrons, making it possible to solve the Schrödinger equation.

However, the HF equation only considers electron exchange but neglects the electron correlation, which limits its computing accuracy. Therefore, the HF method works well with molecular systems, but when it comes to crystalline bulk systems, the accuracy is very limited. Secondly, the variable to be solved in HF equation is still the wave function. Since each electron has 3 Cartesian coordinates, for a system containing Nelectrons, the corresponding wave function will have $3N$ variables [29], making the computational cost extremely expensive.

2.4.4 Density functional theory

Density functional theory plays an important role in first-principles calculation. It simplifies the calculation of a many-electron system to the calculation of electron density. DFT has found its applications in studying material's electrical [34, 35], magnetic [36, 37], optical [38, 39], thermodynamic [40, 41] and catalytic properties [42-44].

2.4.4.1 Hohenberg-Kohn theorem

According to the Hohenberg-Kohn theorem [45], for a many-electron system, its ground-state properties, such as the total energy and wave functions, all depend on the electron density. Therefore, the energy of the system (E) can be treated as a functional of the electron density (n).

$$E = F[n] \tag{2.7}$$

Hohenberg-Kohn theorem is composed of two theorems:

Theorem 1: The external potential of any many-particle system is exclusively determined by the electron density of the ground state, *i.e.*, the total energy of the system is determined by the electron density.

Theorem 2: The energy of the system takes the electron density as the universal functional. For any given external potential, the ground-state energy is the global minimum of the functional, *i.e.*, the ground-state energy of the system is determined by the ground-state electron density.

Therefore, the ground-state properties of a many-electron system can be treated as the functional of the electron density. Given the Hohenberg-Kohn theorem, the basic number of variables of the system has decreased from a $3N$-dimensional wave function to a 3-dimensional electron density.

2.4.4.2 Kohn-Sham equations

According to the Hohenberg-Kohn theorem, the total energy of a many-electron system in its ground state is a functional of the electron density. Therefore, the most critical step is to construct such an energy functional. So far, the energy

functional is constructed by solving the Kohn-Sham equation [46]. The well-known form of the Kohn-Sham equation for a single electron can be expressed as:

$$\left[-\frac{1}{2}\nabla^2 + v(\mathbf{r}) + \int \mathrm{d}r\,\frac{\rho(\mathbf{r})}{|\mathbf{r}-\mathbf{r}'|} + \frac{\delta E_{\mathrm{XC}}[\rho]}{\delta\rho}\right]\varphi_i(\mathbf{r}) = E_i\varphi_i(\mathbf{r}) \qquad (2.8)$$

where $v(\mathbf{r})$ is the nuclear potential. This equation can be solved by the self-consistent field (SCF) method. In the Kohn-Sham equation, the very complex interactions between electrons are included in the exchange and correlation energy, *i.e.*, $E_{\mathrm{XC}}[\rho]$, which is the core of DFT theory. The exchange and correlation energy is also the most difficult term to be determined.

The Kohn-Sham equation provides a practical method to solve the many-body Schrödinger equation. It is theoretically accurate, such that if the exchange and correlation energy can be determined without error, the simulation result will have a high chemical accuracy. Unfortunately, there is not a direct method to determine the exact form of exchange and correlation, and the only way so far is to construct approximations to the exchange-correlation energy (E_{XC}).

2.4.5 Exchange-correlation functionals

Now the problem is to construct appropriate density functional approximations for exchange and correlation. Different methods such as local-density approximation (LDA), generalized gradient approximation (GGA) and hybrid functionals have been developed to construct such approximations. These functionals require different resources and have different calculation performances. The hierarchy of the exchange-correlation functionals can be described by the "Jacob's Ladder" proposed by Perdew and Schmidt [47], as shown in Figure 2.13.

This ladder connects the "Hartree Earth" ground level to "Chemical Heaven" of high chemical accuracy. There are five rungs in the ladder, corresponding to different levels of exchange-correlation functionals. The functionals in higher rungs retain the benefits of the functionals in lower rungs. From lower rungs to higher rungs, the calculation accuracy becomes higher but also more computational resource will be required.

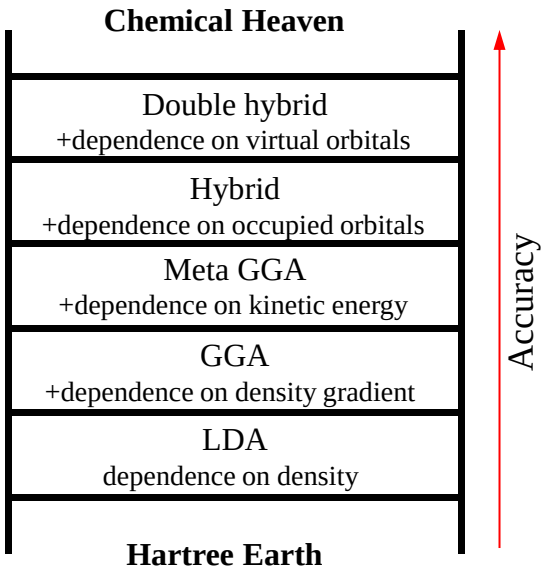

Figure 2.13. 'Jacob's Ladder' of DFT functionals [47].

2.4.5.1 Local density approximation (LDA)

LDA is the simplest form of exchange-correlation functionals, in which the electrons are treated as a homogeneously distributed electron-gas model. The LDA functional assumes that the E_{XC} of any point is only related with its local electron density, which is equal to the value of the E_{XC} of the equivalent electron-gas model with the same density [48].

Using LDA, the exchange-correlation functional can be expressed as

$$E_{XC}^{LDA}[\rho] = \int \rho(r)\varepsilon_{XC}[\rho]\mathrm{d}r \tag{2.9}$$

E_{XC} is divided into exchange $\varepsilon_X(\rho)$ and correlation $\varepsilon_C(\rho)$, where $\varepsilon_X(\rho)$ is given by the Dirac functional [49], and $\varepsilon_C(\rho)$ can be fitted by the Monte Carlo simulation [50].

$$E_{XC} = \varepsilon_X(\rho) + \varepsilon_C(\rho) \tag{2.10}$$

LDA works very well with the homogeneous electron gas such that the calculation results for the system with a homogeneous electron distribution is usually accurate. However, for any system with non-uniform electron distribution, the result will be unreliable. For example, in magnetic or solid surface systems,

because the electron distribution ρ is not uniform, the LDA simulation result is not ideal. To deal with magnetic material by LDA, the electron spins must be taken into consideration such that the modified method is called the local-spin-density approximation (LSDA) [51].

2.4.5.2 Generalised gradient approximation (GGA)

Since LDA is based on the homogeneous electron-gas model, while actual materials often have inhomogeneous electron distributions, the simulated results are very likely to be problematic. To improve the calculation accuracy, the nonuniformity of the electron distribution has to be taken into consideration.

The generalised gradient approximation (GGA) is a method which describes the inhomogeneous electron density by introducing a gradient to the electron density and is often split into exchange and correlation parts [52]

$$E_{\mathrm{XC}}^{\mathrm{GGA}} = E_{\mathrm{X}}^{\mathrm{GGA}} + E_{\mathrm{C}}^{\mathrm{GGA}} \tag{2.11}$$

Compared with LDA, the GGA functional is more suitable for calculating systems with inhomogeneous electron densities, in which E_{XC} plays an important role in the result [53]. GGA functionals have been widely employed for DFT calculations. Some well-known GGA functionals include PW91 (Perdew and Wang in 1991, [54-56]), PBE (Perdew, Burke and Ernzerhof [52]) and BLYP (Becke, Lee, Yang and Parr [57, 58]). It is worth noting that even though the computational cost is increased in GGA, it does not always give better results than LDA. In some cases, the calculation accuracy can be improved further by introducing the second derivative of the electron density, with the modified functional called meta-GGA.

2.4.5.3 Hybrid functionals

A well-known shortcoming of the LDA or GGA functionals is that the calculated band gap is often underestimated compared with the experimental value. It is caused by the self-interaction of the electrons in the DFT exchange functional [59]. In other words, pure DFT methods cannot describe the exchange energy accurately. This error does not exist in the traditional HF method as it is completely cancelled

in the exchange term. However, it is only partially cancelled in pure DFT methods such as LDA or GGA [60].

Hybrid functionals were developed to help DFT describe the exchange energy better. Hybrid functionals incorporate a fraction of exact HF exchange in the calculation of exchange energy, which can be described as the following form,

$$E_{\mathrm{XC}} = (1-a)E_{\mathrm{X}}^{\mathrm{DFT}} + aE_{\mathrm{X}}^{\mathrm{HF}} + E_{\mathrm{C}}^{\mathrm{DFT}} \tag{2.12}$$

where "a" represents the fraction of exact HF exchange. Since the non-local HF exchange is incorporated, this hybrid method requires more computational time and resources compared with a pure DFT method such as GGA or LDA. But compared with a pure DFT method, the hybrid method has a higher accuracy in the calculation of exchange energy, especially for systems which have strong self-interaction between electrons. The calculation results can also be further refined by changing the percentage of HF exchange included in the calculation.

Hybrid functionals can be divided into different types, such as the conventional global hybrid functional and range-separated (screened) functional [61]. Global hybrid functionals such as B3LYP (Becke's 3 parameter functional [62] combined with Lee-Yang-Parr [58]) and PBE0 (hybrid version of PBE [63]) use fixed fractions of HF and DFT exchange [64]. In range-separated functionals, such as the short-range functional HSE06 (revised version of Heyd-Scuseria-Ernzerhof screened hybrid functional [65, 66]), the amount of HF exchange depends on the spatial distance between electrons such that the long-range HF exchange is screened and only the short-range part is included [67]. Therefore, by using the screened hybrid functional, the computational cost can be significantly reduced [34, 66].

2.4.6 Basis set

A basis set is a set of functions used to construct the wave function for atomic or molecular orbitals [68]. Depending on the different types of functions (Slater-type or Gaussian-type functions) employed, the orbitals can be Slater-type orbitals (STOs) or Gaussian-type orbitals (GTOs). STOs are closer to the actual shape of

atomic orbitals, therefore theoretically more accurate, but they also require more computational resources. To save computing time, a linear combination of GTOs is often employed to mimic the behaviour of STOs [69].

According to the different numbers of basis functions adopted, basis sets can be classified into minimal (one basis function for each orbital), double-zeta (two basis functions for each orbital), triple-zeta (three basis functions for each orbital) and so on. The term "zeta" comes from the Greek letter ζ which is used to represent the exponent of the STO function, and the number comes before zeta represents the number of functions per atomic orbital [70].

Minimal basis set

The minimal basis set contains only one basis function for each orbital. It describes only the most basic aspects of the orbitals. The most common minimal basis set is the 'STO-nG' (Slater-type orbital, number of Gaussian primitives) type basis set. Each Slater-type orbital is a linear combination of n contracted GTOs (also known as Gaussian primitives). It is called primitive because each GTO makes up part of the orbital. In STO-3G, for example, each orbital is presented by a linear combination of 3 Gaussian primitives. The minimal basis set is computationally cheap, but the accuracy is very limited.

Compared with the minimal basis set, the double-zeta or triple-zeta basis set contain more basis functions for each orbital. Therefore, the correspondent calculation results are more accurate. However, they also demand more computing time. When the number of basis functions are too many, the calculation will become unaffordable.

Split-valence basis set

Since core electrons usually do not participate in bonding, the calculated results are more influenced by the accuracy of the valence rather than the core orbitals. The split-valence strategy uses only one basis function for each core orbital, but uses more functions for the valence orbitals. Basis sets of this type are called split-valence basis sets because the description of valence orbitals are split into two (or more) functions. In this way, the computing resource is saved while reasonable results can be obtained.

For example, in the 6-21G basis set, the first number "6" means each core orbital is composed of a linear combination of 6 Gaussian primitives. The two numbers after the hyphen indicate that this basis set is a double-zeta basis set such that each valence orbital is composed of 2 basis functions, in which the first one is composed of a linear combination of 2 Gaussian primitives and the other composed of 1 Gaussian primitive.

Polarisation and diffusion functions

Orbital polarisation happens when two atoms approach each other. However, a basis set with minimal basis functions cannot describe such a polarisation property, *i.e.*, it cannot describe the molecular or chemical bonds. Therefore, adding a polarisation basis function becomes necessary to help describe any polarisation properties. The rule is whatever the highest angular momentum is, a higher one will be added. Polarization functions can be denoted by an asterisk, for example the basis set 6-21G* [71]. It can also be denoted in other forms such as pob-TZVP [72] (Triple Zeta Valence Polarisation, developed by Peintinger, M. F.; Oliveira, D. V. and Bredow, T., J.). Diffuse functions are at the end of the basis set. Diffuse functions have very small exponents, such that the electrons are far away from the nucleus, but are very necessary for analysing binding energies.

2.4.7 CRYSTAL package

The CRYSTAL package (latest version 17) was developed by Dovesi et al., [73] for *ab initio* calculations. CRYSTAL package consists of two programs: *crystal*, which is for geometry optimisation calculation, and *properties*, which is for calculating electron properties. HF or DFT methods can be used in this package. It is able to calculate different geometry systems such as molecules, polymers, slabs and crystals [74]. The input script for CRYSTAL is composed of three blocks: geometry, basis set and SCF parameters. Each block is controlled by different keywords.

In this thesis, all the theoretical calculations were performed in CRYSTAL 17 installed on BlueCrystal Phase 4, the high-performance computing facility of Advanced Computing Research Centre, University of Bristol (https://www.bristol.ac.uk/acrc/).

2.5 References

[1] P.W. May, Diamond thin films: a 21st-century material, Philos. Trans. R. Soc. A 358 (2000) 473-495.

[2] O.J.L. Fox, J.O.P. Holloway, G.M. Fuge, et al., Electrospray Deposition of Diamond Nanoparticle Nucleation Layers for Subsequent CVD Diamond Growth, Mater. Res. Soc. Symp. Proc. 1203 (2009) 1203-J17-27.

[3] E.M. Yuill, N. Sa, S.J. Ray, et al., Electrospray Ionization from Nanopipette Emitters with Tip Diameters of Less than 100 nm, Anal. Chem. 85 (2013) 8498-8502.

[4] J.E. Butler, R.L. Woodin, L.M. Brown, et al., Thin film diamond growth mechanisms, Philos. Trans. R. Soc. A 342 (1993) 209-224.

[5] P.W. May, J.N. Harvey, N.L. Allan, et al., Simulations of chemical vapor deposition diamond film growth using a kinetic Monte Carlo model, J. Appl. Phys. 108 (2010) 014905.

[6] S.J. Harris, Mechanism for diamond growth from methyl radicals, Appl. Phys. Lett. 56 (1990) 2298-2300.

[7] L.G. Benning, G.A. Waychunas, Nucleation, Growth, and Aggregation of Mineral Phases: Mechanisms and Kinetic Controls, in: S.L. Brantley, J.D. Kubicki, A.F. White (Eds.), Kinetics of Water-Rock Interaction, Springer New York, New York, NY, 2008, pp. 259-333.

[8] E. Bauer, Phänomenologische Theorie der Kristallabscheidung an Oberflächen. I, Z. Kristallogr. Cryst. Mater. 110 (1958) 372-394.

[9] Q. Wei, T. Yang, K.C. Zhou, et al., Effect of sputtered Mo interlayers on Si (100) substrates for the deposition of diamond film by hot filament chemical vapor deposition, Surf. Coat. Technol. 232 (2013) 456-463.

[10] X. Jiang, C.-P. Klages, Recent Developments in Heteroepitaxial Nucleation and Growth of Diamond on Silicon, Phys. Status Solidi A 154 (1996) 175-183.

[11] M.N.R. Ashfold, P.W. May, C.A. Rego, N.M. Everitt, Thin film diamond by chemical vapour deposition methods, Chem. Soc. Rev. 23 (1994) 21-30.

[12] S. Kumar, S.M. Eaton, M. Bollani, et al., Laser surface structuring of diamond with ultrashort Bessel beams, Sci. Rep. 8 (2018) 14021.

[13] D.M. Trucchi, A. Bellucci, M. Girolami, et al., Surface Texturing of CVD Diamond Assisted by Ultrashort Laser Pulses, Coatings 7 (2017) 18.

[14] S. Su, J.L. Li, G.C.B. Lee, et al., Femtosecond laser-induced microstructures on diamond for microfluidic sensing device applications, Appl. Phys. Lett. 102 (2013) 5.

[15] H. Ohfuji, T. Okuchi, S. Odake, et al., Micro-/nanostructural investigation of laser-cut surfaces of single- and polycrystalline diamonds, Diam. Relat. Mater. 19 (2010) 1040-1051.

[16] M. Shinoda, R.R. Gattass, E. Mazur, Femtosecond laser-induced formation of nanometer-width grooves on synthetic single-crystal diamond surfaces, J. Appl. Phys. 105 (2009) 4.

[17] R. Zaouk, B.Y. Park, M.J. Madou, Introduction to microfabrication techniques, Microfluidic Techniques, Springer 2006, pp. 5-15.

[18] A. del Campo, E. Arzt, Fabrication approaches for generating complex micro- and nanopatterns on polymeric surfaces, Chem. Rev. 108 (2008) 911-945.

[19] M.J. Madou, Manufacturing techniques for microfabrication and nanotechnology, CRC press 2011.

[20] H. Yang, A. Jin, Q. Luo, et al., Electron beam lithography of HSQ/PMMA bilayer resists for negative tone lift-off process, Microelectron. Eng. 85 (2008) 814-817.

[21] Y.F. Chen, K.W. Peng, Z. Cui, A lift-off process for high resolution patterns using PMMA/LOR resist stack, Microelectron. Eng. 73-74 (2004) 278-281.

[22] P. Carlberg, M. Graczyk, E.L. Sarwe, et al., Lift-off process for nanoimprint lithography, Microelectron. Eng. 67-68 (2003) 203-207.

[23] C. Maragliano, A. Glia, M. Stefancich, M. Chiesa, Effective AFM cantilever tip size: methods for in-situ determination, Meas. Sci. Technol. 26 (2014) 015002.

[24] B. Bhushan, Encyclopedia of nanotechnology, Springer, Dordrecht 2012.

[25] O. Kazakova, R. Puttock, C. Barton, et al., Frontiers of magnetic force microscopy, J. Appl. Phys. 125 (2019) 060901.

[26] L. Abelmann, A. Van den Bos, C. Lodder, Magnetic force microscopy—Towards higher resolution, Magnetic Microscopy of Nanostructures, Springer 2005, pp. 253-283.

[27] J. Filik, Raman spectroscopy: a simple, non-destructive way to characterise diamond and diamond-like materials, Spectrosc. Eur. 17 (2005) 10.

[28] S.R. Sails, D.J. Gardiner, M. Bowden, et al., Monitoring the quality of diamond films using Raman spectra excited at 514.5 nm and 633 nm, Diam. Relat. Mater. 5 (1996) 589-591.

[29] F. Giustino, Materials modelling using density functional theory: properties and predictions, Oxford University Press 2014.

[30] M. Born, R. Oppenheimer, Zur Quantentheorie der Molekeln, Ann. Phys. 389 (1927) 457-484.

[31] L.S. Cederbaum, Born–Oppenheimer approximation and beyond for time-dependent electronic processes, J. Chem. Phys. 128 (2008) 124101.

[32] D.R. Hartree, The Wave Mechanics of an Atom with a Non-Coulomb Central Field. Part II. Some Results and Discussion, Math. Proc. Cambridge Philos. Soc. 24 (1928) 111-132.

[33] D.R. Hartree, W. Hartree, Self-consistent field, with exchange, for beryllium, Proc. R. Soc. Lond. A 150 (1935) 9-33.

[34] A.J. Garza, G.E. Scuseria, Predicting Band Gaps with Hybrid Density Functionals, J. Phys. Chem. Lett. 7 (2016) 4165-4170.

[35] J.P. Goss, R.J. Eyre, P.R. Briddon, Theoretical models for doping diamond for semiconductor applications, Phys. Status Solidi B 245 (2008) 1679-1700.

[36] R.A.P. Ribeiro, J. Andrés, E. Longo, S.R. Lazaro, Magnetism and multiferroic properties at MnTiO3 surfaces: A DFT study, Appl. Surf. Sci. 452 (2018) 463-472.

[37] H.X. Gao, J.B. Li, J.B. Xia, Origins of ferromagnetism in transition metal doped diamond, Physica B Condens. Matter 407 (2012) 2347-2350.

[38] N. Durante, A. Fortunelli, M. Broyer, M. Stener, Optical Properties of Au Nanoclusters from TD-DFT Calculations, J. Phys. Chem. C 115 (2011) 6277-6282.

[39] P.D. Borges, L.M.R. Scolfaro, H.W. Leite Alves, E.F. da Silva, DFT study of the electronic, vibrational, and optical properties of SnO2, Theor. Chem. Acc. 126 (2010) 39-44.

[40] F. Colmenero, A.M. Fernández, J. Cobos, V. Timón, Periodic DFT Study of the Thermodynamic Properties and Stability of Schoepite and Metaschoepite Mineral Phases, ACS Earth Space Chem. 3 (2019) 17-28.

[41] F. Mollaamin, Z. Varmaghani, M. Monajjemi, Dielectric effect on thermodynamic properties in vinblastine by DFT/Onsager modelling, Phys. Chem. Liq. 49 (2011) 318-336.

[42] A.J. Logsdail, C.A. Downing, T.W. Keal, et al., Hybrid-DFT Modeling of Lattice and Surface Vacancies in MnO, J. Phys. Chem. C 123 (2019) 8133-8144.

[43] D.O. Scanlon, C.W. Dunnill, J. Buckeridge, et al., Band alignment of rutile and anatase TiO_2, Nat. Mater. 12 (2013) 798-801.

[44] R. Su, R. Tiruvalam, A.J. Logsdail, et al., Designer Titania-Supported Au–Pd Nanoparticles for Efficient Photocatalytic Hydrogen Production, ACS Nano 8 (2014) 3490-3497.

[45] P. Hohenberg, W. Kohn, Inhomogeneous Electron Gas, Phys. Rev. 136 (1964) B864-B871.

[46] W. Kohn, L.J. Sham, Self-Consistent Equations Including Exchange and Correlation Effects, Phys. Rev. 140 (1965) A1133-A1138.

[47] J.P. Perdew, K. Schmidt, Jacob's ladder of density functional approximations for the exchange-correlation energy, AIP Conf. Proc. 577 (2001) 1-20.

[48] C. Kittel, Introduction to solid state physics, 1976.

[49] P.A.M. Dirac, Note on Exchange Phenomena in the Thomas Atom, Math. Proc. Cambridge Philos. Soc. 26 (1930) 376-385.

[50] D.M. Ceperley, B.J. Alder, Ground State of the Electron Gas by a Stochastic Method, Phys. Rev. Lett. 45 (1980) 566-569.

[51] F. Lechermann, F. Welsch, C. Elsässer, et al., Density-functional study of Fe_3Al: LSDA versus GGA, Phys. Rev. B 65 (2002) 132104.

[52] J.P. Perdew, K. Burke, M. Ernzerhof, Generalized Gradient Approximation Made Simple, Phys. Rev. Lett. 77 (1996) 3865-3868.

[53] J.P. Perdew, K. Burke, Comparison shopping for a gradient-corrected density functional, Int. J. Quantum Chem. 57 (1996) 309-319.

[54] J.P. Perdew, J.A. Chevary, S.H. Vosko, et al., Atoms, molecules, solids, and surfaces: Applications of the generalized gradient approximation for exchange and correlation, Phys. Rev. B 46 (1992) 6671-6687.

[55] J.P. Perdew, K. Burke, Y. Wang, Generalized gradient approximation for the exchange-correlation hole of a many-electron system, Phys. Rev. B 54 (1996) 16533-16539.

[56] J.P. Perdew, P. Ziesche, H. Eschrig, Electronic structure of solids' 91, Akademie Verlag, Berlin, 1991.

[57] A.D. Becke, Density-functional exchange-energy approximation with correct asymptotic behavior, Phys. Rev. A 38 (1988) 3098-3100.

[58] C. Lee, W. Yang, R.G. Parr, Development of the Colle-Salvetti correlation-energy formula into a functional of the electron density, Phys. Rev. B 37 (1988) 785-789.

[59] T. Tsuneda, K. Hirao, Self-interaction corrections in density functional theory, J. Chem. Phys. 140 (2014) 18A513.

[60] P.J. Hasnip, K. Refson, M.I.J. Probert, et al., Density functional theory in the solid state, Philos. Trans. R. Soc. A 372 (2014) 20130270.

[61] A.V. Krukau, G.E. Scuseria, J.P. Perdew, A. Savin, Hybrid functionals with local range separation, J. Chem. Phys. 129 (2008) 124103.

[62] A.D. Becke, Density-functional thermochemistry. I. The effect of the exchange-only gradient correction, J. Chem. Phys. 96 (1992) 2155-2160.

[63] C. Adamo, V. Barone, Toward reliable density functional methods without adjustable parameters: The PBE0 model, J. Chem. Phys. 110 (1999) 6158-6170.

[64] G.I. Csonka, J.P. Perdew, A. Ruzsinszky, Global Hybrid Functionals: A Look at the Engine under the Hood, J. Chem. Theory Comput. 6 (2010) 3688-3703.

[65] A.V. Krukau, O.A. Vydrov, A.F. Izmaylov, G.E. Scuseria, Influence of the exchange screening parameter on the performance of screened hybrid functionals, J. Chem. Phys. 125 (2006) 5.

[66] J. Heyd, G.E. Scuseria, M. Ernzerhof, Hybrid functionals based on a screened Coulomb potential, J. Chem. Phys. 118 (2003) 8207-8215.

[67] I.C. Gerber, J.G. Ángyán, Hybrid functional with separated range, Chem. Phys. Lett. 415 (2005) 100-105.

[68] C.J. Cramer, Essentials of computational chemistry: theories and models, John Wiley & Sons 2013.

[69] W.J. Hehre, R.F. Stewart, J.A. Pople, Self-Consistent Molecular-Orbital Methods. I. Use of Gaussian Expansions of Slater-Type Atomic Orbitals, J. Chem. Phys. 51 (1969) 2657-2664.

[70] E.R. Davidson, D. Feller, Basis set selection for molecular calculations, Chem. Rev. 86 (1986) 681-696.

[71] M. Catti, A. Pavese, R. Dovesi, V.R. Saunders, Static lattice and electron properties of MgCO3 (magnesite) calculated by ab initio periodic Hartree-Fock methods, Phys. Rev. B 47 (1993) 9189-9198.

[72] M.F. Peintinger, D.V. Oliveira, T. Bredow, Consistent gaussian basis sets of Triple-Zeta valence with polarization quality for solid-State Calculations, J. Comput. Chem. 34 (2013) 451-459.

[73] R. Dovesi, A. Erba, R. Orlando, et al., Quantum-mechanical condensed matter simulations with CRYSTAL, Wiley Interdiscip. Rev. Comput. Mol. Sci. 8 (2018) 36.

[74] R. Dovesi, V. Saunders, C. Roetti, et al., CRYSTAL17 User's Manual, 2017.

CHAPTER 3

DIAMOND FILM GROWN ON COBALT

In this chapter, we report the results of studies of diamond film grown on Co. Two forms of Co, carbon-coated Co nanoparticles and stripe-patterned Co film, were employed to imbue diamond film with ferromagnetic properties. Owing to the robustness of diamond, the magnetic diamond composites may have applications in harsh or chemically-corrosive environments. Co was also investigated and compared with Si as a substrate material for growing diamond.

3.1 Introduction

Diamond is a special material with many extraordinary mechanical, optical, electrical and biochemical properties, giving rise to a large number of diverse applications in these fields [1]. The emergence of diamond synthesis techniques, especially the CVD method, makes it possible to apply diamond into many fields, for example, electronic devices [2], bio-sensors [3] and waste-water treatment [4, 5]. Although diamond can be doped to change its electrical conductivity, it remains a non-magnetic material.

In contrast, magnetic films or particles made from elements such as Fe, Ni, Co or their alloys may have applications in magnetic data storage [6, 7], magnetic detection [8] and logic devices [9]. The stability of magnetic materials can be influenced by the environment, such as temperature, external forces and magnetic or electric field. However, in some cases, electronic/magnetic devices have to work in extreme environments of such as high temperature, vibration, chemical corrosion or radiation [10]. Therefore, to make sure the electronic devices operate reliably, the magnetic material must be protected from any potential wear, tear, overheat, mechanical or electrical damage. To do so, magnetic materials are

usually protected by a robust, non-magnetic material in the form of a coating or casing. For example, diamond-like carbon (DLC) film has been used as a coating for hard-disk drives to protect the magnetic layers from wear or corrosion [11, 12].

The superior robustness of diamond makes it a promising candidate for protecting more delicate materials. Because diamond also has an extremely high thermal conductivity, the heat generated during the working of the device can be dissipated quickly through any protective diamond coating. If electronic or magnetic devices are coated by diamond film, they can be protected from mechanical wear, chemical corrosion, overheating and even radiation [13].

Patterning of magnetic material is an essential step for making magnetic logic devices or hard disk drives. The magnetic properties of patterned films or particles are also different from that of a bulk material [14]. Patterned magnetic films used for data-storage media are often in the form of patterned tracks [15] or isolated features 'bits' [16], the latter scheme usually being adopted for high-density data storage.

In this chapter we report growth of diamond on the magnetic material, Co, which has been patterned in various ways. The aim was to demonstrate that it is possible to fabricate a magnetic diamond-Co composite, and to characterise its performance.

3.2 Experimental

The rationale for the initial experiments was to deposit a thin film of magnetic material, either as nanoparticles or as an evaporated metal onto a Si substrate, and then pattern this into stripes or dots. The second stage would be to seed the entire surface with nanodiamond, and then deposit a diamond film using standard CVD process conditions. In this way, some areas of the diamond film would lie directly on top of the Si, while other areas would lie on top of the magnetic layer. MFM could then be used to detect the position of the magnetic regions underneath the protective diamond coating.

3.2.1 Diamond on Co nano particles

Here, the magnetic material consisted of Co nanoparticles in powder form purchased from Sigma-Aldrich (product number 697745). They had an average diameter of < 50 nm and came pre-coated with a thin graphite layer (10–20 nm) that protects the Co from being oxidized in ambient air. This C coating may also work as an interlayer to improve the interaction between the diamond and Co. 3.0 mg of this Co nanopowder was mixed in 30 mL methanol and sonicated in a water bath for 30 min to ensure uniform dispersion in the liquid immediately before use.

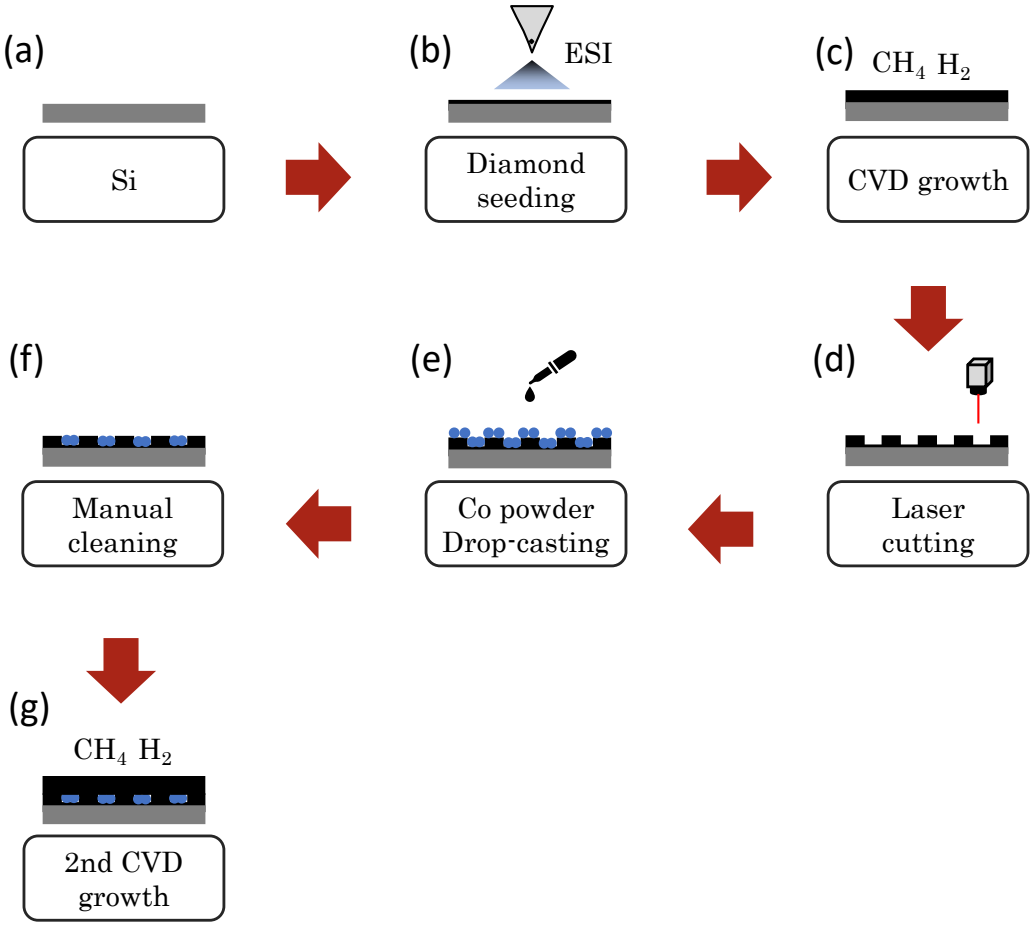

Figure 3.1. Fabrication process of growing diamond on Co nano particles.

The fabrication process is shown in Figure 3.1. The substrate for CVD diamond film growth was n-type Si (10 mm × 10 mm, see section 2.1.1). The Si sample was then seeded with nanodiamond by ESI method (section 2.1.2), and then placed into a HFCVD reactor, and then a diamond layer was deposited using standard

conditions (1% CH_4 in H_2, 20 Torr) for 3 h (see section 2.1.3). The diamond layer was microcrystalline with faceted grain sizes around 0.5 μm on the surface and a thickness of around 1-1.5 μm (see Figure 3.20).

The Oxford Laser Micromachining System (see section 2.2.1) was employed to cut trenches into diamond film surface at the speed of 0.5 mm/s and power of 0.088 W, which were able to cut through the 1.6 μm thick diamond film. The trenches were then used as templates for containing the Co powder on the diamond film surface. 2 mL of the Co suspension was dropped onto the diamond surface using a pipette and allowed to spread out to cover the entire surface. The liquid was then removed and the diamond surface cleaned using a lens-cleaning tissue. The expectation was that the tissue would mechanically remove any Co nanoparticles sitting on top of the diamond, but the Co particles inside the trenches would remain. Ideally, we would be left with an almost flat surface with the trenches filled with nanoparticles up to the level of the diamond, as illustrated in Figure 3.1e. The samples were then put back to the HFCVD reactor for a second 3-h diamond growth. The existing exposed diamond grew upwards, but also and laterally across the top of the trenches, burying the Co nanoparticles beneath a coating of diamond. The results for this are given later in section 3.3.

3.2.2 Diamond film on stripe-patterned Co film

The experimental process of growing diamond film on stripe-patterned Co film is shown schematically in Figure 3.2. This work involved the preparation of stripe-patterned Co film followed by the growth of diamond onto this Co film.

A standard lift-off microfabrication method was employed to prepare stripe-patterned Co film on Si. The same Si substrates (10 mm × 10 mm) were cleaned sequentially using Decon 90 cleaning solution, deionized (DI) water, acetone, methanol and isopropyl alcohol for 5 min in each liquid, and baked at 100 °C in air for 2 min to remove any residual adsorbates on the surface. The Si substrates were then spin-coated with photoresist.

For a lift-off process, the sidewall profile of the resist is crucial. If the resist has a standard vertical or sloped profile, the evaporated metal layer can conformally

coat the resist in a single continuous film. This can cause problems when the resist is removed, as the entire continuous metal layer can be lifted off as well. A method to prevent this is to use a resist with an undercut (overhanging) profile, such that the evaporated metal layer forms on the two horizontal surfaces (the Si and the top of the resist) but not on the sidewall, such that the metal film is not continuous. Now removal of the resist lifts off the metal layer on top of the resist only, and leaves the unattached metal layer on the Si behind. Fabricating an undercut profile using a single layer of resist is quite tricky, so instead 2 resist layers are used with different developing rates, such that the lower resist develops slightly faster than the upper one. In this way, with the correct developing time, the lower resist undercuts the upper resist producing the required overhanging profile. More details have been explained in section 2.2.3.

To investigate the difference between single-layer and bi-layer resists for the microfabrication of Co film, the two strategies were employed separately. For the single-layer resist scheme, S1805 resist (MicroChem), was spin-coated and baked at 115 °C for 1 min. For the bi-layer scheme, LOR 3B resist (MicroChem) was spin-coated onto the Si substrate and baked at 190 °C for 3 min, followed by spin-coating of S1805 resist on top of this, which was baked at 115 °C for 1 min. UV exposure was carried out in a Karl Suss MJB3 Contact Mask Aligner. A 5 mm × 5 mm stripe-patterned mask with width and space of ~ 0.6 μm was placed between the UV beam and the Si substrate, and the substrates were exposed for 50 s to transfer the pattern onto the substrate. The exposed substrates were then developed in developer solution (Microposit MF-319) for 15-20 s and rinsed in DI water.

The Si substrate with patterned resist was then placed into a thermal evaporator (section 2.2.2) for evaporation of Co, with thickness of ~ 36 nm. Finally, the sample was placed into acetone and MF-319 to enable 'lift-off' of the Co-covered resist. The resulting Si substrate with a patterned Co film was then seeded with diamond using ESI (section 2.1.2). Diamond film was deposited in the HFCVD reactor using 1% CH_4 in H_2 for 3 h, and characterised by SEM, Raman, and MFM. The results are given in sections 3.3.1 and 3.3.2.

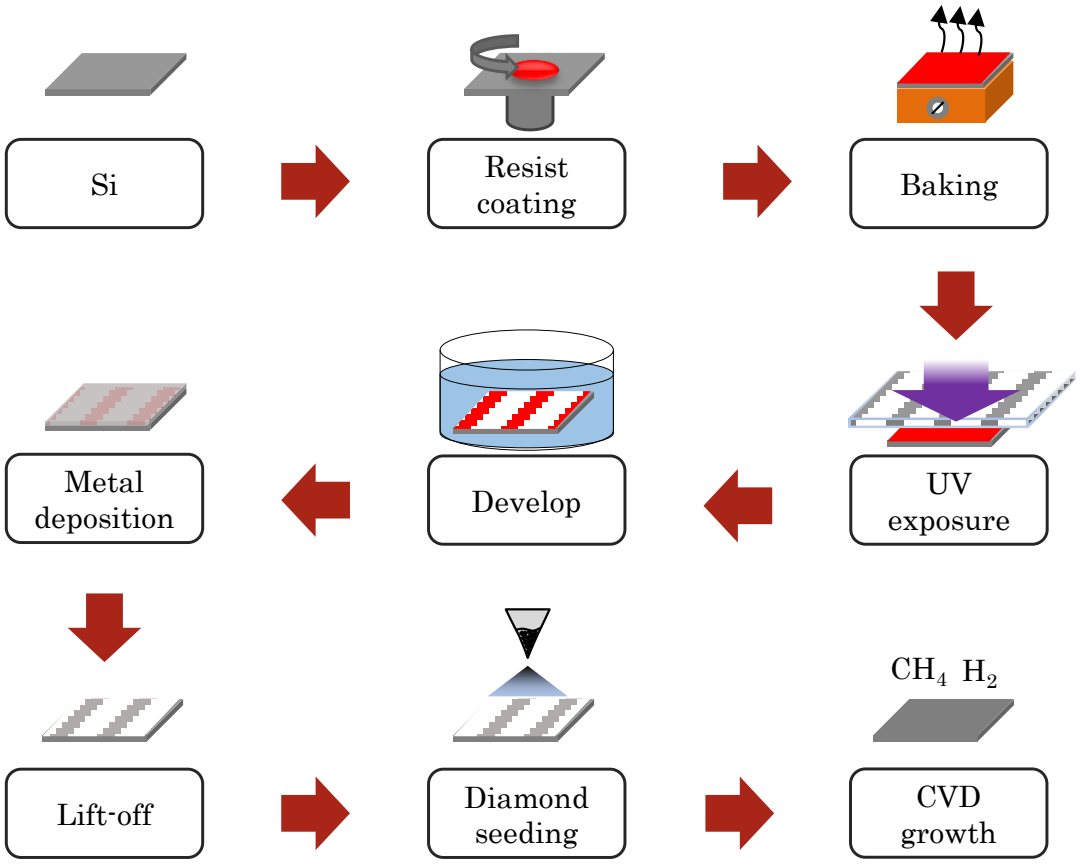

Figure 3.2. Experimental process of growing diamond film on stripe-patterned Co film.

3.2.3 The comparison of diamond films on Si and Co

To study different growth process of diamond on Si and Co, the two materials were employed as substrates for growing diamond. The same n-type Si substrates were selected to study the growth of diamond on Si. To investigate diamond growth on Co, Co film with thickness of ~ 18 nm was thermally evaporated onto the n-type Si. All the substrates were seeded by the ESI method, and put into HFCVD reactor using 1% CH_4 in H_2 for different growth times (1, 2 and 3 h). SEM images were then taken of the surfaces and cross section of the diamond films to view the growth morphology.

3.2.4 Nanodiamond growth and use of interlayers

In addition to using the standard 1% concentration of methane during diamond CVD, high-concentration methane (2% and 4%) was employed, allowing

nanocrystalline diamond to be deposited. To improve the interfacial connection between diamond and Co, an interlayer material such as Ti and Al, with thickness of ~15 nm were deposited by thermal evaporation.

3.3 Results and discussion

3.3.1 Diamond film on Co nano particles

An SEM image of the polycrystalline diamond film on Si deposited following 3 h growth is in Figure 3.3a. The microcrystalline diamond is dominated by the {111} facets on the surface, with crystal size of ~1 µm. The assignment of diamond was confirmed by the sp^3 carbon peak in the Raman spectrum at ~ 1332 cm^{-1} shown in Figure 3.3b.

Co nano particles were characterised by TEM before being deposited on diamond. As shown in Figure 3.4a, most Co particles have a diameter ~10 nm while the thin graphite layer can be observed in Figure 3.4b.

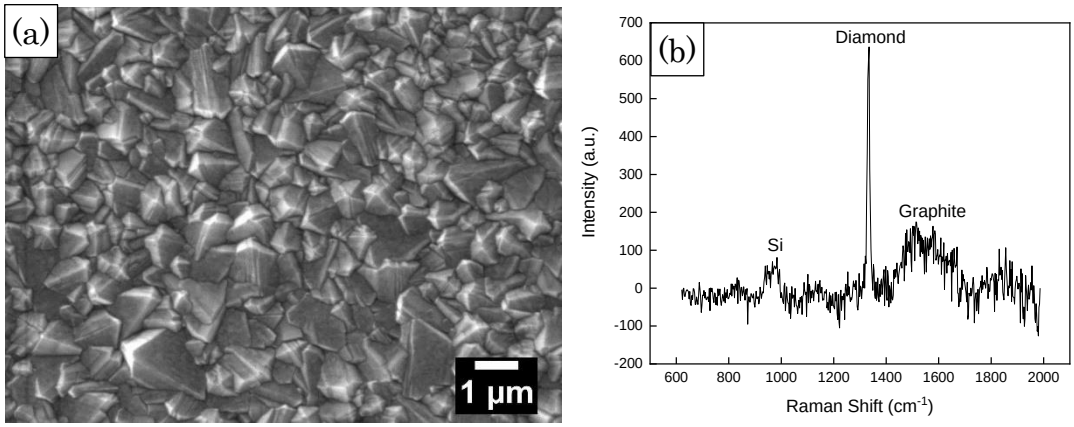

Figure 3.3. (a) Surface morphology and (b) Raman spectrum (laser 512 nm) of the diamond film on Si after 3 h growth.

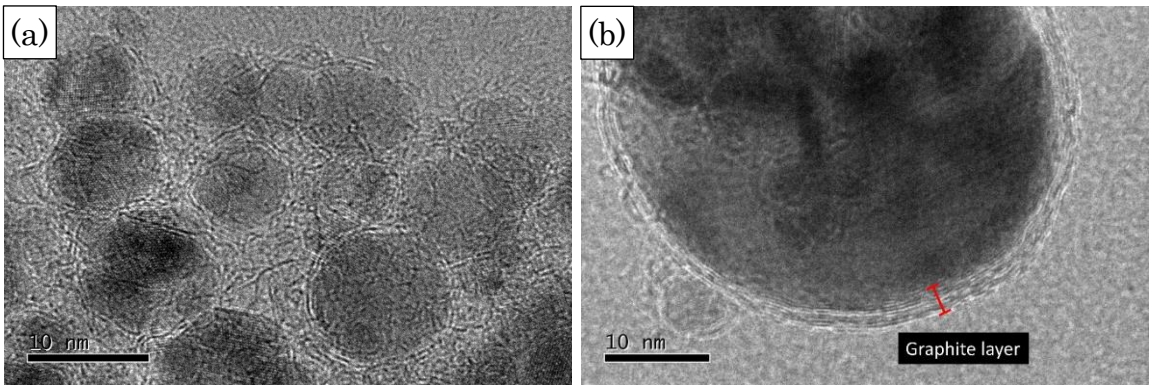

Figure 3.4. TEM images of carbon-coated cobalt nanoparticles. (a) Some of the Co nanoparticles showing a representative range of sizes. (b) High magnification image of one Co nanoparticle showing the thin graphitic coating surrounding the nanoparticle.

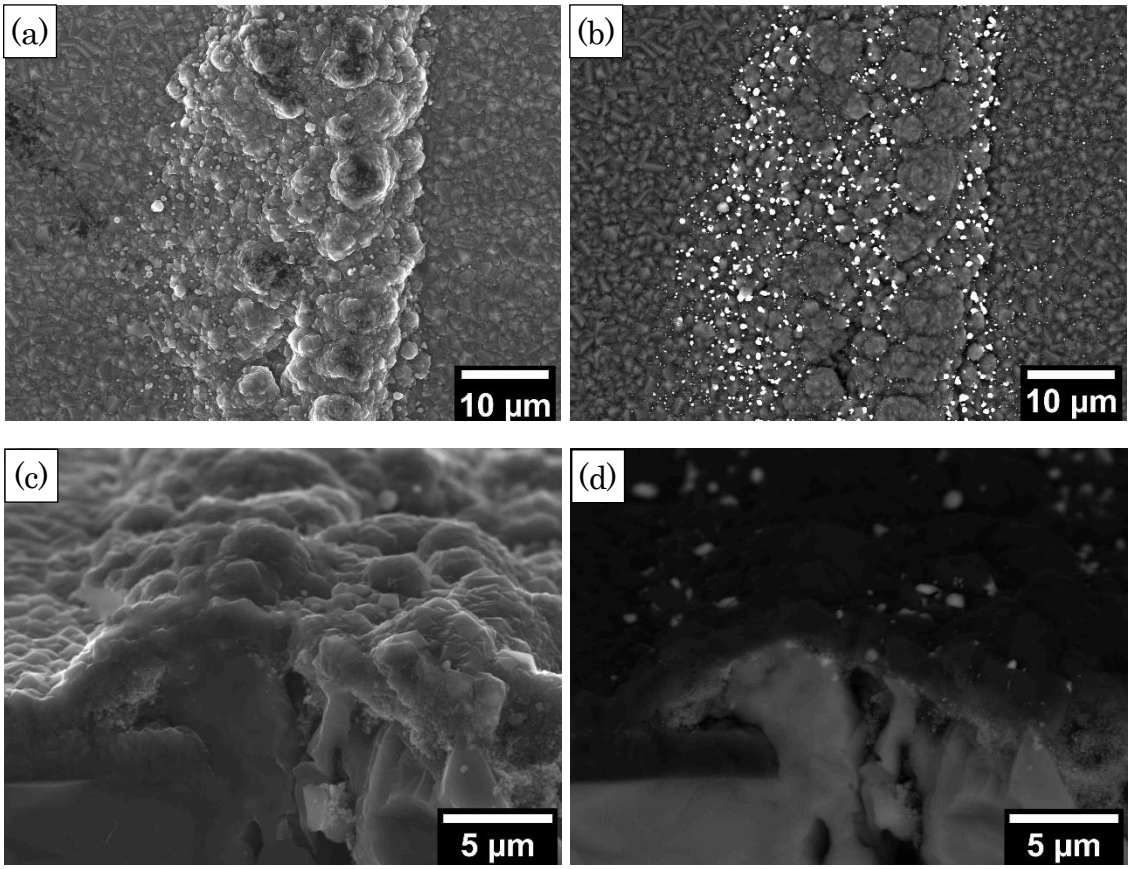

Figure 3.5. Surface morphologies and cross section of the diamond film overcoating a Co stripe in the centre of the image. (a) and (b) are the SE and BSE images of the surface, and (c) and (d) the SE and BSE images of the cross section.

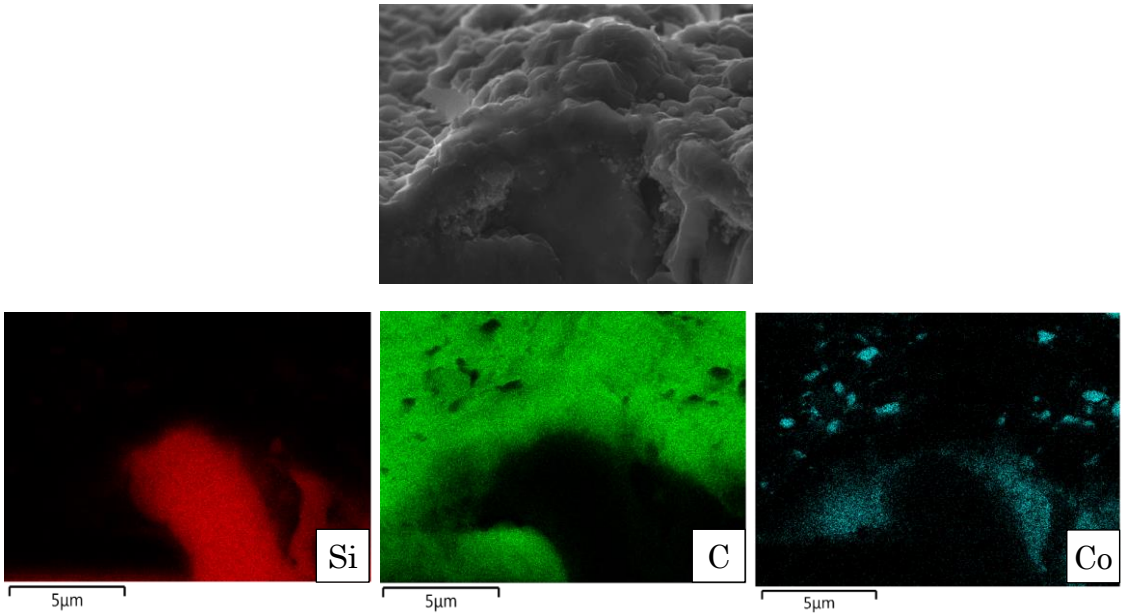

Figure 3.6. EDX Elemental distributions for Si, C and Co of a selected area through the cross-sectional plane shown in the top image.

Figure 3.5 shows the surface and cross-sectional morphology of the diamond film grown both on the Si beside the trench, and on the Co nanoparticles within the trench area. Away from the trench, the diamond film grown on Si looks similar to the control sample in Figure 3.3a. But covering the laser-cut trench the diamond surface grown on top of the Co nanoparticles filling the trench becomes rougher with larger lumps observed. There are also many small particles located on the surface of the diamond here. These particles appear brighter in the BSE image in Figure 3.5b, indicating that they belong to an element with a greater atomic number than carbon. Therefore, they are most likely aggregated Co particles that have made their way to the surface of the diamond. As seen in Figure 3.5c and Figure 3.5d, diamond grown on the trench area is about 2 µm above the height of the diamond grown on Si. There are some brighter particles embedded in the diamond film in the BSE image in Figure 3.5d, which are also likely to be the same Co nanoparticles.

To confirm the element distribution, EDX analysis was carried out. The element distributions of Si, C and Co are shown in Figure 3.6. The EDX result agrees well with the BSE images that most Co is located between diamond film and Si substrate, while some Co particles also appear on the surface. It is worth noting

that the Co distribution is not uniform across the sectional plane, which was due to the uncertainty of the drop casting process of Co.

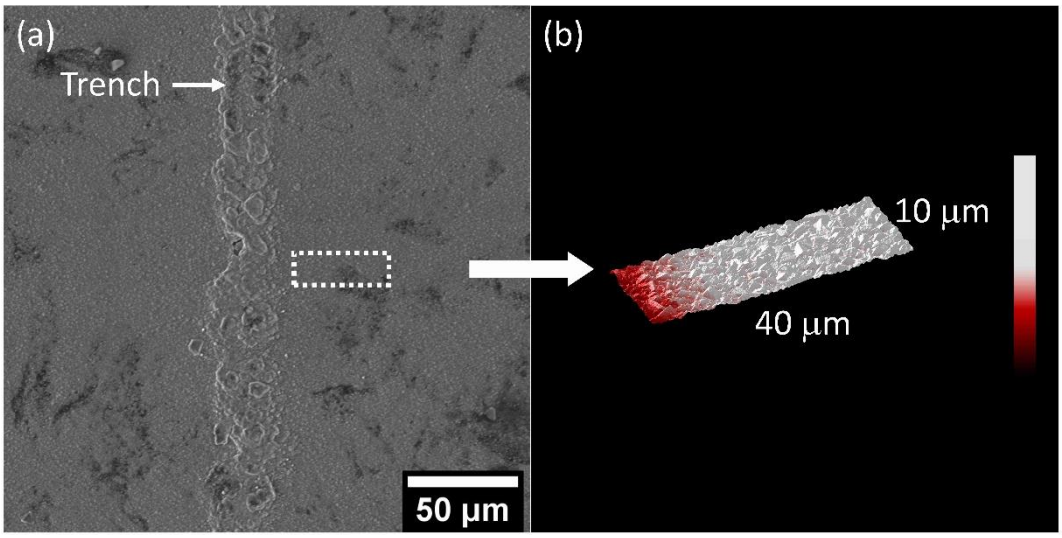

Figure 3.7. (a) SEM Surface morphology of diamond film grown over the laser-cut trench area filled with Co nano particles and (b) magnetic signal of the 40 µm × 10 µm area near the trench area, where the red colour represents the magnetic signal detected from the samples.

MFM was employed to detect the magnetic signal from the Co in the trench underneath the diamond film. Due to the high roughness of the surface in the trench area, this sample was not suitable for a full scan across the trench due to possible damage to the AFM tip. Therefore the 40 µm × 10 µm surface area scan was stopped just before the edge of the trench, as indicated by the rectangle in Figure 3.7a. This area is off the trench area, therefore is almost free from Co on the surface. The result is displayed in Figure 3.7b, where the red colour represents the magnetic signal. Because most of the Co nano particles were buried in the trench, a strong magnetic signal was detected when the probe was close to the trench, and not on the Si area. The result showed that it was possible to detect the magnetic Co particles beneath 1 µm of polycrystalline diamond film.

To find out the influence of laser-cutting speed on the surface quality of the cut diamond, diamond films were cut at three different speeds (0.1, 0.25 and 0.5 mm/s) by the laser cutting system. Images of the diamond films after laser cutting are shown in Figure 3.8. In the presence of air, diamond can easily react with oxygen to form the gaseous CO_2 at ~ 800 °C. Therefore, diamond at the high temperature

laser focused spot was easily etched away. Unfortunately, it appears that the power of the laser was too high, and so as well as removing the diamond, the underlying Si was also melted by the laser. However, since Si cannot form any gaseous phase during laser cutting, the melted Si stayed on the surface and the resolidified to form many lumpy features within the trench. These Si features prohibited the formation of a flat diamond film in the subsequent second diamond growth process. With increasing cutting speed, the trench became shallower and thinner, whilst the Si lumps were less pronounced. Ideally, the laser power and focus should be adjusted to only cut the diamond film while leaving the Si substrate intact. However, in practice, it proved difficult to adjust these parameters accurately while maintaining the laser focusing point and scanning across the surface, as the sample was never exactly horizontal such that the laser focus (and hence energy density) varied with position.

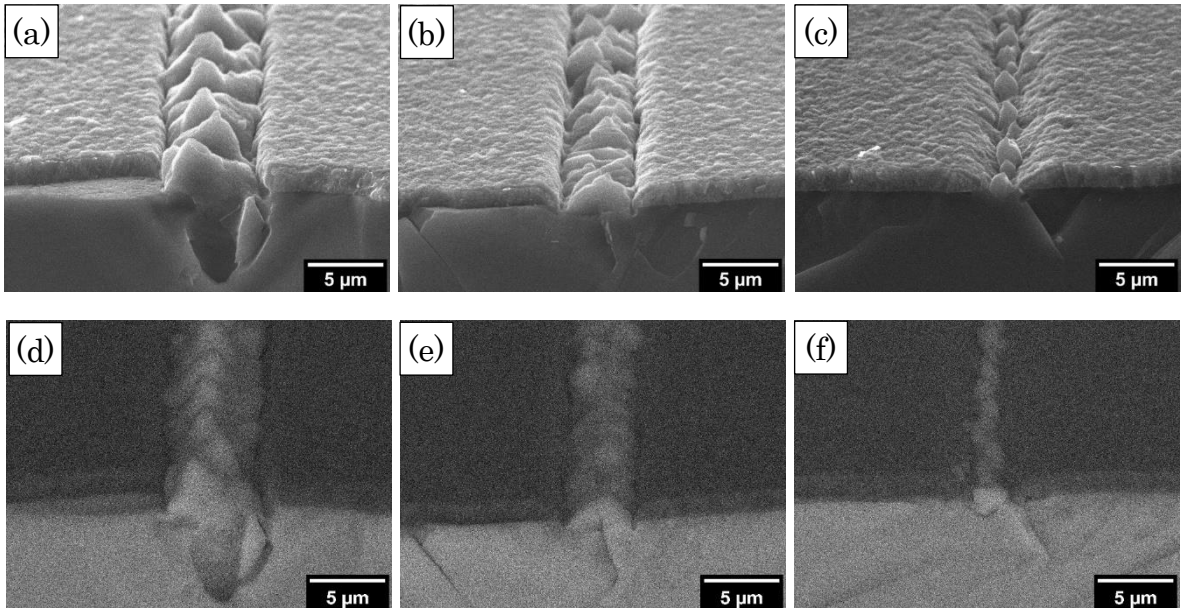

Figure 3.8. Cross-section images of the diamond films cut by laser at (a) and (d) 0.1 mm/s, (b) and (e) 0.25 mm/s, and (c) and (f) 0.5 mm/s. (a), (b) and (c) are the SE images and (d), (e) and (f) the BSE images.

Another factor which influenced the surface quality obtained from laser cutting was the localised heating. Figure 3.9 shows the different laser cutting profiles obtained using a nanosecond laser and femtosecond laser [17, 18]. The nanosecond laser has a longer pulse duration, which leads to a larger heat affected zone. More material is melted and re-solidified in the laser focus area such that the actual

machining path is wide and rough. The thermal effect can also lead to microcracks in the specimen. In comparison, a femtosecond laser has a very short pulse duration and therefore less total heat is delivered to the surface. The laser beam can focus on a very small point of the surface and cut narrow trenches with high precision.

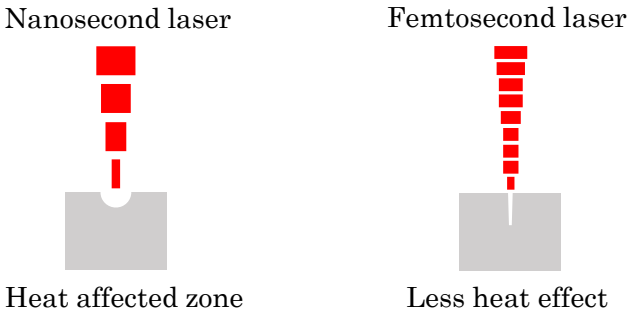

Figure 3.9. Schematic representation of different heat effects when using a nanosecond laser and a femtosecond laser when cutting a substrate.

To cut a narrow trench or groove of high precision into a diamond surface, it is necessary to use ultrashort pulse laser to minimise the heat effect. For example, a femtosecond laser has been employed to cut submicron or nano structures into diamond [19-21]. Unfortunately, in this study, the only laser cutting system available to use had a pulse duration of 10-500 ns, which is far from ideal for the high-precision machining task we required. This resulted in the trenches being too wide and filled with resolidified Si lumps. Because this approach was not as successful as we had hoped, the patterning experiments moved to a new approach, described in the following section.

3.3.2 Diamond film on stripe-patterned Co film

Figure 3.10 shows the cross-sectional profiles of the developed resist patterns. The two resists form micropatterned stripes, with width and spacing of ~ 1 μm onto the Si surface. The single-layer resist has an over-cut profile, as shown in Figure 3.10a. In the bi-layer resist scheme, due to the fact that the LOR 3B resist was developed faster than the S1805 resist, an under-cut profile was obtained, as shown in Figure 3.10b.

Surface morphologies of the two samples after Co thermal evaporation and lift-off are displayed in Figure 3.11. BSE images and EDX maps are presented to show the distribution of Co. The homogeneous colour in the BSE image of the single-layer resist indicates a continuous Co film formed on the surface, which is confirmed by the EDX map. For the sample using bi-layer resist, stripe-patterned Co film was obtained, and the Co stripes can also be identified in the EDX map in Figure 3.11d. The width and spacing of the Co stripe are ~ 1 μm, which agrees well with the pattern of the developed photoresist.

The two different distributions of Co film can be explained by the lift-off mechanism. Due to the sloped profile of the single-layer resist, the thermal evaporated Co on Si was a whole film, making the lift-off extremely difficult. On the other hand, the under-cut profile of the bi-layer resist separated the Co film into isolated stripes. Therefore, the Co film deposited onto the resist was removed in the lift-off process afterwards and only the film attached onto the Si surface was left.

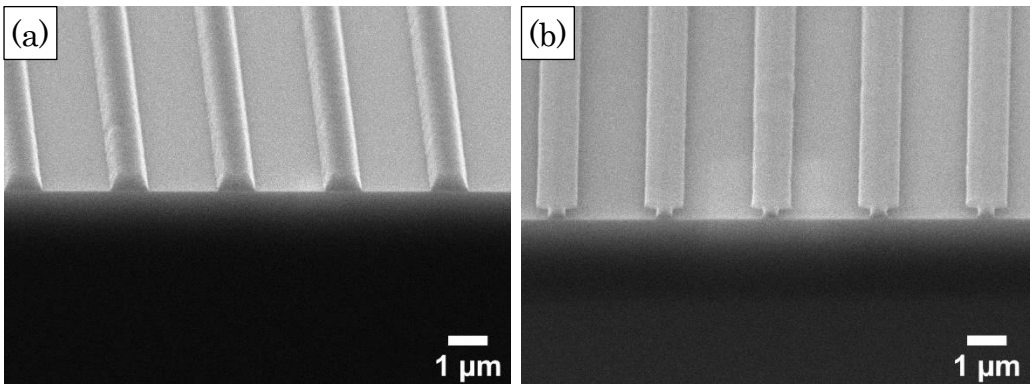

Figure 3.10. Developed profiles of (a) single-layer resist S1805 and (b) bi-layer resist (LOR3B + S1805).

In order to have diamond film as a protective layer on Co, these Si samples with patterned Co stripes were used as the substrate for diamond growth. As shown in Figure 3.12a, diamond film grown on patterned Co exhibits a striped morphology, with larger grain size (~ 2 μm) than that on Si in Figure 3.3a. However, such diamond film still has a high quality, which was confirmed by the Raman spectrum in Figure 3.12b. The small peak at ~1580 cm^{-1} can be attributed to the G band of graphitic carbon.

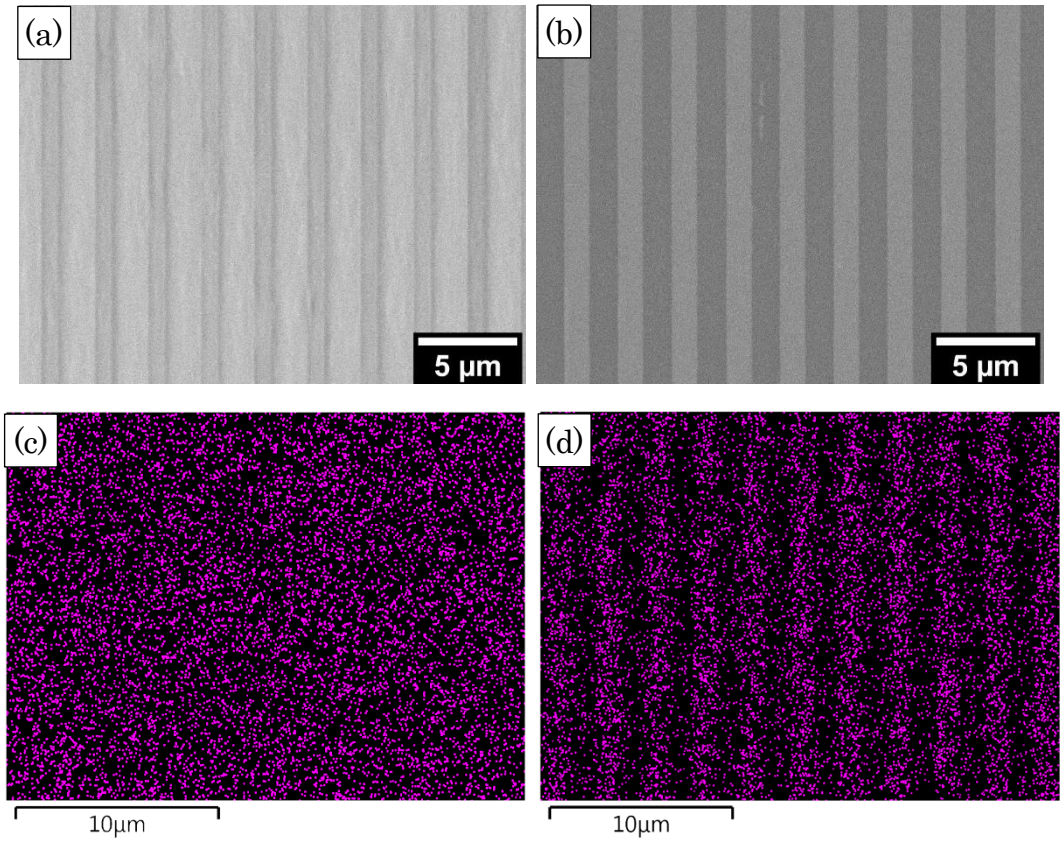

Figure 3.11. BSE images of Co films prepared by (a) single-layer resist and (b) bi-layer resist, and the corresponding EDX maps in (c) and (d), respectively.

The cross-section of the diamond film on top of the patterned Co stripes was also checked by SEM. As seen in Figure 3.13a, the film is ~1.6 μm in thickness. As shown in Figure 3.13b, some periodic bright areas between Si and diamond were observed in the BSE image. These bright areas are believed to be patterned Co, which is confirmed by the EDX analysis displayed as an inset in Figure 3.13a. The selected area shows a periodical distribution of Co, indicating Co has been embedded between diamond film and Si substrate. It is worth noting that for the diamond film grown on the Co stripes, some Co nano particles were observed on the surface, as shown in Figure 3.13b. These Co particles came from the thermally evaporated Co film, and were melted and diffused up to the surface during growth. This growth process will be discussed in the next section.

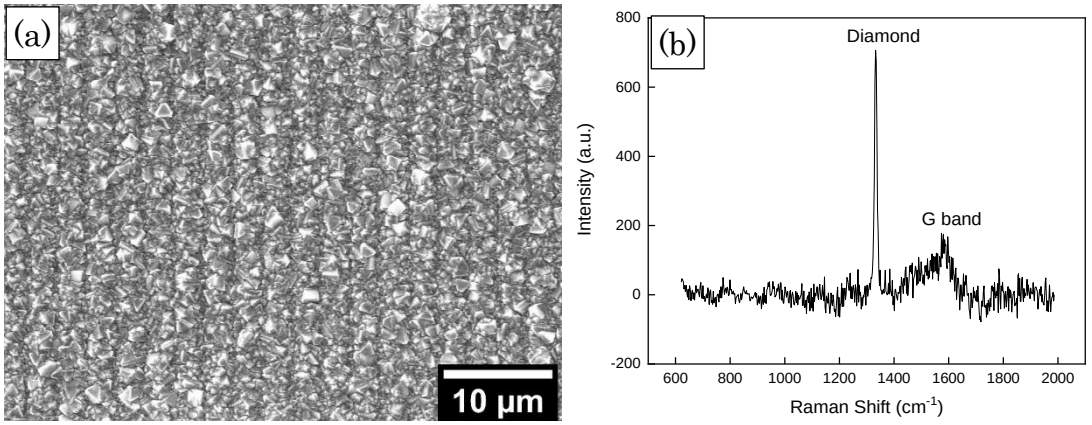

Figure 3.12. Diamond film grown on stripe-patterned Co and its Raman spectrum.

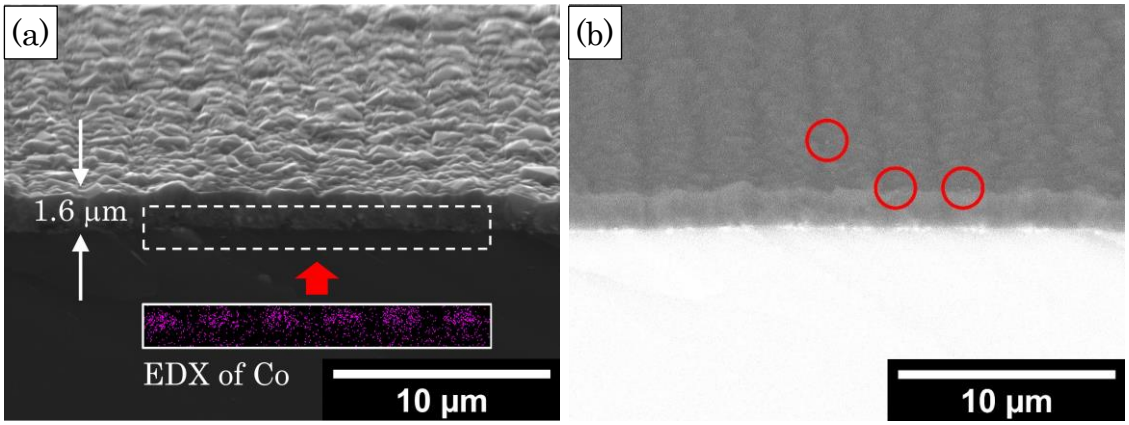

Figure 3.13. Cross-section images of diamond film grown on stripe patterned Si: (a) the SE image with the inset EDX map of Co in the dashed rectangle area, and (b) the BSE image. The red circles in b indicate Co nano particles on the surface.

Compared with the diamond film grown on laser-cut diamond film with Co nanoparticles in trenches, the diamond film grown on thin Co film has a better surface quality. No obvious lumps were observed on the surface, making it possible to run a full MFM scan across the surface.

A 35 μm × 5 μm square area on the surface was selected for the MFM scanning. The selected region contains the diamond film on stripe-patterned Co and Si, as shown in Figure 3.14a, while the height, amplitude and phase maps are displayed in Figure 3.14b, c and d, respectively. According to the height map (Figure 3.14b), diamond film grown on the Co area had an average roughness (R_a) of ~100 nm, while the R_a of the diamond on the Si area was ~50 nm. Because of the height of the Co film, the height of the diamond film shows a periodical distribution, as the MFM tip traverses the Si and Co regions. The amplitude map (Figure 3.14c) has

a similar distribution to the height map, indicating that the amplitude was influenced by the surface morphology.

The diamond film shows a periodic magnetic phase signal on the Co area, while the phase signal on the Si area is low and featureless, indicating that phase map is not affected by the morphology as much as the amplitude. Therefore, the phase shift (the change in phase) in the Co area is believed to represent the magnetic field gradient. The magnetic signal exhibits a periodical distribution across the surface, which agrees well with the location of the underlying Co film. However, the phase map still shows some connection with the morphology. For example, the region with maximum height also has the strongest phase. The phase shift in the Co region is also small (±100°), indicating that the Co-induced magnetic field is weak. One reason may be that the diamond film on Co is rather thick (~ 1.6 μm). Because the magnetic field decays rapidly with distance from the Co film, the magnetic signal becomes very weak at 1.6 μm above the Co.

Another reason may be that even though the surface roughness is less than that of the laser-cut diamond, it is still high for MFM scanning, and this roughness not only increased the distance from the Co stripes to the MFM tip, but also the chance of MFM tip being damaged. The Co stripe had a thickness of ~36 nm. However, as shown in Figure 3.14a and illustrated in Figure 3.15, the diamond film grown on the Co area had a height of > 100 nm more than that on Si. Even though the constant-distance mode has some advantages over the constant-height mode (see section 2.3.2), this substantial height difference made it inappropriate to run MFM at the constant-distance mode because it would make the probe much closer to Co during scanning in the gaps between Co stripes, which would artificially introduce more errors. Therefore, the MFM was operated at the constant-height mode (50 nm from the highest point of the surface), which apparently is not the most sensitive way for MFM to detect magnetic field. The constant-distance mode is only suitable when Co percolates through the diamond and is uniformly distributed within the diamond layer above where the Co stripe was.

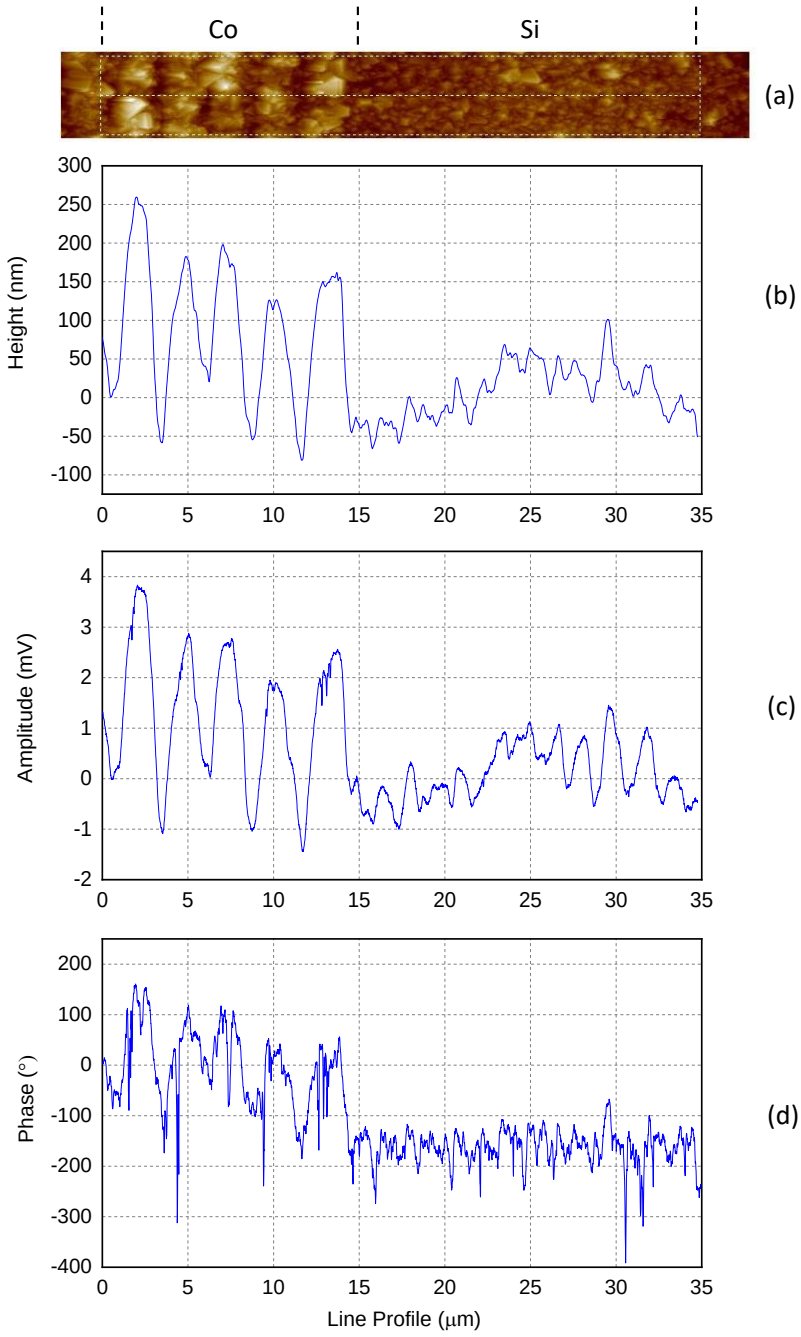

Figure 3.14. (a) surface morphology, (b) height, (c) amplitude and (d) phase maps of the selected area of the diamond film on Co stripes characterised by MFM.

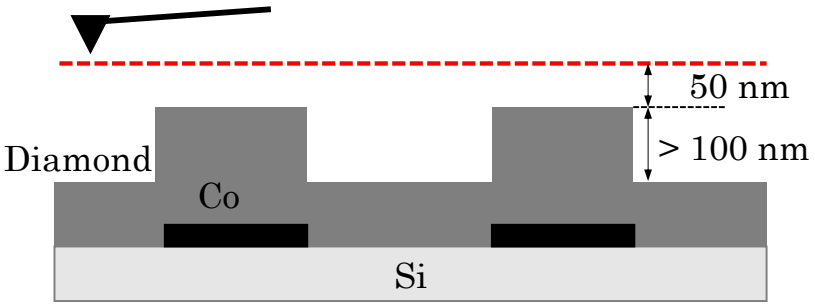

Figure 3.15. Schematic diagram of the constant-height operating mode of MFM.

Nevertheless, this is a very encouraging result. To our knowledge, this is the first report of magnetic field detection through a protective diamond layer, and we have demonstrated that diamond film grown on stripe-patterned Co can be used for magnetic signal detection. These isolated magnetic stripes embedded in diamond film can work as different magnetic domains and may be modified or magnetised independently. Apart from Co, different magnetic materials (metals or alloys) may be patterned and embedded in diamond film using the lift-off process. Due to the robustness of diamond, the prepared magnetic composites can work in extreme environments such as those that are chemically corrosive, or have high/low temperatures and radiation levels (*e.g.*, in space), or as implantable biosensors.

3.3.3 Growth behaviour of diamond on Si and Co

According to the above SEM and AFM images, with the same growth conditions (1% CH_4 in H_2), diamond grown on Co has a larger grain size (~ 2 μm) than that on Si (~ 1 μm), and the grain size has influenced the surface morphology. To compare the growth process of diamond on Co and Si, the two materials were employed separately as substrates for growing diamond film.

1-h growth

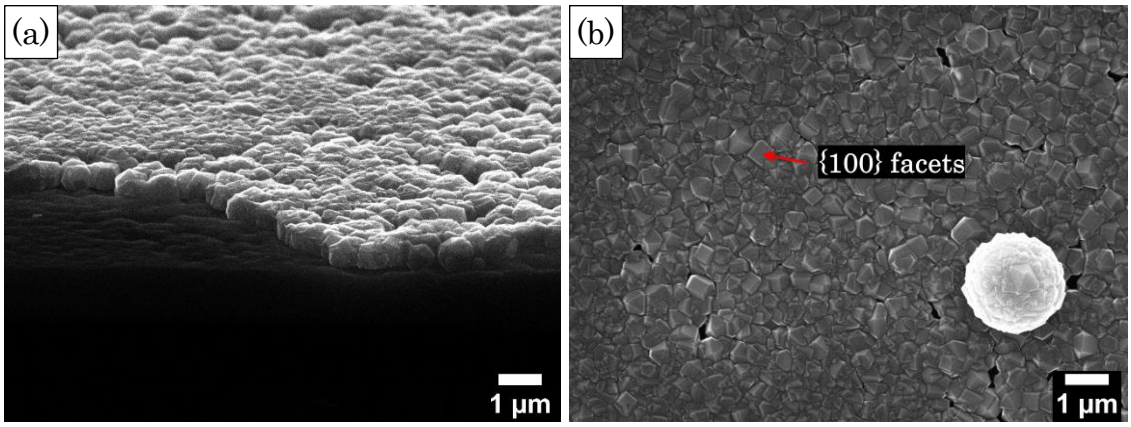

Figure 3.16. Diamond film grown on Si for 1h: (a) cross section, (b) the top view image.

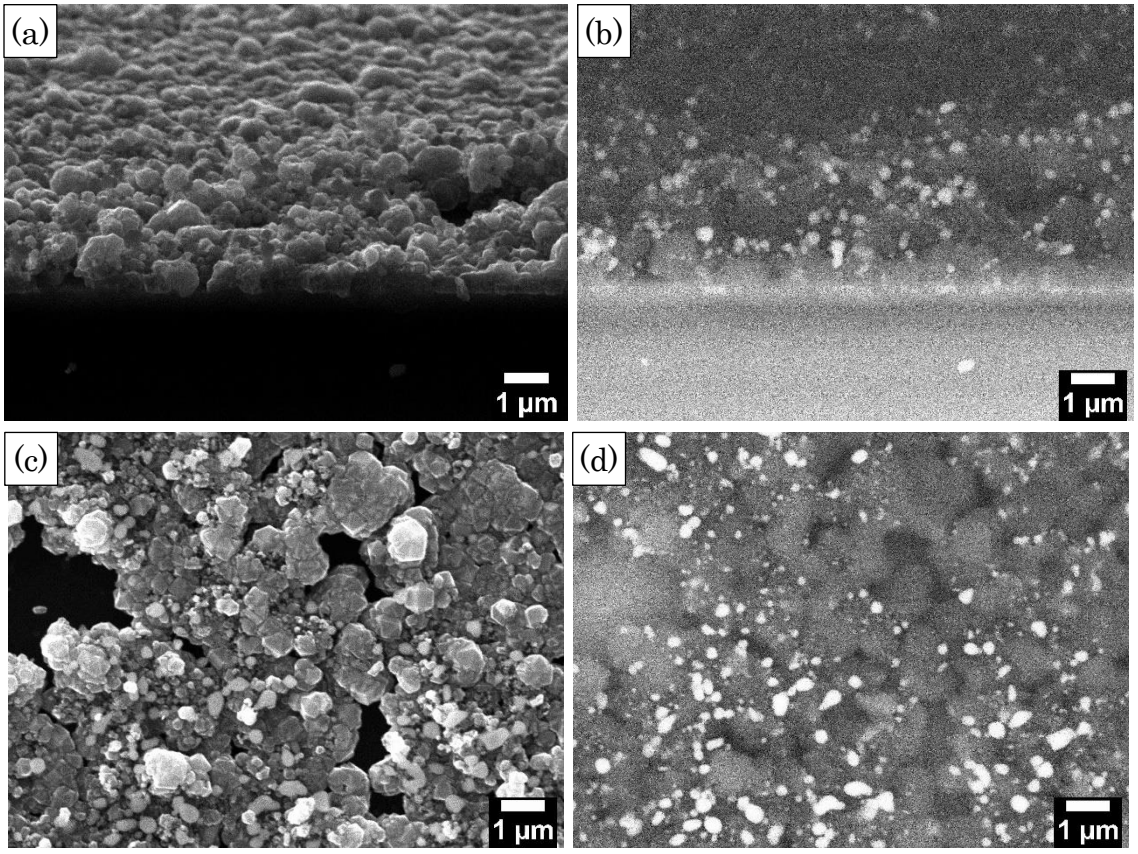

Figure 3.17. Diamond film grown on Co thin film for 1h: (a) and (b) are SE and BSE images of the cross section, and (c) and (d) the SE and BSE images of the surface.

Carbon has a solubility of ~1 at.% in Co at 900 °C, and ~4 at.% at 1200 – 1400 °C [22]. On the other hand, the solubility of C in Si is extremely low, only 10^{-3} – 10^{-4} at.% at 1200 – 1400 °C [23]. Because diamond growth only begins after a substrate surface is fully saturated with C, diamond growth occurs much more rapidly on Si

than Co. Co is also well-known to act as a catalyst that can help convert diamond into graphite or *vice versa* [24]. Under low-pressure conditions, some of the newly formed diamond is likely to have been converted into graphitic forms of carbon by Co, which would be etched away by H_2 during the CVD process, leading to a lower overall growth speed. Even though a diamond film was also observed on Co, the film was not as dense as that on Si. It was also hard to form a robust carbide interface between diamond and Co, such that the diamond grains were not well attached on the substrate and not able to form a homogeneous and flat film. Therefore, the many free-standing grains kept growing to all directions, and evolved into large grains.

2-h growth

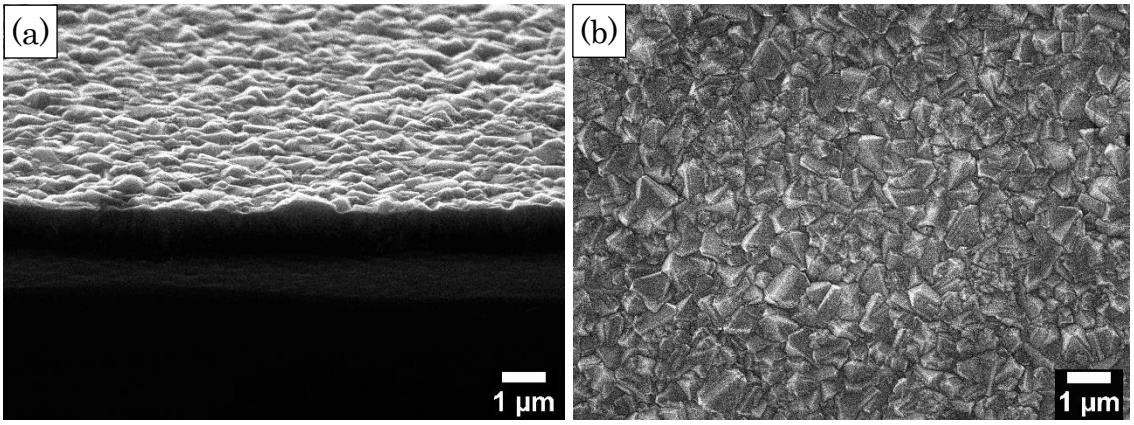

Figure 3.18. Diamond film grown on Si for 2h: (a) cross section, (b) top surface.

After 2-h growth, the diamond had formed a dense film on the Si substrate (Figure 3.18a). In this process, the previously formed diamond layer worked as a new template for growing further diamond, such that some diamond grains continued growing and became large crystals. Therefore, more diamonds with larger size (~ 1 μm) were observed on the surface, as seen in Figure 3.18b, compared with the grain size of ~ 0.5 μm after 1h (Figure 3.16b). At the same time, less {100} facts were observed on the surface.

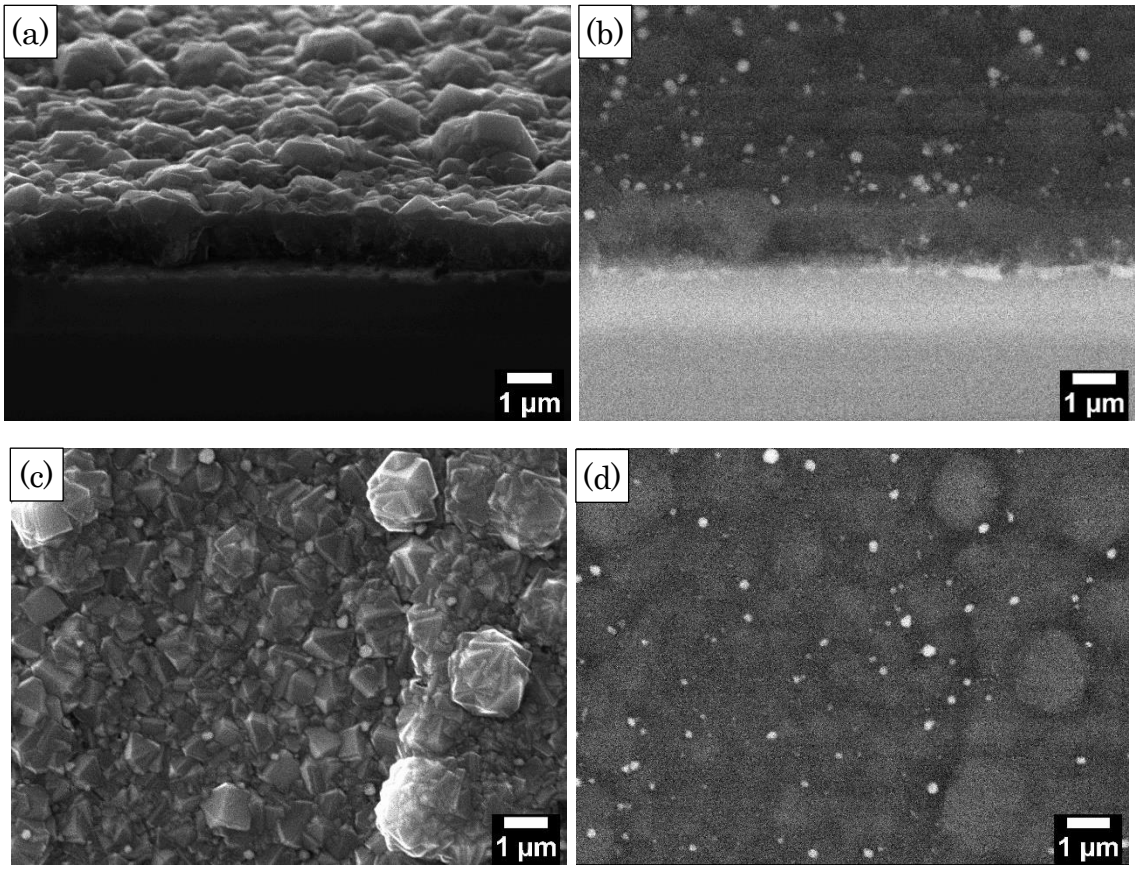

Figure 3.19. Diamond film grown on Co thin film on Si for 2h: (a) and (b) are SE and BSE images of the cross section, and (c) and (d) the SE and BSE images of the top surface.

For the sample grown on Co, a continuous polycrystalline diamond layer was formed after 2-h growth. The cobalt layer can be observed between diamond and Si substrate (see the BSE image in Figure 3.19b). As the reaction proceeded, diamond nucleation and growth preferred to happen on the surface of the diamond crystals rather than on the Co nanoparticles, such that the previously formed Co nanoparticles were 'lifted up' to the surface (see Figure 3.19b and Figure 3.19d). There was also a chance that the Co nanoparticles became trapped between two or more diamond grains such that they were embedded in the film, as can be seen in Figure 3.17b. Due to the poor interface between diamond and Co, the randomly distributed diamond grains continued to grow and many larger grains formed, making the surface rough.

3-h growth

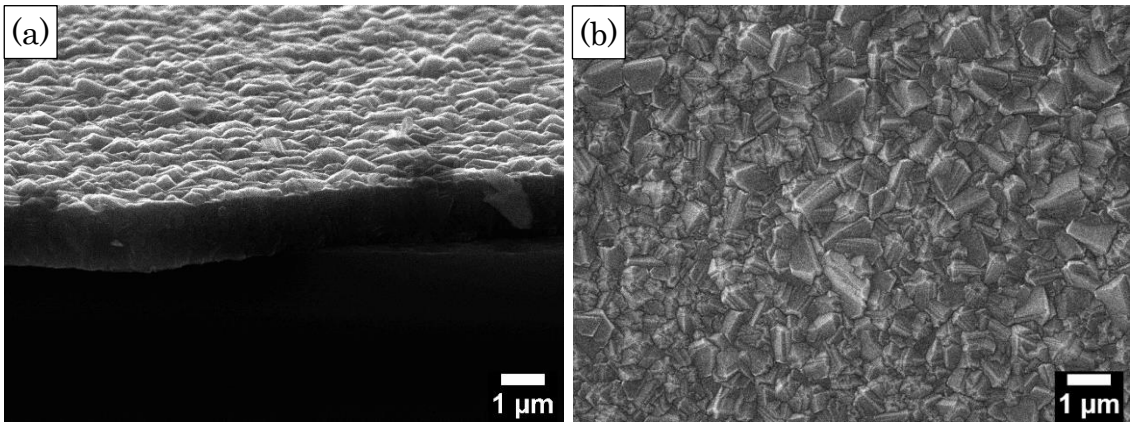

Figure 3.20. Diamond film grown on Si for 3h: (a) the cross section, (b) the top surface.

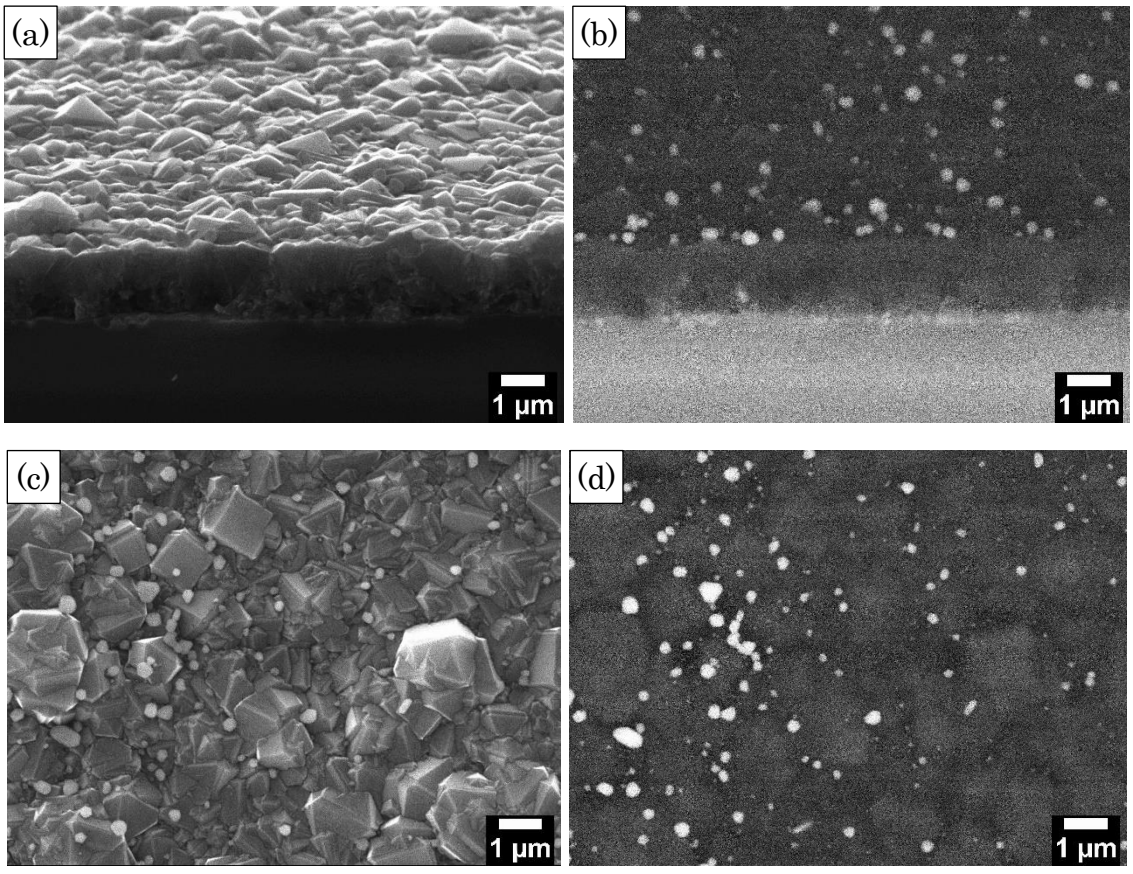

Figure 3.21. Diamond film grown on Co thin film for 3 h: (a) and (b) are SE and BSE images of the cross section, and (c) and (d) the SE and BSE images of the top surface.

After 3 h growth, diamond films with thickness of ~ 1.5 μm were obtained for the samples both on Si and Co, with the surfaces consisting of even larger crystallites compared with the 2h sample. The Co layer was adherent on the Si substrate,

which can be seen in the BSE image in Figure 3.21b, while the Co nanoparticles could also still be observed on the surface.

Based on the above comparison of using Si and Co as substrates, it can be seen that there are several factors affecting the surface morphology of the diamond film. The first factor is the size of the diamond crystallites, such that a larger sized crystallite leads to a higher surface roughness. The second factor is the interface between the substrate and diamond film. When a uniform interface such as a carbide layer is formed, diamond crystallites can attach on the substrate well, therefore forming a homogeneous layer. However, as in the case of using Co as substrate, the non-uniform interface resulted in a rougher film.

3.3.4 Nanodiamond film and the use of an interlayer

To prepare a polycrystalline diamond film with low surface roughness, one strategy is to make the diamond crystallite size as small as possible. The crystallite size can be controlled by adjusting the methane concentration in hydrogen, such that a higher methane concentration leads to a smaller crystal size [25].

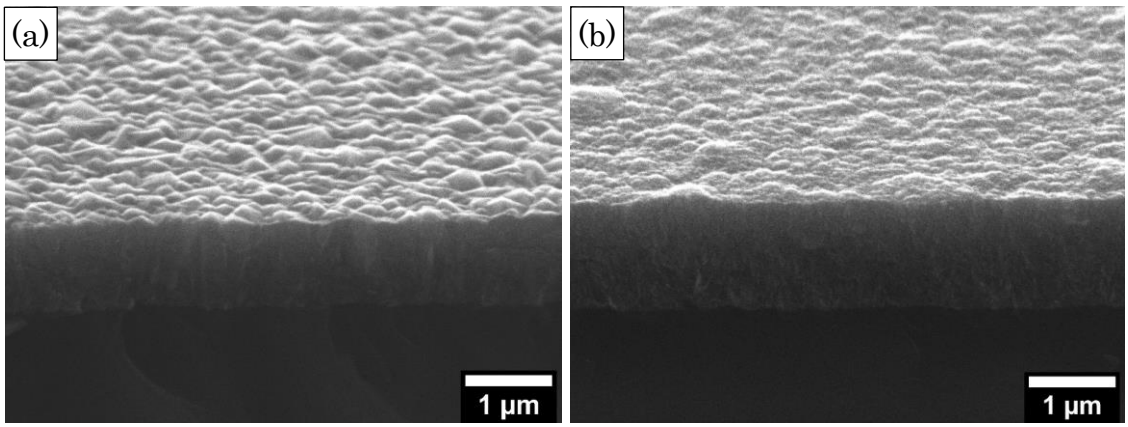

Figure 3.22. Cross-section images of diamond films deposited using (a) 2% and (b) 4% CH_4 in H_2 after 1 h growth.

The cross sections of polycrystalline diamond films using 2% and 4% CH_4 are shown in Figure 3.22a and b, respectively. Compared with the sample grown using 1% CH_4 (Figure 3.20a), with the increase in methane concentration the crystallite size has become smaller. For the sample using 4% CH_4, the nano-size crystallites are now barely distinguishable under SEM. Also, with high methane

concentration more C atoms were introduced into the reaction chamber thus the growth rate also increased. However, high concentrations of methane also introduces more sp^2 C into the sample, especially in the grain boundaries [25].

As discussed in the last session, the connection between substrate and diamond film plays an important role in the quality of the sample. To improve the interfacial connection between Co and diamond, Ti and Al (~ 15 nm thickness) were introduced as interlayers. The surface morphologies of CVD diamond films grown on Ti and on Al on top of stripe-patterned Co are shown in Figure 3.23. Using high-concentration methane for the CVD with Al and Ti as interlayer materials, the resulting diamond films have a smaller grain size than the sample in Figure 3.13, and also appear to be well attached to the substrate. Diamond grown on Ti has a smaller grain size than that on Al. However, the stripe patterns are still clear under SEM, meaning that the surface is still not flat enough for MFM test.

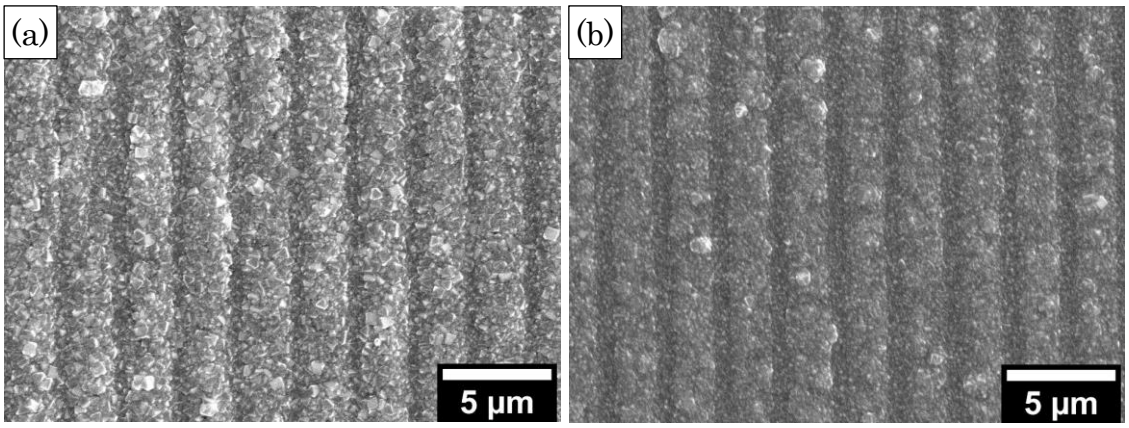

Figure 3.23. SEM images of diamond film on stripe-patterned Co for 30 min, using 2% CH_4 in H_2, and (a) Al and (b) Ti as interlayer, respectively.

In this case, due to the existence of the Co stripes, an ideal result is that with the growth of the diamond film, the bump feature will be compensated by the high thickness such that a flat surface can be obtained. However, in the real situation, diamond grows not only on the flat substrate, but also on the bump area, as illustrated in Figure 3.24. As the growth continues, the bump becomes bigger and bigger. Therefore, it is hard to have a film with flat surface unless some post processing such as polishing is introduced.

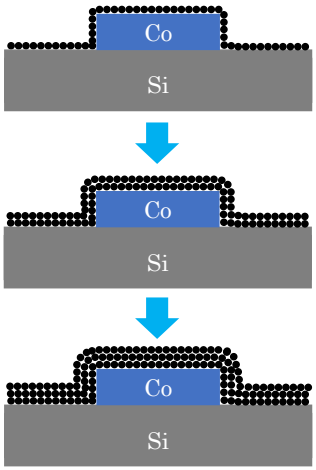

Figure 3.24. Schematic of nanodiamond film growth on a rugged surface.

3.4 Conclusions

In this chapter, Co nanoparticles and films were used to make magnetic diamond film composites. Si and Co were compared as substrates for CVD diamond growth. The main conclusions are as follows.

1) Carbon-coated cobalt nanoparticles can be embedded into polycrystalline diamond film by laser cutting followed by a second diamond growth. Diamond can grow over the cobalt nanoparticles and the magnetic signal can be detected by MFM. However, due to the heating effect of the nanosecond laser melting and resolidifying the Si substrate, the laser-cut surface was rough. This meant the diamond film after the second growth was not smooth enough for a magnetic signal reading. It is recommended that for future work an ultrashort pulse laser (*e.g.* femtosecond laser) is required to have the high-precision laser structuring without the Si melting.
2) Stripe-patterned Co film was prepared by a standard lift-off fabrication process. Diamond film was grown on the Si substate with stripe-patterned Co. The Co-induced magnetic field was detected by MFM through the 1.6 μm-thick protective diamond coating. Although this is preliminary work, it has demonstrated the proof-of-principle that diamond films can act as a robust protective layer for magnetic composite devices, which may have applications in some extreme environments. Future work would involve optimising the fabrication procedures, in terms of the thickness of Co and

diamond, as well as using dots instead of stripes for discreet magnetic memory applications.

3) Co was studied as a substrate for CVD diamond growth and compared with Si. Carbon has a high solubility in Co, so diamond growth did not start until Co was saturated with C. Diamond cannot form a stable carbide layer on Co, so the growth was not uniform as that on Si.
4) To reduce the surface roughness of diamond film, nanodiamond film was obtained using a high concentration of methane. Al or Ti can be employed as thin film interlayer materials between diamond and Co to improve the quality of diamond on Co. However, it is still hard to obtain a flat nanodiamond film on a rugged substrate because any surface feature will be enlarged after growth.
5) Future work may also involve studying other magnetic metals such as alloy of neodymium which has larger magnetic moments than Co and Fe and so it may be possible to read magnetic signals buried beneath deeper layers of diamond than was possible with Co.

3.5 References

[1] P.W. May, Diamond thin films: a 21st-century material, Philos. Trans. R. Soc. A 358 (2000) 473-495.

[2] H. Okushi, High quality homoepitaxial CVD diamond for electronic devices, Diam. Relat. Mat. 10 (2001) 281-288.

[3] F. Picollo, S. Gosso, E. Vittone, et al., A New Diamond Biosensor with Integrated Graphitic Microchannels for Detecting Quantal Exocytic Events from Chromaffin Cells, Adv. Mater. 25 (2013) 4696-4700.

[4] X. Zhao, K. Ma, T. Jiao, et al., Fabrication of Hierarchical Layer-by-Layer Assembled Diamond-based Core-Shell Nanocomposites as Highly Efficient Dye Absorbents for Wastewater Treatment, Sci. Rep. 7 (2017) 44076.

[5] X.N. Zhao, K. Ma, T.F. Jiao, et al., Fabrication of Hierarchical Layerby-Layer Assembled Diamondbased Core-Shell Nanocomposites as Highly Efficient Dye Absorbents for Wastewater Treatment, Sci Rep 7 (2017) 13.

[6] H. Luo, D. Wang, J. He, Y. Lu, Magnetic Cobalt Nanowire Thin Films, J. Phys. Chem. B 109 (2005) 1919-1922.

[7] R.M.H. New, R.F.W. Pease, R.L. White, Submicron patterning of thin cobalt films for magnetic storage, J. Vac. Sci. Technol. B 12 (1994) 3196-3201.

[8] D. Jańczewski, Y. Zhang, G.K. Das, et al., Bimodal magnetic–fluorescent probes for bioimaging, Microsc. Res. Tech. 74 (2011) 563-576.

[9] D.A. Allwood, G. Xiong, C.C. Faulkner, et al., Magnetic domain-wall logic, Science 309 (2005) 1688-1692.

[10] J.D. Cressler, H.A. Mantooth, Extreme environment electronics, CRC Press 2017.

[11] B. Tomcik, T. Osipowicz, J.Y. Lee, Diamond-like film as a corrosion protective layer on the hard disk, Thin Solid Films 360 (2000) 173-180.

[12] C.S. Bhatia, E. Rismani-Yazdi, S.K. Sinha, A.J. Danner, Applications of DLC in Magnetic Recording, in: Q.J. Wang, Y.-W. Chung (Eds.), Encyclopedia of Tribology, Springer US, Boston, MA, 2013, pp. 86-95.

[13] W. de Boer, J. Bol, A. Furgeri, et al., Radiation hardness of diamond and silicon sensors compared, Phys. Status Solidi A 204 (2007) 3004-3010.

[14] D.J. Sellmyer, R. Skomski, Advanced magnetic nanostructures, Springer Science & Business Media 2006.

[15] Y. Soeno, M. Moriya, K. Ito, et al., Feasibility of discrete track perpendicular media for high track density recording, IEEE Trans. Magn. 39 (2003) 1967-1971.

[16] T.R. Albrecht, H. Arora, V. Ayanoor-Vitikkate, et al., Bit-Patterned Magnetic Recording: Theory, Media Fabrication, and Recording Performance, IEEE Trans. Magn. 51 (2015) 42.

[17] D.M. Trucchi, A. Bellucci, M. Girolami, et al., Surface Texturing of CVD Diamond Assisted by Ultrashort Laser Pulses, Coatings 7 (2017) 18.

[18] R. Agrawal, C. Wang, Laser Beam Machining, in: B. Bhushan (Ed.), Encyclopedia of Nanotechnology, Springer Netherlands, Dordrecht, 2016, pp. 1739-1753.

[19] S. Kumar, S.M. Eaton, M. Bollani, et al., Laser surface structuring of diamond with ultrashort Bessel beams, Sci. Rep. 8 (2018) 14021.

[20] S. Su, J.L. Li, G.C.B. Lee, et al., Femtosecond laser-induced microstructures on diamond for microfluidic sensing device applications, Appl. Phys. Lett. 102 (2013) 5.

[21] M. Shinoda, R.R. Gattass, E. Mazur, Femtosecond laser-induced formation of nanometer-width grooves on synthetic single-crystal diamond surfaces, J. Appl. Phys. 105 (2009) 4.

[22] K. Ishida, T. Nishizawa, The C-Co(Carbon-Cobalt) system, J. Ph. Equilibria 12 (1991) 417-424.

[23] R.W. Olesinski, G.J. Abbaschian, The C–Si (Carbon-Silicon) system, Bull. Alloy Phase Diagr. 5 (1984) 486-489.

[24] R.C. Burns, J.O. Hansen, R.A. Spits, et al., Growth of high purity large synthetic diamond crystals, Diam. Relat. Mater. 8 (1999) 1433-1437.

[25] P.W. May, Y.A. Mankelevich, Experiment and modeling of the deposition of ultrananocrystalline diamond films using hot filament chemical vapor deposition and Ar / CH4 / H2 gas mixtures: A generalized mechanism for ultrananocrystalline diamond growth, J. Appl. Phys. 100 (2006) 024301.

CHAPTER 4

THEORETICAL STUDY OF Be IN DIAMOND

As mentioned in section 1.5, the preparation of n-type diamond has been extremely difficult, which inhibits the application of diamond into electronic devices. In this chapter, first-principles calculations were carried out to investigate Be as a dopant for diamond. The electronic and magnetic properties of Be-doped diamond were studied. Different doping positions were considered and the electronic properties were compared. Band structures and the empirical marker method were employed to predict the energy levels of the defects, and their formation energies were calculated to predict whether these defects are easy to form.

4.1 Introduction

Beryllium (Be), with atomic number 4, is near the beginning of periodic table. Due to its low density and low number of electrons for each atom, Be is highly transparent to X-rays [1], therefore it is often used as a material for making X-ray windows [2]. For example, Be gasket can be used as a X-ray window to study material properties at extremely high pressure [3]. If diamond can be grown on Be, then the strength of the window can be greatly enhanced. Be is one of the rarest metals on Earth [4], making it more expensive compared with most other elements. Be and its compounds, for example $BeCl_2$ and BeH_2, often exist as solid-state powders, which are not suitable for the pipework of CVD. They are also highly toxic, especially after being inhaled [5]. Because of the high toxicity and high cost, it is very difficult to obtain and handle Be in the lab, not mention to put it into a CVD reactor at the risk of contaminating the chamber. For these reasons, there are only a few experiments reported regarding Be-doped diamond.

Be has been used as substrate for diamond growth in a microwave plasma CVD reactor [6]. Even though it was possible to grow high-purity diamond given the formation of Be_2C carbide layer, this layer only formed when temperature was above 750 °C. Below this temperature, diamond on Be was of bad quality with a lot of amorphous carbon. Another problem was that, due to the large difference of thermal expansion coefficients between Be (11.3×10^{-6} K^{-1}) and diamond (0.8×10^{-6} K^{-1}), the grown diamond film was easily fractured and delaminated.

Ion-implantation was used to introduce Be into Ib-type single crystal diamond, followed by a high pressure and high temperature annealing treatment to reduce the implantation-induced stress [7]. Cathodoluminescence spectroscopy confirmed the existence of Be in diamond film. However, due to damage induced from implantation, the resistivity of the Be-doped diamond was so high that the electrical parameters could not be determined. Later, the same group prepared Be-doped diamond by inserting a Be rod into the reactor during the CVD process, using a single crystal diamond as substrate [8]. Be concentration in diamond was controlled from 10^{16} to 10^{18} cm^{-3} by adjusting the position of Be-rod in the reactor. However, the resistivity was still too high for measuring the electrical parameters such as mobility and carrier concentration.

Compared with the experimental work with a lot of risk and uncertainty, calculation is risk-free, thus easier to perform. Yet, there is not much calculation work done concerning Be-doped diamond. The electronic properties of Be-doped diamond were studied by researchers using GGA functional (PBE), and n-type and p-type semiconductor properties with shallow donor or acceptor level were predicted for diamond doped with Be at interstitial and substituted sites, respectively [9]. However, because the PBE functional cannot describe the exchange interaction accurately [10], the calculated band gap was underestimated using this method. Second, for the interstitial doping, only the tetrahedral defect was studied, while the hexagonal interstitial defect was not reported. Moreover, formation energies of different defects were not calculated, so it is hard to know whether these defects can form easily in diamond or which should be the ground state among these defects. The ground state and its formation energy determines whether Be can be used as a n- or p-type for diamond.

In this work, DFT calculations were employed to study the electronic and magnetic properties of Be-doped diamond. Different doping positions and doping concentrations were considered. Geometry structures and band structures were investigated.

4.2 Method

The CRYSTAL 17 [11] software package was used for the calculations. The range-separated hybrid functional HSE06 [12] was selected for exchange and correlation calculations. Compared with global hybrid functionals, range-separated hybrid functionals are usually lower in computational cost and easier to converge, therefore widely used for the calculation of electrical properties [13]. Two Gaussian basis sets, pob-TZVP-rev2 [14] (hereafter abbreviated as BS1) and 6-21G* [15] (abbreviated as BS2), with polarisation quality were used for the carbon atoms. BS1 consisting of 18 orbitals, is based on the triple-zeta basis set pob-TZVP [16], which consists of one basis function for the core shell, three basis functions per valence shell and one primitive polarisation function. Compared with the original pob-TZVP basis set, the revised version BS1 suffers less from basis-set superposition errors, therefore is more suited for solid-state calculations. BS2, on the other hand, contains one basis function for the core shell, two basis functions per valence shell and one primitive polarisation function. BS2 is cheaper than BS1, therefore suited for calculations in larger supercells. An extended 5-1111-(3p)-(2d) basis set proposed by Grüneich et al. [17] was selected for Be, which contains 24 orbitals for high-precision calculation and diffuse functions to improve the performance in Be metal [18].

To simulate different doping concentrations, four conventional supercells (2×2×2, 2×2×4, 3×3×3 and 4×4×4) were constructed for the calculation, which contain 64, 128, 216 and 512 C atoms and were denoted as S_{64}, S_{128}, S_{216} and S_{512}, respectively. Based on the Monkhorst-Pack method [19], shrinking factors 4 and 2 were selected, which contain 4×4×4 (S_{64} and S_{128}) and 2×2×2 (S_{216} and S_{512}) special k-point meshes in the first Brillouin zone. The truncation criteria for Coulomb and HF exchange were set to 7 for T_1-T_4 and 14 for T_5 (see CRYSTAL17 User's Manual [20]).

Full geometry optimisation was employed in the S_{64} pure diamond system before dopants were added, resulting in calculated lattice parameters of 3.5470 (using BS1) and 3.5637 Å (using BS2), which are close to the experimental value 3.567 Å [21]. The optimised lattice parameters were then used in the subsequent calculations of the system with dopants added. Substitutional and interstitial Be in diamond were calculated separately. Be located at a substitutional site is denoted as Be_s. For interstitial Be defects, as illustrated in Figure 4.1, two possible positions, tetrahedral and hexagonal interstitial sites were considered, and the corresponding defects are denoted as $Be_{i,tet}$ and $Be_{i,hex}$, respectively. To avoid being trapped in the local energy minima, the Be atom was initially placed slightly away (~ 0.05 Å) from the original C lattice site, tetrahedral or hexagonal centre of the perfect diamond structure. Spin-polarised solutions were employed for the calculations in the defect systems to determine the ground-state magnetic ordering. For each open-shell system, the ground-state spin was determined by comparing energies of the system with different spins. The spin (S) of the system was controlled by maintaining a fixed difference between the number of α and ß electrons by using a keyword SPINLOCK, while for any specific atoms, their atomic spins were controlled by a keyword ATOMSPIN [20]. During geometry optimisation of the defective system, all the atomic positions were allowed to relax in the supercells of fixed lattice parameters (3.5470 Å for BS1 or 3.5637 Å for BS2).

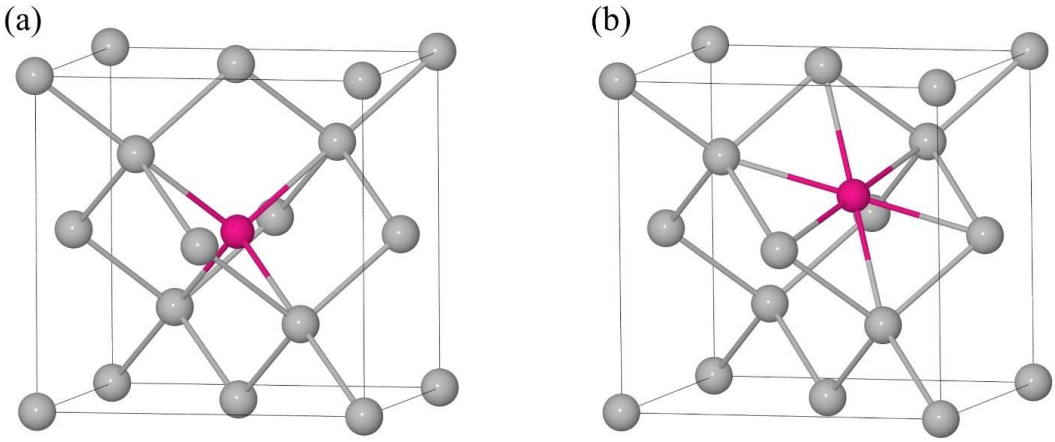

Figure 4.1. Schematic diagram of two interstitial Be sites in diamond: (a) tetrahedral ($Be_{i,tet}$) and (b) hexagonal ($Be_{i,hex}$). Gray and red atoms represent C and Be atoms, respectively.

High-symmetry k points in a Brillouin zone of a simple cubic lattice [22] were selected to plot band structures. The selected path in the reciprocal space is R-Γ-X-M-Γ, as illustrated in Figure 4.2.

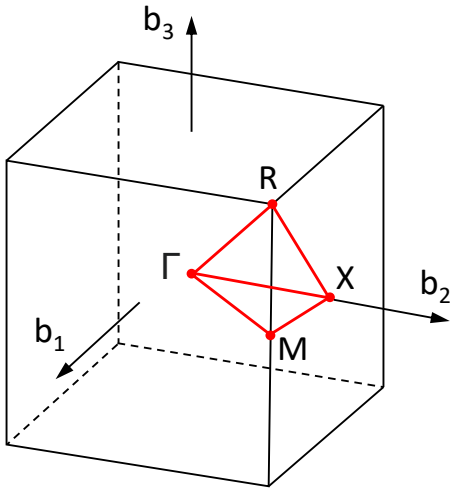

Figure 4.2. Brillouin zone of a cubic lattice, where $\mathbf{b_1}$, $\mathbf{b_2}$ and $\mathbf{b_3}$ are the primitive reciprocal lattice vectors [22], and R, Γ, X, M the high-symmetry k points.

Formation energies (E_f) of defects were calculated using:

$$E_f = E_d - E_p + E_C - E_\mu \qquad 5.1$$

where E_d is the total energy of the supercell with defect, E_p is the energy of the perfect supercell, and E_C is the chemical potential of the carbon atoms removed and E_μ the potential of the dopant atoms added to the diamond bulk.

Although the incorporation of HF exchange helps DFT describe the band gap better, DFT method is still not able to predict the band structure of diamond accurately, and it cannot predict the donor or acceptor level with high accuracy, especially for the shallow donors and acceptors. To overcome this shortcoming, empirical marker method (EMM) was employed to calculate the donor or acceptor level [23, 24]. EMM compares the ionisation energy of a defect with a reference (marker), which has a donor or acceptor level known experimentaly. EMM has been used to predict donor and acceptor states in diamond successfully [24-29], and is especially useful to calculate the electrical levels of the dopant having

similar geometry and energy levels with the reference. To calculate the donor and acceptor levels, EMM can be given as Equations 5.2 and 5.3:

$$X^{(0/+)} = R^{(0/+)} + \{[E(X^0) - E(X^+)] - [E(R^0) - E(R^+)]\} \quad 5.2$$

$$X^{(-/0)} = R^{(-/0)} + \{[E(X^-) - E(X^0)] - [E(R^-) - E(R^0)]\} \quad 5.3$$

where $X^{(0/+)}$ and $R^{(0/+)}$ represent the donor level of the element to be calculated and the donor level of refrence, $E(X^0)$ and $E(X^+)$ the neutral and positively charged states of the element to be calculated, and $E(R^0)$ and $E(R^+)$ the neutral and positively charged states of the reference. Equation 5.2 is also equivalent for the calculation of acceptors in negatively charged state, which can also be expressed in Equation 5.3, where $X^{(-/0)}$ and $R^{(-/0)}$ represent the acceptor level of the element to be calculated and the acceptor level of refrence, $E(X^-)$ and $E(X^0)$ the negative and neutral states of the element to be calculated, and $E(R^-)$ and $E(R^0)$ the negative and neutral states of the reference. The negetively or positivly charged states were generated by adding or removing an electron from the system. B and P were selected as the acceptor and donor references, with electrical levels of $E_v + 0.35$ eV [30, 31] and $E_c - 0.6$ eV [32] reported, where E_v and E_c represent valence band edge and conduction band edge, respectively.

4.3 Results and discussion

4.3.1 Single neutral vacancy

4.3.1.1 Geometry structures

Natural or lab grown diamond often exists with many crystallographic defects, for example, a single vacancy [33, 34]. Therefore, substitutionally doped Be is more likely to form in a diamond structure which already has an existing C vacancy. The formation energy of the Be_s defect given a pre-existing single-vacancy defect is expected to be lower than that from a perfect diamond. Therefore, before considering Be doping, we first studied the properties of a neutral C vacancy in diamond. Single-vacancy calculations were performed using the S_{64} supercell, with a neutral vacancy located in the centre of the model, as shown in Figure 4.3. The

neutral vacancy generates four unpaired electrons, which have three possible spin states, *i.e.*, $S = 0$ (two α and two ß electrons), $S = 1$ (three α and one ß electrons) and $S = 2$ (four α electrons). To determine the ground state, these three possible structures were calculated and compared.

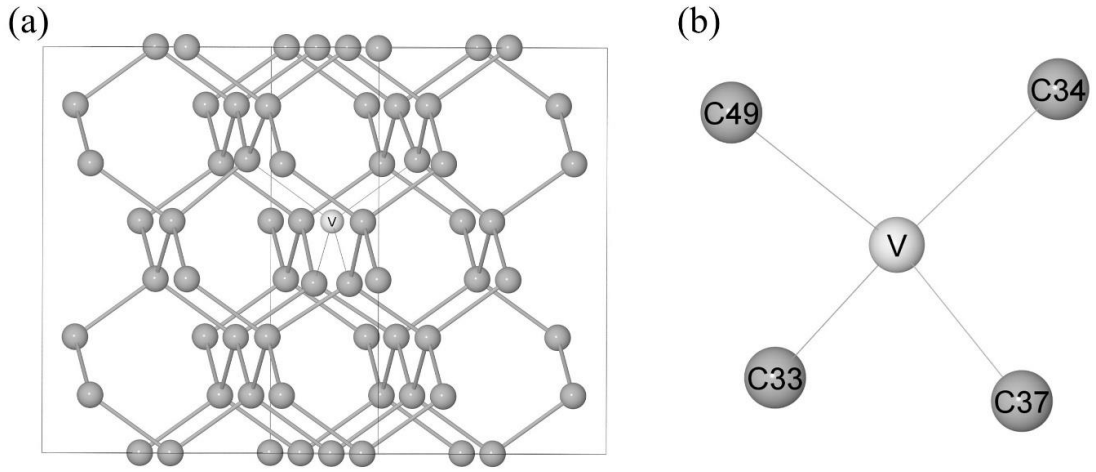

Figure 4.3. (a) Single neutral vacancy in S_{64} and (b) enlarged view in the S_{64} supercell. The 63 carbon atoms are labelled from C2-C64 with the vacancy denoted by "V".

After geometry optimisation, deformation of the lattice mainly occurred around the vacancy site, *i.e.*, C33, C34, C37 and C49 as shown in Figure 4.3(b). Distances from the original vacancy site to its nearest C atoms are given in Table 4.1. These show that compared with the original C–C bond lengths of 1.536 Å (BS1) and 1.543 Å (BS2), the four C atoms around the vacancy all relaxed away from the vacancy for all the spin states. $S = 0$ and 2 resulted in T_d structures while $S = 1$ resulted in a C_{3v} defect. Due to the rigid structure of diamond, C atoms far from the vacancy were not affected as much [35]. In the relaxed structure of the $S = 0$ state using BS1, the C–C bonds nearest to the vacancy site have lengths 1.484 – 1.502 Å, which are 2.21 – 3.39% shorter than the original length, while the second-nearest C–C bonds are 1.534 in length, which are 0.13% shorter than the original.

Table 4.1. Distances (Å) from the vacancy site V to each of the 4 neighbouring C atoms in the S_{64} supercell after geometry optimisation using the 2 basis sets.

	BS1			BS2		
	$S = 0$	$S = 1$	$S = 2$	$S = 0$	$S = 1$	$S = 2$
V-C33	1.646	1.600	1.702	1.640	1.588	1.701
V-C34	1.646	1.659	1.702	1.640	1.655	1.701
V-C37	1.646	1.659	1.702	1.640	1.655	1.701
V-C49	1.646	1.659	1.702	1.640	1.655	1.701

4.3.1.2 Vacancy formation energies

For the BS1 basis set, the $S = 0$ state had the lowest total energy, while $S = 1$ was only ~ 0.12 eV higher in energy than this. For both $S = 0$ and $S = 1$, the spin configurations became stable after 5 cycles of SPINLOCK. $S = 2$ is the highest-energy state at ~1.5 eV higher than that of $S = 0$. To prevent the $S = 2$ state relaxing to a more stable state ($S = 0$ or $S = 1$), the difference between the number of α and ß electrons had to be maintained during the whole self-consistent field (SCF) calculation. The same stability order was obtained using the BS2 basis set, where the $S = 0$ state was ~0.12 and 1.45 eV lower than that of the $S = 1$ and $S = 2$ states, respectively. This relative stability agrees very well with the literature [36, 37]. The calculated vacancy-formation energies for different spins are presented in Table 4.2, indicating good agreement with the literature.

Table 4.2. Formation energies (E_f, eV) of a single neutral vacancy calculated using the 2 carbon basis sets and the comparison with the literature.

S	BS1	BS2	Literature
0	7.12	7.38	7.01 [36], 6.99 [37], 7.62 [38], 7.20 [39]
1	7.24	7.50	7.15 [36], 7.14 [37]
2	8.61	8.83	8.50 [36], 8.49 [37]

4.3.1.3 Band structures

Band structures of the pure diamond is shown in Figure 4.4. Band gaps of 5.33 and 5.29 eV were obtained from the perfect diamond structure using BS1 and BS2,

respectively, which are in good agreement with the experimental value of 5.47 eV [40]. Overall, band structures calculated from the two basis sets are very similar.

For the single-vacancy structure, defect states appear in the band gap due to the vacancy, as plotted in Figure 4.5. Under different spin states, the atomic orbitals below the Fermi level are filled by different numbers of α and ß spin electrons. The band structures agree well with the literature [36, 37].

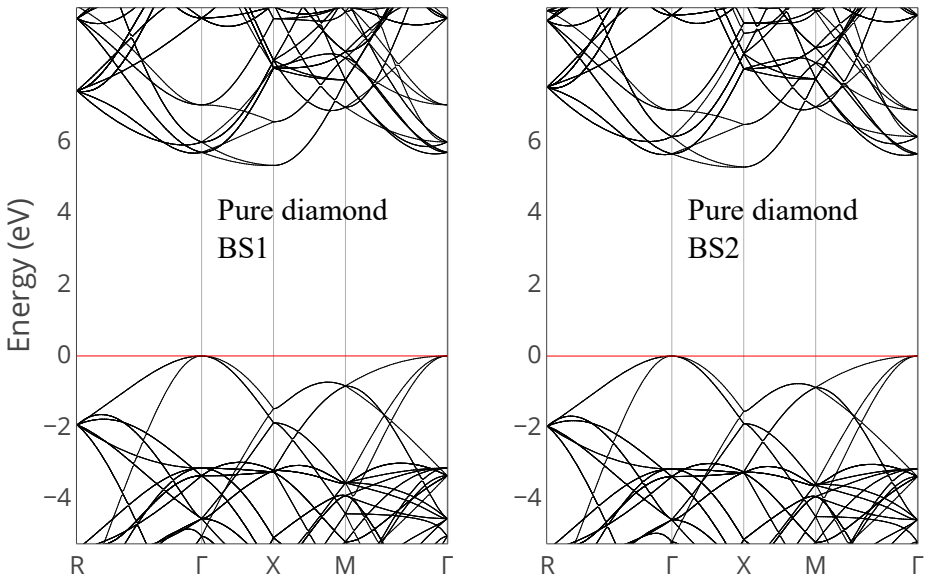

Figure 4.4. Band structures of perfect diamond using BS1 and BS2 basis sets, where the red lines represent the Fermi level.

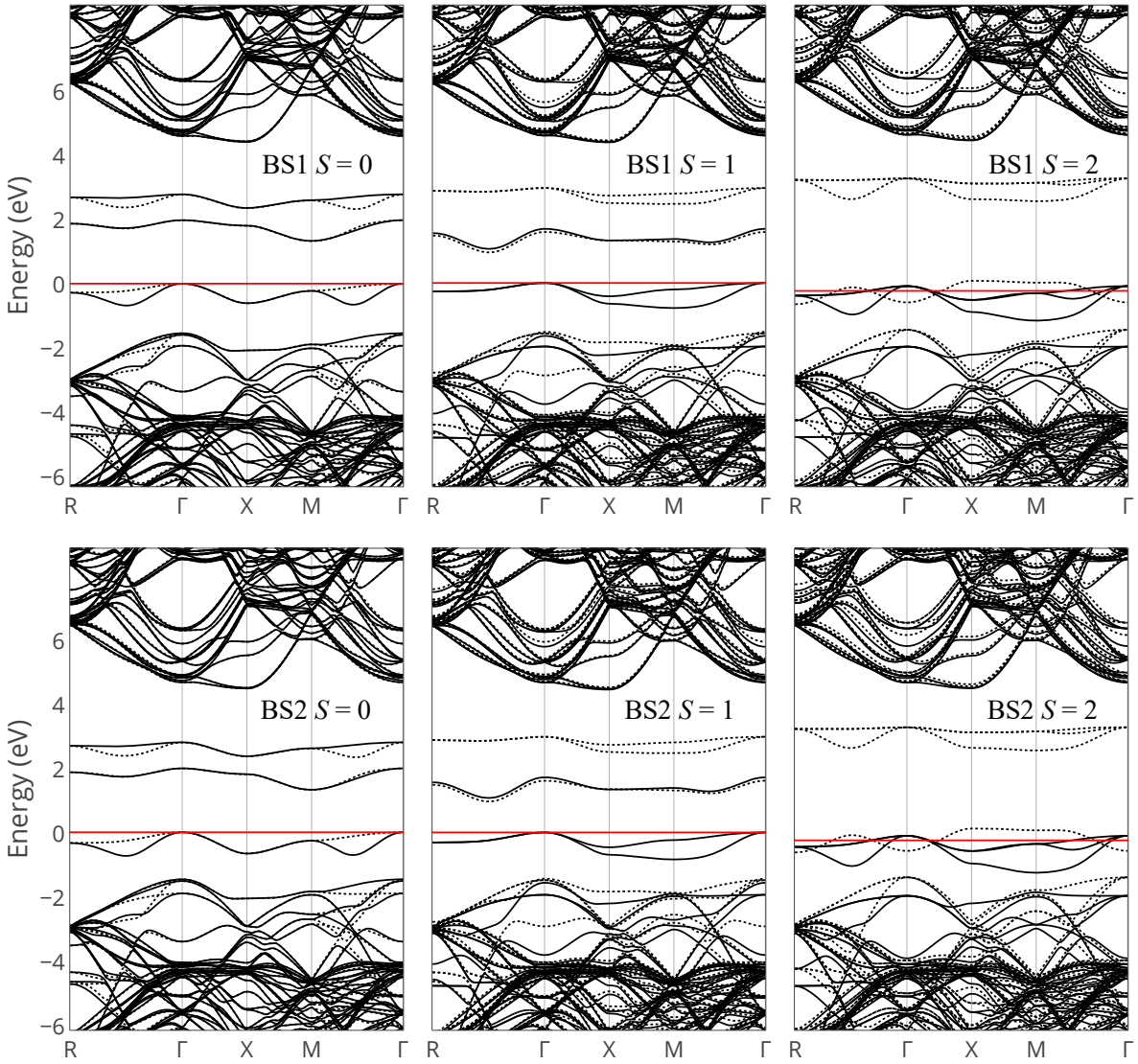

Figure 4.5. Band structures of diamond with a single vacancy calculated for a S_{64} supercell using BS1 and BS2 basis sets with spins of $S = 0$, 1, and 2. Continuous and dotted lines represent α and ß levels, respectively.

4.3.1.4 Electron distribution

The magnetic moment of each C atom is reported by Mulliken population analysis in the output file. The magnetic moments are mainly distributed in the four C atoms (C33, C34, C37 and C49) around the vacancy, as listed in Table 4.3. To visualize this distribution, in Figure 4.6, a plane along the (100) direction was defined as a window to observe the spin density of the C atoms around the vacancy. Considering that BS1 and BS2 give very similar results, only the spin-density maps using BS1 are shown here.

Table 4.3. Total (α + β) and spin (α - β) distribution of the four C atoms around the vacancy in a S_{64} supercell, (unit $|e|$).

	BS1						BS2					
	$S=0$		$S=1$		$S=2$		$S=0$		$S=1$		$S=2$	
	α + β	α - β	α + β	α - β	α + β	α - β	α + β	α - β	α + β	α - β	α + β	α - β
C33	5.830	0.780	5.820	-0.482	5.797	0.978	6.032	0.687	5.998	-0.410	6.029	0.890
C34	5.830	0.780	5.837	0.816	5.797	0.978	6.032	0.687	6.045	0.736	6.029	0.890
C37	5.831	-0.781	5.837	0.816	5.797	0.978	6.032	-0.687	6.045	0.736	6.029	0.890
C49	5.831	-0.781	5.837	0.816	5.797	0.978	6.032	-0.687	6.045	0.736	6.029	0.890

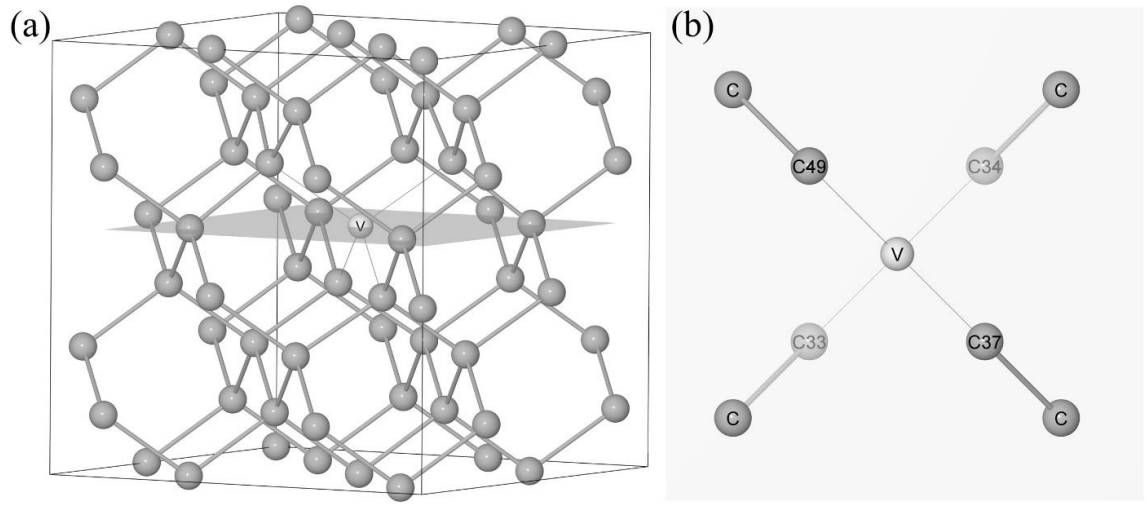

Figure 4.6. (a) The square plane as a window for plotting the spin-density map and (b) the enlarged plan view. C33 and C34 are below the plane whereas C37 and C49 are above the plane.

As shown in Figure 4.7, the spin-density maps agree very well with the result of the Mulliken population analysis in Table 4.3. For different spin settings, there are various numbers of C atoms with spin-up and spin-down electrons. The magnetic moment is mainly distributed in C33, C34, C37 and C49. Other C atoms far from the vacancy also exhibit small magnetic moments, but with increasing distance from the vacancy, the effect becomes very weak, as illustrated by the colour-map in Figure 4.7 (b)-(d). As a reference, in a perfect diamond, spin is zero everywhere.

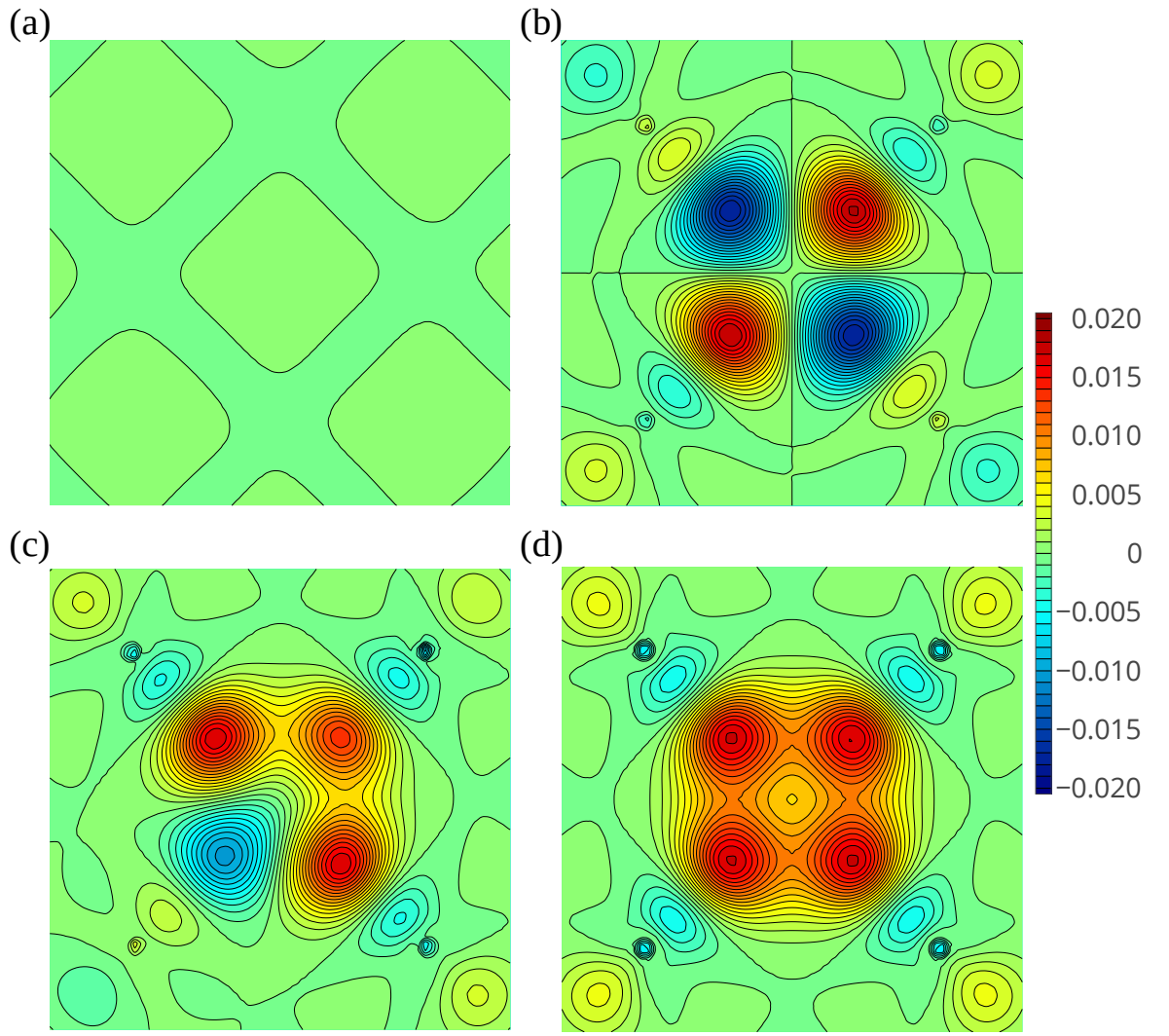

Figure 4.7. Spin (α - β) density maps of the C atoms of (a) perfect diamond, and of defect structures around a vacancy site with spin (b) $S = 0$, (c) $S = 1$ and (d) $S = 2$. Positions of the four neighbouring C atoms are marked in Figure 4.6(b). The isolines are in the range from -0.020 to 0.020 e Å^{-3}, with a step of 0.001 e Å^{-3}.

4.3.2 Substitutional doping of Be

4.3.2.1 Geometry structures

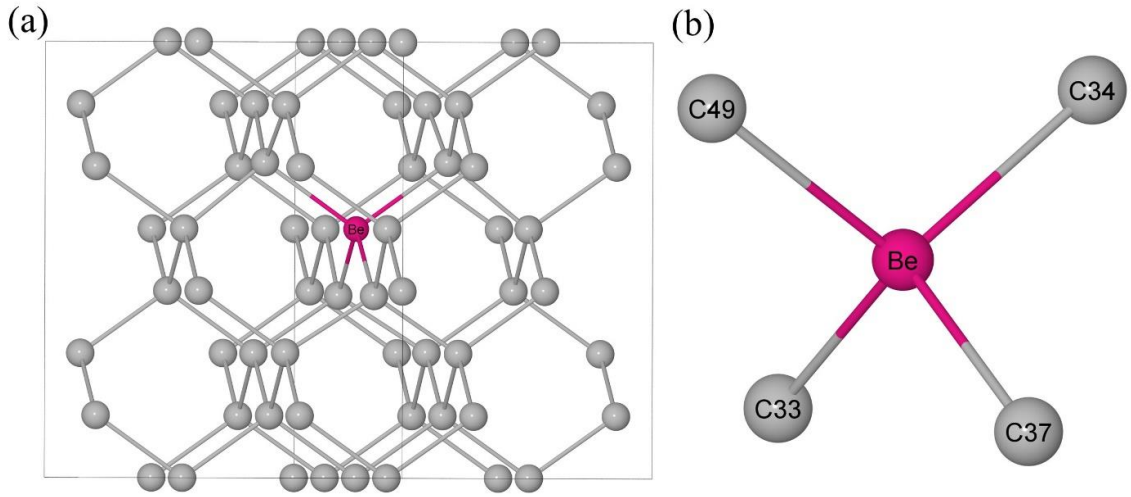

Figure 4.8. (a) Be_s in S_{64} diamond supercell and (b) the enlarged view.

Be was introduced into the S_{64} supercell substitutionally (to form a defect we have named Be_s) and the structure is shown in Figure 4.8. The optimised structures using different basis sets and spin settings are summarized in Table 4.4 and Table 4.5. The same symmetrical structures and stability order are obtained for the two carbon basis sets. $S = 1$ is the ground state, which is more stable than the $S = 0$ state by 0.13 eV (BS1) or 0.12 eV (BS2). $S = 2$ is the least stable state, having energies of 5.85 eV (BS1) or 5.88 eV (BS2) higher than that of $S = 1$. Therefore, only the $S = 1$ and $S = 0$ states are discussed in detail.

Table 4.4. Bond lengths (Å) from Be to the nearest C atoms in the Be_s structure using the 2 carbon basis sets.

	BS1			BS2		
	$S = 0$	$S = 1$	$S = 2$	$S = 0$	$S = 1$	$S = 2$
C33-Be	1.669	1.584	1.701	1.671	1.587	1.704
C34-Be	1.669	1.704	1.697	1.671	1.706	1.699
C37-Be	1.669	1.704	1.697	1.672	1.706	1.699
C49-Be	1.669	1.704	1.697	1.672	1.706	1.699

Table 4.5. Total (α + β) and spin (α - β) distribution of the four C atoms around Be in the S_{64} supercell, (unit $|e|$).

	BS1						BS2					
	$S=0$		$S=1$		$S=2$		$S=0$		$S=1$		$S=2$	
	α + β	α - β	α + β	α - β	α + β	α - β	α + β	α - β	α + β	α - β	α + β	α - β
Be	3.116	0.000	3.169	0.193	3.226	0.361	4.147	0.000	4.147	0.300	4.120	0.534
C33	6.209	0.342	6.335	-0.023	6.158	0.440	6.000	0.265	6.043	0.003	5.987	0.362
C34	6.209	0.342	6.160	0.443	6.152	0.442	6.000	0.265	5.984	0.359	5.985	0.398
C37	6.209	-0.342	6.160	0.443	6.152	0.442	6.000	-0.265	5.984	0.359	5.985	0.398
C49	6.209	-0.342	6.160	0.443	6.152	0.442	6.000	-0.265	5.984	0.359	5.985	0.398

For the $S=1$ state, after geometry optimisation, the structure of the Be-doped S_{64} system changed from original tetrahedral (T_d) to trigonal (C_{3v}) symmetry. Compared with the original C-C bond length, three Be-C bonds (Be-C34, Be-C37 and Be-C49) increased to 1.704 Å (BS1) and 1.706 Å (BS2), while the Be-C33 bonds increased to 1.584 Å (BS1) and 1.587 Å (BS2). For BS1, due to its large number of atomic orbitals, Mulliken population analysis showed that C33, C34, C37 and C49 have negative net charges of -0.335, -0.160, -0.160 and -0.160 $|e|$, respectively, while Be has a net charge of 0.831 $|e|$, indicating that approximately one Be outer-shell electron enters the orbitals of its neighbouring C atoms. Due to the fewer number of orbitals BS2, this electron distribution does not occur when it is used, and so almost all the C atoms show a neutral charge state.

The $S=0$ spin state results in a T_d symmetry structure and different electron distribution compared with that of $S=1$. For the BS1, Be shows a positive net charge (0.884 $|e|$) while its neighbouring C atoms show negative net charge (-0.209 $|e|$). For BS2, the corresponding values are -0.147 $|e|$ for Be and zero charge for the neighbouring C atoms.

4.3.2.2 Band structures and density of states

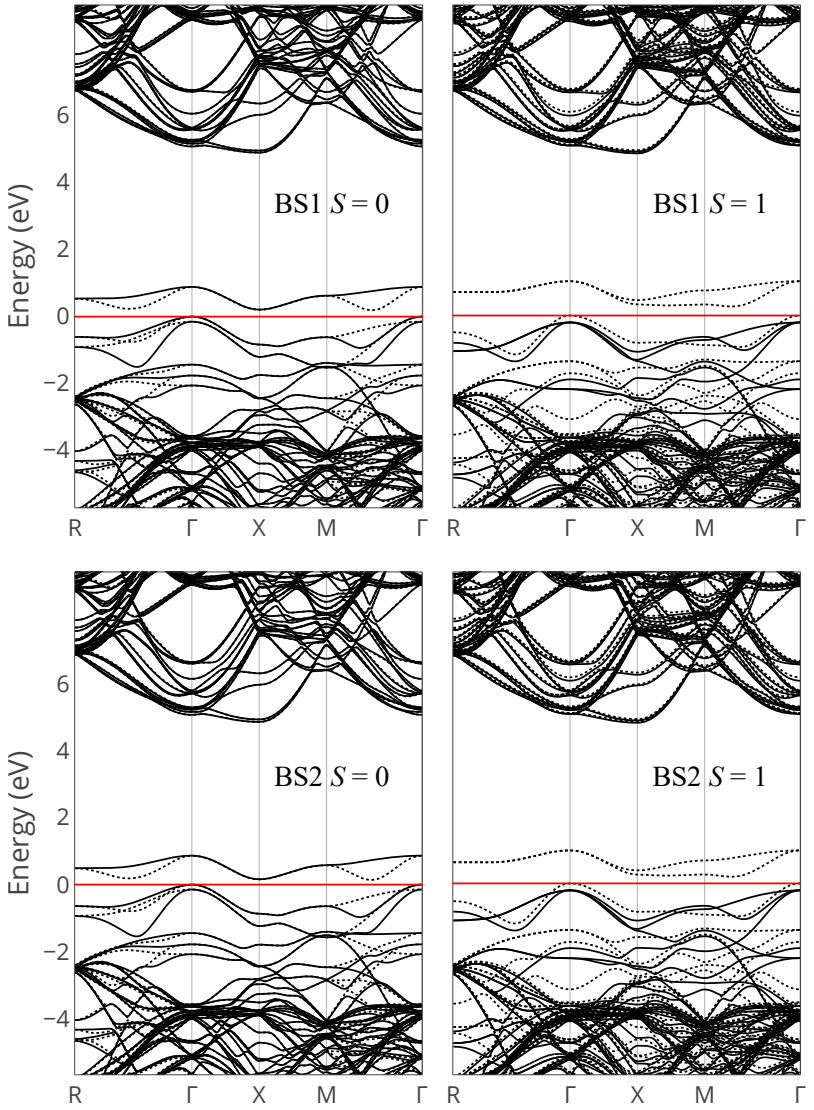

Figure 4.9. Band structures of the S_{64} supercell with Be_s defect using BS1 and BS2 with spins of $S = 0$ and 1, respectively.

The band structure of the Be_s defect system in the S_{64} supercell is shown in Figure 4.9. BS1 and BS2 give very similar results. Compared with the band structure of perfect diamond (see Figure 4.4), the Be_s defect introduces more bands above the valence band maximum (VBM). In the valence bands, some atomic orbitals split between α and ß electrons, with a splitting energy of ~1 eV. For the $S = 0$ state, one empty spin-up band and one empty spin-down band appear above the VBM, resulting in an indirect band gap of 0.17 eV (BS1) and 0.12 eV (BS2). For the $S = 1$ state there are two empty spin-down levels introduced above the valence band,

resulting in α and ß band gaps of 5.04 and 0.21 eV for BS1, and 4.99 and 0.14 eV for BS2. This indicates that there are two electrons only occupying spin-up levels while the corresponding spin-down levels remain unoccupied, resulting in a 2 μB net magnetic moment, which agrees well with Mulliken population analysis.

Compared with the band structures of diamond with a single vacancy, addition of Be has introduced more bands into the valence band. The introduction of Be also stabilised the single-vacancy structure by reducing the overall energy of the system. Compared with pure diamond, the Be_s defect introduced acceptor levels just above the valence band, resulting in a small gap between the VBM and the acceptor level. The Fermi level lies just above the valence band, suggesting that the Be_s defect works as an acceptor and makes diamond show p-type semiconductivity.

4.3.2.3 Electron distribution

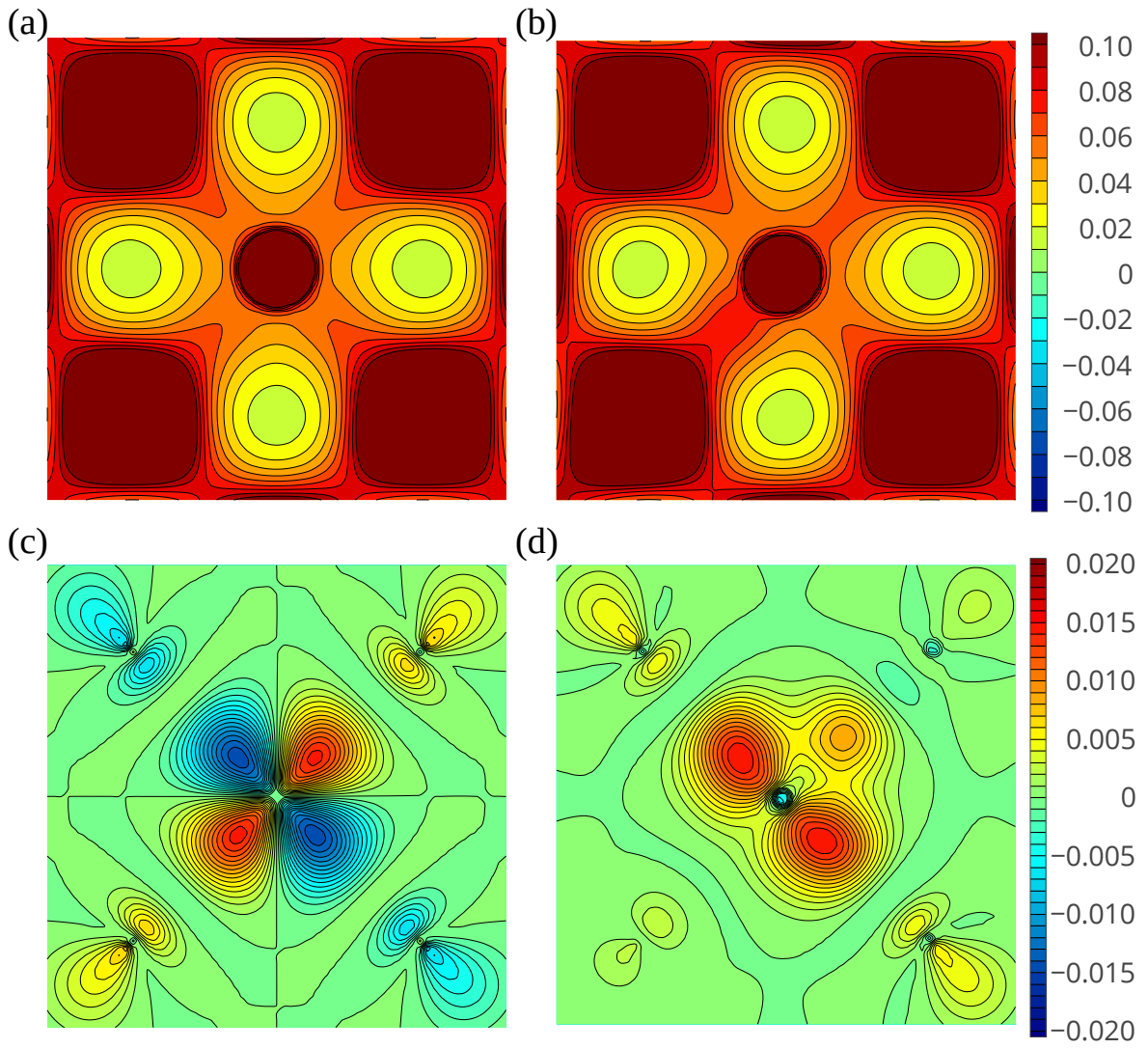

Figure 4.10. Total (α + β) and spin (α - β) density maps of the neighbouring C atoms of the S_{64} with Be_s in $S = 0$ (left) and $S = 1$ (right) states using BS1. For total density maps, the isolines are in the range from -0.1 to 0.1 e Å^{-3}, with a step of 0.01 e Å^{-3}. For spin-density maps, the isolines are in the range from -0.02 to 0.02 e Å^{-3}, with a step of 0.001 e Å^{-3}.

To visualize the electron distribution around the Be defect site, using the same window defined in the vacancy calculation (Figure 4.6), the total and spin-density maps of the Be_s structure are plotted in Figure 4.10. The distribution of spin directions agrees with the spin distribution in Table 4.5. For the $S = 0$ state, positive and negative spins are distributed symmetrically between the four neighbouring C atoms and cancelled each other, resulting in a total spin of zero. For the $S = 1$ ground state, the spin is mainly located at Be, C34, C37 and C49.

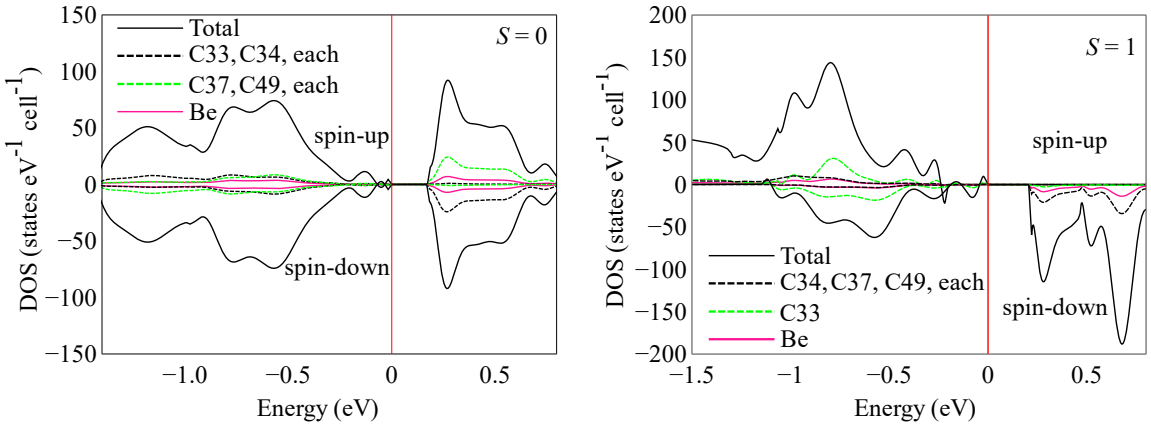

Figure 4.11. Projected DOS of the Be_s structure around the Fermi level calculated using BS1. Red lines represent the Fermi level while continuous and dotted lines represent spin-up and spin-down bands, respectively.

To determine the energy distribution around the Fermi level, the corresponding density of states (DOS) of Be and the surrounding carbon atoms are plotted in Figure 4.11. The DOS map for $S = 0$ indicates that the acceptor level mainly results from the carbon atoms around Be, *i.e.*, C33, C34, C37 and C49. For the $S = 1$ state, the two unoccupied spin-down orbitals above the Fermi level are mainly distributed on Be, C34, C37 and C39. According to the result of Mulliken population analysis, in the defect system, the difference between α and β electrons is mainly located at Be (0.193 $|e|$), C34 (0.443 $|e|$), C37 (0.443 $|e|$) and C49 (0.443 $|e|$). Therefore, the unoccupied spin-down orbitals around the Fermi level are probably mainly situated on Be, C34, C37 and C49, which is consistent with the DOS map in Figure 4.11.

4.3.2.4 Defect formation energies

E_f of the single substitutional defect Be_s was calculated according to Equation 5.1. The chemical potential of Be has a value that depends upon which chemical form the Be is in before it is incorporated into the diamond. According to experimental reports, Be can be incorporated into diamond by using Be metal as the dopant source during CVD [8] or by ion implantation of Be [7]. Therefore, in the first case, chemical potential of Be atom was determined using Be metal, *i.e.*, a hexagonal closed-packed (HCP) Be crystal as a reference. The formation energy calculated

from this value was denoted as $E_{f(1)}$. In the second case, chemical potential of Be was that of an isolated Be atom, and the formation energy was denoted as $E_{f(2)}$. It is worth noting that the last form of Be before it is incorporated into diamond should always be atomic, even though when the Be metal is taken as the reference. Therefore, $E_{f(2)}$, *i.e.*, the formation energy calculated using the atomic reference is more realistic.

The calculated formation energies are listed in Table 4.6. Positive formation energies $E_{f(1)}$ ~ 6 eV were obtained if bulk Be metal was used as reference, while the formation energies decreased to ~ -3 eV if isolated Be atoms were used. This suggests that forming Be_s defects in diamond from a metal source of Be is unfavourable (endothermic), whilst doing so from atomic Be is exothermic and so more likely to succeed.

As discussed above, the Be_s defect could also form in a diamond structure that has existing vacancies. Therefore, we also calculated the formation energy of a Be_s defect in a S_{64} supercell containing a pre-existing single vacancy (see Table 4.7). In this case, the formation energies for metallic Be and atomic Be sources were both exothermic. Indeed, $E_{f(2)}$ ~ -10.5 eV which is extremely large, suggesting that implantation of atomic Be into diamond with pre-existing vacancies may be a facile method to fabricate Be_s defects.

Table 4.6. Formation energies (eV) of the Be_s defect in a perfect S_{64} supercell, calculated using the two carbon basis sets and regarding the Be as originating from (1) bulk Be metal or (2) isolated Be atoms.

	BS1		BS2	
	$E_{f(1)}$	$E_{f(2)}$	$E_{f(1)}$	$E_{f(2)}$
$S = 0$	6.06	-2.86	5.97	-2.95
$S = 1$	5.94	-2.98	5.85	-3.07

Table 4.7. Formation energies (eV) of the Be_s defect in a S_{64} supercell containing a pre-existing single vacancy, calculated using the two carbon basis sets and regarding the Be as originating from (1) bulk Be metal or (2) isolated Be atoms.

	BS1		BS2	
	$E_{f(1)}$	$E_{f(2)}$	$E_{f(1)}$	$E_{f(2)}$
$S = 0$	-1.05	-9.98	-1.41	-10.33
$S = 1$	-1.30	-10.22	-1.64	-10.57

4.3.2.5 The effect of doping concentration

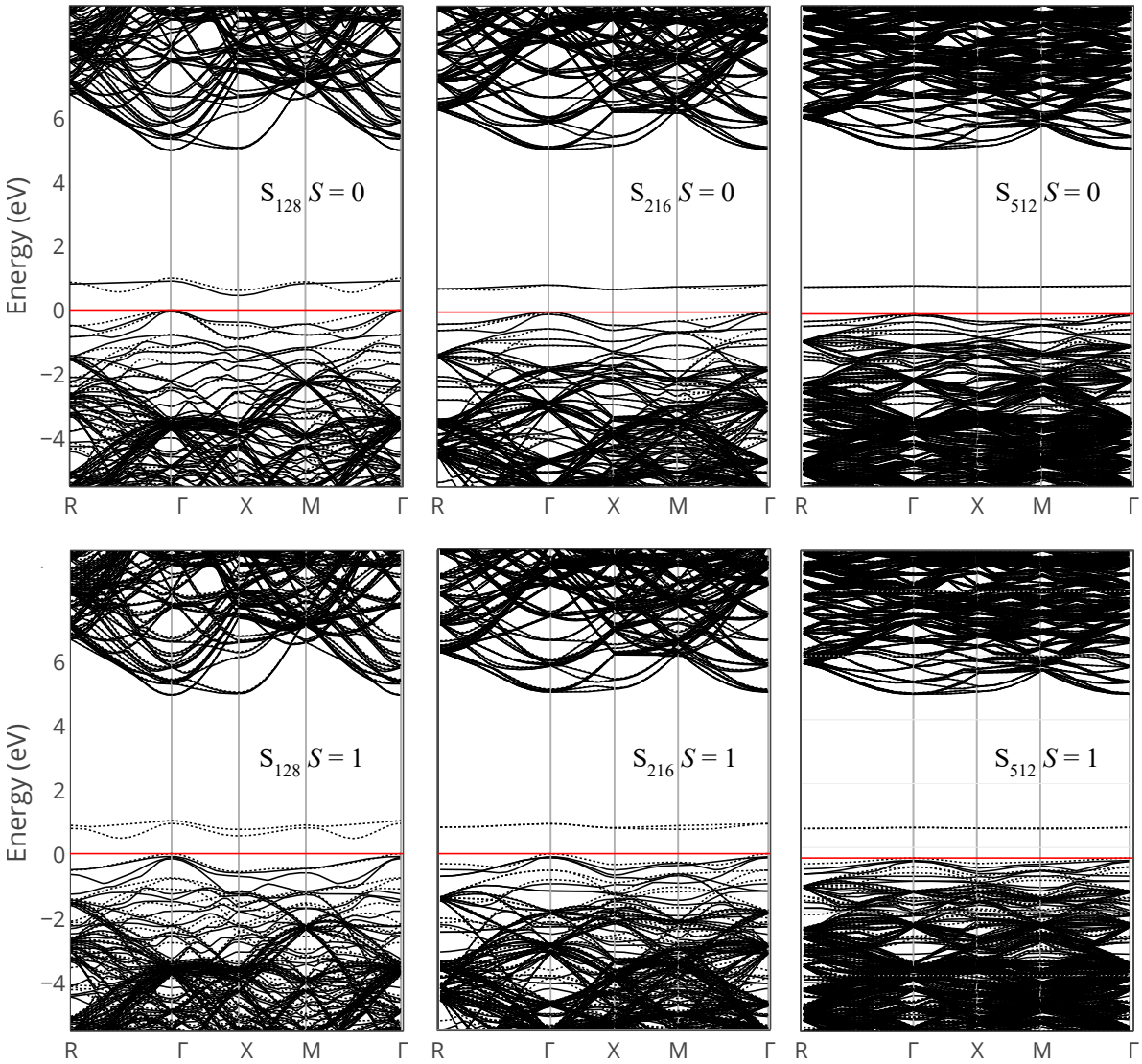

Figure 4.12. Band structures of S_{128}, S_{216} and S_{512} supercells containing a Be_s defect, calculated using the BS2.

To investigate the influence of doping concentration, Be_s was added into the S_{128}, S_{216} and S_{512} supercells, corresponding to doping concentrations of 1.4×10^{21}, 8.1×10^{20} and 3.4×10^{20} atoms cm^{-3}, respectively. Due to the high computational cost of using BS1, only BS2 was employed to do these calculations. Band structures of the S_{128}, S_{216} and S_{512} supercells with a Be_s defect are shown in Figure 4.12. With increasing the supercell size, the energy gap from VBM to the acceptor level (*i.e.*, $E - E_{\mathrm{VBM}}$) increases from ~0.1 to ~0.9 eV (see Figure 4.13). Because of the disadvantage that DFT method cannot predict band gap accurately (5.29 eV, compared with the experimental value of 5.47 eV), and the unrealistically high defect concentration in simulation which causes the strong defect-defect interactions [24], the acceptor energy level obtained from the band structure is not accurate enough. Therefore, EMM was also employed to predict the electronic level. As shown in Figure 4.13, the acceptor levels of Be_s defect calculated by EMM in different-size supercells are very close, with excitation energies of ~1.08 and ~1.20 eV obtained for the S=0 and S=1 states. Moreover, with the increase of the supercell size, the difference of electronic levels calculated by band structure and EMM becomes smaller. More reliable electronic levels can be obtained in larger supercells (*e.g.*, 1000 atoms), but the computational cost will be extremely high. Nevertheless, the excitation energies indicate that the Be_s defect in diamond is a deep acceptor, which is hardly useful at room temperature.

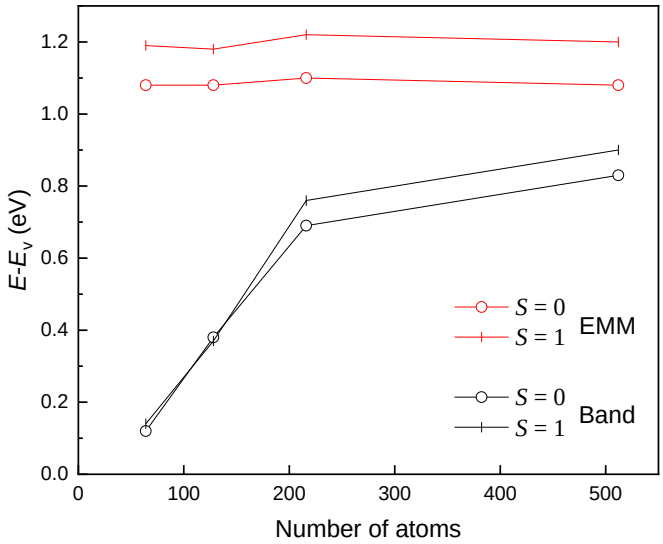

Figure 4.13. Acceptor levels of Be_s defect in different-size supercells, obtained from band structures (black line) and by EMM (red line).

4.3.2.6 Magnetic ordering

As discussed above, when Be was introduced into a substitutional site of diamond, a magnetic moment of 2 μB was obtained in the S_{64} supercell. In a real situation, a diamond crystal with Be_s defects can be regarded as a large supercell containing many Be_s defects and the interaction between these defects cannot be neglected. If these defects line up in the same magnetic direction, the structure will be ferromagnetic (FM). If their magnetic directions are opposite to each other, the magnetism with cancel out, leading to an antiferromagnetic (AFM) state.

A simple method to determine whether FM or AFM configuration is more likely to occur is by calculating and comparing the total energies of FM and AFM configurations of a larger supercell containing two defects. By calculating the energy difference between the FM and AFM states, their relative stability can be determined. This method has been used previously for investigating the magnetic properties of impurity-doped diamond [41-44] and other materials such as ZnO [45].

Two Be_s defects were introduced in the S_{128} supercell built using BS1, allowing both FM and AFM states. The two Be_s defects were placed a distance of 7.09 Å apart, which is believed to be an effective distance for simulating the magnetic interaction within diamond [41]. It is worth noting that in a real crystal, the distribution of the defects will be much more complicated (*e.g.*, the distances between the defects can vary and their concentration non-uniform), nevertheless this simplified model is sufficient to predict the relative stability between FM and AFM states.

The FM configuration was set up first, and the total energy of the system was calculated. To set up the AFM configuration, the spin direction of one of the Be defects was reversed by editing the spin state using the keyword SPINEDIT [20]. The relative stability between the two states ($\Delta E = E_{\mathrm{FM}} - E_{\mathrm{AFM}}$) was then calculated. Since ΔE is usually small, any geometry variation between the FM and AFM states may influence the energy difference [41]. To make sure the energy difference arises from the difference between the magnetic ordering rather than the geometry variation, the FM and AFM energy calculations were carried out

using exactly the same geometry built from the optimised lattice parameter (3.5470 Å) without further geometry optimisation. The results from this calculation predicted that the AFM state is more stable than the FM state by 28 meV.

4.3.3 Interstitial doping

4.3.3.1 Tetrahedral site

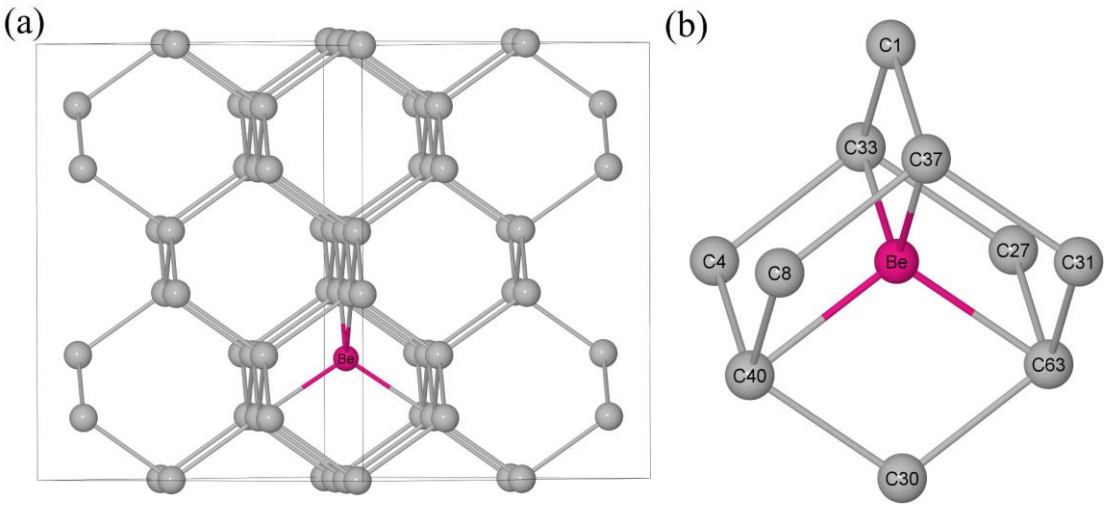

Figure 4.14. (a) $Be_{i,tet}$ in a S_{64} supercell and (b) an enlarged view of $Be_{i,tet}$ with its neighbouring C atoms.

The structure of the interstitial Be-doped diamond at a tetrahedral site (denoted $Be_{i,tet}$) is shown in Figure 4.14. After geometry optimisation, the distances from Be to its nearest C atoms are summarised in Table 4.8. The relaxed structure has C_{3v} symmetry, such that one of the C-Be distances is slightly longer than the other three. All the C-Be distances have become longer compared with the C-Be lengths of 1.536 Å (BS1) and 1.543 Å (BS2) before geometry optimisation. For diamond with an interstitial Be defect, we did not observe any magnetisation effect, and the spin remained zero.

The band structures of the S_{64} supercell with a $Be_{i,tet}$ defect are plotted in Figure 4.15. Fermi level lies within the conduction band but is close to the CBM. To simulate the defect at lower concentration, S_{128} and S_{216} supercells with a $Be_{i,tet}$ defect were calculated, with the band structures shown in Figure 4.16. Since the

band structures cannot show the exact energy level of shallow donor, EMM was employed to do this, and $E_c - 0.38$, $E_c - 0.42$ and $E_c - 0.47$ eV were predicted in S_{64}, S_{128} and S_{216} supercells, indicating the $Be_{i,tet}$ defect works as a shallow donor in diamond. However, this defect structure is metastable and a denser k-point grid (4×4×4) had to be employed for S_{216} in order to get the optimised structure, otherwise it will drift toward an "off-centre" structure with deep donor state. The denser k-point grid in large supercell (*e.g.*, S_{512}) makes the calculation extremely expensive. Therefore, only S_{64}, S_{128} and S_{216} were modelled for the $Be_{i,tet}$ defect.

Table 4.8. Distance (Å) from $Be_{i,tet}$ to the nearest C atoms calculated using both carbon basis sets.

	BS1	BS2
C33-Be	1.620	1.626
C37-Be	1.628	1.635
C40-Be	1.620	1.626
C63-Be	1.620	1.626

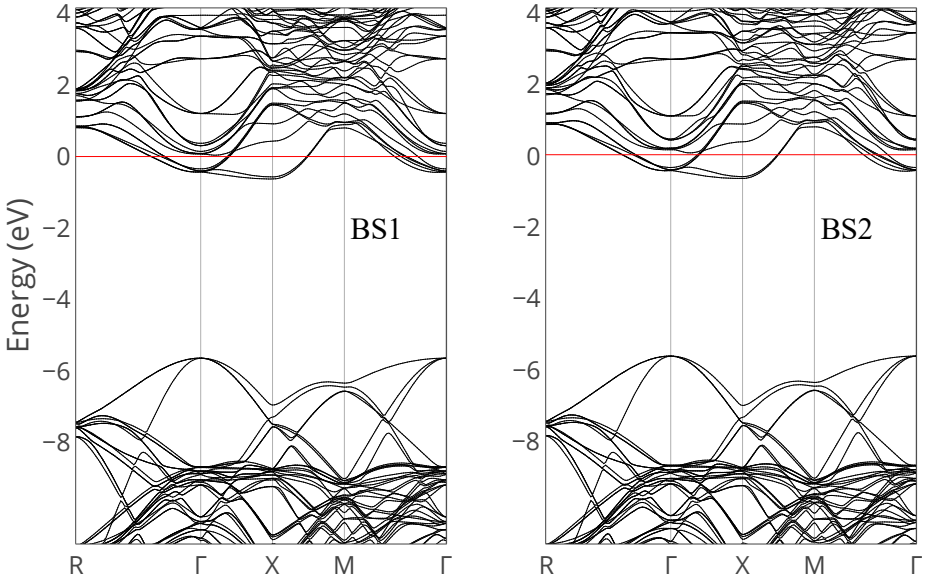

Figure 4.15. Band structures of a S_{64} supercell with a $Be_{i,tet}$ defect calculated using BS1 and BS2.

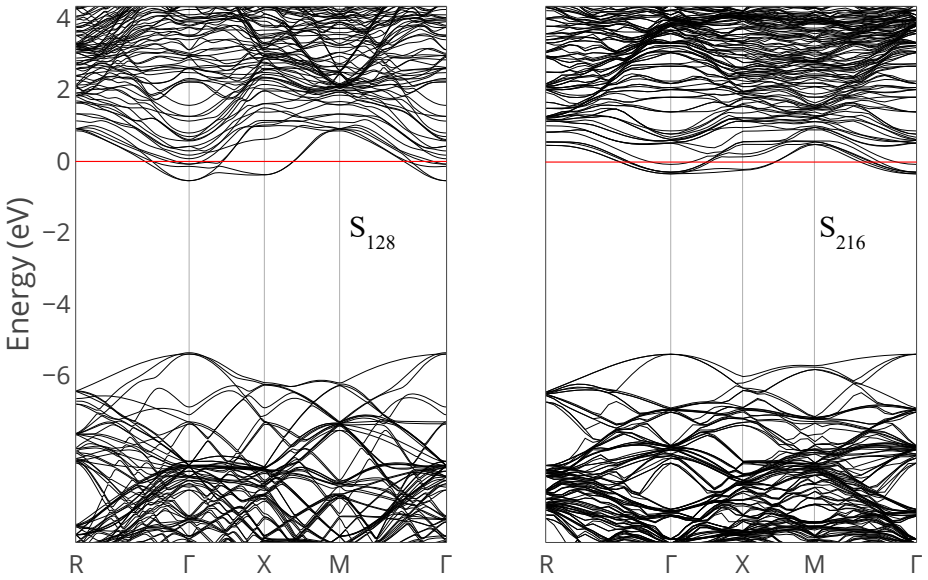

Figure 4.16. Band structures of S_{128} and S_{216} supercells with a $Be_{i,tet}$ defect calculated using BS2.

4.3.3.2 Hexagonal site

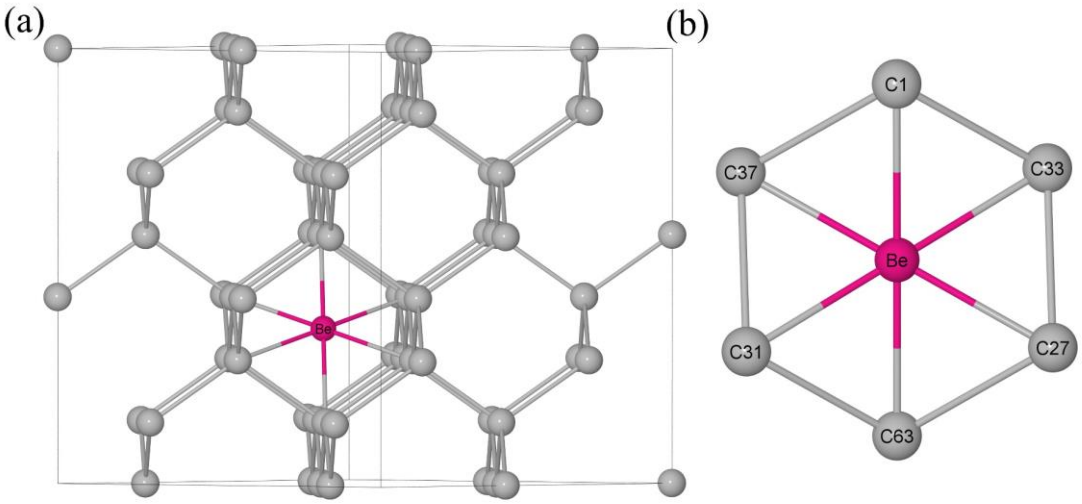

Figure 4.17. (a) The $Be_{i,hex}$ defect site in a S_{64} supercell and (b) an enlarged view of Be with its neighbouring C atoms.

Table 4.9. Bond lengths (Å) from $Be_{i,hex}$ to the nearest C atoms.

	BS1	BS2
C1-Be	1.570	1.575
C33-Be	1.570	1.575
C27-Be	1.570	1.575
C63-Be	1.570	1.575
C31-Be	1.570	1.575
C37-Be	1.570	1.575

For the defect system with interstitial Be at a hexagonal site (denoted $Be_{i,hex}$), the distances from Be to the nearest C atoms (Figure 4.17) are listed in Table 4.9. C-Be lengths increased to 1.570 Å (BS1) and 1.575 Å (BS2) compared with the original lengths 1.470 and 1.477 Å, respectively. Calculations also show that the S_{64} supercell with a $Be_{i,hex}$ defect is more stable than that with a $Be_{i,tet}$ defect by 0.50 eV (BS1) or 0.72 eV (BS2), although it remains extremely endothermic (see Table 4.11).

The band structure of a S_{64} supercell with a $Be_{i,hex}$ defect is shown in Figure 4.18. A Be donor level is introduced 0.25 eV (BS1) or 0.33 eV (BS2) below the conduction band minimum (CBM) of diamond, indicating n-type semiconductivity. To study the influence of doping concentration and determine the donor level, S_{128}, S_{216} and S_{512} supercells with a $Be_{i,hex}$ defect were calculated, with the band structures shown in Figure 4.19. With the increase of supercell size (*i.e.*, the decrease of doping concentration), the energy gap from the donor level to CBM increases from 0.33 to 1.05 eV. The donor level was also calculated by EMM in different-size supercells. As shown in Figure 4.20, with the increase of supercell size, the excitation energies increased from ~1.2 to ~1.3 eV. Therefore, the $Be_{i,hex}$ defect is a deep donor in diamond.

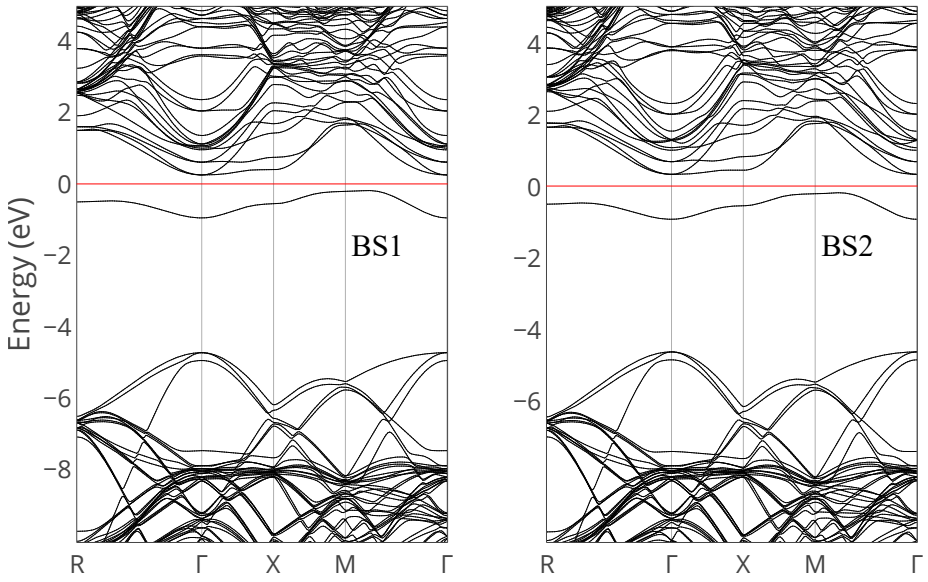

Figure 4.18. Band structures of S_{64} supercell with a $Be_{i,hex}$ defect using BS1 and BS2.

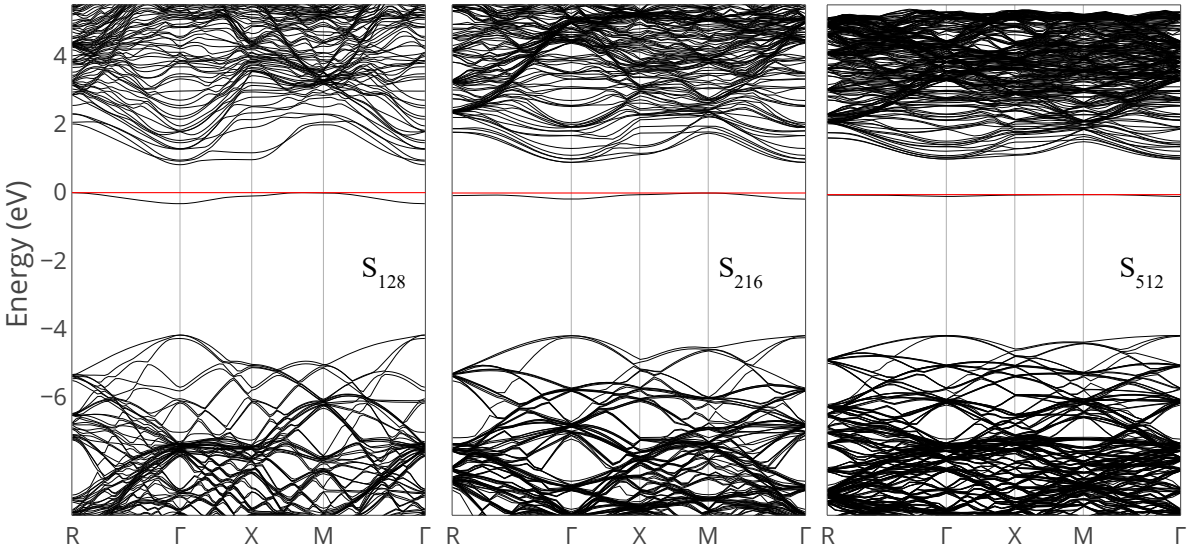

Figure 4.19. Band structures of S_{128}, S_{216} and S_{512} supercells with a $Be_{i,hex}$ defect using BS2.

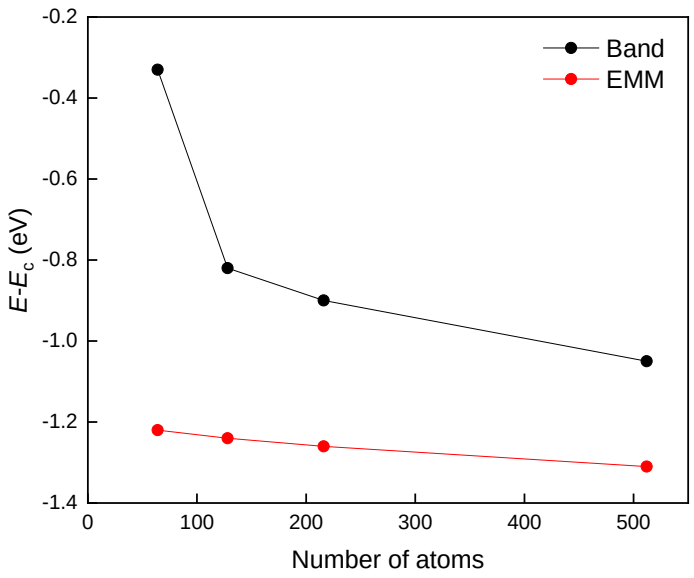

Figure 4.20. Donor levels of $Be_{i,hex}$ defect in different-size supercells, obtained from band structures (black line) and by EMM (red line).

4.3.3.3 Off-centre site

By placing the Be slightly off the tetrahedral or hexagonal position, a same new interstitial structure was obtained following geometry optimisation. This off-centre structure, labelled $Be_{i,oc}$, is compared with that of pristine diamond in Figure 4.21. Distances from the Be to the neighbouring C atoms are given in Table 4.10. Compared with pristine diamond, after geometry optimisation C1 and C33 are separated by the Be atom, and the distance from C1 to C33 has increased from 1.536 to 2.333 Å. The total density map in the defect area (Figure 4.22) indicates that Be has formed new bonds with C1 and C33, with lengths of 1.532 and 1.478 Å, respectively.

Table 4.10. Bond length (Å) from $Be_{i,oc}$ to the nearest C atoms in a S_{64} supercell calculated using the two carbon basis sets.

	BS1	BS2
C1-Be	1.532	1.535
C33-Be	1.478	1.482

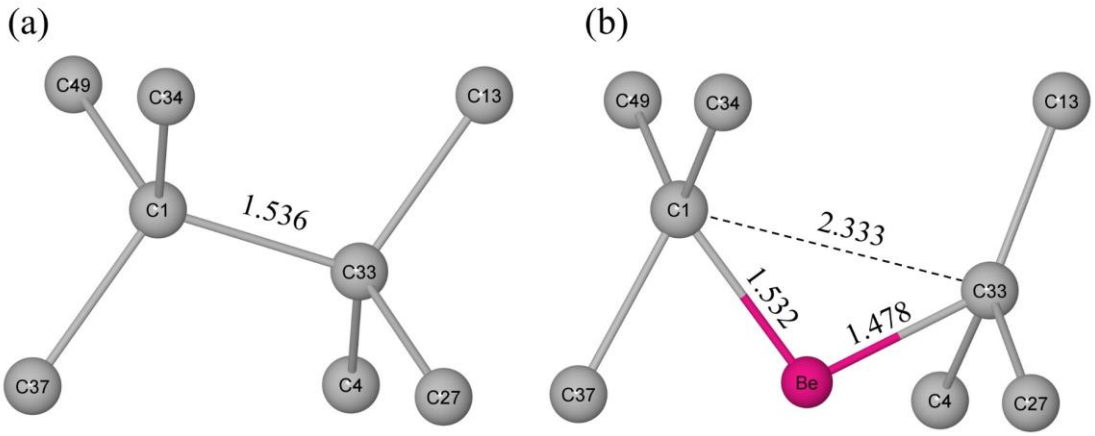

Figure 4.21. Comparison between (a) a perfect diamond structure and (b) an optimised structure of the $Be_{i,oc}$ defect, calculated using BS1. Distances are in Å.

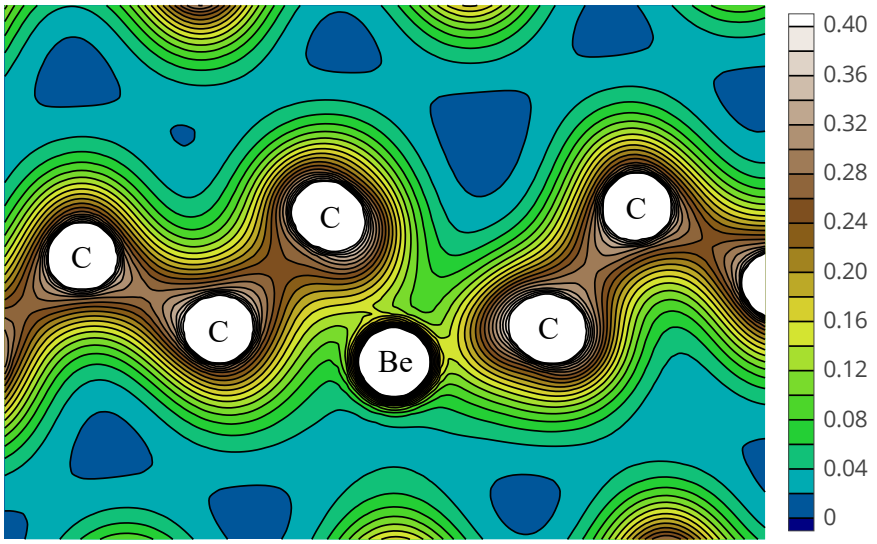

Figure 4.22. Total density map of diamond with the $Be_{i,oc}$ defect. The isolines are in the range 0 – 0.4 e Å^{-3} with a step of 0.02 e Å^{-3}.

Band structures of the $Be_{i,oc}$ defect structure are shown in Figure 4.23. A new donor level has been introduced in the middle of the band gap of the original diamond, resulting in a deep donor level 2.30 eV (BS1) or 2.27 eV (BS2) below the CBM. Therefore, the $Be_{i,oc}$ defect also makes diamond n-type, but with a donor level too deep to be electronically useful. A DOS map around the Fermi level is projected onto Be and its neighbour C atoms. As plotted in Figure 4.24, the defect level is mainly distributed in C1 and C33.

The $Be_{i,oc}$ defect is more stable than $Be_{i,hex}$ by ~ 2.5 eV (see Table 4.11), which would make it the ground state for interstitially Be-doped diamond. Nevertheless,

it is still endothermic with $E_{f(1)}$ ~ 11.5 eV and $E_{f(2)}$ ~ 2.5 eV, and 5.56 eV higher in energy than the Be_s defect.

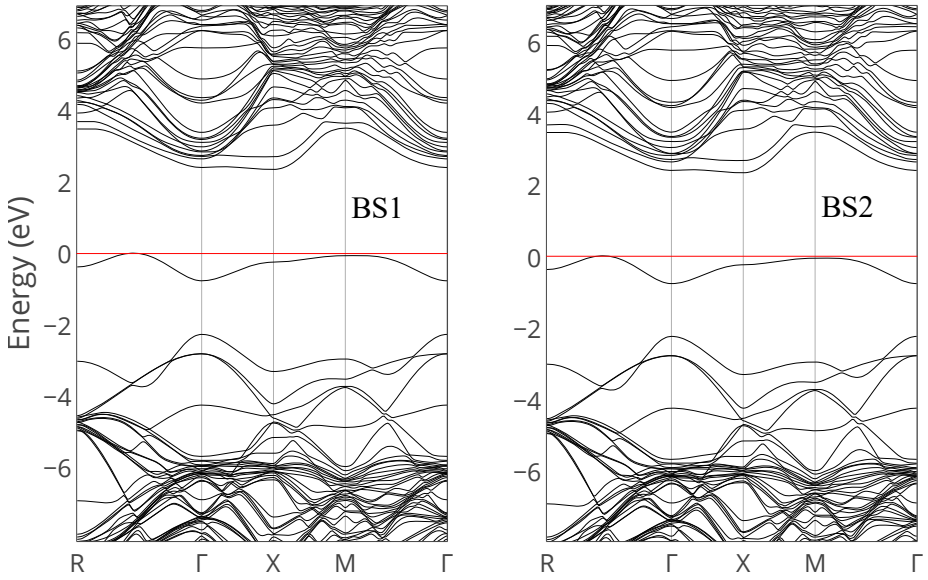

Figure 4.23. Band structures of the $Be_{i,oc}$ defect structure in S_{64} calculated using BS1 and BS2.

To study the influence of different doping concentrations on the electrical properties, the $Be_{i,oc}$ defect was calculated in S_{128}, S_{216} and S_{512} supercells using BS2. The band structures are shown in Figure 4.25. The change of donor level with increasing supercell size is given in Figure 4.26, and clearly shows that with increase of supercell size, the donor level becomes deeper. Donor levels of 2.27 – 2.87 eV were obtained from the band structures and 2.55 – 2.71 eV from EMM. The results indicate that the $Be_{i,oc}$ defect works as a very deep donor in diamond. Considering that larger supercells give better prediction for the energy level, the $Be_{i,oc}$ defect may have a very deep donor level of ~ 3 eV at lower doping concentrations.

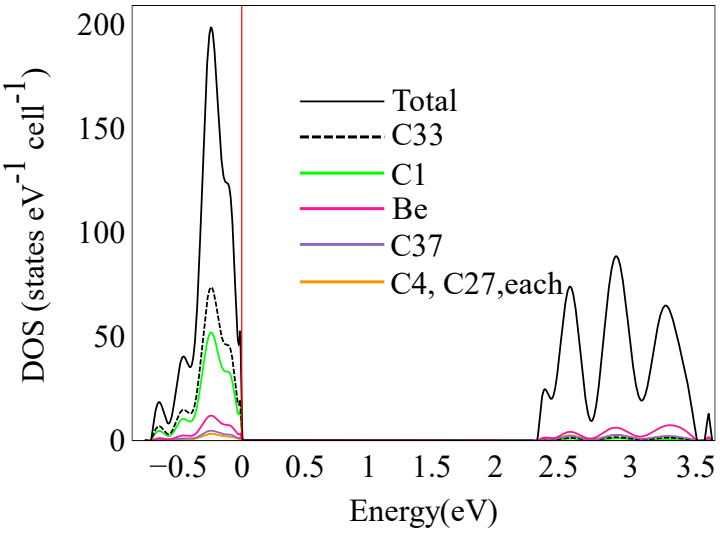

Figure 4.24. DOS map of the $Be_{i,oc}$ defect structure around the Fermi level calculated using BS1. The vertical red line represents the Fermi level.

Table 4.11. Formation energies (eV) of interstitially doped Be in diamond calculated using the two carbon basis sets and regarding the Be as originating from (1) bulk Be metal or (2) isolated Be atoms.

	BS1		BS2	
	$E_{f(1)}$	$E_{f(2)}$	$E_{f(1)}$	$E_{f(2)}$
$Be_{i,tet}$	14.63	5.71	14.57	5.64
$Be_{i,hex}$	14.13	5.21	13.84	4.92
$Be_{i,oc}$	11.50	2.58	11.43	2.51

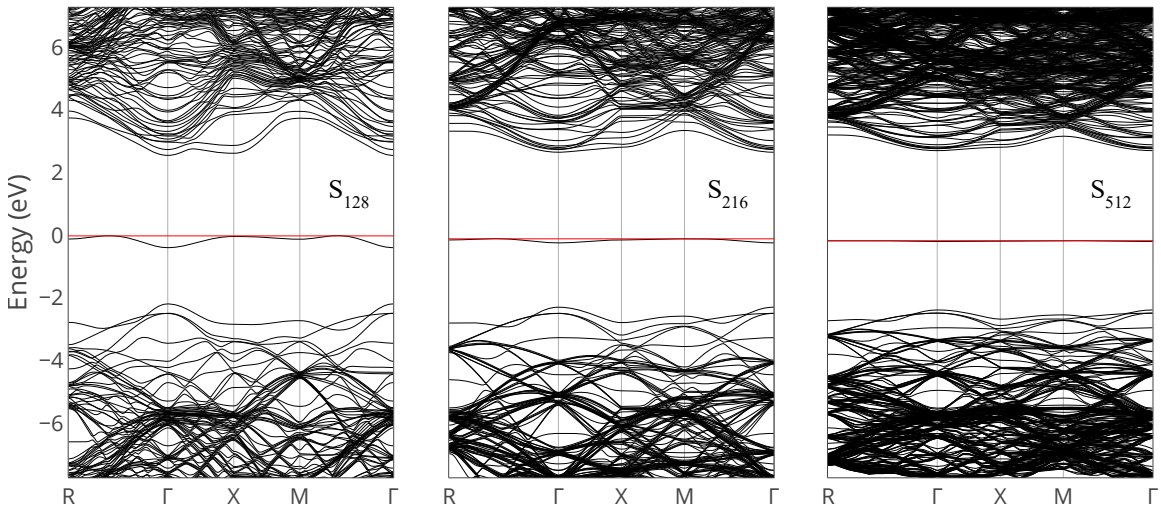

Figure 4.25. Band structures of diamond with the $Be_{i,oc}$ defect in S_{128}, S_{216} and S_{512} supercells calculated using BS2.

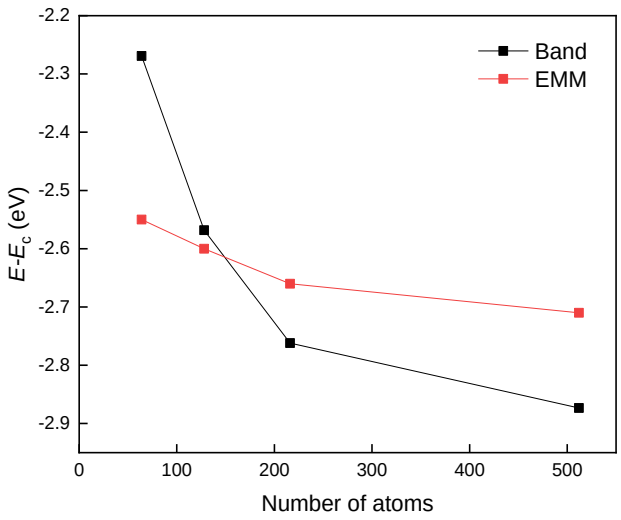

Figure 4.26. The donor level of $Be_{i,oc}$ defect in different-size supercells obtained from band structures and by EMM.

4.4 Conclusions

In this work, first-principles DFT calculations were carried using hybrid functional for Be-doped diamond. We studied the electrical and magnetic properties of Be-doped diamond by performing unrestricted open-shell calculations. To estimate the accuracy of the calculations, two carbon-atom basis sets were used, one (pob-TZVP-rev2) containing 18 orbitals but computationally slow and expensive, and the other (6-21G*) containing 14 orbitals but computationally much cheaper and faster to execute. Both basis sets gave very similar results and compared well with previously reported calculations on diamond systems. Band structures and the empirical marker method were employed to predict the electrical levels of the defects.

1) Diamond with Be in a substitutional site, Be_s, is predicted to exhibit p-type semiconductivity with an acceptor level 1.2 eV above the valence band maximum, which is hardly useful at room temperature. The $S = 1$ ground state is slightly more stable than the $S = 0$ state by ~ 0.1 eV. Magnetic moments resulting from the substitutional Be defects in the $S = 1$ state cancel each other in large supercells, leading to an antiferromagnetic system. The formation energy for this substitutional Be depends upon the initial state of the Be. If Be is taken as originating from metallic Be, the Be_s

formation energy is 7 eV higher than if the Be comes from atomic Be (as might be the case in implantation or CVD processes). For pristine diamond, incorporation of Be from a metallic source is endothermic (6 eV) but exothermic (-1 eV) from an atomic source. Thus, atomic sources of Be are far more likely to succeed as doping strategies. Indeed, the likelihood of successful incorporation can be improved further if the diamond already contains an existing vacancy, because the formation energies are highly exothermic in for both sources of Be (isolated atoms or crystal).

2) Three interstitial positions, one with tetrahedral symmetry, $Be_{i,tet}$, one with hexagonal symmetry, $Be_{i,hex}$, and one in an off-centre position were compared. The off-centre $Be_{i,oc}$ defect has not been reported before and is more stable than the $Be_{i,hex}$ and $Be_{i,tet}$ defects; however, all three interstitial defects have substantially higher formation energies than Be_s, suggesting they will be very difficult to produce. Diamond is predicted to show n-type semiconductivity when doped interstitially with Be. The tetrahedral $Be_{i,tet}$ defect is predicted to be a shallow donor, with a donor level 0.47 eV below the conduction band, whereas the other two defects are deep donors. The $Be_{i,hex}$ defect has a donor level 1.3 eV below the conduction band, and the $Be_{i,oc}$ defect has a very deep donor state 2.7 eV below the conduction band, almost midway in the band gap.

3) Although the three interstitial defects are predicted to show n-type semiconductivity, their extremely high formation energies mean that they will be difficult if not impossible to attain experimentally. Due to an exothermic formation energy, the substitutional defect Be_s is most likely to be formed in any experimental doping process, however, due to the deep acceptor level, it is unlikely to be useful for making room-temperature p-type semiconductors. Thus, it seems, n-type diamond with properties suitable for room-temperature electronics remains elusive.

4.5 References

[1] W.M. Haynes, W.M. Haynes, D.R. Lide, T.J. Bruno, CRC handbook of chemistry and physics: a ready-reference book of chemical and physical data, Ninety-seven edition. ed., CRC Press, Boca Raton, Florida, 2017.

[2] N. Lund, C. Budtz-Jorgensen, N.J. Westergaard, et al., JEM-X: The X-ray monitor aboard INTEGRAL, Astron Astrophys 411 (2003) L231-L238.

[3] H.-k. Mao, J. Shu, G. Shen, et al., Elasticity and rheology of iron above 220 GPa and the nature of the Earth's inner core, Nature 396 (1998) 741-743.

[4] W.F. McDonough, S.s. Sun, The composition of the Earth, Chem. Geol. 120 (1995) 223-253.

[5] T.P. Taylor, M. Ding, D.S. Ehler, et al., Beryllium in the Environment: A Review, J. Environ. Sci. Health A 38 (2003) 439-469.

[6] S.A. Catledge, Y.K. Vohra, Interfacial oxide and carbide phases in the deposition of diamond films on beryllium metal, Diam. Relat. Mater. 9 (2000) 1327-1330.

[7] K. Ueda, A. Kasu, High-pressure and high-temperature annealing of diamond ion-implanted with various elements, Diam. Relat. Mater. 17 (2008) 1269-1272.

[8] K. Ueda, M. Kasu, Beryllium-doped single-crystal diamond grown by microwave plasma CVD, Diam. Relat. Mater. 18 (2009) 121-123.

[9] C.X. Yan, Y. Dai, B.B. Huang, et al., Shallow donors in diamond: Be and Mg, Comput. Mater. Sci. 44 (2009) 1286-1290.

[10] G. Sansone, A. Ferretti, L. Maschio, Ab initio electronic transport and thermoelectric properties of solids from full and range-separated hybrid functionals, J. Chem. Phys. 147 (2017) 6.

[11] R. Dovesi, A. Erba, R. Orlando, et al., Quantum-mechanical condensed matter simulations with CRYSTAL, Wiley Interdiscip. Rev. Comput. Mol. Sci. 8 (2018) 36.

[12] A.V. Krukau, O.A. Vydrov, A.F. Izmaylov, G.E. Scuseria, Influence of the exchange screening parameter on the performance of screened hybrid functionals, J. Chem. Phys. 125 (2006) 5.

[13] A.J. Garza, G.E. Scuseria, Predicting Band Gaps with Hybrid Density Functionals, J. Phys. Chem. Lett. 7 (2016) 4165-4170.

[14] D. Vilela Oliveira, J. Laun, M.F. Peintinger, T. Bredow, BSSE-correction scheme for consistent gaussian basis sets of double- and triple-zeta valence with polarization quality for solid-state calculations, J. Comput. Chem. 40 (2019) 2364-2376.

[15] M. Catti, A. Pavese, R. Dovesi, V.R. Saunders, Static lattice and electron properties of MgCO3 (magnesite) calculated by ab initio periodic Hartree-Fock methods, Phys. Rev. B 47 (1993) 9189-9198.

[16] M.F. Peintinger, D.V. Oliveira, T. Bredow, Consistent gaussian basis sets of Triple-Zeta valence with polarization quality for solid-State Calculations, J. Comput. Chem. 34 (2013) 451-459.

[17] A. Gruneich, B.A. Hess, Choosing GTO basis sets for periodic HF calculations, Theor. Chem. Acc. 100 (1998) 253-263.

[18] B. Soulé de Bas, H.E. Dorsett, M.J. Ford, The electronic structure of Be and BeO: benchmark EMS measurements and LCAO calculations, J. Phys. Chem. Solids 64 (2003) 495-505.

[19] H.J. Monkhorst, J.D. Pack, Special points for Brillouin-zone integrations, Phys. Rev. B 13 (1976) 5188-5192.

[20] R. Dovesi, V. Saunders, C. Roetti, et al., CRYSTAL17 User's Manual, 2017.

[21] T. Hom, W. Kiszenik, B. Post, Accurate lattice constants from multiple reflection measurements. II. Lattice constants of germanium silicon, and diamond, J. Appl. Crystallogr. 8 (1975) 457-458.

[22] W. Setyawan, S. Curtarolo, High-throughput electronic band structure calculations: Challenges and tools, Comput. Mater. Sci. 49 (2010) 299-312.

[23] J.P. Goss, M.J. Shaw, P.R. Briddon, Marker-Method Calculations for Electrical Levels Using Gaussian-Orbital Basis Sets, in: D.A. Drabold, S.K. Estreicher (Eds.), Theory of Defects in Semiconductors, Springer Berlin Heidelberg, Berlin, Heidelberg, 2007, pp. 69-94.

[24] J.P. Goss, P.R. Briddon, R. Jones, S. Sque, Donor and acceptor states in diamond, Diam. Relat. Mater. 13 (2004) 684-690.

[25] A. Croot, M.Z. Othman, S. Conejeros, et al., A theoretical study of substitutional boron-nitrogen clusters in diamond, J. Phys. Condens. Matter 30 (2018) 10.

[26] J. Goss, R. Eyre, P. Briddon, Bound substitutional impurity pairs in diamond: a density functional study, J. Phys. Condens. Matter 20 (2008) 085217.

[27] H. Yilmaz, B.R. Weiner, G. Morell, Formation of lithium clusters and their effects on conductivity in diamond: A density functional theory study, Diam. Relat. Mater. 16 (2007) 840-844.

[28] R.J. Eyre, J.P. Goss, P.R. Briddon, M.G. Wardle, Multi-impurity complexes for n-type diamond: a computational study, Phys. Status Solidi A 204 (2007) 2971-2977.

[29] J.P. Goss, P.R. Briddon, R.J. Eyre, Donor levels for selected n-type dopants in diamond: A computational study of the effect of supercell size, Phys. Rev. B 74 (2006) 245217.

[30] N. Fujimori, H. Nakahata, T. Imai, Properties of Boron-Doped Epitaxial Diamond Films, Jpn. J. Appl. Phys. 29 (1990) 824-827.

[31] G. Braunstein, R. Kalish, Effective p - type doping of diamond by boron ion implantation, J. Appl. Phys. 54 (1983) 2106-2108.

[32] S. Koizumi, T. Teraji, H. Kanda, Phosphorus-doped chemical vapor deposition of diamond, Diam. Relat. Mater. 9 (2000) 935-940.

[33] W. Banholzer, Understanding the mechanism of CVD diamond, Surf. Coat. Technol. 53 (1992) 1-12.

[34] Y. Bar-Yam, T.D. Moustakas, Defect-induced stabilization of diamond films, Nature 342 (1989) 786-787.

[35] C.A. Coulson, M.J. Kearsley, Colour centres in irradiated diamonds. I, Proc. R. Soc. Lond. A 241 (1957) 433-454.

[36] D.E.P. Vanpoucke, K. Haenen, Revisiting the neutral C-vacancy in diamond: Localization of electrons through DFT+U, Diam. Relat. Mater. 79 (2017) 60-69.

[37] A. Zelferino, S. Salustro, J. Baima, et al., The electronic states of the neutral vacancy in diamond: a quantum mechanical approach, Theor. Chem. Acc. 135 (2016) 74.

[38] D. Hyde-Volpe, B. Slepetz, M. Kertesz, The [V−C═C−V] Divacancy and the Interstitial Defect in Diamond: Vibrational Properties, J. Phys. Chem. C 114 (2010) 9563-9567.

[39] J. Shim, E.-K. Lee, Y.J. Lee, R.M. Nieminen, Density-functional calculations of defect formation energies using supercell methods: Defects in diamond, Phys. Rev. B 71 (2005) 035206.

[40] C.J.H. Wort, R.S. Balmer, Diamond as an electronic material, Mater. Today 11 (2008) 22-28.

[41] E.M. Benecha, E.B. Lombardi, First principles study of Fe in diamond: A diamond-based half metallic dilute magnetic semiconductor, J. Appl. Phys. 114 (2013) 8.

[42] H.X. Gao, J.B. Li, J.B. Xia, Origins of ferromagnetism in transition metal doped diamond, Physica B Condens. Matter 407 (2012) 2347-2350.

[43] E.M. Benecha, E.B. Lombardi, Cr in diamond: A first-principles study, Phys. Rev. B 84 (2011) 235201.

[44] E.B. Lombardi, Co in diamond: Ferromagnetic ordering of a transition metal in diamond, Diam. Relat. Mater. 17 (2008) 1345-1348.

[45] K. Osuch, E.B. Lombardi, W. Gebicki, First principles study of ferromagnetism in $Ti_{0.0625}Zn_{0.9375}O$, Phys. Rev. B 73 (2006) 075202.

CHAPTER 5

THEORETICAL STUDY OF Be-N CO-DOPED DIAMOND

Be-N co-doped diamond was studied by first-principles calculations in this chapter, with the aim of finding out if this doping scheme might be a useful n-type dopant at room temperature. Be and N atoms were placed at different positions in the diamond lattice and the geometric, thermodynamic and electronic properties of the Be-N clusters were studied. Results show that although neither Be nor N works as a shallow n-type dopant, they may facilitate the incorporation of each other, and more complex Be_sN_x clusters may form a shallow n-type semiconductivity.

5.1 Introduction

The co-doping strategy uses two or more complementary dopants to enhance the conductivity of a material. By introducing multiple different elements into diamond, the electrical behaviour, such as carrier mobility and activation energy, may be improved compared with that using a single dopant. Different co-doping schemes have been reported for diamond, such as H-P, H-S, B-Li, B-N, B-S and Li-N, which were introduced in section 1.5.

Our calculations in Chapter 4 predict that Be prefers the substitutional site in diamond and behaves as a p-type dopant when located at this position. In contrast, diamond shows n-type semiconductivity if doped by Be at an interstitial site; however, the interstitial defect is less stable than the substitutional one by ~ 5.5 eV, and the donor level is deep.

According to the literature, N is mainly located at a single substitutional site in diamond [1-4], which is known as the "C centre". This defect has a negative formation energy but also forms a deep donor in diamond, making it ineffective as an n-type semiconductor for most room temperature devices. To try to find a

system with shallower donor levels, several N-containing complexes, such as N-B [5, 6] and N-Li [7-9], were studied theoretically. While B-N complexes were predicted to be deep donors, substitutional LiN_4 clusters were predicted to be a shallow donor in diamond, with negative formation energy and a low activation energy of 0.2 – 0.4 eV reported by DFT calculations [7, 9]. However, LiN_4 clusters have yet to be made experimentally, and so the search continues for alternative co-doping schemes that may produce useful n-type diamond.

In this chapter, the C-centre and various Be-N clusters in diamond were studied by DFT calculations. Be was placed at interstitial and substitutional positions to form different clusters with substitutional N. The geometric, thermodynamic and electronic properties of diamond with Be-N clusters were investigated.

5.2 Method

DFT calculations were carried out using the CRYSTAL 17 package [10]. The range-separated hybrid functional HSE06 [11] was employed for exchange and correlation. Based on the work in Chapter 4, the two C basis sets, pob-TZVP-rev2 and 6-21G* gave very similar results for our calculations, but the 6-21G* basis set was much cheaper. Therefore, in this chapter, only the 6-21G* basis set was chosen for C, while the 5-1111-(3p)-(2d) [12, 13] basis set used in Chapter 4 was selected for Be. The pob-TZVP-rev2 [14] basis set consisting of one basis function for core orbital, three functions for each valence orbital, and a polarization function was selected for N. This basis set of N is believed to be accurate for this work and has been employed for the previous calculations [5, 7].

An optimized lattice parameter of 3.5637 Å obtained from the 6-21G* basis set in Chapter 4 was used for the geometry optimization of the defect systems, in which only the atomic coordinates were allowed to move while the lattice parameters were fixed. Four conventional supercells, 2×2×2, 2×2×4, 3×3×3 and 3×3×3 were constructed and denoted as S_{64}, S_{128}, S_{216} and S_{512} to simulate different doping concentrations.

The N-doped diamond was calculated in a S_{64} supercell, where N was placed at a single substitutional site. To study the properties of Be-N co-doped diamond, Be

was placed at single substitutional and interstitial sites, which were denoted as Be_s and Be_i, while N was placed at the nearest single substitutional site, and denoted by N_x ($x = 1 - 4$, indicating the number of N atoms). For the interstitial Be_i, tetrahedral and hexagonal interstitial sites were considered, and denoted as $Be_{i,tet}$ and $Be_{i,hex}$, respectively. Hence, depending on the different positions of Be, the Be-N clusters were denoted as $Be_{i,tet}N_x$, $Be_{i,hex}N_x$ and Be_sN_x, respectively, as shown schematically in Figures 5.1a, b and c. To investigate the influence of Be - N separation on the structure stability, in the case of the Be_sN_1 defect, the Be and N atoms were placed with different numbers (1 or 2) of C atoms in the middle, and the defect structures were denoted as Be_sCN_1 and Be_sCCN_1, as shown in Figures 5.1d and e. Figure 5.1f shows the schematic structure of Be_sN_4, while the structures of Be_sN_2 and Be_sN_3 are obtained by changing the value of x in Be_sN_x.

The cohesive energy, or binding energy (E_b) is the energy needed to separate a solid into separate atoms [15]. In this case, E_b is defined as the energy required to separate a Be-N cluster into isolated atoms, which can be calculated using the following equation [16, 17],

$$E_b = \sum E_{f,isolated} - E_{f,cluster} \qquad 5.1$$

where $\sum E_{f,isolated}$ is the sum of the formation energies of every isolated dopant, and $E_{f,cluster}$ is the formation energy of the Be-N cluster. The binding energy calculated from Equation 5.1 is also equal to the difference between the sum of the energies of isolated atoms and the energy of the cluster [18, 19]. A high positive binding energy indicates a high stability of the cluster.

Other computational details, such as the selection of shrinking factors and truncation criteria, band structure plotting, energy level and formation energy calculations, are the same as used for the calculation of Be-doped diamond in Chapter 4.

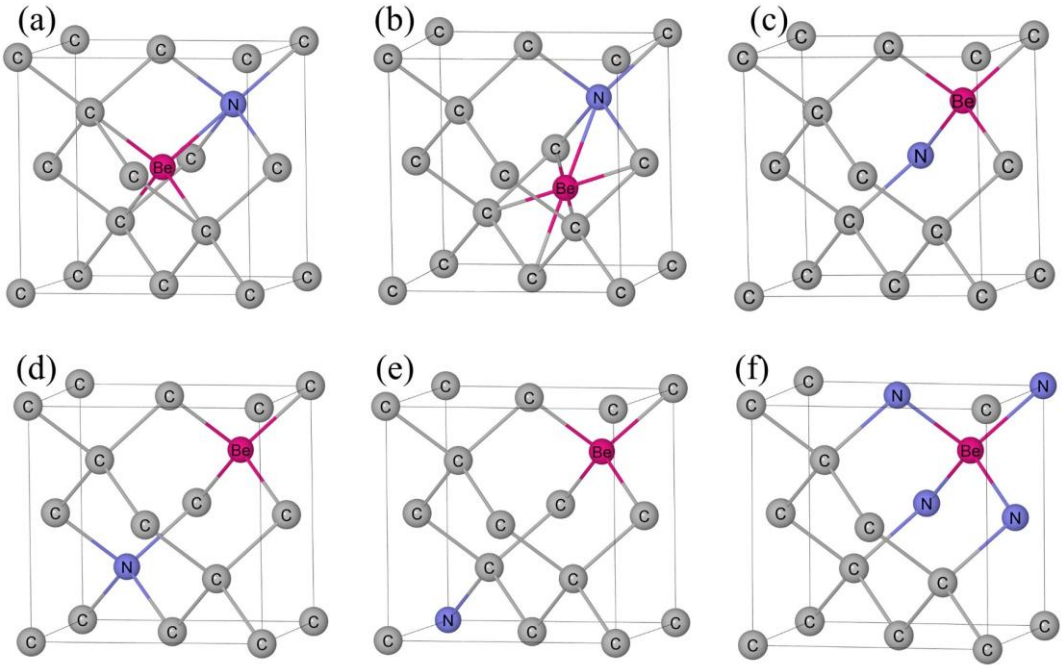

Figure 5.1. Schematic structures of various Be-N clusters: (a) $Be_{i,tet}N_1$, (b) $Be_{i,hex}N_1$, (c) Be_sN_1, (d) Be_sCN_1, (e) Be_sCCN_1 and (f) Be_sN_4.

5.3 Results and discussion

5.3.1 N-doped diamond (the 'C-centre')

5.3.1.1 Geometry structures

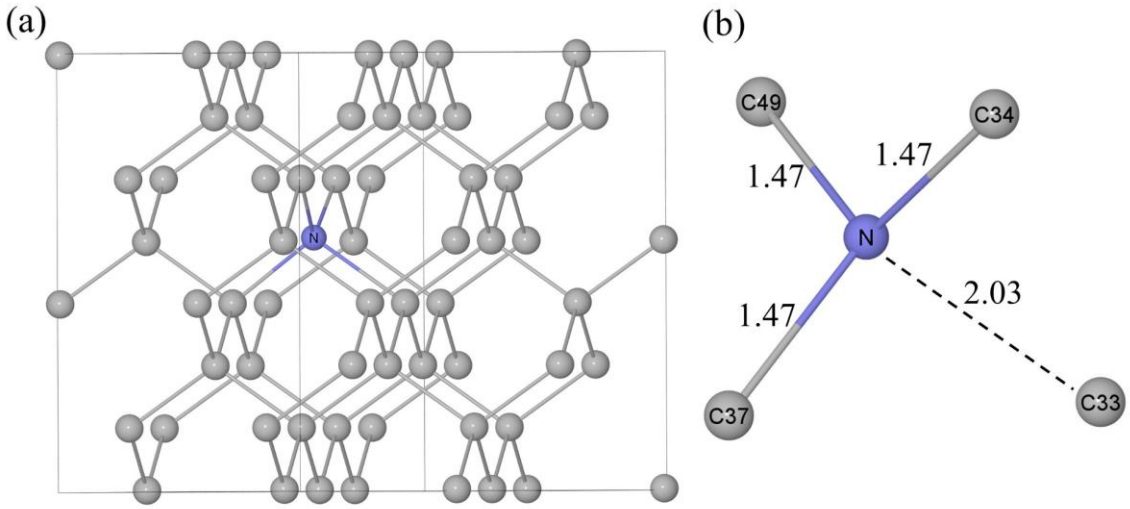

Figure 5.2. (a) Geometry structures of S_{64} with a substitutional N and (b) enlarged view of the optimised structure. Distances are in Å. The N atom is labelled as 'N', and the 63 C atoms labelled from C2 to C64.

Before adding Be, it is worth benchmarking the model against a known system, *i.e.* the C-centre. The optimised diamond structure with a C-centre is shown in Figure 5.2. The symmetry of the diamond with substitutional N was reduced to C_{3v} after geometry optimization. Due to the lone-pair electrons on N and the dangling bond on C33 (the unique C), the two atoms repulsed each other along the <1 1 1> direction, resulting in the elongation of the N-C33 bond and the compression of the N-C34, N-C37 and N-C49 bonds. The long N-C bond (N-C33) distance is 2.03 Å, which is 32% longer than the bond distance (1.543 Å) in the pristine diamond. The elongation percentage agrees with the values widely reported in experimental and calculations (Table 5.1). The three short C-N bonds are 1.47 Å, *i.e.*, 4.5% shorter compared with the C-C bond in pristine diamond, which is also close to the values reported in theoretical calculations (4.5% [20], 4.2% [21] and 3.9% [22]). The structure distortion is mainly located at the N and its four neighbouring C atoms such that the C-C bond lengths far from the defect site have barely changed. In the optimised structure, the C-C bonds nearest to N are 1.481 – 1.554 Å in length, *i.e.*, ± 3.5% in change compared with the length in pristine diamond, while the second-nearest C-C bonds are 1.546 – 1.547 Å in length, which is an increase of 0.19 – 0.26 %.

Table 5.1. Elongation of the unique N-C bond in diamond with C-centre reported in experimental and calculations.

	Method	Elongation of N-C	References
Experimental	Electron spin resonance	36%	[20, 23]
Calculations	*ab initio*	25%	[24]
	ab initio	28%	[20]
	extended Huckel theory	26.2%	[25]
	DFT–LSDA	32.9%	[26]
	ab initio Green's function	29%	[21]
	DFT–B3LYP	31.3%	[22]
	DFT–HSE06	32%	This work

5.3.1.2 Electron distribution

Mulliken population analysis indicates that N has a net charge of -0.979 |*e*|, while the net charges are 0.289 |*e*| for the nearest three C atoms (*i.e.*, C34, C37 and C49) and 0.102 |*e*| for C33 at the distance of 2.03 Å. For the C atoms further away, their charge states are almost neutral. The bond population between N and the nearest three C atoms (*e.g.*, C34) is 0.304, compared with a bond population of 0.351 for a C-C bond in perfect diamond. In contrast, the bond population between N and the C33 is 0.006, indicating the bonding interaction between them is weak. Due to the unpaired electron in the defect structure, a magnetic moment of 1 μB was calculated. The unpaired electron comes from C33, therefore the magnetic moment is mainly distributed in C33 (0.724 μB) and the neighbouring N (0.183 μB). The magnetic moment distribution agrees well with the reported experimental results that the unpaired electron is mainly localised in N and the unique C [23, 27-29], and matches the values reported from calculation [22] (0.763 μB on the unique C and 0.201 μB on N).

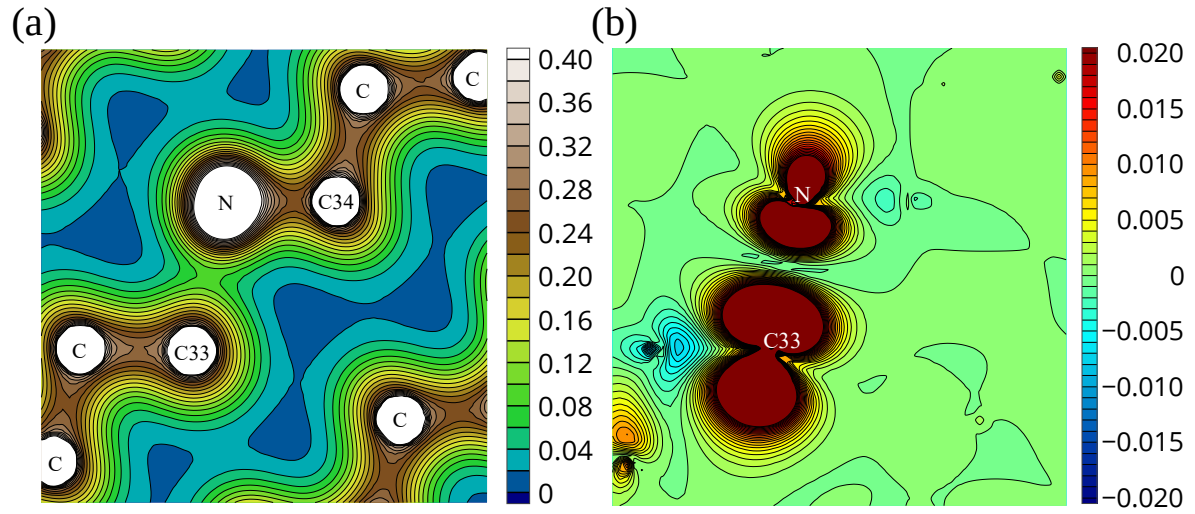

Figure 5.3. (a) total density and (b) spin-density maps around the N atom in S_{64}. The total density map is from 0 to 0.4 *e* Å^{-3} with a step of 0.02 *e* Å^{-3}, and the spin-density map from -0.02 to 0.02 *e* Å^{-3}, with a step of 0.001 *e* Å^{-3}. The plane to plot the electron density map is defined by C33, N and C34 in Figure 5.2b.

The electron distribution around the defect area can also be observed in the electron density maps. As shown in the total density map in Figure 5.3a, a bond has formed between N and C34, like the C–C bond in diamond, while the bonding

between N and C33 is barely seen. The spin density map in Figure 5.3b shows the distribution of spin density is mainly localised near C33 and N.

5.3.1.3 Band structure and formation energies

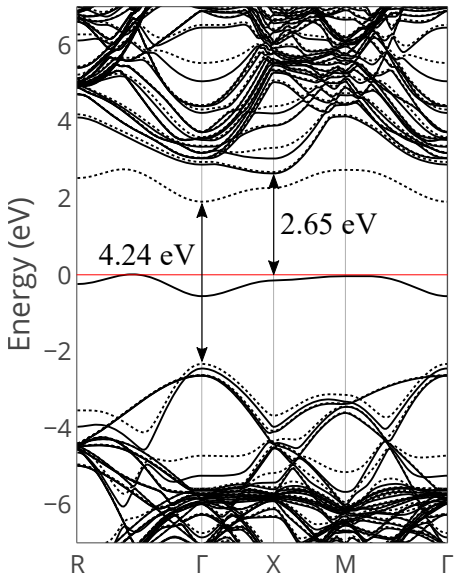

Figure 5.4. Band structure of S_{64} with a substitutional N. Continuous and dotted lines represent α and β electrons. The red line represents the Fermi level.

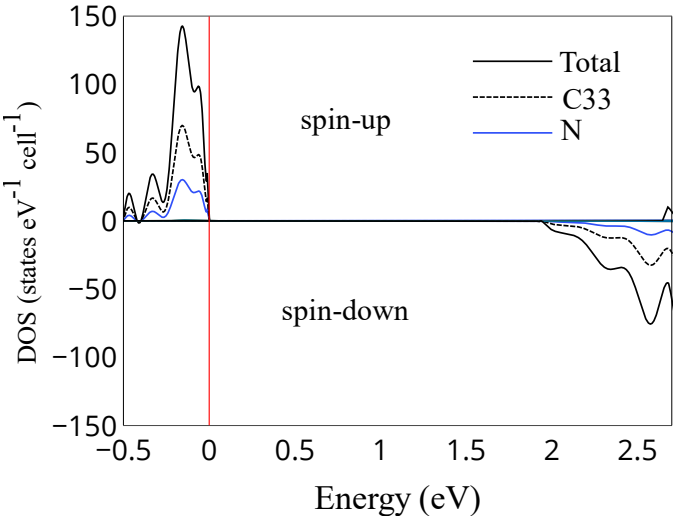

Figure 5.5. Projected DOS of S_{64} with a substitutional N.

The band structure of the N-doped diamond is shown in Figure 5.4. The spin-up donor band introduced by the unpaired electron is localized in the middle of the band gap. A spin-down acceptor band appears below the CBM, resulting in an

indirect energy gap of 2.65 eV for alpha electrons and a direct energy gap of 4.24 eV for beta electrons. The band structure agrees well with the literature [22] and also indicates the donor level is very deep, which is not useful as a n-type semiconductive material at room temperature.

The projected DOS map is shown in Figure 5.5 to reveal the compositions of the states around the Fermi level. The spin-up donor level and the spin-down acceptor level are contributed to mostly by C33 and N, while the contributions from C34, C37 and C49 are almost zero.

Formation energies (E_f) of the C-centre were calculated in the S_{64} supercell using Equation 4.1 in Chapter 4. Similar with that in Chapter 4, the two cases where N might be incorporated as molecular N_2 (case 1) or atomic N (case 2) were calculated separately, and the formation energies were denoted as $E_{f(1)}$and $E_{f(2)}$, respectively. As shown in Table 5.2, a high positive formation energy of $E_{f(1)}$= 3.53 eV was obtained when molecular N_2 was selected, indicating that direct doping by N_2 is not favourable. However, when atomic N was employed, the formation energy remained positive but at a much lower value of $E_{f(2)}$ ~0.87 eV. Moreover, if the structure contained a pre-existing vacancy, the formation energies were much lower, with $E_{f(1)} = -3.85$ eV and $E_{f(2)} = -8.25$ eV, suggesting that the incorporation of gaseous N_2 and atomic N are both exothermic under these conditions.

5.3.2 Be-N co-doped diamond

5.3.2.1 Be_iN_1 and Be_sN_1 clusters

As shown in Figure 5.6, the $Be_{i,tet}N_1$ and $Be_{i,hex}N_1$ clusters relaxed into very similar structures. After geometry optimisation, both Be and N atoms relaxed into the off-centre sites such that the original symmetries were broken. The two relaxed Be_iN_1 structures also have very similar energies, with a total energy difference of only ~ 0.002 eV. The significant difference between the original and the optimised structures indicates that both Be_iN clusters may have high formation energies (which is proved in Table 5.2) and are very likely to worsen the intrinsic properties of diamond.

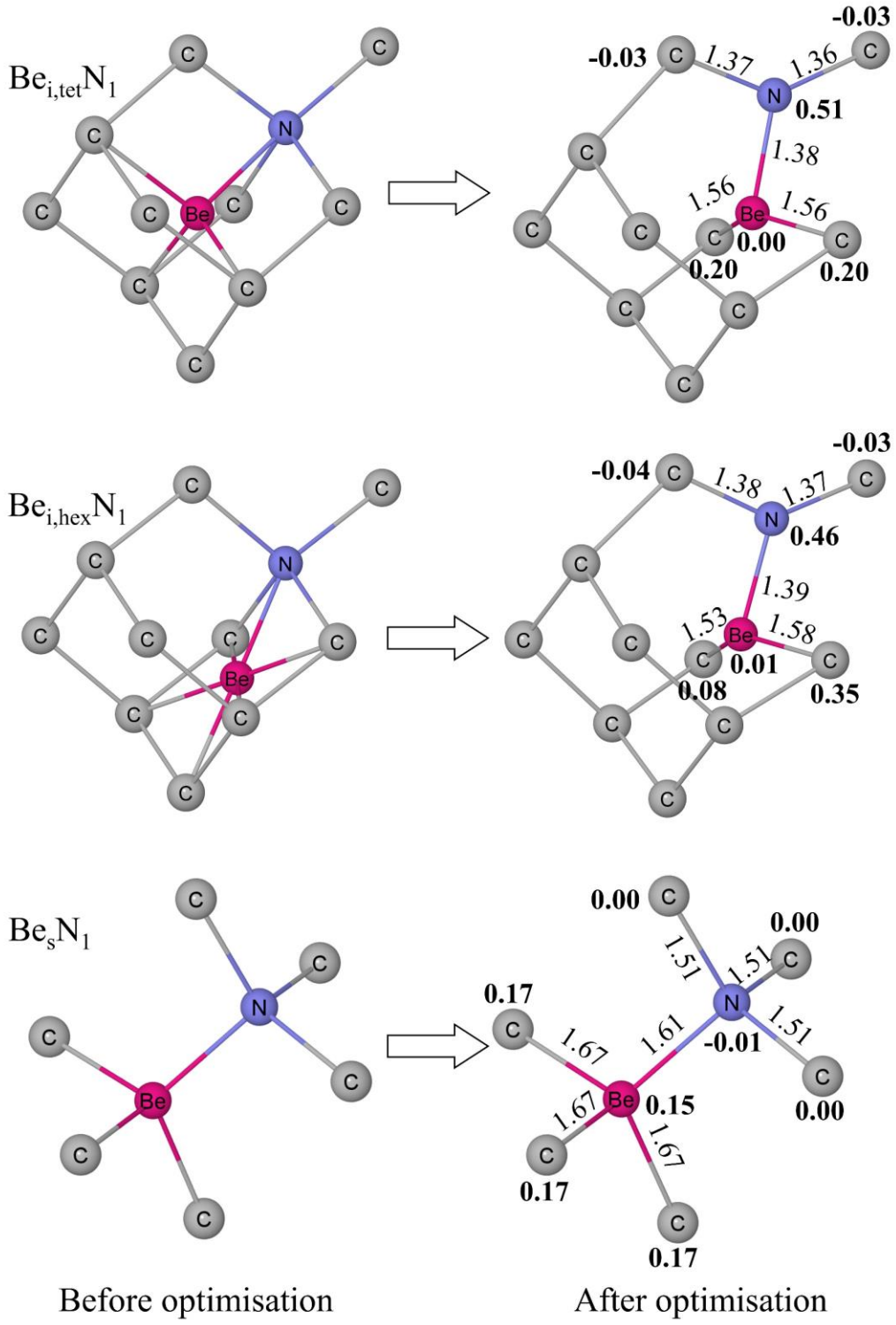

Figure 5.6. BeN_1 clusters and their neighbouring C atoms in a S_{64} supercell. Distances are in Å. Spin moments are in bold text.

The Be_sN_1 cluster, on the other hand, relaxed into a C_{3v} structure such that most symmetries remained the same. The Be–C and Be–N bond lengths are 1.67 and 1.61 Å, which are respectively 8 % and 4 % longer than the C–C bonding in pristine

diamond. The N–C bond lengths are all 1.51 Å, which is 2 % shorter than the original C-C bond.

A magnetic moment of 1 μB was obtained in $Be_{i,tet}N_1$, $Be_{i,hex}N_1$ and Be_sN_1. As shown in Figure 5.6, for the Be_iN_1 defect, the magnetic moment is mainly distributed around the N and the two C atoms adjacent to Be, while for the Be_sN_1 cluster, the magnetic moment is mainly localised on the Be and the three adjacent C atoms.

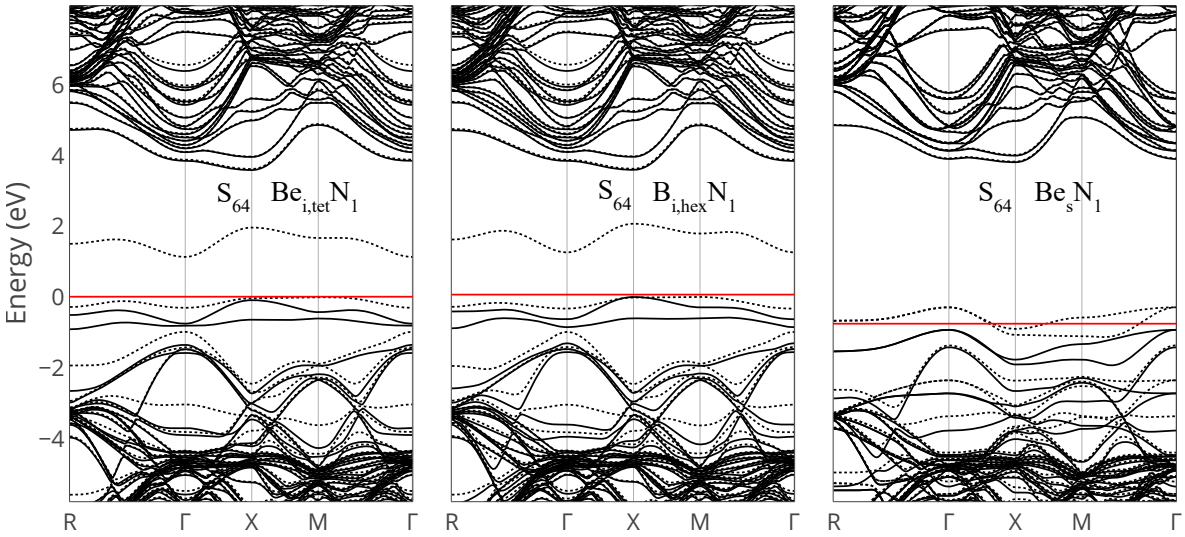

Figure 5.7. Band structures of the S_{64} supercell with different BeN_1 clusters. Continuous and dotted lines represent α and ß electrons. The red line represents the Fermi level.

The optimised $Be_{i,tet}N_1$ and $Be_{i,hex}N_1$ structures also have very similar band structures, as shown in Figure 5.7. Some occupied bands were introduced in the band gap just above the VBM. A spin-down acceptor level was introduced midway up the band gap, resulting in a direct energy gap of 3.60 eV for α-electrons and an indirect energy gap of 1.15 eV for ß-electrons. Such large energy gaps and deep occupied levels indicate that the Be_iN_1-doped diamond would not make a useful semiconducting material. The partially occupied levels will also compensate other donors in diamond.

For the Be_sN_1 structure, partially occupied bands were also introduced in the band gap. This defect is self-passivated and will also compensate other donors, which will lead to electrical inactivity [30]. We also calculated the band structures of

Be_iN_1 and Be_sN_1 in a S_{216} supercell to show the position of the defect level in the band gap more clearly, as shown in Figure 5.8.

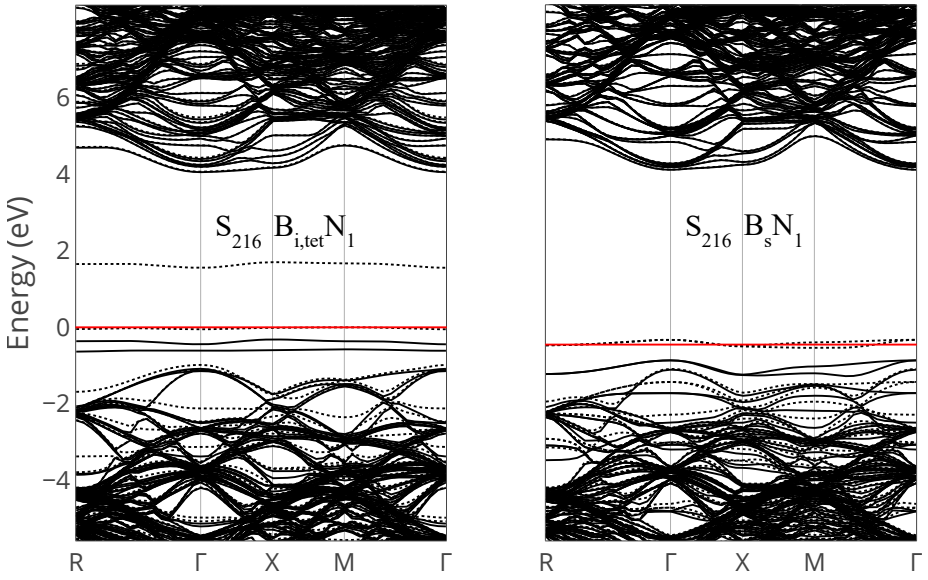

Figure 5.8. Band structures of a S_{216} supercell with $Be_{i,tet}N_1$ and Be_sN_1 clusters. Continuous and dotted lines represent α and ß electrons. The red line represents the Fermi level.

Because $Be_{i,tet}N_1$ and $Be_{i,hex}N_1$ relaxed into almost the same structure and energy, they also have the same formation energy. Therefore, the formation energies of $Be_{i,tet}N_1$ and $Be_{i,hex}N_1$ were recorded together, and denoted as Be_i,N_1 for convenience, as shown in Table 5.2. Taking the original source of Be to be a solid Be (hcp) crystal and N to be N_2 gas, the Be_iN_1 defect was calculated to have a high formation energy of 10.86 eV, compared with 3.65 eV for the Be_sN_1 defect, which is similar to the formation energy of the C-centre. In contrast, taking the sources of Be and N to be in the form of single atoms, the formation energies decreased by ~13 eV, such that the formation of the BeN_1 clusters became exothermic (Be_iN_1: -2.47 eV and Be_sN_1: -9.67 eV). Therefore, the Be_sN_1 defect is much easier to form, with its formation energy ~7.21 eV lower than that of Be_iN_1 defect. This is consistent with findings in Chapter 4 where we showed that the Be_s defect has a formation energy ~ 5.58 eV lower than the Be_i defect.

To determine whether the presence of N facilitates the incorporation of Be, we calculated the formation energies of Be_iN_1 and Be_sN_1 into a diamond that has been

doped by substitutional N already. As shown in Table 5.2, the formation energy of the Be_iN_1 defect is 4.11 eV lower, and that of the Be_sN_1 defect 5.73 eV lower than for Be_i and Be_s into pure diamond, respectively. Similarly, the formation energies of Be_iN_1 and Be_sN_1 into diamond that has been doped with Be_i and Be_s are also 4.11 and 5.73 eV lower than that of the C-centre. These values, 4.11 and 5.73 eV, are also the binding energies for the Be_iN_1 cluster and Be_sN_1 cluster calculated using Equation 5.1. Therefore, due to this high positive binding energy, the presence of substitutional N favours the incorporation of Be, especially the Be_s defect, and *vice versa*, the presence of Be, especially the Be_s, also favours the incorporation of the C-centre.

When substitutional Be and N were both placed in the supercell with a C atom between them, the total energy and the formation energy of the new Be_sCN_1 defect increased by 2.11 eV above that of the Be_sN_1 defect. Instead, when Be and N were separated by two C atoms, the defect formation energy of Be_sCCN_1 increased by a further 0.08 eV above that of Be_sCN_1. Therefore, Be and N atoms should remain substitutionally adjacent to each other in order to attain the minimum energy.

Table 5.2. Formation energies (eV) of Be, N and their clusters in a S_{64} diamond supercell. (Since the last form of the dopants before they are incorporated into diamond are always isolated atoms, *e.g.* atomic Be from Be crystal or atomic N from NH_3, $E_{f(2)}$ is more realistic.)

Defects		$E_{f(1)}$	$E_{f(2)}$
Be doping	Be_i	11.43	2.51
	Be_s	5.85	-3.07
N doping	C-centre	3.53	-0.87
	C-centre from vacancy	-3.85	-8.25
Be-N co-doping	Be_iN_1	10.86	-2.47
	Be_sN_1	3.65	-9.67
	Be_sCN_1	5.76	-7.56
	Be_sCCN_1	5.84	-7.48
	Be_iN_1 from N-doped	7.32	-1.60
	Be_sN_1 from N-doped	0.12	-8.80
	Be_iN_1 from Be-doped	-0.58	-4.98
	Be_sN_1 from Be-doped	-2.21	-6.61
	Be_sN_2	1.26	-16.47
	Be_sN_3	3.69	-18.43
	Be_sN_4	6.36	-20.16
	VN_1	6.42	2.02
	VN_2	4.77	-4.03
	VN_3	3.17	-10.03
	VN_4	1.80	-15.80
	VN_1 from vacancy	-0.96	-5.36
	VN_2 from vacancy	-2.61	-11.41
	VN_3 from vacancy	-4.21	-17.41
	VN_4 from vacancy	-5.58	-23.18
	Be_sN_1 from VN_1	-2.77	-11.69
	Be_sN_2 from VN_2	-3.51	-12.44
	Be_sN_3 from VN_3	0.52	-8.40
	Be_sN_4 from VN_4	4.56	-4.36

5.3.2.2 Be_sN_x clusters

Be_sN_2 cluster

As shown in Figure 5.9, the Be_sN_2 cluster relaxed into a structure with C_{2v} symmetry, but the Be-to-N (1.639 Å) and the Be-to-nearest-C (1.637 Å) separations are very similar. They are stretched by 6.2% and 6.1%, respectively, compared to the original C–C bond in pristine diamond.

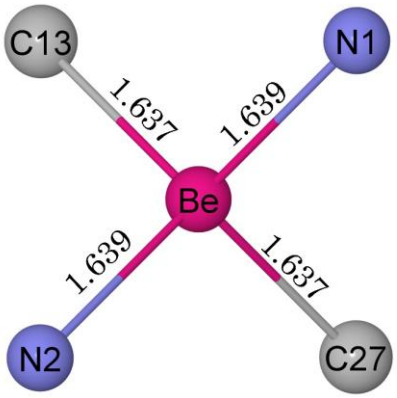

Figure 5.9. Optimised structure of the Be_sN_2 cluster in a S_{64} supercell.

Because Be has two valence electrons in its 2s orbital while the two C atoms (C13 and C27) have two unpaired electrons, the Be atom can form a bond with each of the two C atoms. Moreover, there are two lone-pair electrons on each of the N atoms. This configuration promoted the formation of a closed-shell system. The electronic interactions between Be and N contribute to the occupied levels at the VBM, resulting in an indirect energy gap of 4.39 eV, as shown in the band structure in Figure 5.10. Composition of the highest-occupied energy levels was analysed by the projected DOS map. As shown in Figure 5.11, Be and its nearest C atoms (C13 and C27) contribute a large part of the highest occupied level, but the contribution from the N atoms is negligible.

The Be_sN_2 cluster has a formation energy of $E_{f(1)}$ = 1.26 eV and $E_{f(2)}$ = -16.47 eV, which are both lower than that of Be_sN_1. However, the large energy gap in the band structure suggests this defect will not be useful as a n- or p- type dopant.

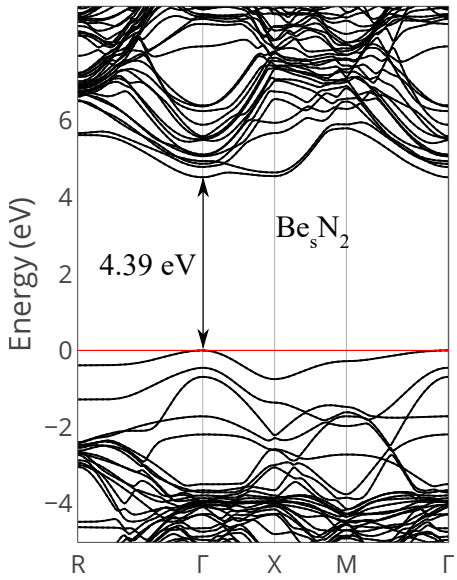

Figure 5.10. Band structure of the S_{64} supercell with a Be_sN_2 defect.

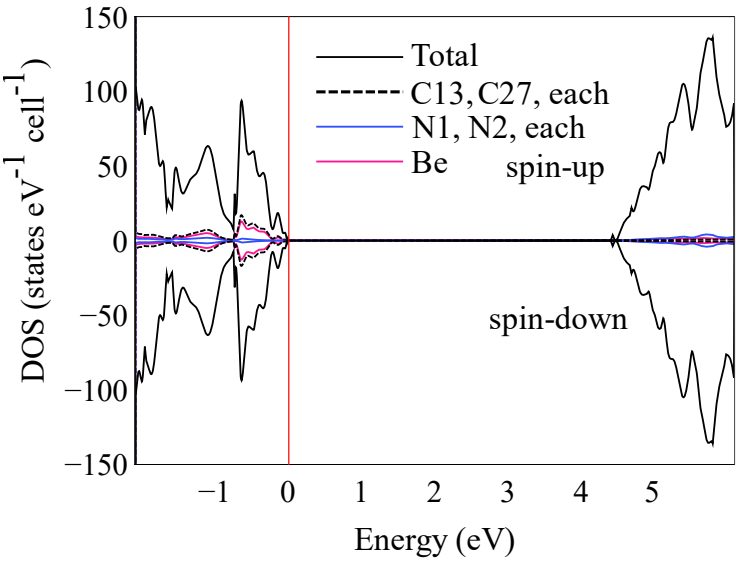

Figure 5.11. Projected DOS map of the S_{64} supercell with a Be_sN_2 defect. The red vertical line represents the Fermi level.

Be_sN_3 cluster

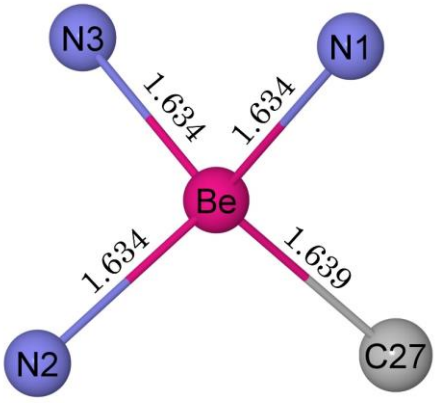

Figure 5.12. Structure of the Be_sN_3 cluster.

The Be_sN_3 cluster relaxed into a structure with C_{3v} symmetry after geometry optimisation. As shown in Figure 5.12, the distances from Be to the three N atoms and to C are 1.634 and 1.639 Å, respectively, which are 5.9% and 6.2% longer than the original C-C bond. The structural change mainly occurred around the defect centre such that the distance from N to the nearest C atoms has a maximum change of 2.1% compared with the original C-C bond, and the change becomes almost zero for C atoms further away from the defect centre.

When the sources of Be and N were taken to be a solid Be (hcp) crystal and molecular N_2, respectively, the Be_sN_3 cluster had a formation energy of $E_{f(1)} = 3.69$ eV, which is similar to that of Be_sN_1 and the C-centre. In contrast, when the impurity atoms were incorporated from isolated Be and N atom sources, a very negative formation energy $E_{f(2)} = -18.43$ eV was obtained, indicating the doping of Be_sN_3 cluster from isolated atoms is energetically favourable.

The band structure of a S_{64} supercell with a Be_sN_3 cluster is shown in Figure 5.13. The Fermi level lies in the conduction band but is close to the CBM, such that the band structure shows a metallic conductivity. This band structure agrees well with our expectation for a shallow donor of high doping concentration. Because of the extremely high doping concentration (a defect in 64-atom supercell is equivalent to a concentration of ~ 2.75×10^{21} atoms cm^{-3}), the impurity bands have merged with the conduction band.

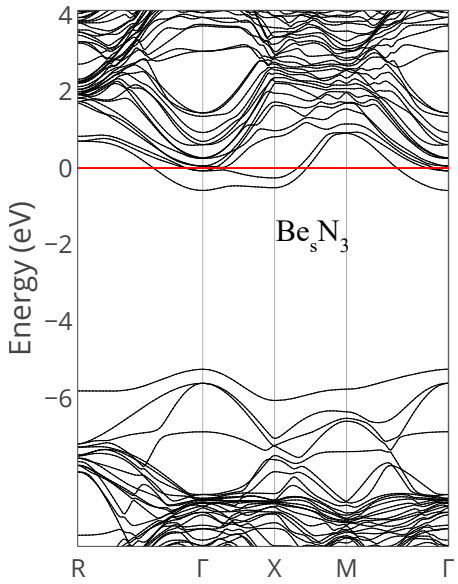

Figure 5.13. Band structure of the S_{64} supercell with a Be_sN_3 cluster.

The projected DOS map is shown in Figure 5.14. In the Be_sN_3 structure, the defect contributes to the energy level in the conduction band. It is worth noting that the defect state at the conduction band edge is not localised on the Be or N, but distributed around the Be-N cluster and the nearest C atoms (similar to the distribution seen in Be_sN_4 later in Figure 5.19), such that the Be and each N atom only make a small contribution to the defect level at the conduction band edge.

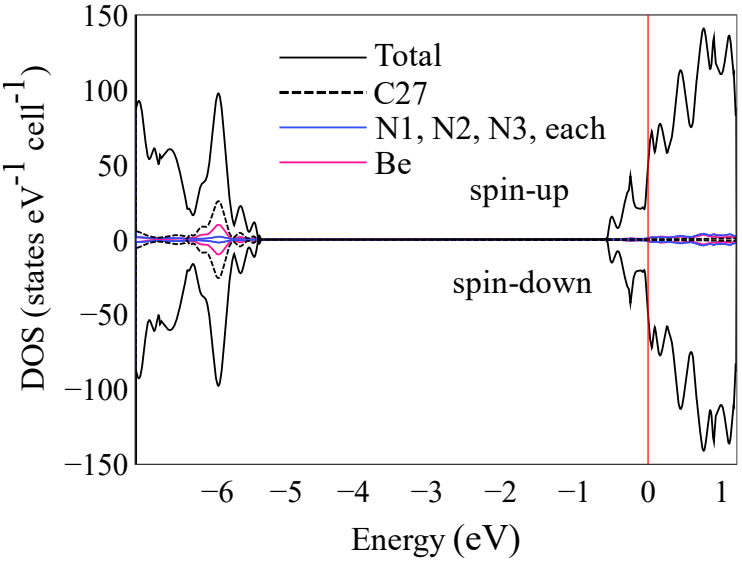

Figure 5.14. Projected DOS map of Be_sN_3-doped diamond in a S_{64} supercell.

To simulate low doping concentrations, the Be_sN_3 cluster was also calculated in S_{128}, S_{216} and S_{512} supercells, and their band structures are shown in Figure 5.15. With increasing supercell size (*i.e.*, decreasing defect concentration), the Fermi level moves within the conduction band toward the CBM. However, even for the simulation of one cluster in the S_{512} supercell, the defect concentration is still unrealistically high, which results in a band structure still showing metallic conductivity, as for S_{64}. Comparison with experimental results show that when the defect concentration is low (*e.g.*, 10^{18} atoms cm^{-3} typical for P-doped diamond [31]), a n-type semiconductivity can be obtained. However, to simulate such low concentrations require a huge supercell; for example, 17600 (or $13 \times 13 \times 13$ supercell) C atoms are needed to simulate a concentration of 10^{18} atoms cm^{-3}, which is far beyond our calculation ability.

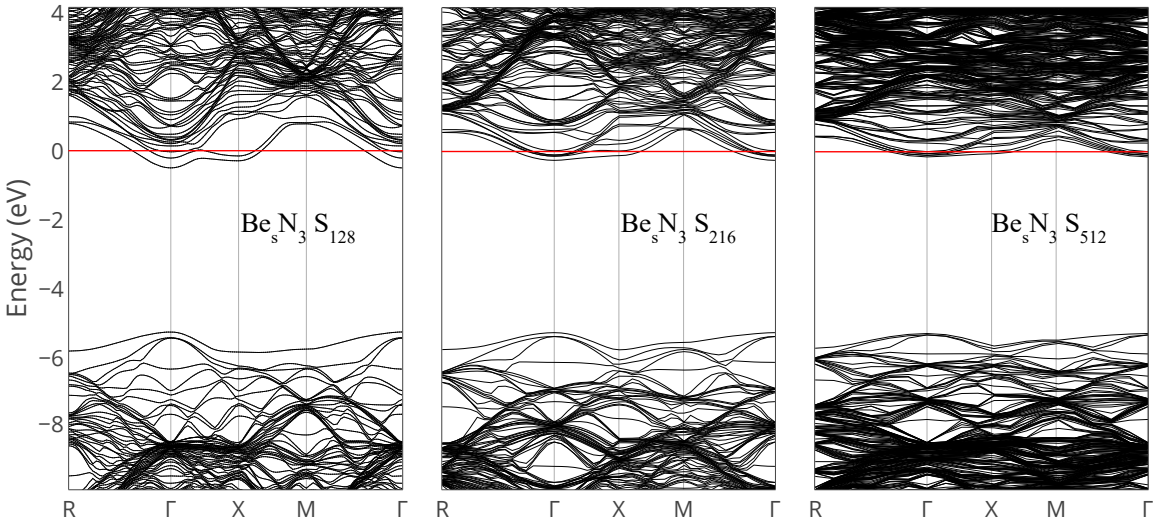

Figure 5.15. Band structure of S_{128}, S_{216} and S_{512} with a Be_sN_3 cluster.

Therefore, EMM was employed to predict the donor level. As shown in Table 5.3, from S_{64} to S_{512}, the Be_sN_3 cluster was calculated having a donor level from $E_c - 0.86$ to $E_c - 0.51$ eV. EMM is more accurate for calculating the energy levels of impurities that have a similar defect position as a reference dopant. In this case, the reference element (P) was a single interstitial dopant but the dopant to be calculated was a co-doped cluster occupying the substitutional sites. Therefore, the calculated energy level was not as accurate as that calculated for the single interstitial Be in Chapter 4, such that the calculated ionization energy for diamond

containing a Be_sN_3 cluster has a wider range (0.86 – 0.57 eV from S_{64} to S_{216}, compared with 0.38 – 0.47 eV for $Be_{i,tet}$ doping in Chapter 4). Nevertheless, taking both band structures and EMM results into account, it is predicted that the Be_sN_3 cluster behaves as a shallow donor in diamond, with a donor level of 0.51 eV below the conduction band. This value was calculated from S_{512} and was taken because larger supercells tend to give more reasonable predictions for the donor or acceptor levels at lower concentrations [32].

Table 5.3. Donor levels ($E - E_c$, eV) of Be_sN_3 and Be_sN_4 calculated by EMM in different-sized supercells from S_{64} to S_{512}.

Supercell	Be_sN_3	Be_sN_4
S_{64}	-0.86	-0.65
S_{128}	-0.62	-0.63
S_{216}	-0.57	-0.42
S_{512}	-0.51	-0.46

Be_sN_4 cluster

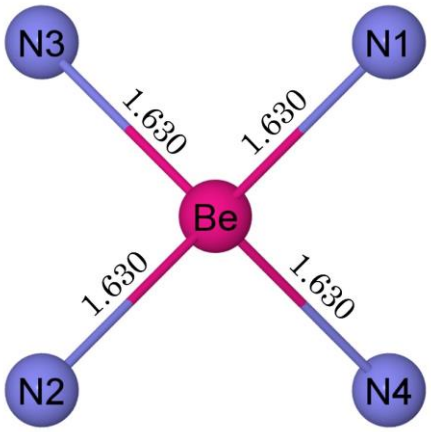

Figure 5.16. Structure of the Be_sN_4 cluster. Distances are in Å.

The Be_sN_4 cluster relaxed into a structure of T_d symmetry. As shown in Figure 5.16, the distances from the Be to the four N atoms are all 1.630 Å, which have increased 5.6% above that of the C-C bond in pristine diamond. The geometry changes mainly occurred at the defect centre such that the distance from each N to its nearest C is 1.1 % shorter, while the next-nearest C-C bond is only 0.7 %

shorter than the original C-C bond. Be_sN_4-doped diamond has a diamagnetic ground state therefore no magnetic spin was calculated.

When the sources of Be and N were taken to be a solid Be (hcp) crystal and molecular N_2, respectively, the Be_sN_4 cluster had a positive formation energy of $E_{f(1)} = 6.36$ eV, which is higher than that of the Be_sN_3 cluster. In contrast, when the dopants sources were taken to be isolated Be and N atoms, a very negative formation energy of $E_{f(2)} = -20.16$ eV was obtained, indicating this doping scheme is exothermic and energetically favourable.

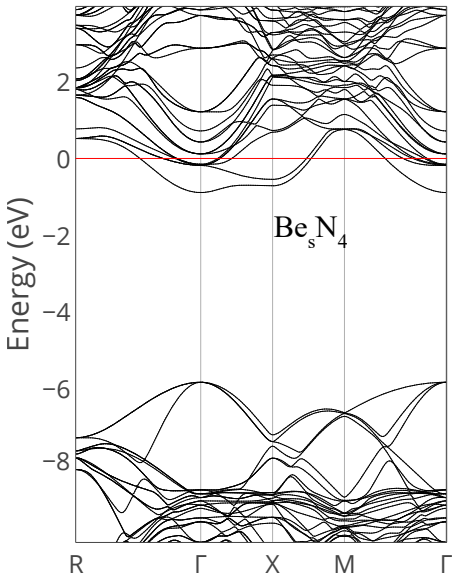

Figure 5.17. Band structure Be_sN_4-doped diamond in a S_{64} supercell.

Be_sN_4-doped diamond shown in Figure 5.17 has a band structure similar to that of the Be_sN_3 doped diamond (Figure 5.13). Due to the extremely high doping concentration, the Fermi level again lies within the conduction band, making the structure show metallic conductivity. The projected DOS map is in Figure 5.18. It is very likely that the two valence electrons of Be instead contributed to the defect energy level at the conduction band edge. Similar to the Be_sN_3 cluster, the donor state of Be_sN_4 is not localised in the orbitals of Be or N, but is distributed around Be, N, and the neighbouring C atoms. As shown in the DOS map in Figure 5.18, the Be and its surrounding N atoms all contribute to the defect level in the conduction band.

To simulate a lower defect concentration, the DOS map for the Be_sN_4-doped diamond in a S_{512} supercell is plotted in Figure 5.19. Because the ground spin-state of the Be_sN_4-doped diamond is $S = 0$, the calculation for the S_{512} supercell with a Be_sN_4 cluster was employed using a closed-shell scheme in order to save computational time. The DOS at the conduction band edge projected onto Be, N and three selected C atoms at different distances from the defect centre (Be) are plotted in this map. From Be and N to the C atom at 12.35 Å, although the atoms are further away from the defect centre, their contribution to the conduction band edge becomes less. Therefore, the main contributions to the donor level are from the Be-N cluster and the nearest C atoms.

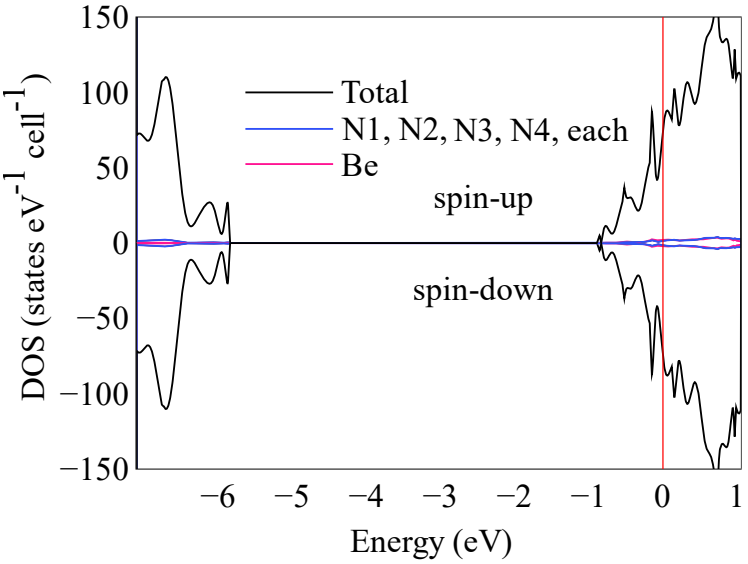

Figure 5.18. Projected DOS map of Be_sN_4-doped diamond in a S_{64} supercell.

As shown in Figure 5.20, with the increase of the supercell size from S_{64}, to S_{512}, the Fermi energy level moves from within the conduction band to the conduction band edge, but the structures all show a metallic conductivity. The Be_sN_4 cluster has a donor state of 0.46 eV below the conduction band edge calculated by EMM in S_{512} (see Table 5.3), indicating it is a shallower donor than the Be_sN_3 cluster.

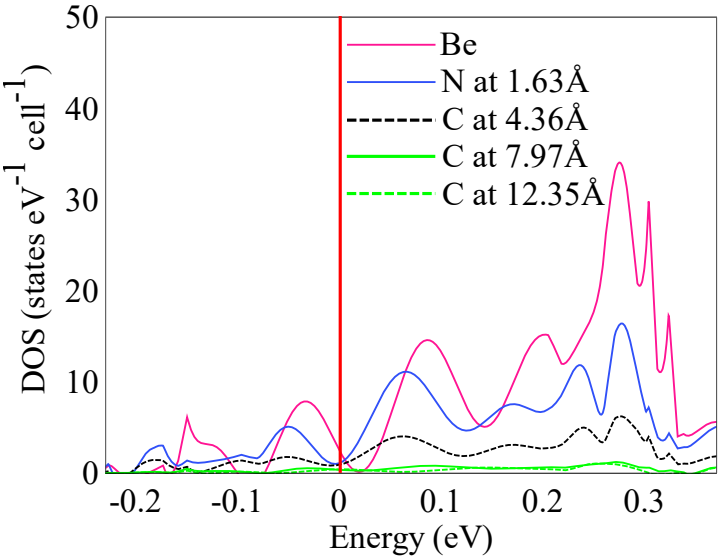

Figure 5.19. The DOS at the conduction band edge projected onto Be, N and C at different distances from the defect in a S_{512} supercell doped by a Be_sN_4 cluster.

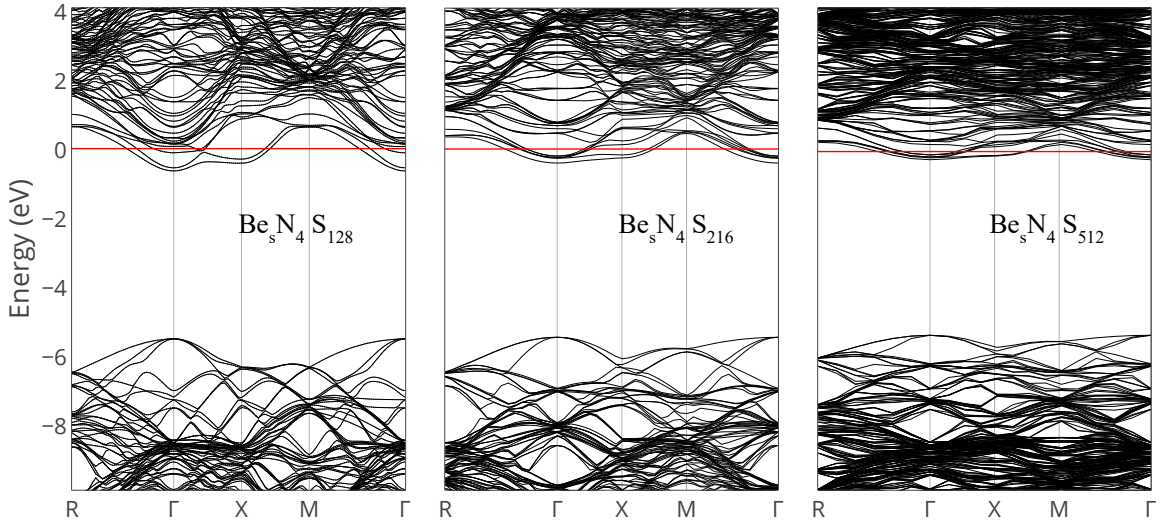

Figure 5.20. The band structure of Be_sN_4-doped diamond in S_{128}, S_{216} and S_{512} supercells.

5.3.2.3 Formation of the Be_sN_x clusters

According to the above calculations for Be-N clusters in diamond, both Be_sN_3 and Be_sN_4 clusters are predicted to show shallow donor properties. Similar to the LiN_4 complex in diamond [7, 9], the Be_sN_3 and Be_sN_4 clusters are more complicated than single-element doping at single substitutional or interstitial sites, therefore they may have a very small chance to form spontaneously in pristine diamond.

To avoid the unlikely prospect of these defects forming in pristine diamond, we now propose a route whereby the formation of the Be_sN_x clusters occurs via a two-step process, where the diamond already has some vacancies incorporated. The first step is the formation of a VN_x complex, where "V" denotes the vacancy and N_x the adjacent x substitutional N atoms around the vacancy. Because N is easily incorporated into diamond, the formation energy of a VN_x cluster decreases as x increases. As shown in Table 5.2, when the source of N is taken to be an N_2 molecule, the incorporation reaction is endothermic, with formation energies decreasing from 6.42 – 1.80 eV as x increases from 1 – 4. In contrast, when the source of N is taken to be atomic N, the formation energies are much lower, especially for the VN_3 and VN_4 defects, which become -10.03 and -15.80 eV, respectively. In the previous chapter, we argued that although the single-vacancy defect has a high positive formation energy of 7.38 eV, they nevertheless often appear in natural or lab-grown diamond as an intrinsic defect. This, the VN_x complex should be more likely to form in diamond with pre-existing vacancies. In this case, the formation energies of the VN_x defects will be 7.38 eV lower than in a perfect diamond, such that the incorporation reactions are all exothermic independent of whether the source of N was N_2 or atomic N. This suggests that if sufficient N atoms are incorporated into CVD diamond, there may be a realistic chance that the diamond may include many VN_3 and VN_4 clusters. Meanwhile, N atoms should be prevented from filling the vacancies.

The second step is the incorporation of Be into the vacancy in the VN_3 or VN_4 defect. Starting from the VN_x defect, the Be_sN_2 cluster has the lowest formation energy (-12.44 eV), followed by Be_sN_1 (-11.69 eV), Be_sN_3 (-8.40 eV) and finally Be_sN_4 (-4.36 eV). Among these, Be_sN_2 and Be_sN_1 have negative formation energies for both $E_{f(1)}$ and $E_{f(2)}$. However, both Be_sN_2 and Be_sN_1 are the structures that should be avoided because they are not semiconductive at room temperature. Therefore, it is necessary to have sufficient VN_3 and VN_4 present and also to incorporate Be in the form of single atom, so that the formation of Be_sN_1 and Be_sN_2 can be avoided and the reactions to form Be_sN_3 ($E_{f(2)} = -8.40$ eV) and Be_sN_4 ($E_{f(2)} = -4.36$ eV) will be exothermic. One possible method to do this would be ion

implantation using low Be doses, and this is suggested as a challenge for experimentalists!

5.4 Conclusions

With the aim of identifying a new shallow n-type dopant for diamond, first-principles calculations were employed for N-doped and Be-N co-doped diamond. The geometries, thermodynamic and electronic properties of various Be-N defect structures were studied in detail. The Be_i-N and Be_s-N clusters were investigated and their stabilities were compared in order to find the ground state for the Be-N clusters. By changing the distance between N and Be and the number of N atoms in the Be_sN_x clusters, two clusters (Be_sN_3 and Be_sN_4) with shallow-donor properties were predicted and their possible formation processes were proposed. The main conclusions are as follows:

1) N is a deep donor in diamond. The C-centre has a positive formation energy of 3.53 eV when the N source is taken to be N_2, but a negative formation energy of -0.87 eV if the source is taken to be atomic N. The C-centre is more likely to be incorporated in diamond with a pre-existing vacancy, such that the formation energy is 7.38 eV lower than that in pristine diamond and the reaction will be exothermic.

2) The $Be_{i,tet}N_1$ and $Be_{i,hex}N_1$ clusters relaxed into structures with very similar geometries without retaining any symmetry. In contrast, the Be_sN_1 cluster relaxed to a C_{3v}-symmetry structure after geometry optimisation. The presence of N favours the incorporation of Be and *vice versa* due to the positive binding energies between them (4.11 eV for Be_i-N and 5.73 eV for Be_s-N), and they should remain at adjacent single substitutional sites in order to reach the ground state. Compared with the $Be_{i,tet}N_1$ cluster, the Be_sN_1 cluster is easier to form, with its formation energy 7.21 eV lower than that of $Be_{i,tet}N_1$.

3) Among the Be_sN_x ($x = 1 - 4$) clusters, Be_sN_1 and Be_sN_2 did not show any semiconductor properties, while the Be_sN_3 and Be_sN_4 showed shallow donor properties, with donor levels of $E_c - 0.51$ eV and $E_c - 0.46$ eV predicted in a

S_{512} supercell using the empirical marker method. The Be_sN_3 and Be_sN_4 clusters had positive formation energies of 3.69 and 6.38 eV when the sources for Be and N were taken to be the bulk Be metal and N_2, respectively, but negative formation energies of -18.43 and -20.16 eV when the sources were taken to be isolated B and N atoms.

4) A theoretically possible two-step preparation method was proposed for Be_sN_3 and Be_sN_4 in diamond. In the first step, VN_3 and VN_4 complexes can be made in diamond with pre-existing vacancies by incorporation of a high concentration of N. Then, Be can be incorporated into the vacancies of VN_3 and VN_4 using low-dose ion implantation.

5.5 References

[1] R.M. Chrenko, R.E. Tuft, H.M. Strong, Transformation of the state of nitrogen in diamond, Nature 270 (1977) 141-144.

[2] R.G. Farrer, On the substitutional nitrogen donor in diamond, Solid State Commun. 7 (1969) 685-688.

[3] H.B. Dyer, F.A. Raal, L. Du Preez, J.H.N. Loubser, Optical absorption features associated with paramagnetic nitrogen in diamond, Philos. Mag. A 11 (1965) 763-774.

[4] W. Kaiser, W.L. Bond, Nitrogen, A Major Impurity in Common Type I Diamond, Phys. Rev. 115 (1959) 857-863.

[5] A. Croot, M.Z. Othman, S. Conejeros, et al., A theoretical study of substitutional boron-nitrogen clusters in diamond, J. Phys. Condens. Matter 30 (2018) 10.

[6] H. Katayama-Yoshida, T. Nishimatsu, T. Yamamoto, N. Orita, Codoping method for the fabrication of low-resistivity wide band-gap semiconductors in p-type GaN, p-type AlN and n-type diamond: prediction versus experiment, J. Phys. Condens. Matter 13 (2001) 8901-8914.

[7] S. Conejeros, M.Z. Othman, A. Croot, et al., Hunting the elusive shallow n-type donor – An ab initio study of Li and N co-doped diamond, Carbon 171 (2021) 857-868.

[8] Z. Delun, L. Tang, Y. Geng, et al., First-principles calculation to N-type LiN Co-doping and Li doping in diamond, Diam. Relat. Mater. 110 (2020) 108070.

[9] J.E. Moussa, N. Marom, N. Sai, J.R. Chelikowsky, Theoretical Design of a Shallow Donor in Diamond by Lithium-Nitrogen Codoping, Phys. Rev. Lett. 108 (2012) 226404.

[10] R. Dovesi, A. Erba, R. Orlando, et al., Quantum-mechanical condensed matter simulations with CRYSTAL, Wiley Interdiscip. Rev. Comput. Mol. Sci. 8 (2018) 36.

[11] J. Heyd, G.E. Scuseria, M. Ernzerhof, Hybrid functionals based on a screened Coulomb potential, J. Chem. Phys. 118 (2003) 8207-8215.

[12] A. Gruneich, B.A. Hess, Choosing GTO basis sets for periodic HF calculations, Theor. Chem. Acc. 100 (1998) 253-263.

[13] B. Soulé de Bas, H.E. Dorsett, M.J. Ford, The electronic structure of Be and BeO: benchmark EMS measurements and LCAO calculations, J. Phys. Chem. Solids 64 (2003) 495-505.

[14] D. Vilela Oliveira, J. Laun, M.F. Peintinger, T. Bredow, BSSE-correction scheme for consistent gaussian basis sets of double- and triple-zeta valence with polarization quality for solid-state calculations, J. Comput. Chem. 40 (2019) 2364-2376.

[15] B.G. Yacobi, Semiconductor materials: an introduction to basic principles, Springer Science & Business Media 2003.

[16] M.O. Zacate, L. Minervini, D.J. Bradfield, et al., Defect cluster formation in M_2O_3-doped cubic ZrO_2, Solid State Ion. 128 (2000) 243-254.

[17] L. Minervini, M.O. Zacate, R.W. Grimes, Defect cluster formation in M_2O_3-doped CeO_2, Solid State Ion. 116 (1999) 339-349.

[18] F. Ye, T. Mori, D.R. Ou, A.N. Cormack, Dopant type dependency of domain development in rare-earth-doped ceria: An explanation by computer simulation of defect clusters, Solid State Ion. 180 (2009) 1127-1132.

[19] F. Ye, T. Mori, D.R. Ou, et al., Simulation of ordering in large defect clusters in gadolinium-doped ceria, Solid State Ion. 179 (2008) 1962-1967.

[20] P.R. Briddon, R. Jones, Theory of impurities in diamond, Physica B Condens. Matter 185 (1993) 179-189.

[21] N.A. Katcho, J. Carrete, W. Li, N. Mingo, Effect of nitrogen and vacancy defects on the thermal conductivity of diamond: An ab initio Green's function approach, Phys. Rev. B 90 (2014) 094117.

[22] A.M. Ferrari, S. Salustro, F.S. Gentile, et al., Substitutional nitrogen in diamond: A quantum mechanical investigation of the electronic and spectroscopic properties, Carbon 134 (2018) 354-365.

[23] C. Ammerlaan, Defects and radiation effects in semiconductors, Inst. Phys. Conf. Ser. No. 59 (1981) 81.

[24] S.A. Kajihara, A. Antonelli, J. Bernholc, R. Car, Nitrogen and potential n-type dopants in diamond, Phys. Rev. Lett. 66 (1991) 2010-2013.

[25] R.P. Messmer, G.D. Watkins, Molecular-Orbital Treatment for Deep Levels in Semiconductors: Substitutional Nitrogen and the Lattice Vacancy in Diamond, Phys. Rev. B 7 (1973) 2568-2590.

[26] E.B. Lombardi, A. Mainwood, K. Osuch, E.C. Reynhardt, Computational models of the single substitutional nitrogen atom in diamond, J. Phys. Condens. Matter 15 (2003) 3135-3149.

[27] A. Cox, M.E. Newton, J.M. Baker, ^{13}C,^{14}N and ^{15}N ENDOR measurements on the single substitutional nitrogen centre (P1) in diamond, J. Phys. Condens. Matter 6 (1994) 551-563.

[28] J.H.N. Loubser, J.A.v. Wyk, Electron spin resonance in the study of diamond, Rep. Prog. Phys. 41 (1978) 1201-1248.

[29] J.H.N. Loubser, L.D. Preez, New lines in the electron spin resonance spectrum of substitutional nitrogen donors in diamond, Br. J. Appl. Phys. 16 (1965) 457-462.

[30] E.B. Lombardi, A. Mainwood, Li and Na in diamond: A comparison of DFT models, Physica B Condens. Matter 401-402 (2007) 57-61.

[31] S. Koizumi, K. Watanabe, M. Hasegawa, H. Kanda, Ultraviolet Emission from a Diamond pn Junction, Science 292 (2001) 1899-1901.

[32] J.P. Goss, P.R. Briddon, R.J. Eyre, Donor levels for selected n-type dopants in diamond: A computational study of the effect of supercell size, Phys. Rev. B 74 (2006) 245217.

CHAPTER 6

CONCLUSIONS AND FUTURE WORK

6.1 Conclusions

This thesis reports the results of studies about electronic and magnetic properties of diamond composites, including the experimental work of diamond film growth on Co by CVD and the first-principles calculations of Be and Be-N complexes in diamond. The study of magnetic and electronic properties of diamond with other metals may provide ideas for making new electromagnetic devices with extraordinary robustness. Patterned Co in the form of stripes or nanoparticles were employed as part of the substrate to imbue diamond film with magnetic properties. DFT calculations were carried out to investigate the magnetic and electronic properties of diamond doped with Be or Be-N clusters, with the formation energies and predicted defect levels summarised shortly in Table 6.1. The main conclusions of the thesis are summarized as follows.

1) Co can be patterned and embedded into diamond film by using laser cutting and a subsequent drop-casting of Co nanoparticles or a standard lift-off fabrication process of the Co film, followed by CVD diamond film growth. In the first method, due to the laser heating effect, the laser-cut diamond surface was rough, which led to a diamond film with high surface roughness after the second growth. Although the magnetic signal of Co nanoparticles can be detected by MFM through the diamond film, the rough surface hinders it to be fully scanned by MFM. In the second method, stripe-patterned Co film with thickness of ~ 36 nm and width of ~ 1 μm was prepared by a standard lift-off process. Diamond film with lower surface roughness was grown on the Si substrate with such patterned Co stripes, and the sample can be scanned by MFM and the magnetic signal detected by MFM through the ~1.6 μm-thick diamond film. This preliminary work demonstrates that

diamond films can act as a robust protective layer for magnetic composite devices. Owing to the robustness of diamond film, this magnetic composite may find applications in some extreme environments.

2) First-principles DFT calculations were employed using hybrid functionals to investigate the electronic and magnetic properties of Be-doped diamond. Substitutional (Be_s) and three interstitial (with tetrahedral symmetry $Be_{i,tet}$, hexagonal symmetry $Be_{i,hex}$ and off-centre site $Be_{i,oc}$) positions were calculated. Among all the possible positions, Be prefers the Be_s site in diamond and this defect system is predicted to exhibit p-type semiconductivity with an activation energy of 1.2 eV. Although the ground state of a diamond supercell with a Be_s is $S = 1$, in a larger supercell with many substitutional Be defects, the magnetic moments are predicted to cancel each other, resulting in an antiferromagnetic system. Be will relax into an off-centre site $Be_{i,oc}$ when doped interstitially. This off-centre defect is less stable than the substitutional site by ~ 5.5 eV and is predicted to be a deep donor, with the donor level almost midway in the bad gap. Diamond shows a n-type semiconductivity with a shallow donor level 0.47 eV below the conduction band if doped by Be at the tetrahedral interstitial site. However, this defect is less stable than the off-centre site by ~ 3 eV. Therefore, according to our calculations, a shallow-donor state is less likely to be obtained in diamond if it is doped only with Be.

3) We also examined co-doping with Be-N clusters in diamond. Due to the positive binding energies between Be and N (4.11 eV for Be_i-N and 5.73 eV for Be_s-N), they enhance the incorporation of each other and should be situated at adjacent single substitutional sites to reach the ground state. The Be_sN_1 cluster is more stable than the Be_iN_1 by 7.21 eV. Among the Be_sN_x ($x = 1 - 4$) clusters, Be_sN_1 and Be_sN_2 do not exhibit semiconductive properties, while the Be_sN_3 and Be_sN_4 have introduced shallow donor defect levels, with activation energies of 0.51 and 0.46 eV predicted by EMM. A two-step preparation method was proposed for introducing Be_sN_3 and Be_sN_4 defects in diamond. First, a high concentration of VN_3 and VN_4 complexes could be made in diamond with pre-existing vacancies by incorporation of a high concentration of N. Then, Be could be incorporated into the VN_3 and VN_4 vacancies using low-dose ion implantation. This calculation may

provide a new idea for making n-type semiconductive diamond with shallow donor states.

Table 6.1. Formation energies and defect energy levels of Be and Be-N clusters in diamond calculated using hybrid functional HSE06 and 6-21G* basis set of C.

Defects		Formation Energies (eV)		Defect level
		$E_{f(1)}$	$E_{f(2)}$	
Be doping	Be_s	5.85	-3.07	$E_v + 1.20$
	$Be_{i,tet}$	14.57	5.64	$E_c - 0.47$
	$Be_{i,hex}$	13.84	4.92	$E_c - 1.31$
	$Be_{i,oc}$	11.43	2.51	$E_c - 2.71$
Be-N co-doping	Be_sN_1	3.65	-9.67	N/A
	Be_sN_2	1.26	-14.67	N/A
	Be_sN_3	3.69	-18.43	$E_c - 0.51$
	Be_sN4	6.36	-20.16	$E_c - 0.46$

6.2 Future work

Although we demonstrated that the magnetic signal from Co can be detected by MFM through 1 um of diamond, the next step would be to see if magnetic domains could be written into the embedded Co layer. This may be in the form of stripes or dots. If this were to be successful, this would demonstrate a read/write capability for magnetic storage – through a protective diamond layer. The stage after that would be to determine the minimum magnetic feature size that could be written and then read back, as this would determine the data storage density of the device.

In order to make magnetic diamond composites with tuneable magnetic properties and readable magnetic signals, other magnetic elements such as neodymium and its alloys may be used to imbue a stronger magnetism to diamond film. Neodymium and its alloys have larger magnetic moments than Co, so the magnetic signals can be read even through a thicker diamond protective layer. Another issue which needs to be overcome is the diamond film surface roughness. The high surface roughness hinders it to be scanned closely by MFM or other possible

instrument. Although the diamond crystal size can be reduced by using higher content of methane in the CVD gas feed, the diamond growth mechanism makes it hard to grow a diamond film with a flat surface on a rugged substrate. Therefore, more work needs to be done to improve this process.

Although the Be_sN_3 and Be_sN_4 clusters were predicted to be shallow donors in diamond, the complex structures indicate that it is not easy to make such clusters. The proposed two-step method provides a possible way to introduce such defects into diamond, but it cannot guarantee the results. There might be a more accurate way to control the doping process. Moreover, Be and N may form clusters of other forms in diamond, which require further calculations. Due to the great demand of n-type diamond, more dopants using single-element doping or co-doping strategies need to be studied by DFT calculations, which can provide a guide to the experimental work for making n-type diamond.

APPENDIX

PATTERNED Fe FILM ON SINGLE-CRYSTAL DIAMOND

Introduction

In parallel with the work described in Chapter 3 about Co/diamond magnetic devices, we also undertook a brief related collaborative project with Prof. Justin W. Wells and Johannes Bakkelund at NTNU. The aim of this was to test another magnetic metal film (iron) on diamond, and determine whether the diamond substrate would enhance or reduce the magnetic domains in the Fe film. The diamond films were prepared at Bristol, while the Fe films and surface analysis were performed in the NTNU by Johannes Bakkelund.

Experimental

Apart from Co, we also tested patterning Fe film on single-crystal diamond (SCD, 145-500-0275-01, 2.6 mm × 2.6 mm × 0.3 mm, <100>, Element Six Ltd.), with the aim of making isolated Fe film work as magnetic domains. First, a thin boron-doped diamond (BDD) layer (~ 375 nm) was grown on top of the SCD in a HFCVD reactor (H_2: 200 sccm, CH_4: 2 sccm, B_2H_6: 0.07 sccm, 45 min) in the diamond lab. The aim of this step is to make the SCD electrically conductive for further characterisation. Then, a thin Fe film (5 – 20 nm) was deposited on the SCD by e-beam evaporation through TEM grids (50 μm × 50 μm) as a mask. Surface magnetic properties (spin polarisation) of the samples were characterised by Photoemission Electron Microscopy (PEEM).

Results

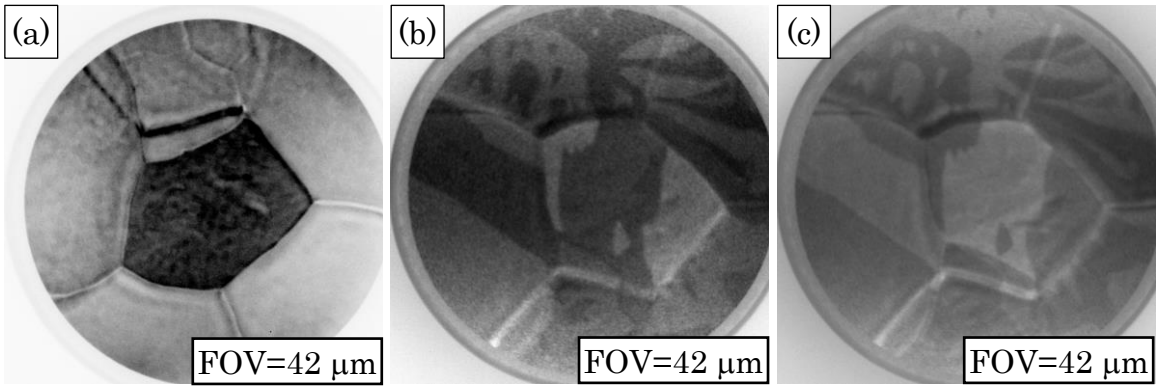

Figure A.1. PEEM images of bulk polycrystalline Fe (a) without spin filter, (b) with spin filter at an acceleration voltage of 11.0 eV and (c) with the spin filter set at an acceleration voltage of 12.3 eV. FOV: field of view. (Samples prepared and images taken by Johannes Bakkelund from NTNU).

As shown in Figure A.1a, without a spin filter, the PEEM images do not show any spin polarisation for the bulk Fe. In contrast, when a spin filter was employed, different magnetic domains were observed on the surface of bulk Fe, as shown in Figure A.1b and Figure A.1c.

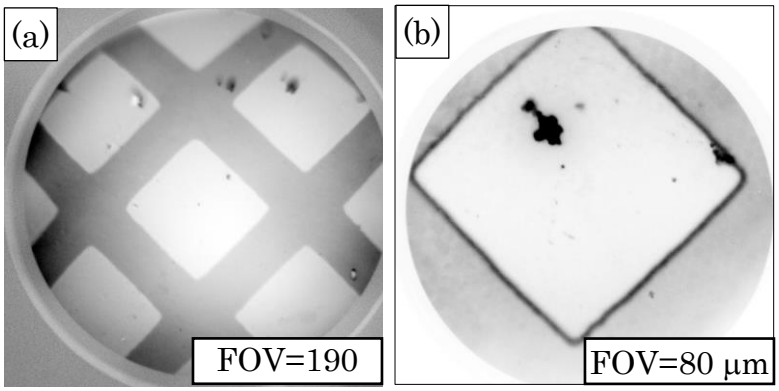

Figure A.2. (a) Patterned Fe film with a thickness of 5 nm on SCD and (b) enlarged view. (Samples prepared and images taken by Johannes Bakkelund from NTNU).

Figure A.2 shows the images of patterned Fe film on SCD. With the help of TEM grids, Fe film was patterned into isolated square features with width of ~ 50 nm. Each square could work as a magnetic domain, which can be magnetised individually.

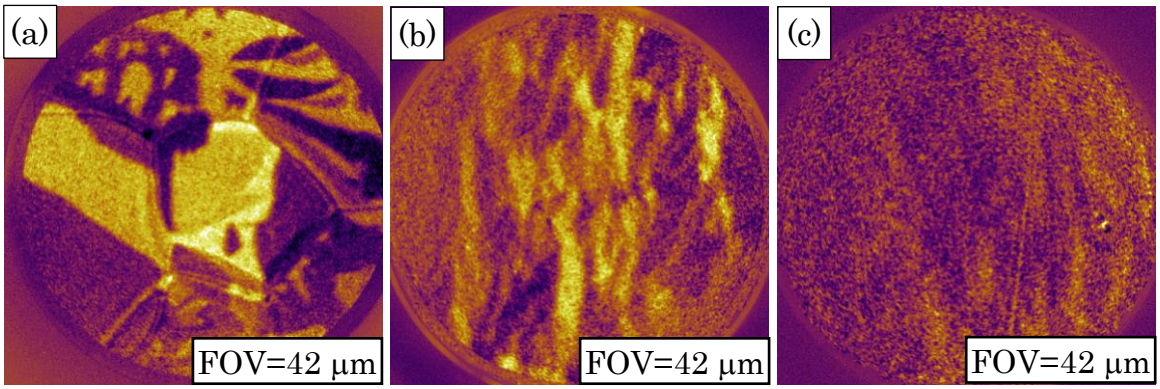

Figure A.3. PEEM magnetic domain images of (a) polycrystalline Fe, (b) 10 nm Fe film on Si, and (c) 20 nm Fe film on SCD. Different colours represent different magnetic domains. (Samples prepared and images taken by Johannes Bakkelund from NTNU)

Magnetic properties were revealed by PEEM. As shown in Figure A.3a, spin polarisation and magnetic domains are clear on the surface of a polycrystalline Fe. When Fe film (10 nm) was deposited on Si, the magnetic domains could also be identified (Figure A.3b). In contrast, when SCD was employed as a substrate for Fe film, the magnetic domain (Figure A.3c) was not as strong as that on Si, even though the film thickness (20 nm) has increased twice compared with that on Si. One possible explanation is that diamond ($\chi_m = -5.9 \times 10^{-6} cm^{-3} mol^{-1}$) is a more diamagnetic material than Si ($\chi_m = -3.12 \times 10^{-6} cm^{-3} mol^{-1}$) [1], and such diamagnetism can influence the spin polarisation of the thin Fe film. Nevertheless, this experiment proves that creating magnetic domains in isolated features on diamond is feasible, at least for Fe.

Reference

[1] W.M. Haynes, W.M. Haynes, D.R. Lide, T.J. Bruno, CRC handbook of chemistry and physics: a ready-reference book of chemical and physical data, Ninety-seven edition. ed., CRC Press, Boca Raton, Florida, 2017.